

Dynamics of smart materials in high intensity focused ultrasound field

Aarushi Bhargava

Dissertation submitted to the faculty of the Virginia Polytechnic Institute and State
University in partial fulfillment of the requirements for the degree of

Doctor of Philosophy
In
Engineering Mechanics

Shima Shahab, Chair
Eli Vlaisavljevich
Nicole Abaid
Raffaella De Vita
Reza Mirzaeifar

April 22, 2020
Blacksburg, Virginia

Keywords: high intensity focused ultrasound, shape memory polymers, piezoelectric,
smart materials, acoustic nonlinearity, nonlinear dynamics, controlled drug delivery,
ultrasound power transfer

Copyright © 2020, Aarushi Bhargava

Dynamics of smart materials in high intensity focused ultrasound field

Aarushi Bhargava

ABSTRACT

Smart materials are intelligent materials that change their structural, chemical, mechanical, or thermal properties in response to an external stimulus such as heat, light, and magnetic and electric fields. With the increase in usage of smart materials in many sensitive applications, the need for a remote, wireless, efficient, and biologically safe stimulus has become crucial. This dissertation addresses this requirement by using high intensity focused ultrasound (HIFU) as the external trigger. HIFU has a unique capability of maintaining both spatial and temporal control and propagating over long distances with reduced losses, to achieve the desired response of the smart material. Two categories of smart materials are investigated in this research; shape memory polymers (SMPs) and piezoelectric materials.

SMPs have the ability to store a temporary shape and returning to their permanent or original shape when subjected to an external trigger. On the other hand, piezoelectric materials have the ability to convert mechanical energy to electrical energy and vice versa. Due to these extraordinary properties, these materials are being used in several industries including biomedical, robotic, noise-control, and aerospace.

This work introduces two novel concepts: First, HIFU actuation of SMP-based drug delivery capsules as an alternative way of achieving controlled drug delivery. This concept exploits the pre-determined shape changing capabilities of SMPs under localized HIFU exposure to achieve the desired drug delivery rate. Second, solving the existing challenge of low efficiency by focusing the acoustic energy on piezoelectric receivers to transfer power wirelessly.

The fundamental physics underlying these two concepts is explored by developing comprehensive mathematical models that provide an in-depth analysis of individual parameters affecting the HIFU-smart material systems, for the first time in literature. Many physical factors such as acoustic, material and dynamical nonlinearities, acoustic standing waves, and mechanical behavior of materials are explored to increase the developed models' accuracy. These mathematical frameworks are designed with the aim of serving as a basic groundwork for building more complex smart material-based systems under HIFU exposure.

Dynamics of smart materials in high intensity focused ultrasound field

Aarushi Bhargava

GENERAL AUDIENCE ABSTRACT

Smart materials are a type of intelligent materials that have the ability to respond to external stimuli such as heat, light, and magnetic fields. When these materials respond, they can change their structural, thermodynamical, mechanical or chemical nature. Due to this extraordinary property, smart materials are being used in many applications including biomedical, robotic, space, microelectronics, and automobile industry. However, due to increased sensitivity and need for safety in many applications, a biologically safe, wireless, and efficient trigger is required to actuate these materials. In this dissertation, sound is used as an external trigger to actuate two types of smart materials: shape memory polymers (SMPs) and piezoelectric materials.

SMPs have an ability to store a temporary (arbitrarily deformed) shape and return to their permanent shape when exposed to a trigger. In this dissertation, focused sound induced thermal energy acts as a trigger for these polymers. A novel concept of focused ultrasound actuation of SMP-based drug delivery capsules is proposed as a means to solve some of the challenges being faced in the field of controlled drug delivery.

Piezoelectric materials have an ability to generate electric power when an external mechanical force is applied and vice versa. In this study, sound pressure waves supply the

external force required to produce electric current in piezoelectric disks, as a method for achieving power transfer wirelessly. This study aims to solve the current problem of low efficiency in acoustic power transfer systems by focusing sound waves.

This dissertation addresses the fundamental physics of high intensity focused ultrasound actuation of smart materials by developing comprehensive mathematical models and systematic experimental investigations, that have not been performed till now. The developed models enable an in-depth analysis of individual parameters including nonlinear material behavior, acoustic nonlinearity and resonance phenomena that affect the functioning of these smart systems. These mathematical frameworks also serve as groundwork for developing more complex systems.

*To my parents, brother, wingies, and Penny for keeping me on the right track and always
being there for me*

Acknowledgements

There are so many instances, situations, and people to be thankful for that I cannot mention them all here and I apologize for that. However, to bring me to a point where I am able to write a dissertation and earn a doctoral degree, few of these factors played a crucial role.

Most importantly, my adviser, Dr. Shima Shahab who has guided, taught, and mentored me into becoming a better researcher from a professional, ethical, and technical aspect. Along with her technical expertise, I immensely benefitted from many of her attributes including her open door policy which allowed me to discuss even the most primitive and futuristic ideas in detail. Her constant guidance in how to conduct productive research without getting lost in the million intricate details, to communicate my research effectively to others, and constant motivation has helped me to maintain a healthy attitude towards my research. She has put endless efforts in creating an environment where I could freely discuss my ideas, my critique, my failures and still take up more difficult challenges, without getting discouraged.

I thank all my committee members for their valuable time and feedback which enabled me to improve my research immensely. I thank Dr. Eli Vlasisavljevich, with who I had many lengthy discussions related to my research, career, and life in general. I admire his enthusiasm and zeal towards new ideas and am very grateful for his guidance throughout my graduate life. I have enjoyed working with Dr. Reza Mirzaeifar who has been very

kind, supportive, and patient in approaching a topic which was completely new to me and guided me at each step of that process. I thank Dr. Nicole Abaid, Dr. Romesh Batra, and Dr. Mark Cramer for being great teachers and teaching me many useful concepts that guided my research. I draw a lot of inspiration from their teaching methods and hope to implement them in my teaching style. I am thankful to Dr. Raffaella De Vita for her very useful inputs on my research and her encouragement.

Next, I would like to thank Manish for being a constant guiding light and giving me both technical and mental support that kept me grounded and in a working condition in these four years. Thank you to all my friends, especially Tapas, Mayank, Prerna, Sarthak, and Hannah for our cellar and Friday sessions which always gave me a much needed reprieve from my work, and for our many random as well as weird discussions. I thank my dance team Amrita and Atashi who were always there to hear me complain and nag, and still dance through it all. Thank you Shreya, Archana, Adbhut, Riya, and Pranav for restoring my faith in non-vegetarian food (because vegetarian is just not good enough). Thank you Puru and Saurabh for easing my transition to Blacksburg in my initial years of graduate life.

A special thanks to all my wingies, especially Kriti, and Tanya who have always been a phone call away and continue to keep me sane since my undergrad years.

I want to thank all of my labmates, Marjan, Omid, Eric, Vamsi, and Ahmed who have always been kind enough to help me whenever I was stuck with my experiments and bearing with my technologically challenged self (installing a software can be difficult but

you people always help me with it). I owe many of my ideas to the lengthy discussions and new concepts that I managed to learn from my labmates, especially Vamsi. I also want to thank Jerry Stieg, with whose help I wrote my first ever journal paper.

This research was partially funded by National Science Foundation (NSF), Grant No. ECCS-1711139.

Above all, I thank my parents, my brother and Penny for their constant support, motivation and their belief in me.

Attribution

Several colleagues and mentors aided in writing this dissertation. A brief description of their contribution is listed here:

Chapter 2: Kaiyuan Peng, Ph.D. and Dr. Mirzaeifar from the Mechanical Engineering department collaborated for modeling in ABAQUS. Jerry Stieg, an undergraduate student at the time helped with experiments

Chapter 3: Kaiyuan Peng, Ph.D. and Dr. Mirzaeifar from the Mechanical Engineering department collaborated for modeling capsule designs in ABAQUS.

Chapter 7: Vamsi C. Meesala, a Ph.D. student in MInDS Laboratory from Engineering Mechanics program collaborated for data collection and analysis.

Table of contents

List of figures.....	xvi
List of tables	xxviii
Chapter 1 : Introduction	1
1.1. Smart materials	1
1.2. Actuation mechanisms	3
1.3. Outline of the dissertation.....	5
References.....	9
Chapter 2 : Focused ultrasound actuation of shape memory polymers; acoustic-thermoelastic modeling and testing	2
Details of publication.....	2
Abstract.....	2
2.1. Introduction	3
2.2. Theory	8
2.3. Experimental results and model validation	25

2.4. SMP container design	46
2.5. Conclusions	49
Appendix A.....	50
A1. Focused ultrasound (FU) induced pressure field in medium; linear acoustic model	50
A2. DMA reported loss modulus and stiffness for various TBA-DEGMA compositions	54
A3. Fast fourier transform of pressure waveforms at focal point for various power and frequency; corresponding to Fig. 2.13.....	55
References.....	55
Chapter 3 : Analysis of ultrasound actuated shape-memory polymer based drug delivery containers in heterogenous environments.....	62
Details of publication.....	62
Abstract.....	62
3.1. Introduction	63
3.2. Theory	67

3.3. Results	68
3.4. 3d-printed SMPs	75
3.5. Conclusions	82
Appendix B	83
References	84
Chapter 4 : Coupling of nonlinear shape memory polymer cantilever dynamics with focused ultrasound field.....	88
Details of publication.....	88
Abstract.....	88
4.1. Introduction	89
4.2. Theory.....	93
4.3. Experimental results and model validation	107
4.4. Conclusions.....	121
Appendix C	122
References.....	127

Chapter 5 : Comparison of hydroelastic and thermal effects in fluid-loaded shape memory polymers in acoustic fields.....132

Abstract..... 132

5.1. Introduction 133

5.2. Theory 136

5.3. Experimental results and discussion 148

5.4. Conclusions 157

References..... 159

Chapter 6 : Contactless acoustic power transfer using high-intensity focused ultrasound162

Details of publication..... 162

Abstract..... 162

6.1. Introduction 163

6.2. Theory 168

6.3. Experimental validation and acoustic-structure interaction characterization 178

Conclusions..... 202

Appendix D.....	204
References.....	207
Chapter 7 : Focused ultrasound for enhanced wireless power transmission; experimental investigation	211
Details of publication.....	211
Abstract.....	211
References.....	225
Chapter 8 : Summary of contributions and prospective future research	227
8.1. Summary of contributions.....	227
8.2. Intellectual merits	233
8.3. Broader impacts.....	235
8.4. Awards, recognitions and media coverage:	236
8.5. Future prospects.....	237
References.....	239

List of figures

Fig. 2.1. 3D (top) and 2D (bottom) schematic representation of the concept for shape memory polymer (SMP) container under focused ultrasound (FU) irradiation. From left to right: the SMP container with a permanent shape is loaded with the particles then heated and deformed to a temporary shape. When delivered to the desired location, the container undergoes shape recovery under FU-induced thermal actuation and releases the loaded particles. The color bar is temperature in K. 7

Fig. 2.2. Schematic representation (left) and finite-element simulation snapshot (right) of acoustic wave from a focused wave source to a shape memory polymer filament. 13

Fig. 2.3. (a) Illustration of experimental setup; (1) the transducer resting on the bottom of the tank, (2) shape memory polymer sample is suspended by the sample holder at the surface of the water, (3) thermal imaging camera directed at the focal point of the transducer (indicated by a red circle), (4) and (5) the water tank, and the stand. (b) Experimental setup and (c) shape recovery of a SMP filament exposed to FU at different time steps during 20 seconds of FU exposure 27

Fig. 2.4. (a) Storage modulus and (b) Tan delta obtained from DMA tests for different compositions 28

Fig. 2.5. (a) Relative axial pressure and (b) temperature rise vs. time at focal point of transducer 31

Fig. 2.6. Thermal images of the SMP filament exposed to ultrasound at the focal point of the transducer and the corresponding deformation with time; here i denotes the initial angle at temporary shape and f denotes the final angle after shape recovery. The red and blue triangles define the highest and lowest temperature locations in the image (the triangles only account for the portion of the image within the circle) 32

Fig. 2.7. Graphical representation of four stages specified in the mechanical model (section 2.2.3.). The SMP is first deformed into a temporary shape and cooled down, followed by unloading. It is then heated by the temperature distributions obtained from the acoustic-thermal model to facilitate shape recovery; the

color bar is temperature in K. The inset shows the experimental and model predicted values of change in deformed angle of the SMP filament vs. time 34

Fig. 2.8. Surface images of the polymer filament exposed to (a) no acoustic power, and (b1) 25 W (b2) 50 W (b3) 75 W (b4) 100 W 35

Fig. 2.9. (a) Relative axial pressure magnitude and (b) linear and nonlinear relative pressure waveform at 6 W and 0.5 MHz 37

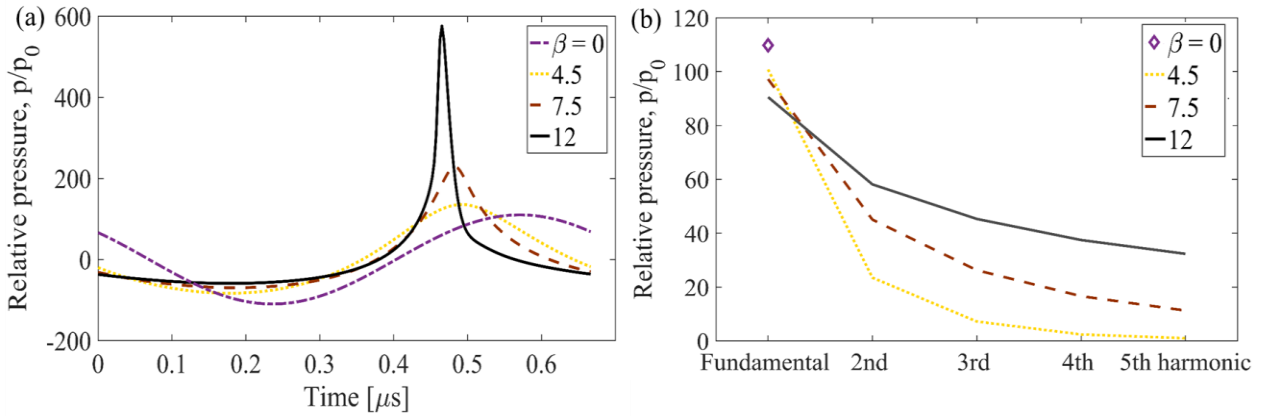


Fig. 2.10. (a) Relative pressure waveforms and (b) amplitudes for first five harmonics at focal point for various nonlinearity parameter β 38

Fig. 2.11. (a) Relative pressure waveforms (with reference pressure as maximum pressure magnitude p_{max}) and (b) relative pressure magnitude in frequency domain at different positions along axis of transducer 39

Fig. 2.12. (a) Relative pressure waveforms and (b) amplitudes for first five harmonics at focal point for various attenuation coefficient, $\bar{\alpha}_0$ 40

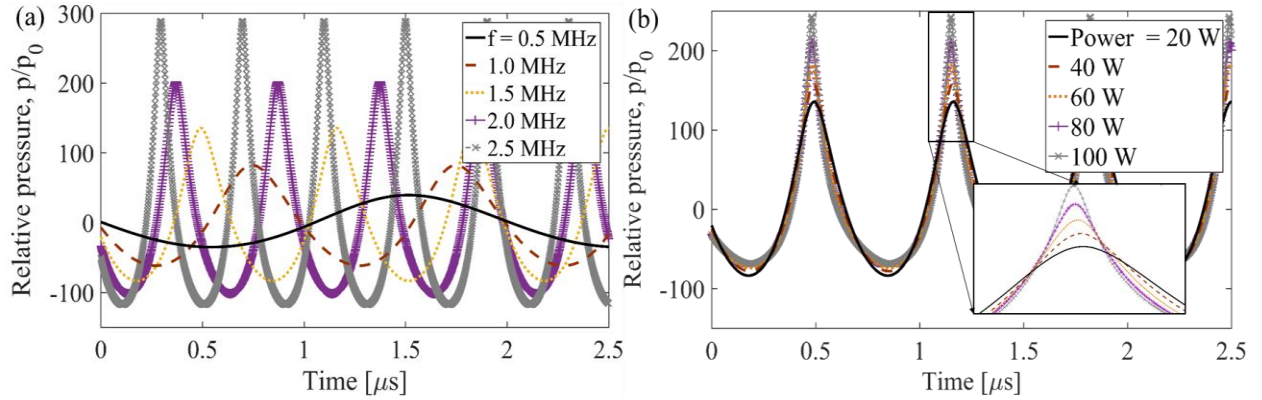


Fig. 2.13. Relative pressure (with reference as source pressure, p_0) at focal point in time domain for (a) various source frequency and 20 W input power; (b) various input power at 1.5 MHz 42

Fig. 2.14. Temperature vs. time plots at focal point for (a) various source frequencies and 20 W input power, and (b) various source input powers at 1.5 MHz. The inset graphs show the corresponding temperature rise rates ($^{\circ}\text{C}/\text{s}$)..... 42

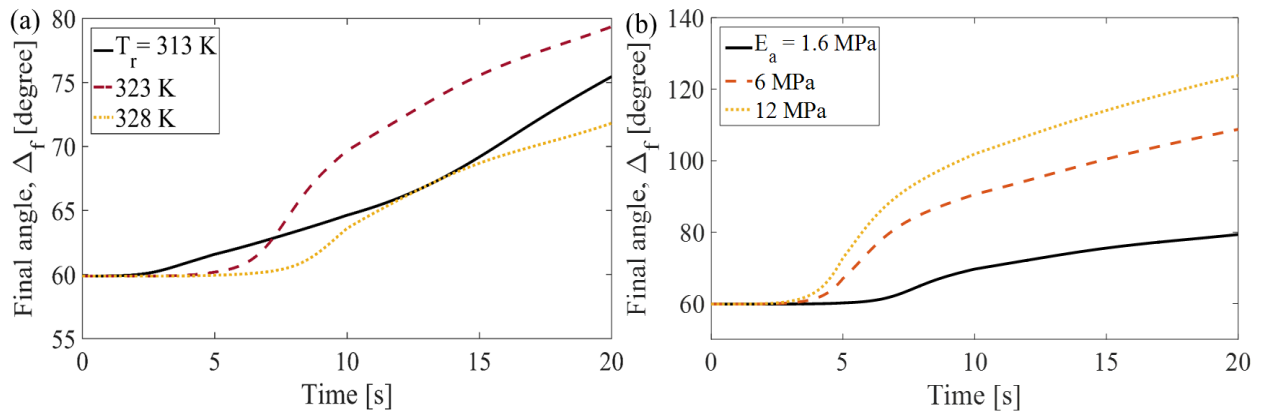


Fig. 2.15. (a) Final angle vs. time for various (a) recovery temperature and (b) elastic moduli of amorphous phase 43

Fig. 2.16. Final angle vs. time for various (a) thickness and (b) width of the SMP filament, (c) initial bending curvatures of the deformed area in mm, and (d) transducer input powers. 46

Fig. 2.17. Thermal distribution of a container kept at focal point of the transducer; the color bar is temperature in K. The intermediary stages represent the movement of the valve with time due to shape recovery under FU..... 48

Fig. 2.18. (a) Angular displacement of valve vs. transverse displacement of diaphragm of the container, (b) normalized velocity vs. time for diaphragm and valve, and (c) velocity vs. time for diaphragm and valve for the time range when they attain maximum..... 48

Fig. 3.1. The graph depicts the heating and cooling cycle of a flower shaped drug delivery container that undergoes ultrasound induced thermal actuation in the last stage, leading to release of the enclosed drug particles at the last stage..... 69

Fig. 3.2. Relative axial pressure along axis of symmetry of transducer in (a) water domain (b) blood artery inside heart. Both domains have SMP placed at the focal point. Normalization is done with respect to source pressure, p_0 70

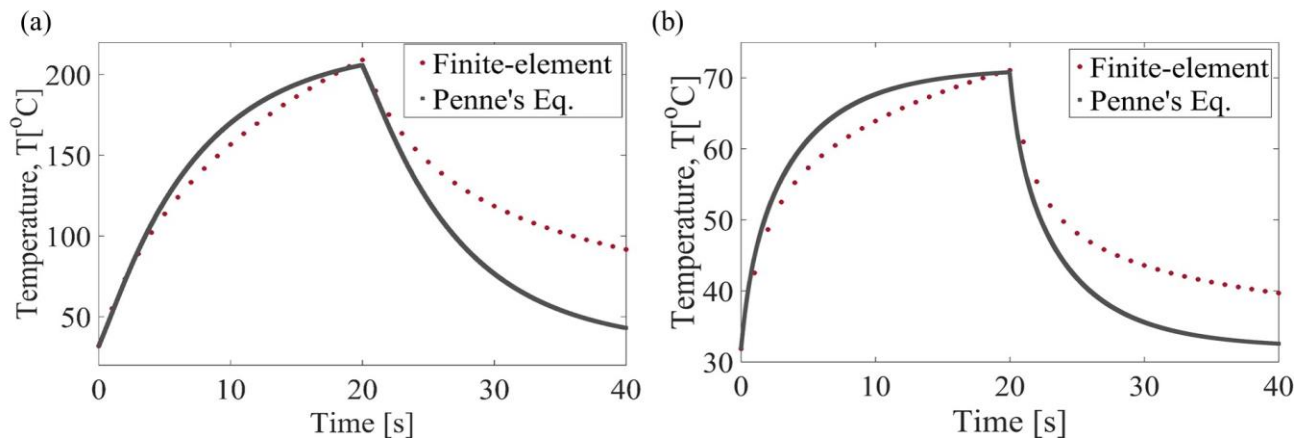


Fig. 3.3. Temperature rise at the focal point of transducer in (a) water domain (b) blood artery inside heart at 15W and 0.5 MHz. Both domains have SMP placed at the focal point..... 71

Fig. 3.4. 2D representations of (a) acoustic pressure field (Pa), (b) acoustic intensity (W/m²) and (c) Thermal field (°C) in a multilayer domain. (d) Temperature rise in different tissue layers during ultrasound actuation of SMP inside the artery..... 73

Fig. 3.5. Proposed capsule designs. (a) A flower shaped SMP capsule. (b) A box shaped capsule. (c) A star shaped capsule where drug particles are stored in the individual arms of the star and releases upon actuation of each arm separately..... 74

Fig. 3.6 (a) Angular displacement of valve with respect to diaphragm of the container (shown in inset) and (b) normalized velocity with respect to time in log scale, of the diaphragm and valve during shape recovery behavior. Normalization is done with respect to the maximum velocity. w is the diaphragm axial displacement. 75

Fig. 3.7. Normalized axial velocity of diaphragm for various (a) input power and (b) source frequency. Normalized angular velocity of valve for various (c) input power and (d) source frequency, during 20 s of ultrasound actuation. 76

Fig. 3.8. Dogbone shape with (S1) criss-cross and (S2) longitudinal 3d printed patterns. Rectangular samples with (S3) criss-cross, (S4) longitudinal, and (S5) transverse 3d printed patterns. Hollow gyroidal shape samples with (S6) small width and (S7) large width. 77

Fig. 3.9 (a) Schematic of the experimental setup consisting (1) FU transducer, (2) SMP filament, (3) positioning system, and (4) water tank. (b) Magnified images of a temporarily deformed SMP filament suspended in (b1) air and (b2) underwater. The polymer is kept such that the focal point lies inside the bent thickness of the filament. 79

Fig. 3.10. The amount of ultrasound induced shape recovery for different samples in Table 3.1, when polymer is suspended in air (Fig. 3.9b1) and underwater (Fig. 3.9b2). The angle change is the angle between the lines joining the center of the bent area (red dot in Fig. 3.9b) with the tip of the free polymer arm at the beginning and end of shape recovery. 81

Fig. 3.11. Shape recovery for (a) thin and (b) wide gyroidal samples in air, and (c) thin and (d) wide gyroidal samples immersed in water. The red dot traces the movement of the tip (red circle) as the sample undergoes shape recovery due to ultrasound actuation. 82

Fig. 4.1. Schematic of deformation of cantilever beam in pure bending due to end point force (positive Y direction) at the free end. The dashed line represents the original position of the beam. X and Y are the global coordinates of the system. 98

Fig. 4.2. (a) Illustration of the experimental setup; (1) thermal imaging camera directed at the focal point, (2) SMP cantilever filament exposed to FU, (3) HIFU transducer, (4) water tank and (5) positioning system. (b) Experimental setup of an SMP filament with fixed-free boundary conditions deformed in a temporary shape. (c) Experimental setup of a needle hydrophone mounted on the positioning system and exposed to FU. The tip of the needle lies at the focal point of the transducer. *R* and *Z* are the radial and axial coordinate axis for the transducer setup, respectively. 109

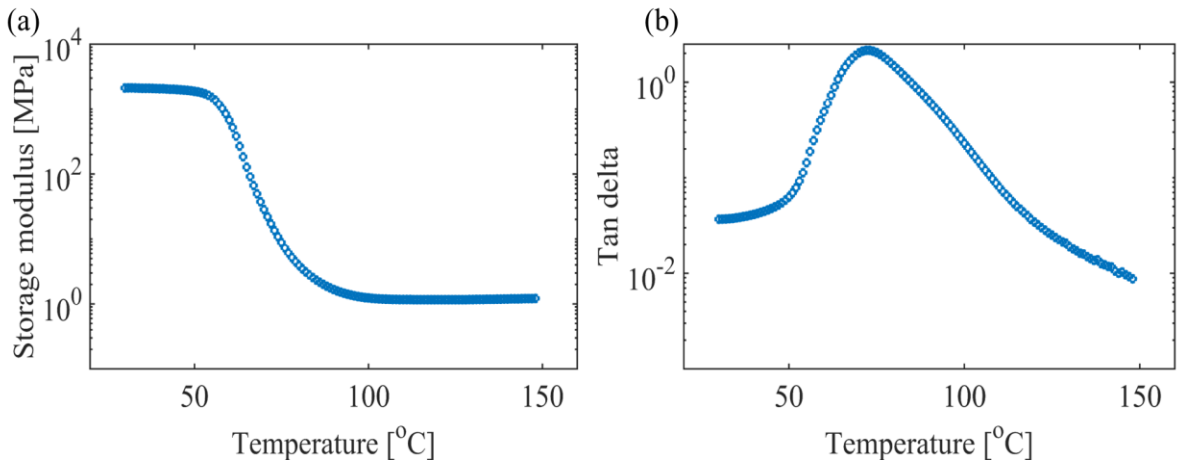


Fig. 4.3. (a) Storage modulus and (b) tan delta obtained from DMA tests for 95% TBA-5% DEGMA composition..... 110

Fig. 4.4. (a) Normalized pressure along axial axis and (b) normalized pressure waveform at focal point (0 mm) at 10 W and 0.5 MHz source frequency in water domain. 111

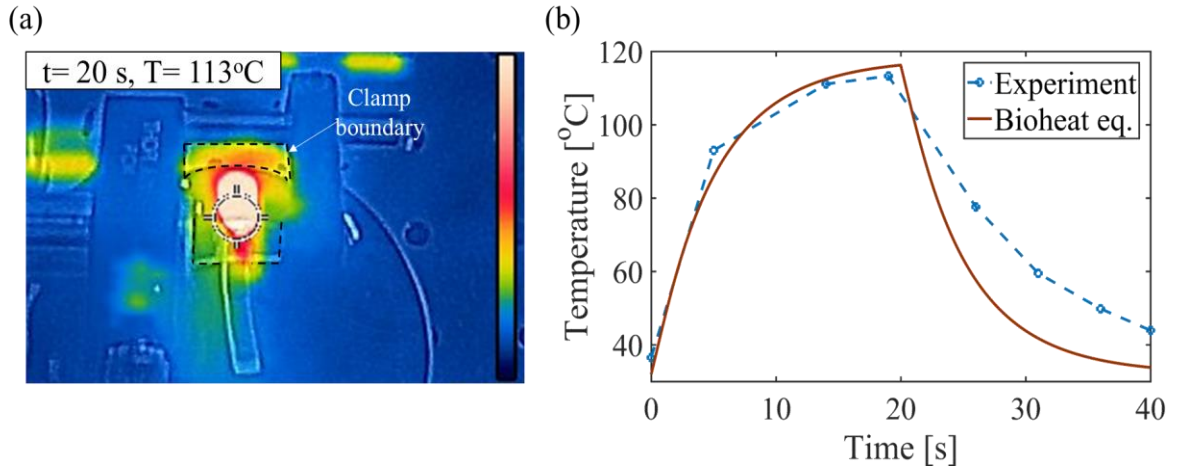


Fig. 4.5. (a) Thermal image of SMP cantilever during ultrasound actuation at 20 s and (b) temperature rise with actuation time at the focal point in SMP. 112

Fig. 4.6. Static loading of cantilever beam showing (a) strain and (b) angular displacement of the beam upon loading. (c) Transverse displacement of the beam at loading stage (force applied), $T > T_g$ and at unloading (no force applied), $T < T_g$ 114

Fig. 4.7. (a) Time history of the individual terms in Eq. 13 starting at the onset of the shape recovery at 7 s. Here F is the term defined in Eq. 19 at the corresponding time. (b) Beam deflection at various instances of time during shape recovery obtained from numerical solution of Eq. 13, hollow circle symbols, and method of multiple scales, dashed lines; the inset shows a magnified image where change in color represents the change in time. 119

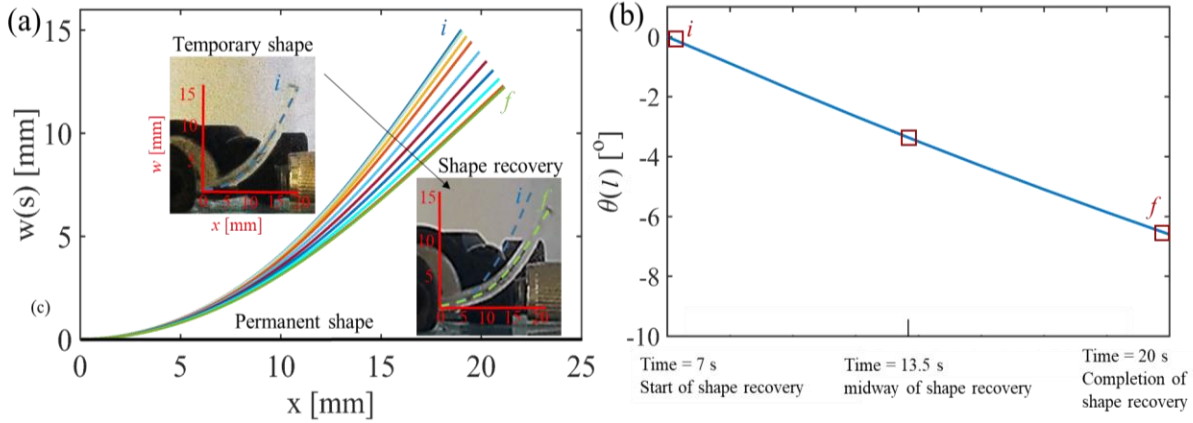


Fig. 4.8. (a) Transverse displacement during shape recovery. The insets show the deformed shape as well as the initial and final position of the beam. (b) Time history of the deformation angle of the free end of the beam. The square markers show the experimentally observed deformation angle at the corresponding time during shape recovery. Here *i* denotes the initial angle at temporary shape and *f* denotes the final angle after shape recovery..... 120

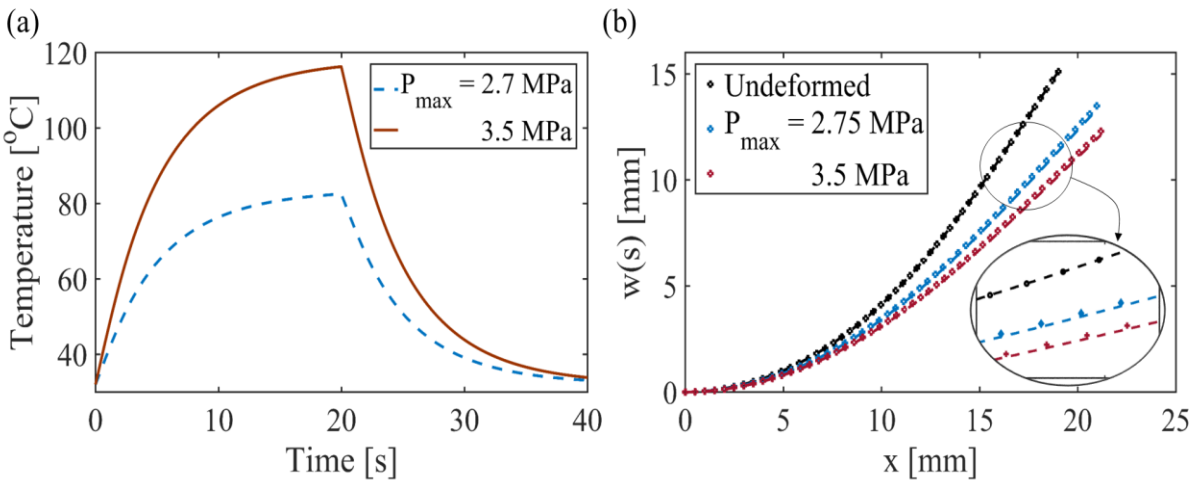


Fig. 4.9. (a) Time history of temperature rise inside SMP at focal point and (b) transverse beam deformation from experiment (dashed) and analytical model (circular symbols) at different P_{max} ; the inset shows a magnified image where change in color shows the change in P_{max} 121

Fig. 5.1. (a) Schematic of a cantilever beam under point force applied at $s = l_c$. (b) A schematic of the deformation of a differential element of length ds of the beam. The dashed lines represent original position of the beam..... 140

Fig. 5.2. Experimental setup with a V-shaped SMP filament suspended in (a) air and (b) water with the help of a positioning system. The letters i and f denote the initial and final position of the polymer arm at the start and end of ultrasound exposure, respectively. The red dot denotes the origin which is connected with the tip of the polymer arm through dotted lines. (c) Change in the angle of the dotted line as the polymer recovers from initial temporary shape to final shape, under ultrasound exposure..... 150

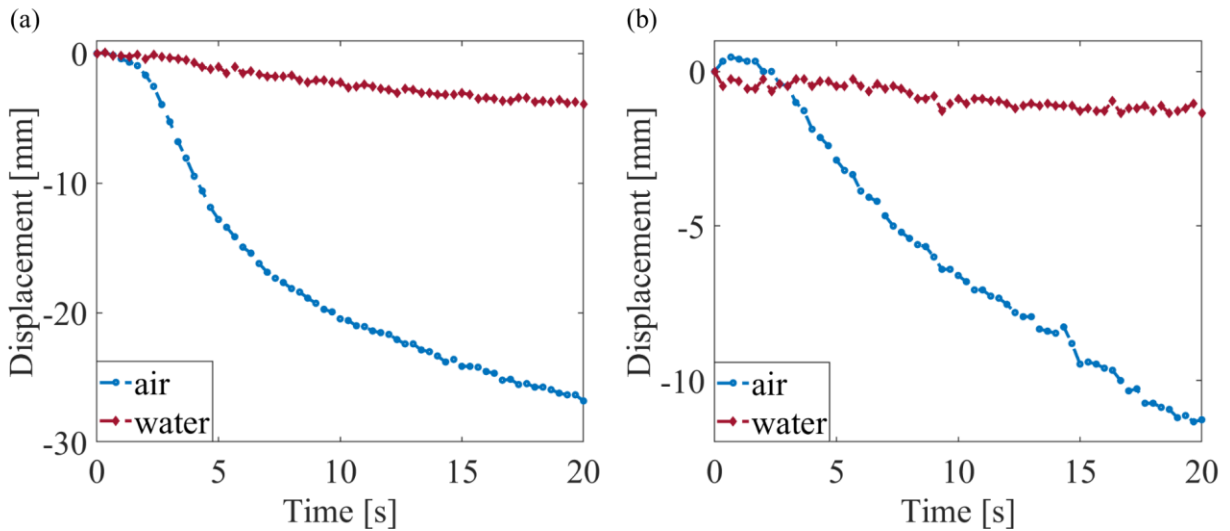


Fig. 5.3. Displacement of the tip of the free polymer arm in (a) Y axis and (b) X axis during shape recovery under FU exposure in air and underwater experiments, Fig. 5.2..... 151

Fig. 5.4. (a) Shape recovery behavior of a SMP Euler-Bernoulli cantilever beam calculated using Eqs. 22 and 24 for air and underwater experiments, respectively. The variable $x(s)$ represents the distance in the X coordinate, Fig. 5.1. (b) Variation of each term in Eq. 24 with time after the onset of shape recovery at 7 seconds..... 153

Fig. 5.5. Finite element predictions of the displacement of the free tip of the SMP cantilever beam in (a) vertical Y axis and (b) horizontal X axis, due to constant end point force in air and underwater..... 153

Fig. 5.6. (a) Finite element simulations showing the pressure field in setup where (a) SMP is exposed to both air and water mediums such that the top surface of polymer filament (farther from FU source) lies at the air-water interface. This situation is similar to the surrounding environment for the bent area of the V-shape filament in Fig. 5.2a, and (b) where SMP filament is immersed in a complete water domain. In both scenarios, the SMP is placed such that the focal point lies inside the polymer thickness. The color bar on the right side tells the magnitude of the total acoustic pressure. 156

Fig. 5.7. (a) Dissipated acoustic power acting as the heat source and (b) corresponding temperature rise in the SMP for the two simulation setups, where the polymer top surface is exposed to air in one setup and to water in the second, Fig. 5.6. 157

Fig. 6.1. Schematic representation of FU actuated piezoelectric receiver in a UPT system; the receiver is located in the focal area of the transducer in free-free boundary conditions. 169

Fig. 6.2. (a) Experimental setup to measure the pressure field of a HIFU transducer in a water tank using a needle hydrophone. (b) A magnified image of the needle hydrophone inside the tank. The tip of the hydrophone traverses in axial and radial directions of the transducer to map the acoustic pressure field. 180

Fig. 6.3. Pressure field of a HIFU source on (a) axial and (b) radial axis ($V_{in} = 4 \text{ V}$ and $p_0 = 8 \text{ kPa}$) in water at 0.5 MHz. 181

Fig. 6.4. Pressure waveforms at the focal point of the HIFU transducer operating at 0.5 MHz in (a) time and (b) frequency domain for various excitation levels in the water. Dashed and dotted lines in (a) represent KZK model calculations and experimental observations, respectively. Circular and square symbols represent KZK model calculations and experimental observations in (b), respectively. 183

Fig. 6.5. Pressure waveform at the focal point in water, obtained from KZK model, for (a) various source pressure, p_0 , at $\beta = 3.5$ and $\bar{A} = 5 \times 10^{-4}$, (b) various coefficient of nonlinearity, β , at $p_0 = 0.34 \text{ MPa}$ and $\bar{A} = 5 \times 10^{-4}$, and (c) various attenuation parameters, \bar{A} , at $p_0 = 0.34 \text{ MPa}$ and $\beta = 6$ 185

Fig. 6.6. Electrical impedance curves obtained from FE simulations (solid line) and experiments (dotted line) in (a) air and (b) water, for the APC760 disk..... 188

Fig. 6.7. (a) Experimental set up of the UPT system using HIFU source to excite a piezoelectric receiver at focal point (≈ 52 mm). The magnified image of the disk exposed to HIFU. The laser pointers fall on the top surface of the disk to mark the focal point of FU. (b) The voltage response of the receiver to signals of 10 ms of burst period having 100 μ s of burst (50 cycles) at 0.5 MHz. 190

Fig. 6.8. (a) The electrical impedance curve of the APC 760 disk in water calculated from FE formulation include five dominant resonant modes of the APC760 piezoelectric disk. (b) Normalized displacement profiles of the acoustically excited disk obtained from the FE model for the first four short circuit resonant frequencies; (b1) 0.18, (b2) 0.32, (b3) 0.50, and (b4) 0.63 MHz. The normalization is done with respect to the maximum displacement in each case. 194

Fig. 6.9. The impinging pressure wave on the disk (solid blue line) and resulting voltage output (red dashed line) of the piezoelectric disk upon acoustic excitation in (a,c, and e) time domain and (b,d, and f) frequency domain, at $p_0 = 0.34$ MPa and $f = 0.5$ MHz ($f = \omega_0/2\pi$). Case studies M1, M2 and M3 are shown by (a)-(b), (c)-(d), and (e)-(f) respectively. The arrows in the frequency domain plots point to the corresponding structural resonant frequencies in Fig. 6.8a. 200

Fig. 6.10. Amplitudes of voltage output solved in the frequency domain for case study M4. The excitation frequencies and amplitudes of the incident pressure field are the same as the frequency components of the pressure field in case study M3. 201

Fig. 7.1. Schematic illustrating the change in location of maximum power output from receiver with increasing level of HIFU source excitation..... 215

Fig. 7.2. (a) The experimental setup for obtaining the disk response in an acoustic nonlinear resonant HIFU field. Magnified images show (b) the hydrophone where the tip of the needle is the pressure recording entity, and (c) the APC disk suspended at the focal point. The axial axis is denoted as Z and radial axis

with X . The focal point is marked as $z = 0$ with negative scale towards the transducer, where z is the distance along the axial axis. 215

Fig. 7.3. Increasing levels of input voltage to the HIFU transducer, (a) and (c). Corresponding output voltage of the disk (b) and (c). The measurements are obtained at different positions along the axial axis. 217

Fig. 7.4. Variation of disk response with different levels of source excitation. The bottom row shows the three regions of (b) linear (L), (c) transition (T), and (d) saturation (S) on a magnified scale. 218

Fig. 7.5. (a) Axial and (b) transverse pressure fields of a HIFU source in water domain under linear conditions. The variable r denotes the radial distance along the along the radial axis, X , of the disk, with $r = 0$ denoting the center of the disk. The variables p and p_0 denote pressure at any observation point and at source, respectively. 220

Fig. 7.6. Impedance, Z , of the APC 760 disk in air and water. 221

Fig. 7.7. Pressure fields along radial axis at varying source pressure at (a) $z = 0$, (b) $z = -2$ mm, and (c) $z = -5$ mm 224

List of tables

Table 2.1. Mechanical and thermal properties of 95%TBA-5% DEGMA polymer.....	29
Table 2.2. Parameters for absorption, nonlinearity and gain used in KZK model.....	30
Table 2.3. Experimental and simulation predicted change in initial angle (degree) upon shape recovery process of the SMP filament.....	33
Table 2.4. Simulation predicted final angles (degree) upon shape recovery process for various polymer compositions	44
Table 3.1. Geometry of the samples used in experiments	78
Table 4.1. Thermomechanical properties of SMP in this study	119
Table C4.2. Mechanical and thermal properties of 95%TBA-5% DEGMA polymer.....	124
Table 6.1: Electroelastic properties of APC760 piezoelectric disk used in this study	189

Chapter 1 : Introduction

1.1. Smart materials

Smart or intelligent materials are engineering materials that respond to an external stimulus in a pre-determined controlled manner [1]. These materials can respond by changing their structural or material properties including change in shape, color, magnetic properties, thermal status, density, mechanical and radiation properties. The stimulus can be of chemical, thermal, magnetic, photo, electrical, and mechanical nature. Due to these extraordinary properties, smart materials are increasingly being used in a wide range of applications including wearable devices, biomedical purposes, space industry, as sensors and actuators in micro- and nano-electromechanical systems, robotics, and environmental and structural engineering [1-5].

Based on the response and the external stimulus, smart materials can be of different types. For example, shape memory polymers and alloys change their shape due to change in elastic modulus in response to heat, light, as well as chemicals [6]. Piezoelectric materials generate an electric current on the application of external mechanical force and vice versa [7]. Electrorheological fluids consist of electro-responsive particles that change the rheological properties of the material including viscosity, and shear stress, in response to an external electrical field [8]. Magnetostrictive materials consist of a magnetic body that converts the energy applied from an external magnetic field into elastic energy and undergoes deformation [9]. Few other examples of such smart materials include thermochromic, thermotropic, thermoelectric, photovoltaic and magnetorheological materials, which are currently incorporated

in many objects used in daily life [10, 11]. This work primarily focuses on two categories of smart materials: shape memory polymers (SMPs) and piezoelectric materials.

In recent years, shape memory polymers have received increased attention due to many advantages including biocompatibility, flexibility of mechanical properties, ease in manufacturing, low cost, light-weightness and ability to undergo large changes in shape [12-14]. These polymers can be broadly categorized as photo-, chemo-, and thermo- responsive, based on the nature of external triggering mechanism. Based on their chemical structure, there are four classes of SMPs: class I, covalently crosslinked glassy thermosets; class II, covalently crosslinked semi-crystalline networks; class III, physically crosslinked glassy copolymers; and class IV, physically crosslinked semi-crystalline copolymers [12]. SMPs can undergo one-way and multi-way shape memory effect based on the width and the number of transition zones in their thermomechanical cycle. In one-way shape memory behavior, only one temporary shape can be attained. Whereas, in multi-way behavior, multiple temporary shapes can lead to the same permanent shape. A two-way shape memory effect is also seen where two different stimuli are employed to create a heating- cooling effect, thus attaining a reversible shape memory behavior [15, 16]. This work focuses on the glassy thermo-responsive SMPs exhibiting one-way shape memory effect.

The other category of smart material explored in this work is piezoelectric material. The direct piezoelectric effect involves the polarization of the material and alignment of dipole moments, on the application of a mechanical force, while the reverse is true for the converse piezoelectric effect [17]. One of the most common piezoelectric material is PZT (lead-zirconate-titanate) due

to its large piezoelectric coefficient, easily tunable properties, and cheap availability [18]. With this unusual property, piezoelectric materials are used in many devices including biomedical, robotic, sensors, actuators, and energy harvesters. Dagdeviren *et al.* [19] used a stack of biocompatible piezoelectric actuator-sensor pairs to measure the mechanical properties of skin [7]. Piezoelectric induced electrical stimulation has been shown to motivate muscle cell differentiation by stimulating the functioning of transcription factors [20]. Piezoelectric materials also form the ideal choice for low power, portable, and small-sized energy harvesting devices, particularly for applications where use of conventional sources of energy is not possible. Ambient vibrations are the most common sources of energy for piezoelectric-based energy harvesters. Several works have investigated energy harvesting from oscillations of vibrating structures placed in turbulent wind and fluid flows [21-23]. Piezoelectric-based energy harvesters in wearable devices and biomedical implants have played a significant role in the advancement of healthcare industry [23-25].

1.2. Actuation mechanisms

With an increase in the usage of smart materials, the need for a suitable external stimulus for actuation, without hindering the smart materials' functioning, is crucial. For many sensitive applications such as in biomedical, space, and nuclear industry, use of a non-invasive and remote trigger is important. While many remote mechanisms such as electrical and magnetic fields, and light have been used to actuate different types of smart materials, they require presence of responsive particles in the material [26-29]. Such particles when not inherently present can

compromise the structural and chemical integrity of the material. Thus, a more compatible trigger is needed. In this work, acoustic actuation is investigated to fulfill this requirement.

In biomedical industry, ultrasound has been in use for many years for several purposes including therapy, imaging, tumor ablation, lithotripsy, and bone healing [30-33]. These applications rely on thermal, mechanical, and gas cavitation effects induced by ultrasound. Focused ultrasound (FU) has also been used for drug delivery using sound responsive microbubbles, liposomes, emulsions, nanodroplets, and micelles [34-37]. Ultrasound has also emerged as one of the most promising methods to transfer energy wirelessly due to biological safety, high-frequency operation, long-distance transmission, and no electromagnetic losses in acoustic waves [38]. The concept of acoustic energy transfer has advanced many applications including wireless charging of biomedical implants, through-wall transmission, and wireless operation of sensors in automobiles, space and other remote locations [39, 40]. Graham *et al.* [41] used ultrasound power transfer (UPT) technique to facilitate data transmission (1-2 Mbps) and communication through enclosure walls of a naval vessel. Maleki *et al.* [42] designed an ultrasound powered micro-oxygen generator implant which can provide in situ tumor oxygenation.

This dissertation aims to use high intensity focused ultrasound (HIFU) as a means to actuate and transfer energy to SMPs and piezoelectric materials. As compared to ultrasound generation from unfocused sources, FU enables concentration of energy in a tight focal spot. This localization of energy enables lower dissipation of energy to the surrounding and higher efficiency of the complete source-receiver system, as compared to systems having spherical or piston-like acoustic sources [43, 44].

1.3. Outline of the dissertation

This research broadly addresses two themes. First, ultrasound induced thermal actuation of SMPs (chapters 1-4) and second, focused UPT in piezoelectric receivers (chapters 5-6). Both these themes explore the fundamentals of acoustic wave propagation in heterogenous mediums, acoustic -structure interaction, and the consequent thermomechanical behavior of SMPs and electroelastic response of piezoelectric disks. Through experimentally-validated multiphysics mathematical frameworks, this work aims to provide an in-depth understanding of dynamics of smart materials in HIFU fields.

In chapter 2, the concept of HIFU actuation of SMPs is addressed with the aim of introducing a novel mechanism to address the current challenges in the field of controlled drug delivery (CDD). CDD refers to the method of transporting a medication/drug compound into human body in a safe and controlled manner and delivering drugs at a desired target location. Despite significant recent achievements in this field, controlled drug releasing systems still face major challenges in practice including chemical issues involved in synthesizing biocompatible drug containers, manipulating the releasing time of drugs in the body, delivering the drugs at a targeted location and utilizing a safe and noninvasive trigger to initiate drug release [45]. In this research, we introduce the concept of a thermo-responsive SMP-based drug delivery system and quantify its activation under FU. For the first time in literature, we perform multiphysics analytical and numerical modeling to estimate the FU stimulation of SMPs. Proof-of-concept experiments are conducted for a simple SMP filament to validate the mathematical model. The underlying mechanism of the proposed concept is based on FU induced generation of a

concentrated thermal field inside the polymer. This thermal field allows activation of the shape recovery process only in a selected part of the polymer, leading to a spatially controlled shape change of the SMP.

Chapter 3 extends the mathematical model developed in chapter 2 to estimate SMP actuation in a multi-medium environment. The model is modified to simulate response of a drug delivery capsule kept inside the artery of a heart. The modified multiphysics framework is validated with finite element simulations and shows how SMP actuation is affected due to acoustic waves propagation through multiple layers of tissues in a human body. The model is used to propose several geometrically optimized capsule designs that can provide the desired drug delivery rate in-vivo, just by manipulating the FU operating parameters. This chapter also experimentally explores 3d printing technique as a method to realize accurate and flexible capsule designs.

The work presented in chapter 4 addresses the requirement of a comprehensive understanding of the thermomechanical process of shape recovery under FU, as a precursor to building complex systems in any application. The past two decades have observed several constitutive models to capture the shape memory behavior [46, 47]. Following the constitutive model developed by Liu *et al.* [46] in combination with acoustic-thermal equations, this chapter develops for the first time, dynamic equations governing the motion of an ultrasound actuated SMP cantilever in all four shape recovery stages. Another aim of this chapter is to develop a simplified analytical expression to estimate the FU induced shape recovery for simple geometries of the polymer. The intention behind this aim is to eliminate the computationally intensive numerical modeling, proposed in chapter 2. To achieve these aims, the behavior of temperature dependent mechanical

properties of SMP during ultrasound exposure is studied using dynamic mechanical analyzer (DMA) tests. A model is built incorporating these properties to predict the shape memory behavior of a SMP based cantilever beam subjected to pure bending. The governing equations of motion are derived, using reduced order mathematical modeling. Finally, a simplified analytical dynamic solution is developed to estimate FU induced shape recovery using perturbation techniques for a weakly geometric nonlinear SMP cantilever. The scope of this work encompasses all applications of thermally actuated SMPs requiring shape recovery estimations such as SMP based switches and drug delivery containers among others.

In chapter 5, the FU-induced shape recovery is investigated for cases when SMP is completely immersed in water. The need for this research arises due to increasing number of robotic, MEMS, and biomedical applications in underwater/fluid environments. For such purposes, demand of SMPs is rising to provide an enhanced flexibility and functionality to underwater devices [48, 49]. However, the shape memory effect is significantly affected in underwater environments due to additional fluid loading and thermal cooling effects, as compared to SMP operation in air. Thus, this chapter performs an in-depth analysis of how these two effects influence the underwater SMP function when exposed to FU. The previously built framework in chapter 4 is extended to include the fluid loading effects. Experimental investigations and finite element simulations are also performed to quantify and segregate the degree of influence of these two effects on the shape recovery behavior of a SMP filament.

In chapter 6, UPT has been addressed from a novel perspective of achieving wireless energy transfer using HIFU. UPT has emerged as the most promising of all the other practiced

techniques to wirelessly transfer energy [50]. In recent years, UPT has found increasing applications in biomedical technology, data delivery and through-wall transmission [38, 51]. Although several works have showed the feasibility of this concept, many challenges including low UPT efficiency and lack of systematic investigations on understanding the physics of the system, are essentially nonexistent. Consequently, this work proposes to study the fully coupled physics by introducing a comprehensive multiphysics mathematical model. The problem of efficiency is solved by introducing FU actuation of piezoelectric receivers. Focusing of energy provides higher efficiency as compared to current acoustic sources as the entire energy is concentrated at the receiver location. This work also investigates the effects of finite size of the disk and acoustic nonlinearity; factors that have remained unreported in literature for UPT systems. Experimentally validated finite element multiphysics model is developed to explore the influence of individual parameters in the HIFU-UPT system.

In chapter 7, experimental investigations are reported for a finite size piezoelectric disk located in a FU standing wave field. The need for this research arises from the requirement of efficient UPT under FU excitation for powering of piezoelectric supported devices. However, under a long duration of excitation, standing waves form which significantly affect the performance of the receiver. Thus, a detailed investigation of performance enhancement techniques needs to be done for designing efficient systems. Thus, in this work, an in-depth analysis is done to understand the interplay of several factors for the first time. These factors include acoustic and material nonlinearities due to high levels of acoustic excitation, and acoustic resonance effects on a HIFU-UPT system.

Lastly, in chapter 8, a summary of conclusions of all the chapters is presented. Discussion on broader impacts, intellectual merits and future scope of this dissertation is done.

References

1. R. Bogue, *Assembly Automation* **32** (1), 3-7 (2012).
2. M. Mrinalini and S. Prasanthkumar, *ChemPlusChem* **84** (8), 1103-1121 (2019).
3. F. Greco and V. Mattoli, in *Piezoelectric Nanomaterials for Biomedical Applications*, edited by G. Ciofani and A. Menciassi (Springer Berlin Heidelberg, Berlin, Heidelberg, 2012), pp. 1-27.
4. W. G. Drossel, H. Kunze, A. Bucht, L. Weisheit and K. Pagel, *Procedia CIRP* **36**, 211-216 (2015).
5. S. Kamila, *American Journal of Applied Sciences* **10** (8), 876 (2013).
6. D. Ratna and J. Karger-Kocsis, *Journal of Materials Science* **43** (1), 254-269 (2008).
7. M. T. Chorsi, E. J. Curry, H. T. Chorsi, R. Das, J. Baroody, P. K. Purohit, H. Ilies and T. D. Nguyen, *Advanced Materials* **31** (1), 1802084 (2019).
8. Y. D. Liu and H. J. Choi, *Soft Matter* **8** (48), 11961-11978 (2012).
9. E. Hristoforou and A. Ktena, *Journal of Magnetism and Magnetic Materials* **316** (2), 372-378 (2007).
10. A. Seeboth, R. Ruhmann and O. Mühling, *Materials (Basel)* **3** (12), 5143-5168 (2010).
11. B. J. Park, F. F. Fang and H. J. Choi, *Soft Matter* **6** (21), 5246-5253 (2010).
12. C. Liu, H. Qin and P. Mather, *Journal of materials chemistry* **17** (16), 1543-1558 (2007).
13. H. Meng and G. Li, *Polymer* **54** (9), 2199-2221 (2013).
14. K. Wang, S. Strandman and X. X. Zhu, *Frontiers of Chemical Science and Engineering* **11** (2), 143-153 (2017).
15. G. Scalet, *Actuators* **9** (1), 10 (2020).
16. K. Wang, Y.-G. Jia and X. X. Zhu, *Macromolecules* **50** (21), 8570-8579 (2017).

17. S. Trolier-McKinstry, S. Zhang, A. J. Bell and X. Tan, *Annual Review of Materials Research* **48** (1), 191-217 (2018).
18. M. Chen-Glasser, P. Li, J. Ryu and S. Hong, *Piezoelectricity-Organic and Inorganic Materials and Applications*, 125-145 (2018).
19. C. Dagdeviren, Y. Shi, P. Joe, R. Ghaffari, G. Balooch, K. Usgaonkar, O. Gur, P. L. Tran, J. R. Crosby and M. Meyer, *Nature materials* **14** (7), 728-736 (2015).
20. D. M. Pedrotty, J. Koh, B. H. Davis, D. A. Taylor, P. Wolf and L. E. Niklason, *American Journal of Physiology-Heart and Circulatory Physiology* **288** (4), H1620-H1626 (2005).
21. X. Xie, Q. Wang and N. Wu, *International Journal of Engineering Science* **81**, 41-48 (2014).
22. R. A. Kishore, D. Vučković and S. Priya, *Ferroelectrics* **460** (1), 98-107 (2014).
23. M. Safaei, H. A. Sodano and S. R. Anton, *Smart Materials and Structures* **28** (11), 113001 (2019).
24. H. Zhang, X.-S. Zhang, X. Cheng, Y. Liu, M. Han, X. Xue, S. Wang, F. Yang, A. Smitha and H. Zhang, *Nano Energy* **12**, 296-304 (2015).
25. M. Safaei, R. M. Meneghini and S. R. Anton, *Smart Materials and Structures* **27** (11), 114007 (2018).
26. J. R. Kumpfer and S. J. Rowan, *Journal of the American Chemical Society* **133** (32), 12866-12874 (2011).
27. A. Lendlein, H. Jiang, O. Jünger and R. Langer, *Nature* **434** (7035), 879 (2005).
28. U. N. Kumar, K. Kratz, M. Heuchel, M. Behl and A. Lendlein, *Advanced Materials* **23** (36), 4157-4162 (2011).
29. P.-C. Yeh, H. Duan and T.-K. Chung, *Micromachines* **10** (10), 710 (2019).
30. D. L. Miller, N. B. Smith, M. R. Bailey, G. J. Czarnota, K. Hynynen, I. R. S. Makin and M. Bioeffects Committee of the American Institute of Ultrasound in, *J Ultrasound Med* **31** (4), 623-634 (2012).
31. C. M. Tempany, E. A. Stewart, N. McDannold, B. J. Quade, F. A. Jolesz and K. Hynynen, *Radiology* **226** (3), 897-905 (2003).
32. H. C. Klingler, M. Susani, R. Seip, J. Mauermann, N. Sanghvi and M. J. Marberger, *European urology* **53** (4), 810-818 (2008).

33. A. Z. Weizer, P. Zhong and G. M. Preminger, *Urologic Clinics of North America* **34** (3), 375-382 (2007).
34. Y.-Z. Zhao, L.-N. Du, C.-T. Lu, Y.-G. Jin and S.-P. Ge, *International journal of nanomedicine* **8**, 1621 (2013).
35. A. Marin, M. Muniruzzaman and N. Rapoport, *J Control Release* **71** (3), 239-249 (2001).
36. J. Medina, A. Salvado and A. del Pozo, *Int J Pharm* **216** (1-2), 1-8 (2001).
37. S. Ibsen, M. Benchimol, D. Simberg, C. Schutt, J. Steiner and S. Esener, *J Control Release* **155** (3), 358-366 (2011).
38. S. Ozeri and D. Shmilovitz, *Ultrasonics* **50** (6), 556-566 (2010).
39. M. G. Roes, J. L. Duarte, M. A. Hendrix and E. A. Lomonova, *IEEE Transactions on Industrial Electronics* **60** (1), 242-248 (2013).
40. M. R. Awal, M. Jusoh, T. Sabapathy, M. R. Kamarudin and R. A. Rahim, *International Journal of Antennas and Propagation* **2016** (2016).
41. D. J. Graham, J. A. Neasham and B. S. Sharif, presented at the Oceans 2009-Europe, 2009.
42. T. Maleki, N. Cao, S. H. Song, C. Kao, S. Ko and B. Ziaie, *IEEE Transactions on Biomedical Engineering* **58** (11), 3104-3111 (2011).
43. A. Bhargava, K. Peng, J. Stieg, R. Mirzaeifar and S. Shahab, *RSC Advances* **7** (72), 45452-45469 (2017).
44. A. Bhargava, K. Peng, J. Stieg, R. Mirzaeifar and S. Shahab, presented at the ASME 2017 Conference on Smart Materials, Adaptive Structures and Intelligent Systems, Utah, USA, 2017.
45. T. Xie, *Polymer* **52** (22), 4985-5000 (2011).
46. Y. Liu, K. Gall, M. L. Dunn, A. R. Greenberg and J. Diani, *International Journal of Plasticity* **22** (2), 279-313 (2006).
47. H. Tobushi, K. Okumura, S. Hayashi and N. Ito, *Mechanics of materials* **33** (10), 545-554 (2001).
48. T. Chen, O. R. Bilal, K. Shea and C. Daraio, *Proceedings of the National Academy of Sciences* **115** (22), 5698 (2018).

49. Y. Guo, Z. Lv, Y. Huo, L. Sun, S. Chen, Z. Liu, C. He, X. Bi, X. Fan and Z. You, *Journal of Materials Chemistry B* **7** (1), 123-132 (2019).
50. M. R. Awal, M. Jusoh, T. Sabapathy, M. R. Kamarudin and R. A. Rahim, *International Journal of Antennas and Propagation* **2016**, 14 (2016).
51. D. J. Graham, J. A. Neasham and B. S. Sharif, *IEEE Transactions on industrial electronics* **58** (10), 4972-4980 (2011).

Chapter 2 : Focused ultrasound actuation of shape memory polymers; acoustic-thermoelastic modeling and testing

Details of publication

Co-authors: Kaiyuan Peng, Jerry Stieg, Reza Mirzaeifar, and Shima Shahab

Citation: Bhargava A, Peng K, Stieg J, Mirzaeifar R and Shahab S, 2017, Focused ultrasound actuation of shape memory polymers; acoustic-thermoelastic modeling and testing RSC Adv. **7** 45452–69

Bhargava, A., Peng, K., Stieg, J., Mirzaeifar, R., and Shahab, S., Ultrasound Actuation of Shape-Memory Polymer Filaments: Acoustic-Thermoelastic Modeling and Testing. Proceedings of the ASME 2017 Conference on Smart Materials, Adaptive Structures and Intelligent Systems. Volume 2: Modeling, Simulation and Control of Adaptive Systems; Integrated System Design and Implementation; Structural Health Monitoring, September 18–20, 2017, Snowbird, Utah, USA, V002T04A014, ASME . (**Best Student Paper Award – 1st place**)

Abstract

Controlled drug delivery (CDD) technologies have received extensive attention recently. Despite recent efforts, drug releasing systems still face major challenges in practice, including low efficiency in releasing the pharmaceutical compounds at the targeted location with a controlled time rate. We present an experimentally-validated acoustic-thermoelastic mathematical framework for modeling the focused ultrasound (FU)-induced thermal actuation of shape

memory polymers (SMPs). This chapter also investigates the feasibility of using SMPs stimulated by FU for designing CDD systems. SMPs represent a new class of materials that have gained increased attention for designing biocompatible devices. These polymers have the ability of storing a temporary shape and returning to their permanent or original shape when subjected to external stimuli such as heat. In this work, FU is used as a trigger for noninvasively stimulating SMP-based systems. FU has a superior capability to localize the heating effect, thus initiating the shape recovery process only in selected parts of the polymer. The multiphysics model optimizes the design of a SMP-based CDD system through analysis of a filament as a constituting base-structure and quantifies its activation under FU. Experimental validations are performed using a SMP filament submerged in water coupled with the acoustic waves generated by a FU transducer. The modeling results are used to examine and optimize parameters such as medium properties, input power and frequency, location, geometry and chemical composition of the SMP to achieve favorable shape recovery of a potential drug delivery system.

2.1. Introduction

In the field of medicine, delivery of drugs in a controlled manner is being realized as a key factor for treating infections, cancer and many other diseases. Drug delivery refers to the methods for transporting a medication/drug compound into human body in a safe manner. Controlled drug delivery (CDD) technology has received extensive attention during the past three decades [1], mainly because of numerous advantages of this technology compared to the conventional methods[2]. Despite significant recent achievements, controlled drug releasing systems still face major challenges in practice including chemical issues involved in synthesizing biocompatible

drug containers, manipulating the releasing time of drugs in the body, delivering the drugs at a targeted location and utilizing a safe and noninvasive trigger to initiate drug release [3, 4]. In this research, we leverage the experimental, analytical and computational techniques to investigate the feasibility of using shape memory polymers (SMPs) and focused ultrasound (FU) for designing a CDD system. The design is used in a conceptual novel mechanism for simultaneously opening the drug container and pushing the particles out, which will significantly improve the rate of drug releasing at a targeted location.

Smart materials are engineering materials that have one or more properties, which can be changed by external stimuli such as temperature, electric field, magnetic field or stress [5-8]. SMPs are a relatively new class of smart materials that have the ability of storing a temporary shape and returning to their permanent or original shape [9] when subjected to external stimuli such as heat, light or ultrasound [10-14]. The shape memory responses to these stimuli fall broadly into three categories namely, chemo-responsive [15, 16], thermo-responsive and photo-responsive. While thermo-responsive SMPs absorb heat to generate molecular motion and modify stiffness above a transition temperature for shape recovery, the shape memory effect in chemo-responsive SMPs is due to interaction with a solvent which alters/softens the transition component in the SMP. The plasticizing effect of the bound solvent molecules on the bonds of SMP molecules such as seen in the peak shift of C=O bond in SMP in DMF solvent evidenced by Lu *et al.* [16], alters the transition temperature of chemo-responsive SMPs to initiate shape memory effect. Compared to other shape memory materials such as shape memory alloys [17-19] and shape memory ceramics [20]. SMPs are light weight, inexpensive, and can recover large

deformations [21-23] in a controlled manner. Development of SMP-based devices for medical applications such as stents for cardiovascular systems and self-tightening sutures has gained a lot of attention recently [3, 9, 24, 25]. Xue *et al.* [26] developed self-expandable stents which exhibited $\approx 98\%$ shape recovery at body temperature at a much faster rate compared to the best known self-expandable stents. Because of these advantages, during the past decade, SMPs have received increased interest in biomedical applications [27] and advancing CDD systems [28]. At present, the commercially available drug release devices still lack the capability of delivering drugs in a spatially and temporally controlled manner [29]. The combination of SMPs and CDD leads us to a multidisciplinary research in order to reduce the drug side effects in patient body and frequency of taking drugs by patient, which means having more reliable and accurate treatment.

The shape memory effect of SMPs relies heavily on the external trigger provided. For use in *in vivo* applications, thermal activation through body heat has often been relied upon to trigger shape recovery [4]. However, there is a need for more flexible stimuli as compared to fixed body heat temperature. Consequently, noninvasive triggers such as light [30-32], magnetic field [33, 34], electrical field [35, 36], and radiofrequency waves [34] have been employed. These triggers require special components such as magnetic or fluorescent particles to generate response, which can compromise the biodegradability and biocompatibility of SMPs. Thus, use of a safer and effective trigger is of utmost importance to achieve remotely controlled shape recovery. The use of FU as an external stimulus fulfills the above criteria. The underlying mechanism involves focusing ultrasound into a tight spot in domain area of millimeter scale, which causes selective

and controlled heating of the medium at the spot. This localized heating also eliminates the need of incorporating special or responsive particles in the medium as shape deformation occurs due to heating caused by viscous shearing oscillation of molecules under ultrasound exposure.

Employing high-intensity FU has been researched for biomedical purposes for many years [37, 38]. The higher penetrating ability of acoustic waves as compared to light has been used for selective tissue necrosis in controlled volumes. Studies have been conducted reporting the use of ultrasound in acoustic energy transfer systems [39-42] and for drug delivery [43-45] especially from polyelectrolyte micro-containers [46], multilayered capsules [44, 47], and polymer micelles [48-51]. In their study, Kost *et al.* [43] irradiated ultrasound on a polymer matrix for releasing drugs entrapped in the matrix. Liu *et al.* [52] and Han *et al.* [53] conducted proof-of-concept experiments using FU to demonstrate shape recovery process of SMPs and obtain various intermediate shapes with the help of FU. The research done in recent years demonstrating the effect of FU on shape recovery behavior of polymers has been experimental in nature. The very limited literature lacks fully coupled modeling efforts to analytically solve the underlying problem and optimize a SMP-based CDD design.

In this research, for the first time, we perform a multiphysics analytical and numerical modeling to optimize the design of a thermo-responsive SMP-based drug delivery system and quantify its activation under FU. This model provides the foundation for designing and testing SMP capsules, an example of which is schematically shown in Fig. 2.1 and further will be discussed in section 2.4. The proposed design has the unique capabilities of (i) releasing the loaded drug at a controlled rate and (ii) releasing the drug accurately at localized areas, thus, addressing the two

major challenges of designing CDD systems. This design is based on the mechanism for simultaneously opening the drug container and pushing the particles out, which will significantly improve the drug release rate. The developed model in Fig. 2.1, uses FU as a trigger for stimulating the drug capsules in order to control the location of drug release. FU localizes the heating effect on a small area (about 1 mm²). This concentrated thermal field allows the activation of the shape recovery process only in a selected part of the polymer, even for the polymer immersed in water or living body [3, 52, 54, 55]. By turning off the ultrasound beam the shape recovery process can be paused at any time, which allows the polymer to have an intermediate but a stable shape [3, 55]. Therefore, by using FU we are able to release the loaded drug in a switchable manner.

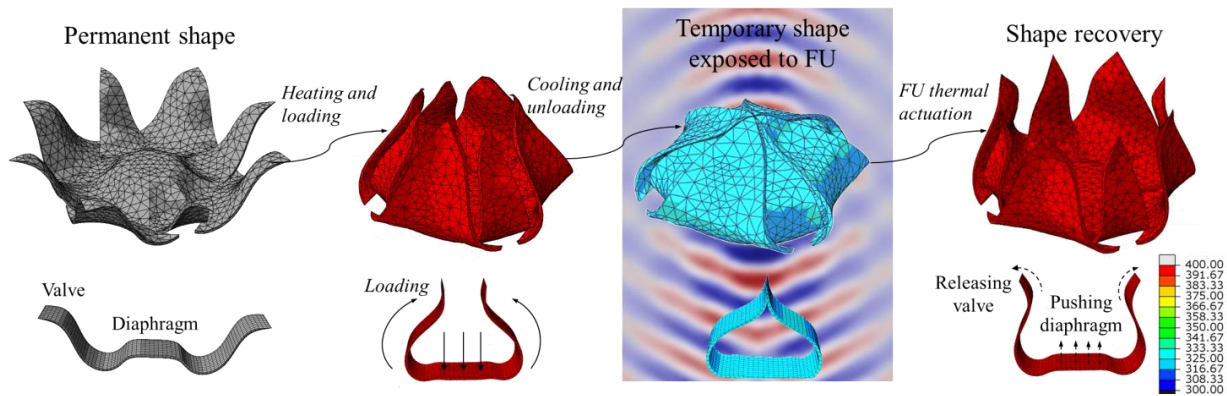


Fig. 2.1. 3D (top) and 2D (bottom) schematic representation of the concept for shape memory polymer (SMP) container under focused ultrasound (FU) irradiation. From left to right: the SMP container with a permanent shape is loaded with the particles then heated and deformed to a temporary shape. When delivered to the desired location, the container undergoes shape recovery under FU-induced thermal actuation and releases the loaded particles. The color bar is temperature in K.

In this chapter, we implement a comprehensive set of analytical, numerical and experimental studies to design, analyze and test a coupled FU and SMP representative mechanism at a millimeter-scale framework. The model studies the acoustic-structure interaction of FU with SMP-based filaments to establish the relationship between input parameters (such as input power and frequency) with the acoustic, thermal and stress fields and shape recovery of SMPs. Medium properties such as absorption and nonlinearity, which significantly affect the pressure field of a propagative wave [56], are studied to analyze their influence on the shape memory behavior of polymer. The analytical-numerical model is validated through experiments using a high-intensity focused transducer in a water tank. Various concepts can be considered for the design of a SMP container subjected to FU, similar to the example shown in Fig. 2.1, however, the modeling effort is focused on the special case of a filament, as fundamental element of any container, stimulated by FU.

2.2. Theory

To design a SMP-based drug delivery system, development of a robust theoretical model which predicts the FU induced acoustic and thermal fields and subsequent mechanical behavior of SMP is essential. In this work, we present multiphysics acoustic-thermoelastic modeling for ultrasound actuation of SMP filaments. The analytical-numerical model is divided into three interconnected parts. The first part studies the focused acoustic pressure field in a multilayer domain which includes a SMP filament submerged in fluid, using Khokhlov-Zabolotskaya-Kuznetsov (KZK) equation [57, 58]. The equation is solved in a hybrid time-frequency domain using operator-splitting method and accounts for the effects of absorption, diffraction and

nonlinear distortion in the medium. The second part provides a model based on Pennes's Bioheat equation [59] to estimate the thermal field developed in SMPs as a result of FU. The temperature distribution of the polymer obtained from the second part is given to the third part which provides a framework to predict the mechanical stresses developed in SMPs and consequent shape recovery. A mechanical model is formulated by a compressible neo-Hookean constitutive equation, which assumes the SMPs behave as a thermoelastic material and predicts the thermally induced shape memory effect under FU. The constitutive model is numerically implemented in a user material subroutine (UMAT) in ABAQUS to model the deformation of the filament.

The two common models used for simulating focused acoustic waves are KZK and Westervelt equations [57, 58, 60]. In both models, the approach is based on the equations of continuum mechanics. However, existing analytical solutions fail to accurately incorporate the effects of nonlinearity, diffraction and absorption which strongly affect the acoustic wave propagation. Therefore numerical approaches have been adopted to obtain the solutions of focused hydroacoustic problems [61]. The KZK equation is based on parabolic approximation and is applicable for quasi-planar waves of limited high frequencies [58]. The equation holds good for directional sound beams and for focused transducers with small aperture angles (not more than $16^\circ - 18^\circ$) [62, 63]. However, Sonesson *et al.* [64, 65] have proved the applicability of KZK equation at higher aperture angles with good accuracy. The method assumes forward-wave propagation with nonlinear distortion in a direction normal to the propagation planes. On the other hand, Westervelt equation is a full-wave solution for wider aperture angles and highly focused beams. However, Westervelt equation requires fine discretization which makes it more

time and memory inefficient. In this work, KZK equation is chosen to model the acoustic field of FU to reduce the computational cost.

Several theoretical models have been developed based on KZK equation, which adopt different numerical techniques to solve for the effects of absorption, diffraction and nonlinearity in the medium. However, the numerical algorithms become very time and memory consuming. Therefore, to reduce the computational burden, several approximations are made [56, 66, 67] which include assuming one way (forward) wave propagation [68], solving governing equations in 2D when the system is axisymmetric [69], optimization of spatial grid [70] and using a perfectly matching layer at the boundaries of computational grid domain to reduce spatial grid size and to avoid reflections from the edges of the grid [67]. The most widely used numerical technique to solve KZK equation is a frequency-domain technique called the spectral method [71]. The method substitutes a Fourier expansion of sound pressure in the KZK equation and then solves numerically. The method originally designed for monochromatic waves and tone bursts, was later modified to include the calculations for far field [72], focused beams [56] and non-axisymmetric sources [73]. In order to overcome the problem of high computational time required for solving nonlinearity term with spectral method, hybrid method was adopted by several researchers [74, 75]. The hybrid method based on KZK equation solves for the effects of absorption and diffraction in frequency domain and of nonlinearity in time domain. Pectorius and Blackstock [76] validated the combined time and frequency-domain approaches through experiments to study the propagation of plane, finite-amplitude sound in the medium. Several

others also adopted a pure time-domain algorithm to solve KZK equation for computational efficiency [70, 77].

The novel feature of the multiphysics model developed in this work is to use KZK equation with the hybrid method to study the behavior of SMPs in an acoustic field (where multiple domains are involved and medium nonlinearity is pronounced) and couple it with thermal and mechanical models to build a comprehensive framework for acoustic-thermal-structural study of SMPs. The theory is divided into three interconnected sections (2.2.1-2.2.3). Section 2.2.1 predicts the focused acoustic pressure field of SMPs immersed in water using nonlinear KZK equation which includes the effects of nonlinearity, absorption and diffraction (a linear analytical model for the pressure field due to focused transducers without including any nonlinear effects is given in supplementary document). We adopt the hybrid time-frequency approach using operator-splitting technique [61] which accounts for these three effects separately at every integration step. Section 2.2.2 provides a model for calculating the thermal field developed in SMPs as a result of focused acoustic pressure. It uses the acoustic pressure field calculated in section A as an input to evaluate the heating response of the polymer. This FU induced thermal field triggers a mechanical response in the polymer and deforms the SMP. Section 2.2.3 provides a framework to estimate these mechanical stresses using the absorbed heat calculated in section 2.2.2 as an input to the framework and predicts the consequent shape recovery of the SMP.

For validation purposes, first we verify our coupled acoustic-thermoelastic theoretical model with simulations in COMSOL Multiphysics and experiments under linear conditions. Then, the developed coupled KZK-Penne's Bioheat theoretical model is employed to extract and optimize

the acoustic and thermal fields under nonlinear effects, which cannot be easily simulated in a standard FEM environment. It is worth noting that although applying the nonlinear parameters in the COMSOL finite-element framework is practically difficult, it is still a valuable tool as it enables us to base the further analysis for optimizing the design of SMP-based drug delivery systems with complex geometrical 3D configurations. The simulation (ABAQUS) predicted deformation in SMP upon shape recovery process is compared with experiments as well.

2.2.1. Multiphysics modeling of acoustic-SMP interaction; nonlinear acoustic model

KZK equation is used to predict the nonlinear acoustic pressure field in fluid and SMP domains (shown in Fig. 2.2) using a numerical approach. This model incorporates absorption, diffraction and nonlinear effects of the medium in the wave equation. KZK equation is derived from mass and momentum conservation equations. In cylindrical form, it is given as [57, 58, 60]

$$\frac{\partial^2 p}{\partial z \partial t'} = \frac{c}{2} \nabla_{\perp}^2 p + \frac{\xi}{2c^3} \frac{\partial^3 p}{\partial t'^3} + \frac{\beta}{2\rho c^3} \frac{\partial^2 p^2}{\partial t'^2} \quad (1)$$

where z is the distance in axial direction Z , t' is the retarded time, $t' = t - z/c$, for the sound wave to travel with speed c and p is the acoustic pressure at arbitrary observation point, Q (Fig. 2.2). The first term on the right-hand side of the Eq. 1 represents diffraction, the second term signifies absorption with ξ as diffusivity parameter and nonlinearity is given by third term, where $\beta = 1 + B/2A$ is the coefficient of nonlinearity and B/A is defined as the nonlinearity parameter. The Laplacian ∇_{\perp}^2 in Eq. 1 in axisymmetric coordinates is given as $\nabla_{\perp}^2 = (\partial^2 / \partial R^2 + \partial / R \partial R)$, where R is the radial distance in Y coordinate. The boundary

condition for the characteristic source pressure, p_0 , of the focused transducer with focal distance D , is given as $p = p_0 \hat{f}(R, t + R^2 / 2cD)|_{z=0}$ [56, 70], where $\hat{f}(R, t + R^2 / 2cD)$ shows the dependence of time on spatial dimension in source plane. A non-dimensional form of the KZK equation is

$$\frac{\partial^2 \bar{p}}{\partial \tau \partial \bar{z}} = \left(\frac{1}{4G} \nabla_{\bar{r}}^2 + \bar{A} \frac{\partial^3}{\partial \tau^3} \right) \bar{p} + \frac{\bar{B}}{2} \frac{\partial^2 \bar{p}^2}{\partial \tau^2} \quad (2)$$

where the non-dimensionalized pressure, \bar{p} , is given as $\bar{p} = p / p_0$.

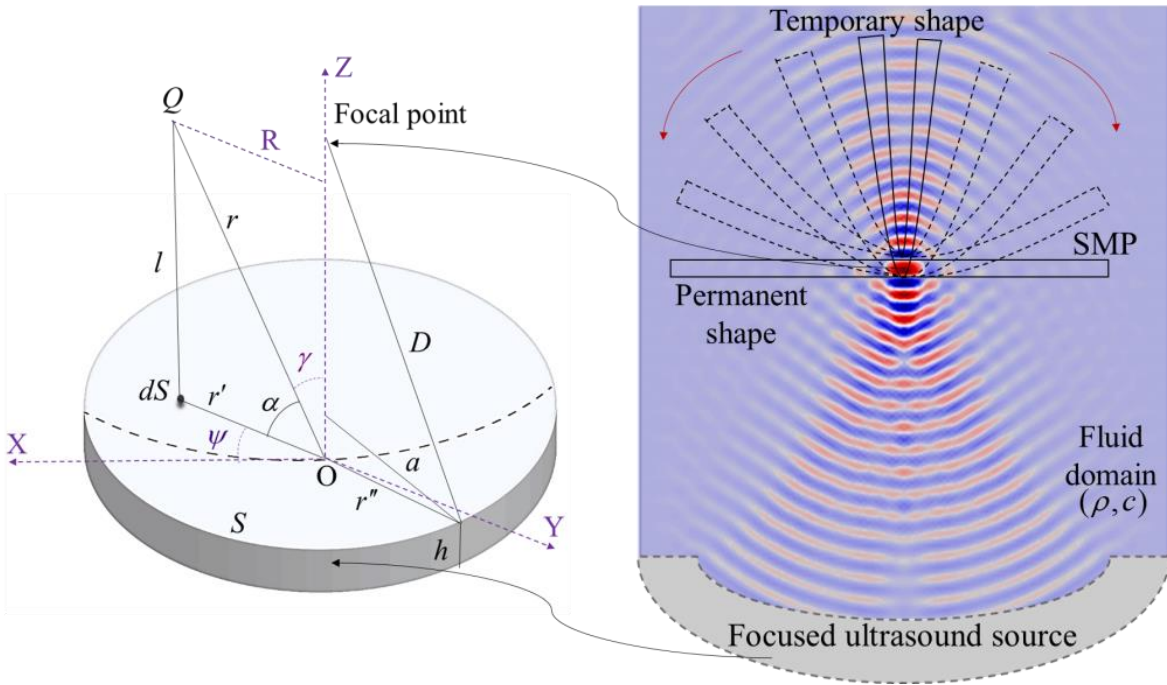


Fig. 2.2. Schematic representation (left) and finite-element simulation snapshot (right) of acoustic wave from a focused wave source to a shape memory polymer filament.

Since the spherical spreading occurs from the focal point area, it becomes more convenient to normalize the z parameter to focal distance. The non-dimensional form of propagation distance, \bar{z} in Eq. 2 is $\bar{z} = z/D$. The retarded time τ is normalized with angular source frequency ω_0 and is given by $\tau = \omega_0(t - z/c)$. In Eq. 2, the non-dimensional parameters G , \bar{B} and \bar{A} account for focusing gain, nonlinearity and attenuation effects in the medium, respectively. The focusing gain is given by $G = z_r/D$, where z_r is the Rayleigh distance of the unfocused source, given as $z_r = \omega_0 a^2 / 2c$ with a as the radius of the transducer. The nonlinearity term is $\bar{B} = D/z_s$, where $z_s = \rho c^3 / \beta p_0 \omega_0$ is the plane wave shock formation distance. In addition, the parameter \bar{A} is defined as $\bar{A} = \bar{a} D$, where $\bar{a} = \xi \omega^2 / 2c^3$ is the attenuation coefficient at frequency ω . The non-dimensionalized form of Laplacian in Eq. 2 is given by $\nabla_{\bar{r}}^2 = (\partial^2 / \partial \bar{r}^2 + \partial / \partial \bar{r} \partial \bar{r})$, where $\bar{r} = R/a$. The source condition in non-dimensional form becomes $\bar{p} = \hat{f}(\bar{r}, \tau + G\bar{r}^2)|_{\bar{z}=0}$, which is valid for spherical transducers under the following three assumptions, given as $\sin^2 \theta \ll 2$, $G \ll 8\pi / \sin^2 \theta$, and $1 \ll k a \ll 16\pi / \sin^3 \theta$ [56]. Here θ is the half aperture angle, Fig. A1a, and $\sin \theta = a/D$. While the first assumption is a relatively weak restriction which requires the half aperture angle to be less than 25° , the other two are analogous and restrict the maximum focusing gain for a given aperture angle. Therefore, the given assumptions limit the domain of validity of KZK equation for a focused transducer. Since, the transducer geometry used for this research satisfies two of the necessary conditions, KZK equation is used to predict acoustic pressure field in SMP for time and memory efficiency.

Absorption refers to the thermal-viscous attenuation of the waves as they propagate through a medium leading to loss of energy of the wave. KZK equation includes the absorption effect in Eq. 2 with the term

$$\frac{\partial \bar{p}}{\partial \bar{z}} = \bar{A} \frac{\partial^2 \bar{p}}{\partial \bar{\tau}^2} \quad (3)$$

where \bar{A} depends on the attenuation coefficient. The attenuation coefficient follows an arbitrary power law dependence on frequency given as [78]

$$\bar{a}(f) = \bar{\alpha}_0 f^\nu \quad (4)$$

where $\bar{\alpha}_0$ represents attenuation at source frequency ω_0 . Classical thermal-viscous attenuation uses a squared frequency dependency of the attenuation for fluids with $\nu = 2$. However, for tissues, various experiments show that ν ranges from 0.60 - 2. A popular approach is to take $\nu = 1$ for soft materials and polymers, but specific values of ν vary according to the type of material [79]. It is assumed that attenuation in SMPs follow a similar frequency dependence law with $\nu = 1$.

Nonlinearity arises due to variations of pressure with variation of density of the medium. It can also be expressed in terms of variations of sound velocity of a propagating wave in a medium. For example, as the wave propagates, the peaks of the wave may travel faster than the troughs thus distorting the structure of the wave. For a state $p = p(\rho, s)$ where s is the specific entropy, Taylor series expansion expressing the variation of pressure p with density ρ under adiabatic

conditions is given as $p = \{p_0 + A[(\rho - \rho_0) / \rho_0] + B[(\rho - \rho_0) / \rho_0]^2 / 2 + \dots\} |_{s=s_0}$ [58, 80], where $p_0 = p_0(\rho_0, s_0)$. Here ρ_0 and s_0 represents the density and the specific entropy in the unperturbed state, respectively. The coefficients A and B represent the first and second order variation of pressure with density and are given as $A = \rho_0 (\partial p / \partial \rho) |_{s=s_0}$ and $B = \rho_0^2 (\partial^2 p / \partial \rho^2) |_{s=s_0}$. The quantity B/A is known as the nonlinearity parameter and is expressed as

$$\frac{B}{A} = \frac{\rho_0}{c_0^2} \left(\frac{\partial^2 p}{\partial \rho^2} \right) \Bigg|_{s=s_0} = 2\rho_0 c_0 \left(\frac{\partial c}{\partial p} \right) \Bigg|_{s=s_0} \quad (5)$$

where c_0 is the small signal speed. Here B/A incorporates the effects of nonlinearity on the speed of the wave through coefficient of nonlinearity β where $\beta = 1 + (B/2A)$. In the dimensionless KZK model, the parameter \bar{B} integrates β into the KZK equation. Thus, the nonlinearity term in KZK equation, neglecting any diffraction and absorption effects, is expressed as

$$\frac{\partial \bar{p}}{\partial \bar{z}} = \frac{\bar{B}}{2} \frac{\partial \bar{p}^2}{\partial \tau} \quad (6)$$

Equation (6) has its origin in a simpler model known as Burger's equation [81]. Burger's equation models quadratic nonlinearities and absorption effects in a propagating wave. It is a basic model to understand shock wave formation and propagation. The full non-dimensionalized

form of Burger's equation is given by $\partial \bar{p} / \partial \bar{z} = \bar{A} \partial^2 \bar{p} / \partial \tau^2 + \bar{B} \bar{p} \partial \bar{p} / \partial \tau$. Equation (6) is the inviscid form of Burger's equation.

The numerical approach to solve KZK equation was first introduced by Lee *et. al.* [70] The approach known as operator-splitting method involves solving for each of the three effects independently at each integration step and combining the effects before proceeding to the next step. Therefore, KZK equation, Eq. 2, can be expressed in terms of independent terms as $\partial \bar{p} / \partial \bar{z} = o_D(\bar{p}) + o_A(\bar{p}) + o_N(\bar{p})$, where first, second and third operators represent diffraction, absorption and nonlinear effects respectively. The current model uses operator splitting method to solve Eq. 2 in a hybrid frequency-time domain approach [82] for harmonic acoustic actuation of a submerged SMP filament. The pressure field is expressed in time domain as

$$p(R, z, t) = \frac{1}{2} \sum_{n=1}^{\infty} [M_n(R, z) e^{in\omega t} + M_n^*(R, z) e^{-in\omega t}] \quad (7)$$

where M_n is the complex pressure amplitude corresponding to n th harmonic and M_n^* is the complex conjugate of pressure amplitude [83]. Substituting Eq. 7 in Eq. 2 and converting it into frequency domain, the non-dimensionalized KZK equation becomes

$$\frac{\partial V_n}{\partial \bar{z}} + \frac{i}{4nG} \nabla_{\bar{r}}^2 V_n + \Upsilon_n V_n = \frac{in\bar{B}}{4} \sum_{m=1}^{\infty} V_m (V_{n-m} + 2V_{m-n}^*) \quad n = 1, 2, \dots \quad (8)$$

where $V_n = M_n / p_0$ and Υ_n is a complex number representing attenuation term, \bar{A} , in frequency domain. The real part of Υ_n follows the frequency dependent power law, Eq (4). The imaginary

part of Υ_n accounts for dispersion effects which occur because of arbitrary frequency dependence of phase velocity. The dispersion effects are necessary to maintain the causality of the system and are determined using Kramers-Kronig relations as $1/c(\omega) = (2/\pi) \int_0^\infty \{[\bar{a}(\omega^*) - \bar{a}(\omega)]/(\omega^{*2} - \omega^2)\} d\omega^*$ [78], where ω^* represents conjugate of the angular frequency and $c(\omega)$ is the phase velocity of the acoustic wave.

At each integration step, the linear terms of Eq. 8, given by,

$$\frac{\partial V_n}{\partial \bar{z}} + \frac{i}{4nG} \nabla_{\bar{r}}^2 V_n + \Upsilon_n V_n = 0 \quad n = 1, 2, \dots \quad (9)$$

are solved in frequency domain while the remaining nonlinear terms are solved in time domain. For integrating Eq. 2 in time domain, the restricted size of the source and a finite time duration limits the integration domain within $\bar{z} \geq 0; 0 \leq \bar{r} \leq r_{\max}, \tau_{\min} \leq \tau \leq \tau_{\max}$. The values of r_{\max}, τ_{\min} and τ_{\max} are chosen such as to minimize numerical errors and depend on geometry of the transducer, absorption and nonlinearity parameters. Boundary conditions used for solving Eq. 2 for a focused transducer are given as $\bar{p}(\bar{r}, \bar{z}, \tau_{\min}) = 0, \bar{p}(\bar{r}, \bar{z}, \tau_{\max}) = 0, \bar{p}(\bar{r}_{\max}, \bar{z}, \tau) = 0,$ and $\partial \bar{p} / \partial \bar{r} |_{\bar{r}=0} = 0$. The time window is chosen large enough to incorporate the effects of absorption, waveform steepening and any singularities [70]. The lower and the upper limits of the time window are chosen as $\tau_{\min} = -(G + \omega_0 T_0 + 10\pi)$ and $\tau_{\max} = \omega_0 T_0 + 20\pi$ where T_0 is the time duration of source wave.

At each integration step, the nonlinear terms in Eq. 8 are converted into time domain using Inverse Fast Fourier Transform (IFFT) and solved for nonlinear pressure field using Eq. 6. Sonesson *et al.* [83] proposed a criterion to determine the cases for which nonlinear effects can be neglected without significant errors, to improve computing efficiency in time domain. The criterion uses attenuation and nonlinearity parameters, Υ and N respectively, to determine a cutoff value and decide if linear model is sufficient for the analysis. Thus, in this work, before the model computes for nonlinearity, a threshold cutoff amplitude is determined. If the pressure amplitude at each grid step is greater than the cutoff value, then the model accounts for nonlinearity and integrates Eq. 6 using upwind method. The solution is then converted back to frequency domain and the numerical code marches to the next step. The term $\beta= 4.50$ in SMP and $\beta= 3.50$ in water [58, 84] incorporate the nonlinear effects in wave propagation. An input pressure at 6 W is used. The number of harmonics (n) included in the model are given by $n = 2^k$, where k is an integer. To accurately model nonlinear effects, $k \geq 6$ is used.

To solve for absorption and diffraction effects in frequency domain, Diagonally Implicit Runge-Kutta (DIRK) and Crank-Nicolson (CN) methods [85, 86] are used. The second order IRK method is used in the near field near boundaries to reduce oscillations while Crank-Nicolson is used in the far field region [82]. The transition from DIRK to CN method is made at an axial grid length of $\bar{z} \approx 0.3$. The methods use an axial step size of 0.06 mm with an axial grid length of up to 78 mm and radial step size of 0.12 mm with a radial grid length of up to 32 mm. A time step of 7.8 e^{-9} is applied for both methods. The axial grid step is taken smaller to account for nonlinearity and provides a stable and accurate solution. In SMP domain, $\bar{\alpha}_0$ of 82.5 dB/MHz/m

and in water, a value of 0.22 dB/MHz/m is used.[84] The methods yield a tridiagonal finite-difference matrix which can be solved using Thomas algorithm [85].

The results of the numerical code in MATLAB are further validated using COMSOL. A 2-D axisymmetric model is developed to solve for acoustic pressure in frequency domain and later for heat transfer in time domain. The input parameters of the transducer and the SMP properties (density, thermal conductivity and specific heat capacity) are obtained from experimental measurements.

2.2.2. Thermal modeling

The effects of FU on soft tissues are well documented [87-89]. A mathematical formulation to analyze the effects of ultrasound on tissues is given by Penne's Bioheat equation which models the transfer of heat and generation of thermal field in the tissue domain. In this work, similar framework is used to evaluate the temperature T rise of the soft polymer as a result of FU heating. The modified Penne's Bioheat equation for SMP is given as [59]

$$\rho_m C_{hm} \frac{\partial T}{\partial t} = \kappa \nabla^2 T + H \quad (10)$$

where heating rate H is given by

$$H = \frac{1}{\rho_m c_m} \sum_{n=1}^k \text{Re}(\bar{a}_n) |p_n| \text{ where } n = 1, 2, \dots \quad (11)$$

In Eq. 10, ρ_m , C_{hm} and κ denote the density, specific heat capacity and thermal conductivity of polymer. Parameter c_m in Eq. 11 denotes the sound speed in polymer and p_n denotes the pressure field associated with each harmonic predicted by KZK equation in section 2.2.1. The thermal equation is coupled with KZK equation through heating rate H . Heating rate takes into account the cumulative heating by all harmonics. The absorption \bar{a}_n in polymer associated with each harmonic n obeys the frequency dependent power law given by Eq. (4) where $\nu=1$. The numerical algorithm in this chapter solves Eq. 10 using Crank-Nicolson operators for 40 s with a time step of 0.10 s. The radial and the axial step sizes are 0.24 mm and 0.25 mm, respectively.

2.2.3. Mechanical modeling of SMPs

Having obtained the temperature distribution from section 2.2.2, in this section, a SMP filament is modeled to predict the shape recovery process under FU by applying the obtained thermal boundary conditions. SMPs are categorized as semi-crystalline shape memory polymers (CSMPs) and glassy shape memory polymers (GSMPs). GSMPs have both amorphous and glass regions, with T_g defined as the glass transition temperature above which the SMPs exist in amorphous form. In this study, the selected constitutive model takes into account the stress-strain response which depends on thermal expansion of polymers to predict the glass transition of GSMPs [90-92]. The constitutive model involves four steps, the loading (amorphous phase), cooling (phase transition), unloading (glassy phase) and heating (phase transition) of the polymer filament. The constitutive model is numerically implemented in a user material subroutine (UMAT) in ABAQUS, a commercial finite-element software, to model the deformation and

shape recovery of an L-shaped filament which is thermally activated by FU. The governing equations calculating the stresses during the whole cycle and the evolution rules for the glass volume fraction are given as following [90].

SMPs above the glass transition temperature show the characteristics of an elastomer. The stress \mathfrak{S} in the amorphous part of the SMPs is given as

$$\mathfrak{S} = -\bar{c}I + \mu_a B_{k_a} \quad (12)$$

where \bar{c} is the Lagrange multiplier due to the constraints of incompressibility, I is an identity tensor, B_{k_a} is the left Cauchy stretch tensor and μ_a is the shear modulus of the amorphous phase. Here B_{k_a} is related to deformation gradient in amorphous phase, \tilde{F}_{k_a} , as $B_{k_a} = \tilde{F}_{k_a} \tilde{F}_{k_a}^T$. The stored energy function for the amorphous phase, Ψ_a is given as

$$\Psi_a = \tilde{C}_{10}(\bar{I}_{\tilde{c}_a} - 3) + \frac{1}{\tilde{D}_1}(\tilde{J}_a - 1)^2 \quad (13)$$

where $\tilde{C}_{10} = \mu_a/2$ and $\tilde{D}_1 = 2/K_a$ are the coefficients related to shear modulus and bulk modulus, K_a , of the amorphous phase, respectively. Here $\bar{I}_{\tilde{c}_a} = \text{tr}(\bar{B}_{k_a})$ and \tilde{J}_a is the volume ratio that can be determined by $\tilde{J}_a = \det(B_{k_a})^{1/2}$.

During cooling, as the temperature goes below the glass transition temperature, the glassy phase starts forming and both amorphous and glassy phase coexist at the same time. The stress for cooling phase of the cycle is given by

$$\mathfrak{S} = -\bar{c}I + (1-\bar{h})\mu_a \mathbf{B}_{k_a} + \mu_g \bar{h} \mathbf{B}_{k_g} \quad (14)$$

where μ_g is the shear modulus of the glassy phase and \bar{h} is the glassy volume fraction. In Eq. 14, \mathbf{B}_{k_g} is left Cauchy stretch tensor which is related to deformation gradient in glassy phase,

$$\bar{\mathbf{F}}_{k_g}, \text{ as } \mathbf{B}_{k_g} = \bar{\mathbf{F}}_{k_g} \bar{\mathbf{F}}_{k_g}^T.$$

After cooling stops and the polymer is below T_g , the formation of glassy phase stops. While the amorphous phase may not totally transit to glassy phase, the stress in the mixture is still given by Eq. 14. The stored energy function for the glassy phase, Ψ_g is given as,

$$\Psi_g = \bar{C}_{20}(\bar{I}_{C_g} - 3) + \frac{1}{\bar{D}_2}(\bar{J}_g - 1)^2 \quad (15)$$

where $\bar{C}_{20} = \mu_g / 2$ and $\bar{D}_2 = 2 / K_g$ are the coefficients related to shear modulus and bulk modulus, K_g , of the glassy phase respectively, and $\bar{I}_{C_g} = \text{tr}(\bar{\mathbf{B}}_{k_g})$.

In the heating phase, SMPs return to the original shape as the temperature goes above T_g . Due to the melting of glassy phase, the final state of the material is stress free and is given by $\mathfrak{S} = 0$.

The activation criterion for heating (starting of phase change) is governed by

$$(1-\bar{h})\mu_a \mathbf{B}_{k_a} + \mu_g \bar{h} \mathbf{B}_{k_g} = \bar{c}I \quad (16)$$

In a thermomechanical cycle, the change of glassy volume fraction controls the strain storage and release. Consistent with experimental results [92], this volume fraction is assumed to be a

function of temperature T only. Based on this assumption, a phenomenological function is given by [93]

$$T = 1 - \frac{1}{1 + \exp\left(\frac{T_r - T}{\zeta}\right)} \quad (17)$$

where T_r is the reference temperature [94] at which the recovery stress has a maximum value. Here ζ is the parameter determining the width of the phase transition zone. In this study, we set $T_r = 328$ K and $\zeta = 1.5$. These two parameters are obtained from curve-fitting of the experimental results in previous literatures [94].

To implement the constitutive model in ABAQUS, UMAT provides the updated stress and the local tangent stiffness matrix, \mathfrak{N} . Here \mathfrak{N} is a fourth-order tensor which is termed as the Jacobian matrix and provides the relationship for the stress and strain. The required Jacobian matrix format is given as

$$\mathfrak{N} = \frac{1}{J} \frac{\partial \tau^J}{\partial \tilde{D}} \quad (18)$$

where τ^J is the Jaumann rate of Kirchoff stress defined as $\tau^J = \dot{J}\tilde{\mathfrak{T}} + \tilde{\mathfrak{T}}^J$. Substituting τ^J into Eq. 18 gives $\mathfrak{N} = \tilde{\mathfrak{T}} \otimes I + \partial \tilde{\mathfrak{T}}^J / \partial \tilde{D}$, where for a mixture of amorphous and glassy phases, \mathfrak{N} is given as

$$\mathfrak{N} = [1 - h(T)]\mathfrak{N}_a + h(T)\mathfrak{N}_g \quad (19)$$

Solving Eqs. 18 and 19 delivers \aleph , which relates stresses to strains thus predicting shape recovery based on the detailed derivation given by Barot [95]. In Eqs. 12-16, the shear modulus of the amorphous and glassy phases, μ_a and μ_g , are given as $\mu_a = E_a / 2(1 + \nu_a)$ and $\mu_g = E_g / 2(1 + \nu_g)$ where $\nu_a = 0.49$ and $\nu_g = 0.40$ are Poisson's ratios for the rubbery and glassy phases, respectively [27]. The bulk modulus, K_a and K_g , in Eqs. 13 and 15 are given as $K_a = E_a / 3(1 - 2\nu_a)$ and $K_g = E_g / 3(1 - 2\nu_g)$.

2.3. Experimental results and model validation

2.3.1. Experimental setup and SMP filament preparation

Experiments are conducted for a flat 25 mm long, 3 mm wide, 1.5 mm thick 95%TBA-5%DEGMA polymer filament. The H-104-4A SONIC Concepts FU transducer rests on the bottom of the tank (Figs. 2.3a and 2.3b). The tank of water is filled to a depth such that the focal point of the FU transducer is located at the surface of the water. Special care is taken to ensure the water doesn't spray when the transducer is activated, and that the exposure power is low enough to prevent sample degradation. In an attempt to prevent acoustic interference, a rigid sample holder is placed outside of the tank to suspend the SMP sample at the surface of the water. The sample is suspended in a way such that the lower surface is submersed in water, and the upper surface is exposed to air. The FLIR C2 thermal imaging camera is fixed so that the images are focused around the exposure area of the FU, as shown in Fig. 2.3. The camera has an imaging rate of once every four seconds. Duration of sinusoidal exposure is 20 continuous seconds, with most thermal measurements reaching 40 seconds to capture cool down. Data is

processed with FLIR Tools software. Exposure power can be varied within the sample damage range. Figure 2.3c shows shape recovery of a SMP filament exposed to FU.

The monomer and the crosslinker that are utilized for fabrication of the SMP filament during the experiments are Tert-Butyl acrylate (TBA) and Di (ethylene glycol) dimethacrylate (DEGMA) (molecular weight 550) respectively. The photo-initiator used for the UV curing process is 2,2-Dimethoxy-2-phenyl-acetophenone. All chemicals are purchased from Sigma-Aldrich, and are not altered prior to use. Molds are created with dimensions of 150 mm x 100 mm from clear ultra-scratch resistant acrylic, and sealed with Loctite silicon sealant. Thickness of polymer filaments developed is varied as per the needs of the experiment, but is typically 1.5 mm. Curing is completed with a 100 W Blak-Ray B-100 AP high intensity UV Lamp.

Depending on the desired composition, TBA is mixed with DEGMA in different volumetric ratios of 80-20; 90-10; 95-5; and 100-0, respectively. The crosslinker-monomer combination is mixed well for ten minutes with a stir plate after adding 1 wt% photo-initiator. The mixture is then transferred to the acrylic molds for curing. The UV light exposure lasts 20 minutes for each mold. The prepared SMP is then removed from the mold. All SMP samples have a permanent shape of a flat rectangle. The SMP film is cut to the desired geometry by either scoring the material or use of a rotary tool.

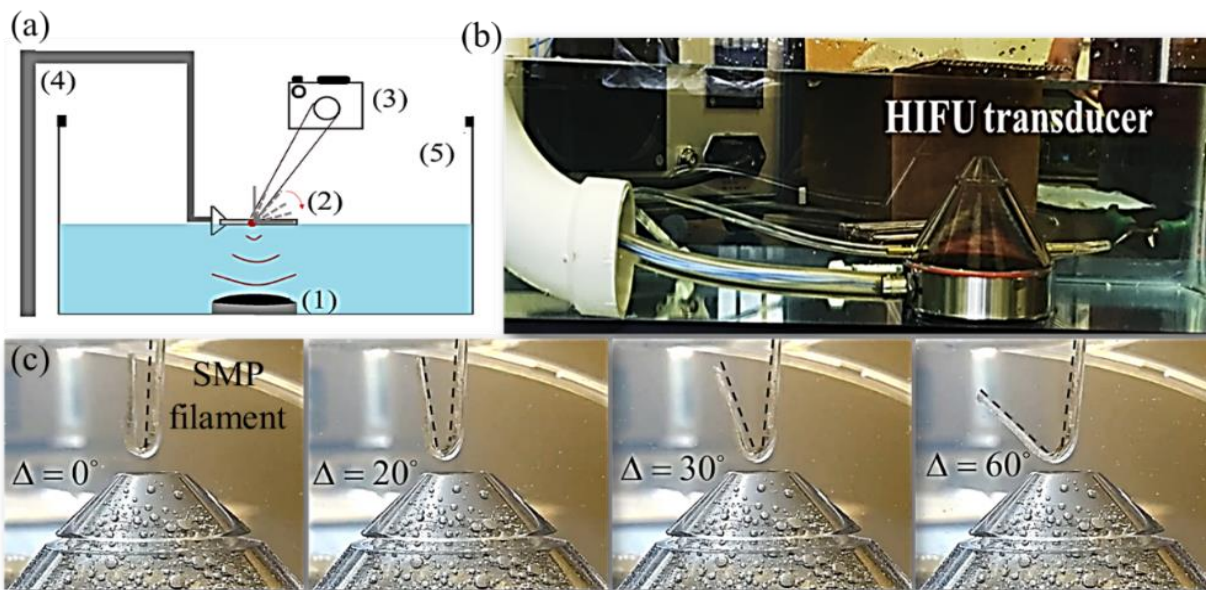


Fig. 2.3. (a) Illustration of experimental setup; (1) the transducer resting on the bottom of the tank, (2) shape memory polymer sample is suspended by the sample holder at the surface of the water, (3) thermal imaging camera directed at the focal point of the transducer (indicated by a red circle), (4) and (5) the water tank, and the stand. (b) Experimental setup and (c) shape recovery of a SMP filament exposed to FU at different time steps during 20 seconds of FU exposure

Dynamic mechanical analysis (DMA) is done for each of the aforementioned compositions. DMA measures storage modulus, Fig. 2.4a and Tan delta, Fig. 2.4b (Loss modulus and stiffness values are given in the supporting information; Figs. A2a and A2b, respectively). The ratio of the loss modulus to the storage modulus is the Tan delta and is often called damping. It is a measure of the energy dissipation from a material. A TA Instruments-Q800 DMA is used with an oscillation rate of 1 Hz. The data is collected in 0.5°C steps, and the temperature is ramped at a rate of 2°C per minute. DMA analysis and the preliminary experiments for shape recovery behavior show that 95%TBA-5%DEGMA is the most suitable composition and is used for all

further experiments and theoretical analysis in this chapter. The preliminary tests show that the other compositions are either too brittle to be used practically or are easily damaged even at low input power to the transducer.

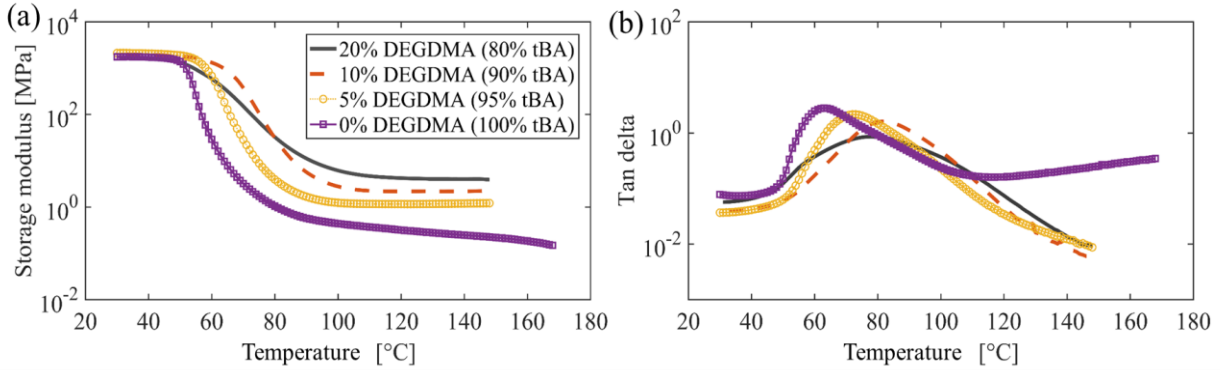


Fig. 2.4. (a) Storage modulus and (b) Tan delta obtained from DMA tests for different compositions

A hot disk thermal constants analyzer is utilized for evaluating thermal properties of the SMP filament. The hot disk hardware consists of a Keithley 2000 voltmeter, a Keithley 2400 sourcemeter, a Hot-disk bridge, and a computational device. After fabrication of SMP films, 14 disks of 15 mm diameter and 1 mm thickness are cut with a rotary tool. These sheets are clamped tightly in the sample holder for testing. The measurement method is verified with solid porcelain and sheets of PMMA with known thermal properties. The values of mechanical and thermal properties extracted from DMA analysis and hot disk experiment for 95%TBA-5%DEGMA are reported in Table 2.1. These values are later used in the entire research work for theoretical and experimental analysis of SMP filaments. The results obtained from DMA tests are also used to set the values of following parameters for the mechanical modeling in ABAQUS as $\check{C}_{10} = 0.28$, $\check{C}_{20} = 375$, $\check{D}_1 = 0.072$ and $\check{D}_2 = 0.00054$.

Table 2.1. Mechanical and thermal properties of 95% TBA-5% DEGMA polymer

Property	Value
T_g	72 °C
Density, ρ_m	1100 Kg/m ³
Amorphous phase elastic modulus, E_a	1.66 MPa
Glassy phase elastic modulus, E_g	2100 MPa
Thermal conductivity, κ	0.175 W/m/K
Specific heat capacity, C_{hm}	1050 J/kg/K

2.3.2. Experimental results and acoustic-thermoelastic model validation

The acoustic-thermoelastic model in section 2.2 is used to study the FU induced acoustic and thermal field as well as the shape memory behavior of the crossed-linked polymer. The theoretical acoustic pressure model is validated by finite-element simulation in COMSOL (Figs. 2.5a and 2.5b) and experiments. The SMP filament is exposed to focused acoustic waves in fluid domain (water), and boundaries of the fluid domain are defined to allow no reflection by employing perfectly matched layers in COMSOL. For harmonic actuation at the resonance frequency (0.5 MHz) of the FU transducer and 6 W input power, Fig. 2.5a shows the relative

acoustic pressure field of the fundamental harmonic along axis of symmetry of the transducer, obtained from the KZK and finite-element models. The calculated acoustic pressure is normalized with respect to source pressure amplitude, p_0 . A good agreement is observed between the finite-element simulations and proposed analytical-numerical multiphysics model. The sudden jump observed in the pressure field at $z \cong 52$ mm in Fig. 2.5a is due to the amplified effects of diffraction at the focal point and nonlinearity in the polymer. Figure 2.5b experimentally validates the temperature of the thermal field developed at the focal point for a sonication period of 20 s with finite-element analysis. The overall agreement of temperature and pressure values between experiments, finite-element analysis and acoustic-thermoelastic model proves the robustness of the theoretical model developed in this work. The parameters used in the acoustic model, accounting for gain, attenuation and nonlinearity effects in water and polymer are listed in Table 2.2.

Table 2.2. Parameters for absorption, nonlinearity and gain used in KZK model

Parameter	Medium	
	Water	SMP
$\bar{\alpha}_0$ (dB/MHz/m)	0.217	82.5
β	3.5	4.5
G	20.87	11.25

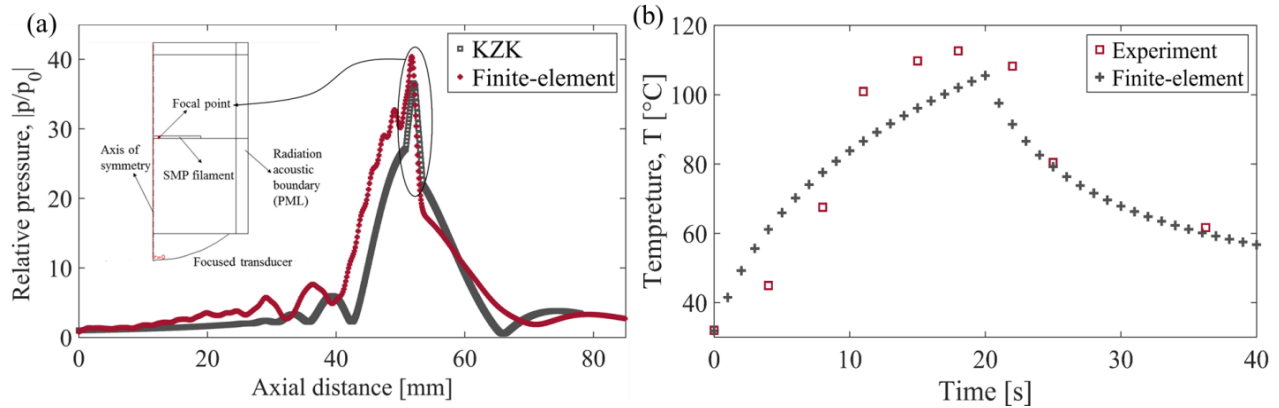


Fig. 2.5. (a) Relative axial pressure and (b) temperature rise vs. time at focal point of transducer

Figure 2.6 shows the thermal images of the polymer to demonstrate the temperature rise with respect to time corresponding to Fig. 2.5b. The heating of polymer is due to absorption of acoustic energy as a result of viscous shearing exerted by ultrasound focused waves and subsequent release of energy in the form of heat [52]. In the images, the highly concentrated spot in the center has the maximum temperature while the immediate surroundings outside of the focal spot has significantly lower temperatures. This shows a sharp temperature gradient from center to the edges of the polymer demonstrating the highly localized heating effect of FU. As seen in the temperature curve in Fig. 2.5b, after 20 s, the ultrasound is switched off and the polymer immediately begins cooling down which is shown by the sharp temperature decay. This ability to change the temperature of the polymer in short range of time shows the capability of FU to control the heating effect which is an important parameter to consider in designing of SMP-based CDD systems.

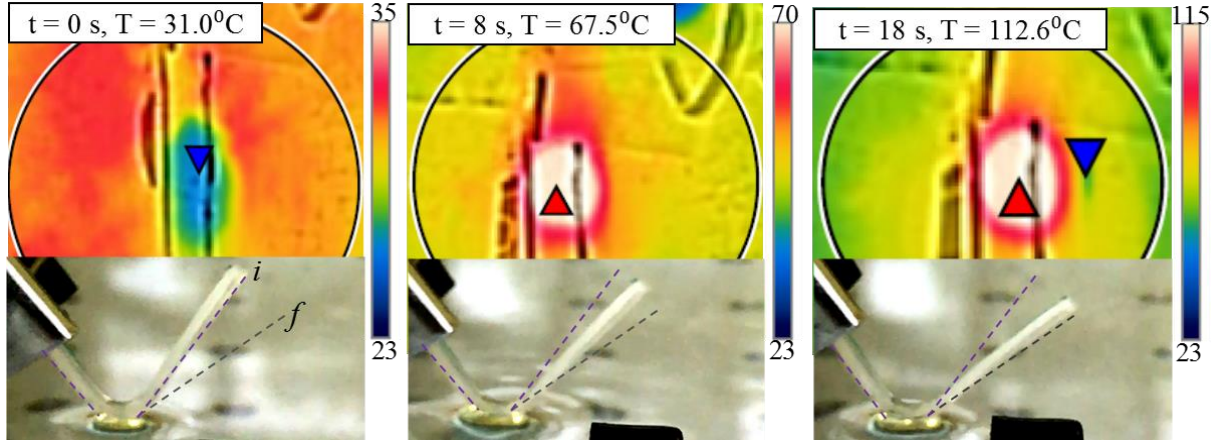


Fig. 2.6. Thermal images of the SMP filament exposed to ultrasound at the focal point of the transducer and the corresponding deformation with time; here i denotes the initial angle at temporary shape and f denotes the final angle after shape recovery. The red and blue triangles define the highest and lowest temperature locations in the image (the triangles only account for the portion of the image within the circle)

Having validated the acoustic-thermal model results and identified the mechanical and thermal parameters, a three dimensional filament is modeled to investigate the shape recovery of SMPs thermally induced by FU. The simulations of SMP's recovery process are performed by using a commercially available finite-element software package in ABAQUS (version 6.14, Dassault Systems Simulia Corp., Providence, RI, USA), with a user material subroutine (UMAT).

The SMP filament is modeled in ABAQUS using the properties given in Table 2.1. For the filament, the symmetry in x -direction and y -direction is applied to nodes that are on the central cross section and perpendicular to the x - y directions. Referring to Fig. 2.7, a punch and a die, defined as analytical rigid parts, are also introduced for modeling the loading process. The die is fixed and the punch is constrained in x and y directions, $u_x = 0$ and $u_y = 0$, while only z -

direction movement is allowed. Contact between the punch/die parts and the filament is modeled as frictionless and we assume there is no thermal transfer between punch/die parts and the filament.

The initial temperature is set above the glass transition temperature and the filament is deformed at different angles ranging from 60° to 120°. After cooling and unloading, ultrasound thermal field data from acoustic-thermal model is imported and applied as a mapped temperature distribution field in the finite-element model, to simulate the heating stage of the mechanical model, at 6 W power of the transducer as shown in Fig. 2.7. The thermal field data obtained from section 2.2.2 is exported from 0 to 20 s, divided into 4 sub steps (0~1, 1~5, 5~10, and 10~20 s) and applied as boundary conditions successively in the heating stage in the model. The inset in Fig. 2.7 compares the experimental and model predicted values of change in deformed angle against time for a filament with temporary initial angle of 60°. According to Fig. 2.7 and Table 2.3, the simulation results show a good agreement with experiments.

Table 2.3. Experimental and simulation predicted change in initial angle (degree) upon shape recovery process of the SMP filament

Initial angle, Δ_i	Final angle, Δ_f		Angle change, Δ	
	Model	Experiment	Model	Experiment
60	84.06	85	24.19	25
90	110.14	110	20.23	21
120	135.38	135	15.52	15

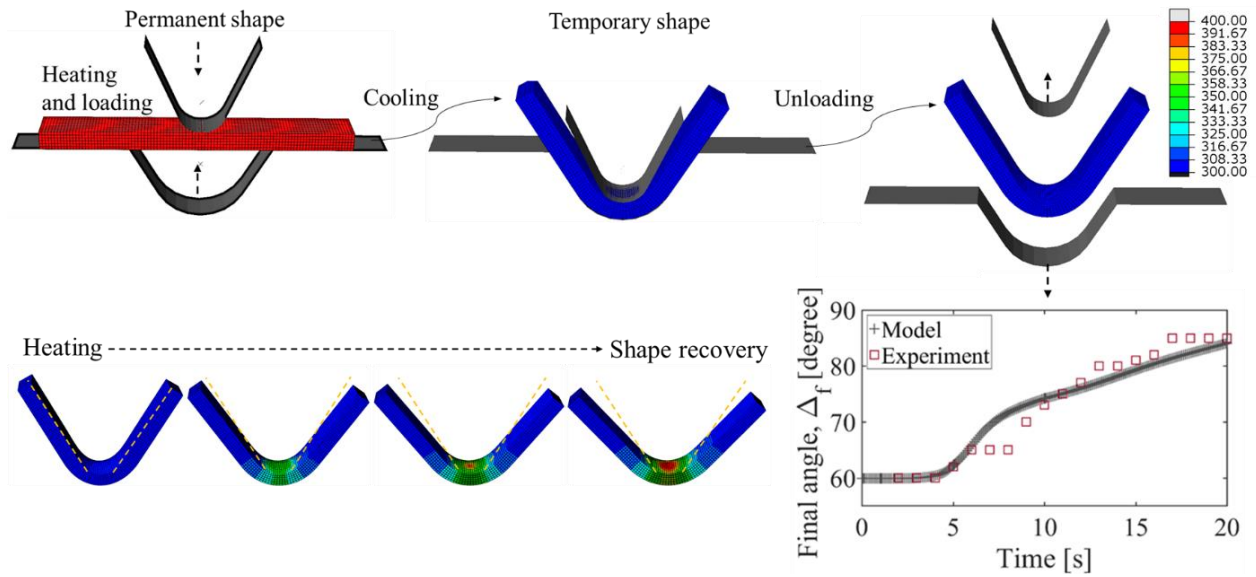


Fig. 2.7. Graphical representation of four stages specified in the mechanical model (section 2.2.3.). The SMP is first deformed into a temporary shape and cooled down, followed by unloading. It is then heated by the temperature distributions obtained from the acoustic-thermal model to facilitate shape recovery; the color bar is temperature in K. The inset shows the experimental and model predicted values of change in deformed angle of the SMP filament vs. time

2.3.3. Effects of various parameters

Experiments are conducted to estimate the threshold input acoustic power to the SMP filament beyond which the polymer gets damaged. Polymer filaments are exposed to input power ranging from 0-100 W. The filaments are then observed under OME-TOP metallurgical microscope PM-304I at a resolution of 100 μm . Experiments reveal that after a certain range of power, actuating polymers at higher powers result in surface scarring and cracking of the polymer filament as shown in Fig. 2.8. Besides visible changes, the polymer also undergoes structural changes such as temporary melting during ultrasound exposure which lead to unpredictable and non-repetitive

rise in temperature of the polymer. The threshold power range is found to be within 6 -10 W for the 1.5 mm thick filament above which the observed changes in temperature are non-uniform.

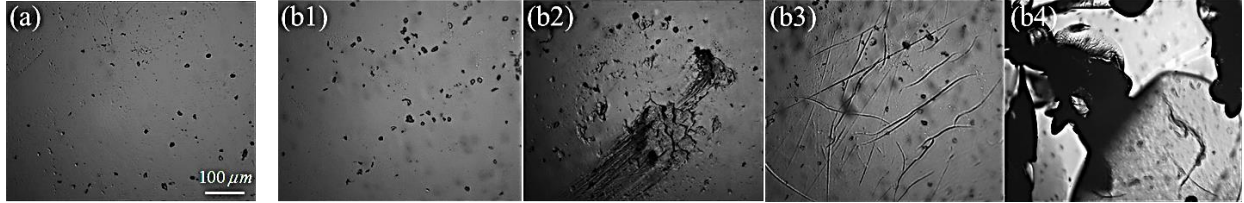


Fig. 2.8. Surface images of the polymer filament exposed to (a) no acoustic power, and (b1) 25 W (b2) 50 W (b3) 75 W (b4) 100 W

In the usage of FU technology combined with SMPs for designing an ultrasound responsive SMP-based CDD system, focused acoustic waves are strongly affected by the mutual influence of diffraction, absorption and nonlinearity of the medium. Therefore, investigating the influence of these effects in the focal area, on the FU induced heat generation in polymer and the resultant shape recovery are clearly of importance. In this section, various acoustic parameters are investigated in the polymer domain and the resulting acoustic and heating responses are explored in both the time and frequency domains. The nonlinear acoustic-thermal model is then coupled with the constitutive equations of SMPs to explore the dependence of shape recovery on the nonlinear parameters and compared with the results reported in the literature. Specifically, the input power and frequency-dependent nonlinear effects on shape recovery are studied.

Nonlinearity is a property which arises due to variation of speed of a propagating wave in a medium. Presence of higher harmonics due to transfer of energy from fundamental to higher harmonic components and distortion of waveform characterizes a nonlinear wave. The localization of the fundamental pressure field as well as the harmonics at the focal point is of

utmost importance in evaluating the thermal effects of FU on SMP filament, because the amount of energy deposition is directly proportional to frequency-dependent absorption and on higher frequencies according to Eq. 11. Thus, stronger nonlinear effects lead to stronger and higher number of harmonics creating enhanced localized energy deposition and therefore enhanced shape recovery of SMP.

The relative pressure against axial distance from the transducer and the time histories of the relative acoustic pressure at the focal point, located in the polymer domain, are shown in Fig. 2.9, in response to harmonic excitation of the transducer at 6 W and 0.5 MHz. To study the nonlinearity effects and distortion of pressure waves in our experiments, a simulation using KZK equation is performed for the experimental case study in section 2.2 with the parameters mentioned in Tables 2.1 and 2.2. Figure 2.9a shows that the fundamental component has the highest pressure amplitude which indicates that most of the energy is concentrated in the fundamental component, with the second harmonic having only small amount of energy due to a low pressure amplitude. The remaining harmonics have negligible pressure amplitudes and therefore, negligible energy. The results in Fig. 2.9b show that the transducer settings assigned for the experimental case study to obtain the results in Fig. 2.5, result in a weak distortion of the waveform from the linear case, due to low value of nonlinear parameter β , and energy contribution of only two harmonics (fundamental and second).

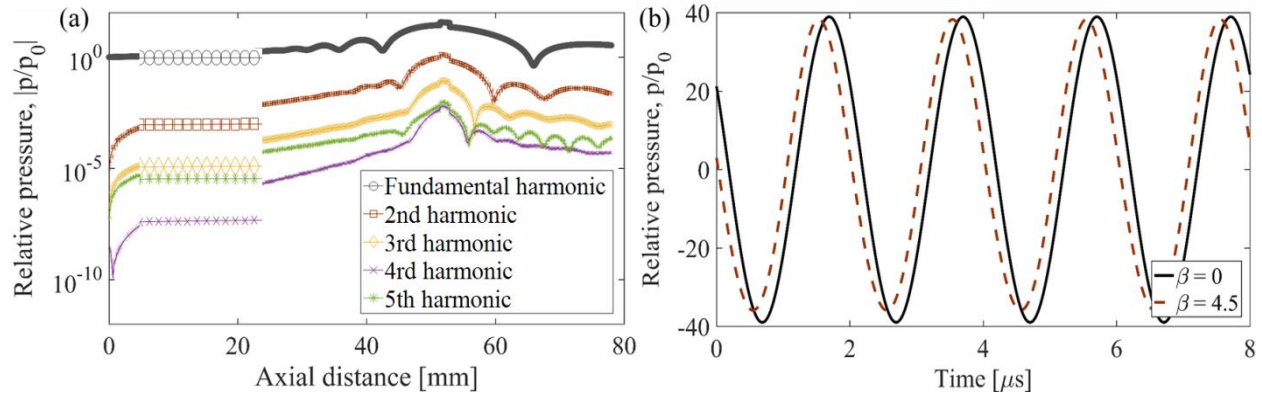


Fig. 2.9. (a) Relative axial pressure magnitude and (b) linear and nonlinear relative pressure waveform at 6 W and 0.5 MHz

Having validated the analytical-numerical acoustic model in Fig. 2.5a against FEM simulations for the experimental case study with weak nonlinear effects, finite cases with strong nonlinearity are considered next (which cannot be efficiently simulated in a standard FEM environment). With increase in β alone for the polymer, the variation of speed with pressure in the polymer increases, which leads to stronger nonlinear effects with stronger harmonics and more distorted waveform as shown in Fig. 2.10. The waveforms are obtained at higher power and frequency (20 W and 1.5 MHz) to observe the nonlinear effects at a reasonable spatial scale and these values are different from input values used for experiments. With increase in β in Fig. 2.10a, the peak amplitude of the waveforms become narrower and increase drastically due to cumulative effect of stronger harmonics. This is further demonstrated in Fig. 2.10b where the increased transfer of energy from fundamental to other harmonic components with β leads to decrease in the relative pressure amplitude of the fundamental frequency and increased pressure amplitudes of higher harmonics.

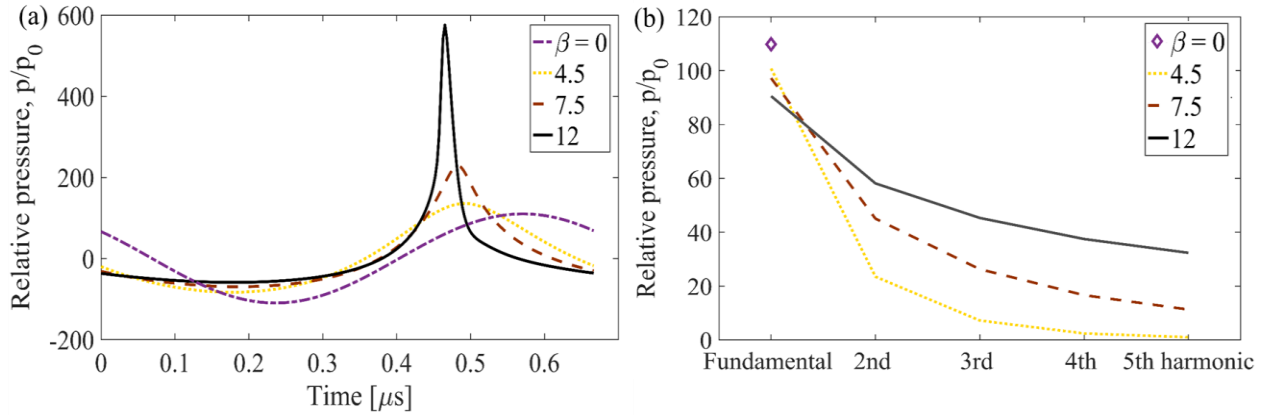


Fig. 2.10. (a) Relative pressure waveforms and (b) amplitudes for first five harmonics at focal point for various nonlinearity parameter β

Nonlinear effects become more dominant with distance as well [58]. The speed of a particle is different at various points in the waveform. Figure 2.11 shows the distortion of the waveform at four different points along the propagation axis at 1.5 MHz and 20 W of power with $\beta = 12$ in water and $\beta = 13$ in polymer. The values of β are chosen to observe the nonlinear effects at a reasonable spatial scale. The increased distortion of the waves with distance is due to the increased strength of harmonics with wave propagation in the medium, Fig. 2.11b. In other words, nonlinear effects cumulate with distance. However, we observe that at the focal point where SMP filament is located, the narrowing of the waveform and the strength of the harmonics is the maximum. This is due to the presence of polymer at the focal point which has a higher β as compared to water and thus has increased nonlinear effect on the propagating acoustic waveform as compared to distance.

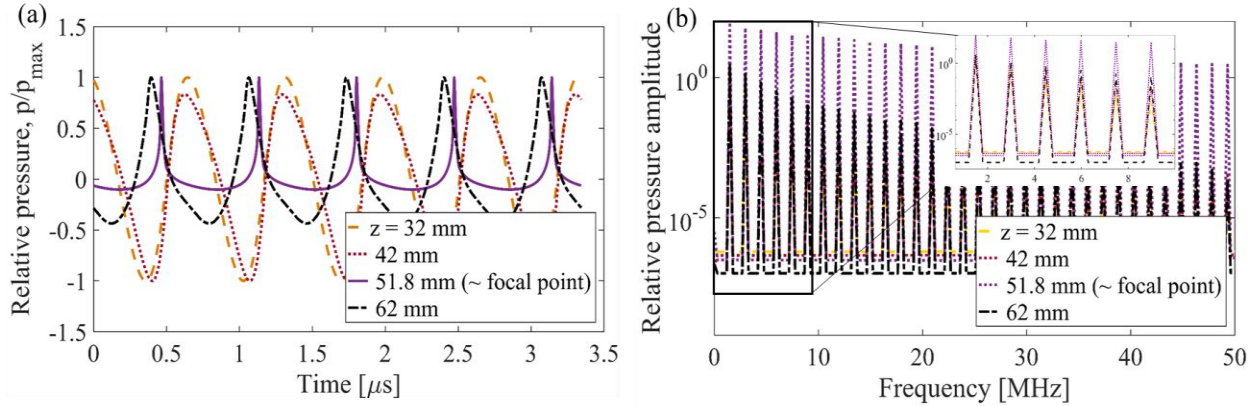


Fig. 2.11. (a) Relative pressure waveforms (with reference pressure as maximum pressure magnitude p_{\max}) and (b) relative pressure magnitude in frequency domain at different positions along axis of transducer

Absorption causes loss in the transmitted energy of the wave as it passes through a medium. The effect of absorption on wave attenuation is explained in section 2.2.1. The contribution of absorption to the pressure field is incorporated through the attenuation coefficient $\bar{\alpha}$ in the KZK model. To evaluate the influence of variation of attenuation coefficient of SMP at source frequency, $\bar{\alpha}_0$, on the distortion of waveform and generation of harmonics, simulations are performed at 20 W and 1.5 MHz, keeping other properties of the polymer according to Tables 2.1 and 2.2. Figure 2.12 shows that with increase in attenuation coefficient of the polymer, the relative pressure amplitude and the number of harmonics do not increase or decrease. Attenuation counters the nearfield and nonlinearity effects. However, for focused sources [56] the effect of absorption on the waveform is significantly less in the nearfield region due to dominant effects of nonlinearity. Similar observations by Hart *et al.* [56] confirm the suppression of dissipation effects and their negligible influence on pressure field in the nearfield region.

Figures 2.13 and A3 show the relative pressure amplitudes at focal point in time and frequency domains for various excitation frequency and input power level, respectively. As input power is increased at a particular frequency, the amplitudes of all the harmonics increase, adding more energy available to each harmonic; however, there is no change in number of harmonics, Fig. A3b. This results in low distortion of the waveform for increasing input power, Fig. 2.13b. On the other hand, increase in frequency at a fixed power level gives rise to more number of harmonics and significant distortion of waveform, Figs. 2.13a and A3a. This occurs due to increased change of sound speed in the medium with increase in frequency. It is inferred that between the two transducer input parameters, frequency plays a more significant role, as compared to input power, in inducing nonlinearity in acoustic pressure field exposed to the SMP. The effects of acoustic nonlinearity on the induced thermal field in polymer is explained further in Fig. 2.14.

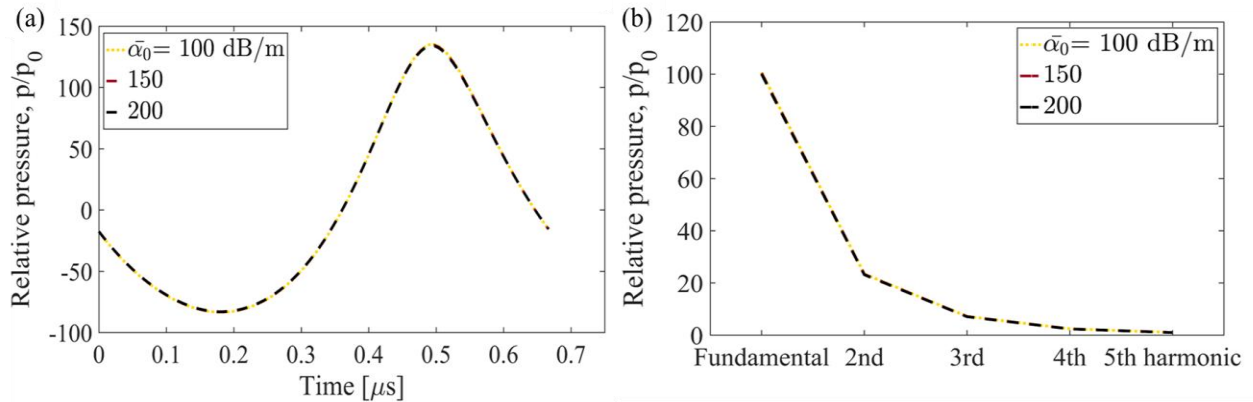


Fig. 2.12. (a) Relative pressure waveforms and (b) amplitudes for first five harmonics at focal point for various attenuation coefficient, $\bar{\alpha}_0$

The concentration of the acoustic pressure fields of the higher harmonic components at the focal point leads to increased energy deposition because higher frequencies significantly influences the heating response of polymer, Eq. 11. From Figs. A3a and A3b, it is seen that at a particular acoustic pressure field in SMP domain, an increment in input power level causes more energy distribution from the fundamental to higher harmonics. Therefore, stronger high frequency components appear, as compared to applying an increment in the source frequency. Increase in power level enhances more localized energy deposition on the surface of SMP and therefore rapid increase of temperature. Figure 2.14 shows that the temperature rise rate in SMP with power variations is significantly higher than the temperature rise rate due to increase in frequency. As a result, the rise in input power level onsets an earlier shape recovery and plays a more influential role in triggering heating effect in the polymer filament. However, increasing power should be done with care since the experiments in Fig. 2.8 show that actuating polymers at higher power levels result in surface damages. It is concluded that, the acoustic nonlinearity has a significant role in controlling the onset of shape recovery in ultrasound SMP-based systems; increment in excitation frequency results in smoother shape recovery whereas increase in power level makes a sudden shape recovery of the SMP.

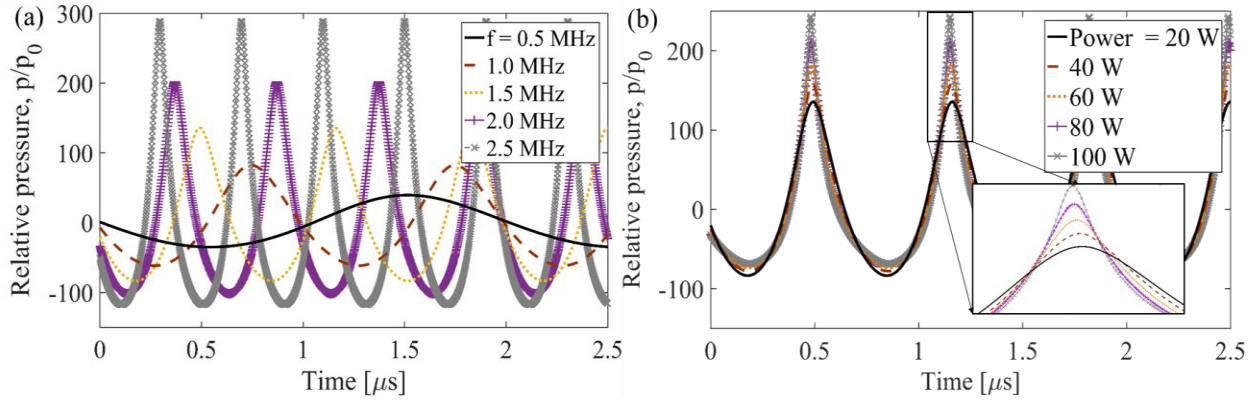


Fig. 2.13. Relative pressure (with reference as source pressure, p_0) at focal point in time domain for (a) various source frequency and 20 W input power; (b) various input power at 1.5 MHz

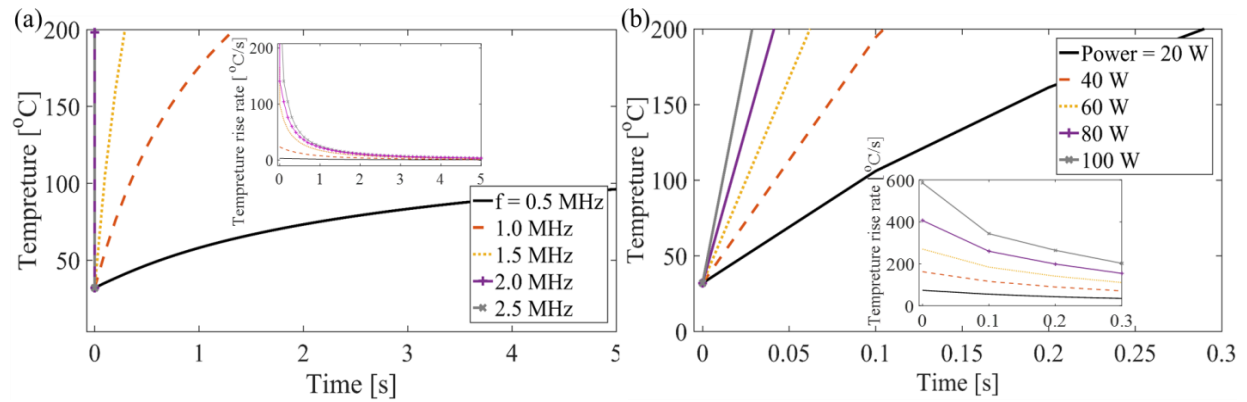


Fig. 2.14. Temperature vs. time plots at focal point for (a) various source frequencies and 20 W input power, and (b) various source input powers at 1.5 MHz. The inset graphs show the corresponding temperature rise rates ($^{\circ}\text{C/s}$)

Simulations are performed to explore the effects of polymer constitutive composition on the shape recovery behavior of SMP filament at a fixed ultrasound actuation power. Reference temperature, T_r in Eq. 17, and the elastic modulus of amorphous phase, E_a , are the two parameters considered as variables in the simulations, while all other parameters are kept constant. Figure 2.15a shows that the onset of shape recovery is delayed for the SMP with higher

characteristic recovery temperature ($T_r = 328\text{ K}$), however the recovery ratios do not show a uniform trend. Figure 2.15b shows that the SMP with higher elastic modulus in rubbery phase gives better shape recovery and therefore achieves larger change in initial angle. The reason is that the polymer with high elastic modulus (hard material) has a higher stored energy under the same deformation during loading stage as compared to a softer polymer with lower elastic modulus. Since for different compositions, the elastic moduli in glass phase are same, the polymer with larger stored energy has a better recovery ratio.

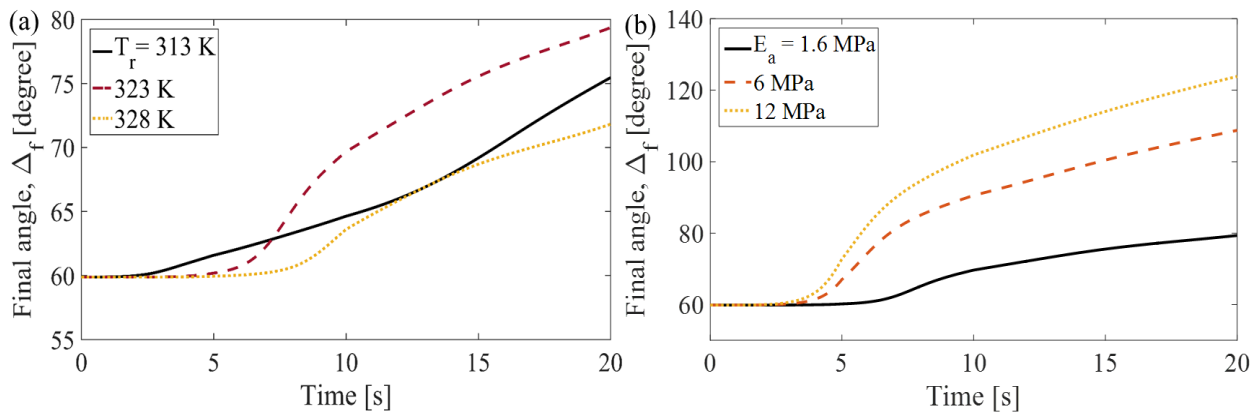


Fig. 2.15. (a) Final angle vs. time for various (a) recovery temperature and (b) elastic moduli of amorphous phase

The effects of increasing the crosslinker content on material properties are shown in Figs. 2.4 and A2. In Table 2.4, the results from simulation show that the sample with heavier crosslinking (with higher elastic modulus in amorphous phase) will have more shape recovery, which is consistent with Fig. 2.15b. It is worth emphasizing that in Fig. 2.15, the reference temperature and elastic modulus of amorphous phase are the only parameters which are varied in the simulations which is not the case in Table 2.4 (both reference temperature and elastic modulus are different for various compositions).

Table 2.4. Simulation predicted final angles (degree) upon shape recovery process for various polymer compositions

Composition (%TBA-%DEGMA)	T_g [°C]	Final angle, Δ_f	Angle change, Δ
70-30	106	105.20	45.20
80-20	78	87.87	27.87
90-10	82	79.36	19.36

To study the effect of geometric parameters and input power on the thermally induced shape recovery behavior of polymers, simulations are performed for varying thickness, width, initial angle of bending curvature of the filament and input power to the transducer. Figure 2.16a shows the final angle (the angle of the deformed area after undergoing shape memory behavior) with time for a 3 mm wide filament with initial deformation of 60° at 6 W of input power for varying thickness. The change in final angle and therefore shape recovery is more in thicker filaments. The reason behind this trend is the increase in the available sample volume with increased thickness for absorbing heat, resulting in increased bulk temperature of the exposed sample and therefore more shape recovery [55]. Thus, thickness plays an important role in determining shape memory behavior of a given filament.

Figure 2.16b explores the effect of change in width of polymer filament on shape recovery behavior for a 1.5 mm thick filament with initial bending curvature of 60° at 6 W. The increase

in width delays the onset of shape recovery and decreases the amount of shape recovery. It is observed that angle recovery onset time is related to the temperature at the edge nodes. Since the filaments have different width, the time taken by edge nodes of filaments with larger width to reach glass transition temperature is more. Thus, a larger width increases the zone of phase transformation and requires more time and energy to transform the overall exposed area and initiate the shape recovery, resulting in lesser change in initial angle.

The simulations of the filaments for various initial radii of curvature, Φ are conducted for a 3 mm wide and 1.5 mm thick filament heated at 6 W power of FU. Figure 2.16c shows that even though the filaments have almost same onset time, a sharper bending area leads to a larger deformation. Since the filaments have same width, the time for edge nodes on central cross section to reach the glass transition temperature is approximately the same. Hence, the filaments with different bending radius but same width have almost same recovery onset time. However, for a sharper bending area, the spreading phase transformation zone easily covers the whole bending area which results in a larger deformation for the sharper filament.

Figure 2.16d shows the final angle with respect to time at various input powers. The thickness of the polymer filament is kept constant at 1.5 mm and initial angle of 60° is used for all powers. It is seen that higher input power results in higher shape recovery (more change in initial angle) of the polymer. This is expected as the increase in power will result in increase in absorption of energy, Eq. 11, due to higher internal friction and therefore increase in energy subsequently released as heat [55]. As power increases, the bulk temperature crosses T_g at an earlier time step thus initiating early shape recovery.

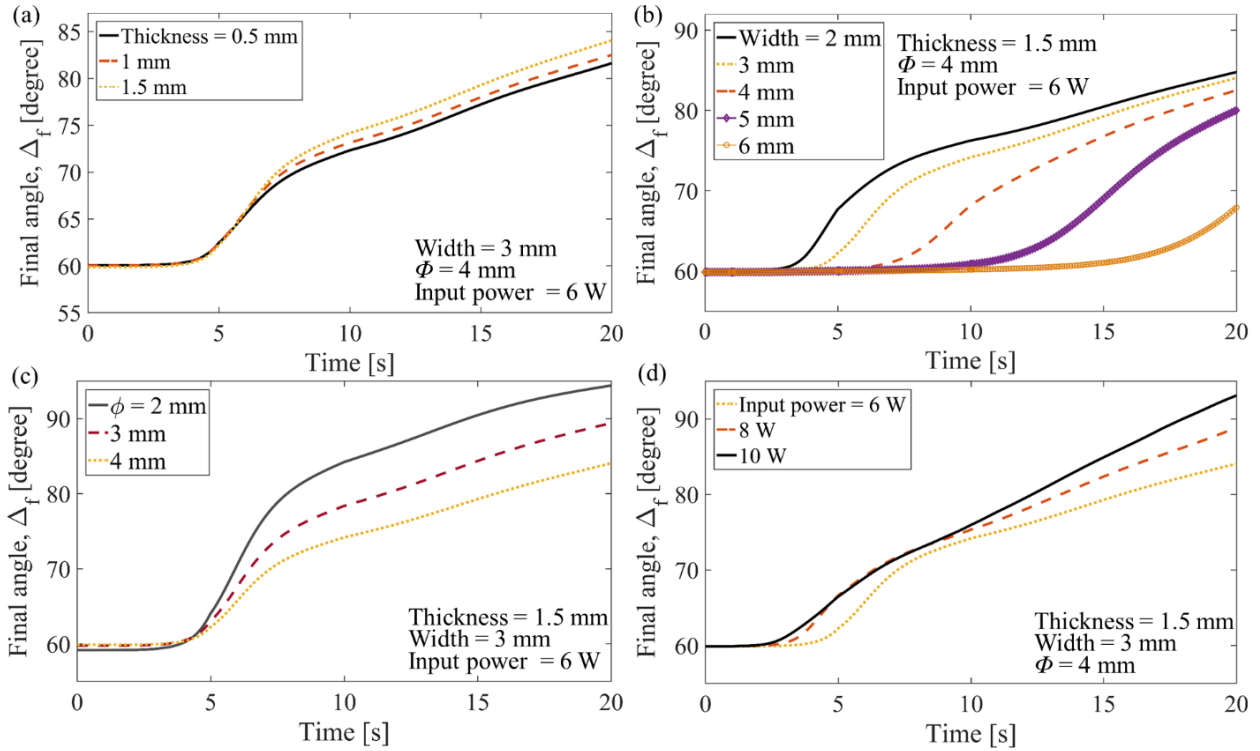


Fig. 2.16. Final angle vs. time for various (a) thickness and (b) width of the SMP filament, (c) initial bending curvatures of the deformed area in mm, and (d) transducer input powers.

2.4. SMP container design

The theoretical model in this research aims to develop a mathematical framework for optimizing and evaluating the role of different input parameters, geometrical configuration, and medium properties on ultrasound actuated shape memory behavior of polymers through experimental validation. The efforts lead to propose a design for an ultrasound activated drug delivery container. A possible design for such a container is shown in Fig. 2.17. The 0.3 mm wide (diameter) container is a 2D representation of Fig. 2.1 and is composed of 0.01 mm thick layer of 95% TBA-5% DEGMA kept at the focal point of the ultrasound transducer. Figure 2.17 shows the simultaneous displacement of the valve and diaphragm with time and the intermediary stages

due to shape recovery under FU at 6 W. The color contour gives the temperature distribution inside the container.

The design proposes a novel mechanism for simultaneously opening the drug container and pushing the particles out, which will significantly improve the rate of drug releasing. The movement of valve with respect to diaphragm is shown in Fig. 2.18a. Figure 2.18b shows the normalized velocity (normalization is done with respect to the maximum velocity) of the diaphragm and valve is maximum within first five seconds suggesting the maximum release of drug particles occurs within first 5 seconds of ultrasound exposure. The time at which the normalized velocity attains maximum can be manipulated by varying the input power or geometric parameters of the container, thus controlling the drug release rate. Since the diaphragm velocity is lower than the valve velocity as shown in Fig. 2.18c, the drug release of particles is expected to be uniform, unhindered and regulated. It is worth noting here that we are only showing a proof of concept and the developed experimental-computational framework can be utilized for designing various ultrasound activated drug delivery containers, specifically tailored for different applications depending on the size of drug particles, target time for releasing the particles, and the size/shape of the container. This is the topic of a future communication by the authors.

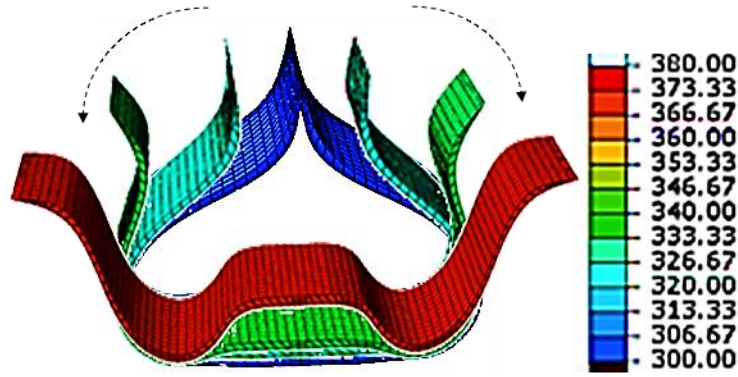


Fig. 2.17. Thermal distribution of a container kept at focal point of the transducer; the color bar is temperature in K. The intermediary stages represent the movement of the valve with time due to shape recovery under FU

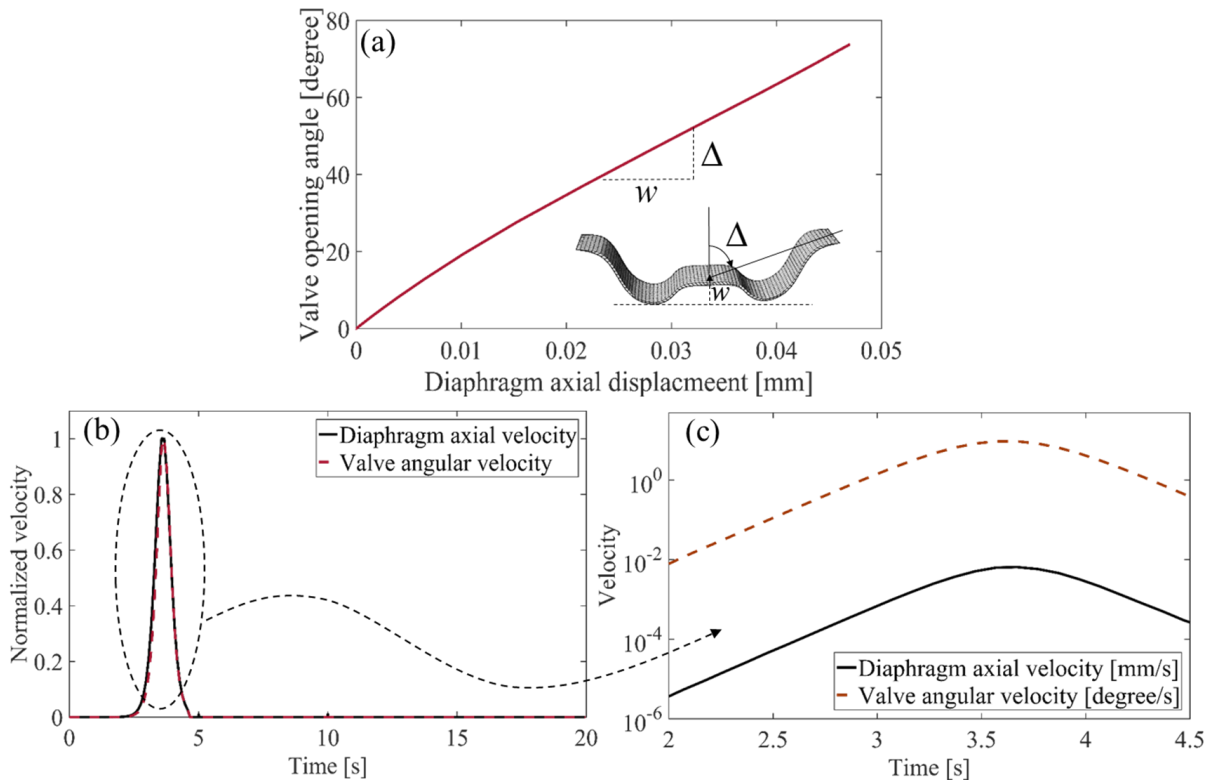


Fig. 2.18. (a) Angular displacement of valve vs. transverse displacement of diaphragm of the container, (b) normalized velocity vs. time for diaphragm and valve, and (c) velocity vs. time for diaphragm and valve for the time range when they attain maximum

2.5. Conclusions

This chapter aims to present a combined acoustic-thermal-structural model to predict the shape recovery behavior of polymers under focused ultrasound (FU). The numerical model provides the basis for designing spatially and temporally controlled drug delivery (CDD) systems. A theoretical framework is used to predict acoustic pressure field due to focused transducers, and the acoustic model is coupled with a thermal model to predict the developed temperature field due to FU. The thermal field is then coupled to the mechanical model which solves for the stresses developed in the polymer and predicts the shape recovery of the system. Experiments are conducted to validate the numerical model. In addition to successful model validations against 3D finite-element simulations, a study on the effects of several system parameters is performed. The model is used to explore the effects of medium properties (nonlinearity and absorption), geometrical properties (thickness, width and initial deformation of the polymer filament) and input parameters (power and frequency) on shape recovery behavior of the polymer. The results show that while input source frequency has more influence on nonlinearity, input power plays a major role in achieving high temperature rise rates and thereby faster onset and increased shape recovery. Observations related to medium properties show that the coefficient of nonlinearity of the medium plays a significant role in distorting the waveform and generating more harmonics, thus increasing the energy deposition at the focal point and enhancing the shape recovery behavior. Our results will pave the way for designing more efficient drug delivery capsules at meso to nanoscale, and will shed light into the details of utilizing FU for stimulating SMP-based mechanisms in drug delivery applications.

Appendix A

A1. Focused ultrasound (FU) induced pressure field in medium; linear acoustic model

An analytical model is developed to obtain the ultrasound pressure field from a spherical concave transducer in fluid domain. The model is based on O'Neil's method and is used to calculate a linear pressure field at the focal point of the curved transducer [63]. It is assumed that the amplitude of acoustic waves is sufficiently low so that the acoustic field can be considered as linear where the effects of absorption and nonlinear distortion are negligible. Diffraction effects are also neglected as the diameter of the transducer is assumed to be considerably large as compared to the wavelength of the transducer. The analytical solutions describe the pressure field along the axis of symmetry and in the focal plane of the transducer having the geometric properties as shown in Fig. 2.2 [63, 96]. Under the given assumptions, the velocity potential Φ in the region of a curved transducer is given as

$$\Phi = \iint_S \frac{u}{2\pi l} e^{-ikl} dS \quad (\text{A1.E1})$$

where u is the harmonic normal velocity of the transducer surface given as $u = u_0 e^{i\omega t}$ and u_0 is the velocity amplitude. The surface of the transducer, S , is composed of several point source elements, which focus acoustic waves at the focal point. In Eq. (A1.E1), l is the distance from a source point lying in surface element dS , to the point of observation Q . The wavenumber k is defined as $k = \omega / c = 2\pi / \lambda$ where c is the sound velocity, ω is the angular frequency of

acoustic wave in the domain and λ is the wavelength (i is unit imaginary number). Using Eq. (A1.E1) the acoustic pressure field is defined as $p = \rho \partial \Phi / \partial t = i k c \rho \Phi$, where ρ is the acoustic medium density.

A1.1. Acoustic pressure along axis of symmetry of transducer and in focal plane.

For ease in calculations, the velocity potential in Eq. (A1.E1) is converted from cylindrical (Z, R, ψ) to spherical (r, γ, ψ') coordinates. From Fig. 2.2, the spherical geometry of transducer is related to its dimensions as $Z = r \cos \gamma$ and $R = r \sin \gamma$. The velocity potential in spherical coordinates is

$$\Phi(r, \gamma) = \frac{u}{2\pi} \int_0^{2\pi} \int_0^{r''} l^{-1} e^{-ikl} r' dr' d\beta' \quad (\text{A1.E2})$$

where r'' is the distance from the center of the transducer to the edge boundary given as $r''^2 = h^2 + a^2$ and $r' = 2D \cos \alpha$ as shown in Figs. 2.2 and A1. The term $r' dr' d\beta'$ in Eq. (A1.E2) represents the surface element dS , in Eq. (A1.E1), in spherical coordinates. The focal depth is represented with D , a is the radius of the transducer and h is the depth of the concave surface. In Eq. (A1.E2), $\beta' = \psi' - \psi$ (ψ' is the azimuthal angle at the transducer surface), $d\beta'$ represents a small change in angle β' and l in spherical coordinates is given as $l = (r^2 - 2r r' \sin \alpha \sin \gamma \cos \beta' + m r'^2)^{1/2}$, where $m = 1 - 2h z' / r''^2$ (z' is the axial distance from origin O at the transducer surface to point of observation Q). The wavelength λ and depth h

are assumed to be comparatively small as compared to radius a to satisfy the assumptions used in Eq. (A1.E1).

For obtaining acoustic pressure on the axis of symmetry, β' vanishes and Eq. (A1.E2) becomes

$$\Phi = \frac{u}{m} \int_{z'}^{D'} e^{-ikl} dl = \frac{1}{ikm} u (e^{-ikz'} - e^{-ikD'}) \quad (\text{A1.E3})$$

where D' is the distance of Q (located on symmetrical axis) from the edge boundary at r'' (Fig. A1) and given as $D' = (z'^2 + m r''^2)^{1/2} = [(z' - h)^2 + a^2]^{1/2}$. To separate the amplitude and the phase factors in Eq. (A1.E3), two parameters δ and C are introduced as $\delta = D' - z'$ and $C = (D' + z') / 2$. Equation (A1.E3) in terms of δ and C is $\Phi = u(e^{ik\delta/2} - e^{-ik\delta/2})e^{-ikC} / ikm = u_0 P e^{i(\omega t - kC)} / k$, where $P = 2 \sin(k\delta/2) / m$. The corresponding axial acoustic pressure is given as $p = ik \rho c \Phi = i \rho c u_0 P e^{i(\omega t - kC)}$. Figure A1b shows the relative pressure along symmetrical axis where p_0 is the characteristic acoustic pressure at the surface of the transducer; the maximum pressure is achieved at focal point $z' / D = 1$. For a transducer with an input power, P' , the characteristic source pressure, p_0 , is calculated as $p_0 = (2\rho c P' / \pi a^2)^{1/2}$ [97].

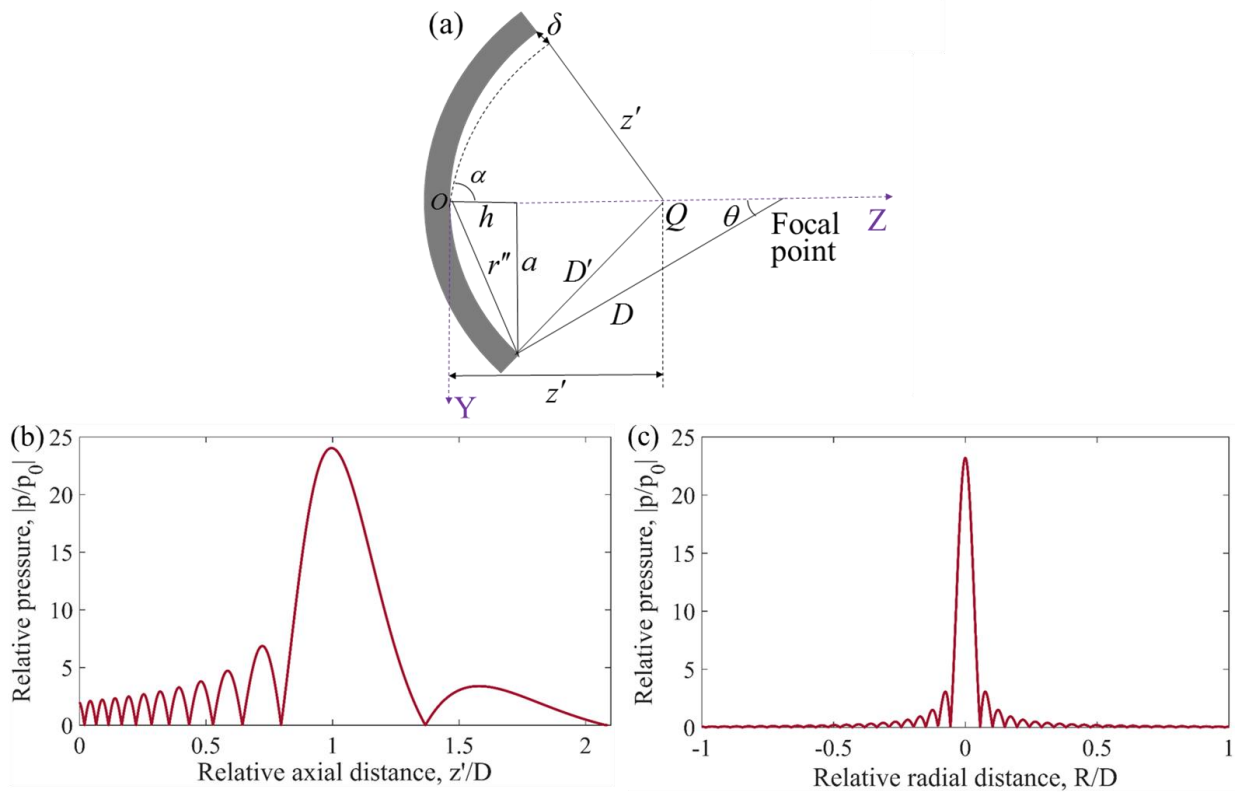


Fig. A1. (a) Geometrical details of the transducer with point of observation on the axis of symmetry, (b) relative acoustic pressure along axis of symmetry and (c) in focal plane

To calculate acoustic pressure in the focal plane $z' = D$, Eq. (A1.E2) is modified as

$$\Phi(r, \gamma) = \frac{p}{ik\rho c} = u S \left(\frac{e^{-ikr}}{2\pi r} \right) F(g) \quad (\text{A1.E4})$$

where $F(g) = (2/g) \sum_{j=0}^{\infty} (-1)^j (h/a)^{2j} J_{2j+1}(g)$ and the variable g is expressed as

$g = (1 - i/kr) k a \sin \gamma = k a \sin \gamma$. Here $J_{2j+1}(g)$ represents the Bessel function. Figure A1c

shows relative acoustic pressure at the focal plane where peak pressure occurs at focal point

($R = 0$). The

closed-form solutions are possible only for linear regime. To account for nonlinearity, absorption and diffraction effects in both fluid and polymer domains, numerical approach is adopted to obtain the acoustic pressure field by focused transducers, which is discussed in detail in the following section.

A2. DMA reported loss modulus and stiffness for various TBA-DEGMA compositions

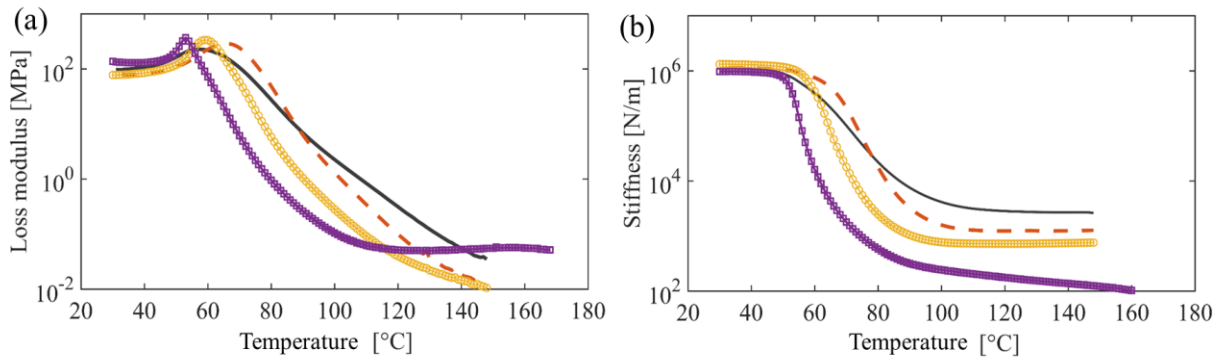


Fig. A2. (a) Loss modulus and (b) stiffness curves obtained from DMA tests for different compositions; the legend used in these two plots is consistent with Fig. 2.4.

A3. Fast fourier transform of pressure waveforms at focal point for various power and frequency; corresponding to Fig. 2.13

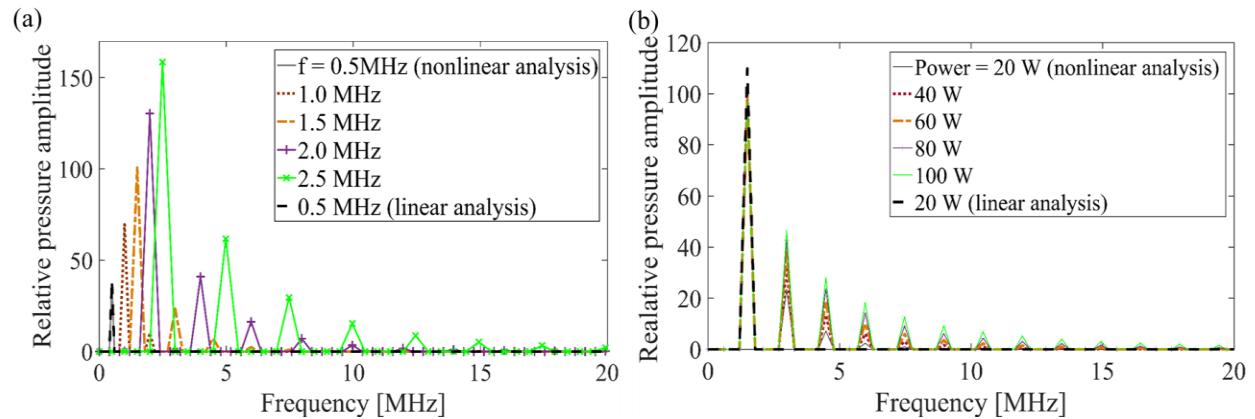


Fig. A3. Relative pressure (with reference as source pressure, p_0) at focal point in frequency domain (a) for various source frequency and 20 W input power (b) for various input power at 1.5 MHz

References

1. R. H. MuÈller, K. MaÈder and S. Gohla, *European journal of pharmaceutics and biopharmaceutics* **50** (1), 161-177 (2000).
2. K. E. Uhrich, S. M. Cannizzaro, R. S. Langer and K. M. Shakesheff, *Chemical reviews* **99** (11), 3181-3198 (1999).
3. S. Martel-Estrada, I. Olivas-Armendàriz, C. MartÌnez-PÈrez, T. Hernàndez, E. Acosta-Gómez, J. Chacón-Nava, F. Jiménez-Vega and P. García-Casillas, *Journal of Materials Science: Materials in Medicine* **23** (12), 2893-2901 (2012).
4. T. Xie, *Polymer* **52** (22), 4985-5000 (2011).
5. R. Bogue, *Assembly Automation* **32** (1), 3-7 (2012).
6. V. Giurgiutiu, *Journal of Intelligent Material Systems and Structures* **11** (7), 525-544 (2000).
7. I. Chopra, *AIAA journal* **40** (11), 2145-2187 (2002).

8. M. V. Gandhi and B. S. Thompson, *Smart materials and structures*. (Springer Science & Business Media, 1992).
9. A. Lendlein and S. Kelch, *Angewandte Chemie International Edition* **41** (12), 2034-2057 (2002).
10. X. Chen, M. A. Dam, K. Ono, A. Mal, H. Shen, S. R. Nutt, K. Sheran and F. Wudl, *Science* **295** (5560), 1698-1702 (2002).
11. X. Chen, F. Wudl, A. K. Mal, H. Shen and S. R. Nutt, *Macromolecules* **36** (6), 1802-1807 (2003).
12. C. e. Yuan, M. Z. Rong, M. Q. Zhang, Z. P. Zhang and Y. C. Yuan, *Chemistry of Materials* **23** (22), 5076-5081 (2011).
13. B. Ghosh and M. W. Urban, *Science* **323** (5920), 1458-1460 (2009).
14. Y. Amamoto, H. Otsuka, A. Takahara and K. Matyjaszewski, *Advanced Materials* **24** (29), 3975-3980 (2012).
15. W. M. Huang, Y. Zhao, C. C. Wang, Z. Ding, H. Purnawali, C. Tang and J. L. Zhang, *Journal of Polymer Research* **19** (9), 9952 (2012).
16. L. Haibao, H. Wei Min, Y. Q. Fu and L. Jinsong, *Smart Mater. Struct.* **23** (12), 125041 (2014).
17. R. Mirzaeifar, Georgia Institute of Technology, 2013.
18. R. Mirzaeifar, R. DesRoches, A. Yavari and K. Gall, *International Journal of Solids and Structures* **50** (10), 1664-1680 (2013).
19. R. Mirzaeifar, R. DesRoches and A. Yavari, *Continuum Mech. Thermodyn.* **23** (4), 363-385 (2011).
20. K. Uchino, *Shape Memory Materials*, 184-202 (1998).
21. H. Meng and G. Li, *Polymer* **54** (9), 2199-2221 (2013).
22. C. Liu, H. Qin and P. Mather, *Journal of materials chemistry* **17** (16), 1543-1558 (2007).
23. D. Ratna and J. Karger-Kocsis, *Journal of Materials Science* **43** (1), 254-269 (2008).
24. S. S. Venkatraman, L. P. Tan, J. F. D. Joso, Y. C. F. Boey and X. Wang, *Biomaterials* **27** (8), 1573-1578 (2006).

25. C. M. Yakacki, R. Shandas, C. Lanning, B. Rech, A. Eckstein and K. Gall, *Biomaterials* **28** (14), 2255-2263 (2007).
26. L. Xue, S. Dai and Z. Li, *Biomaterials* **31** (32), 8132-8140 (2010).
27. B. L. Volk, Texas A&M University, 2012.
28. C. Wischke and A. Lendlein, *Pharm. Res.* **27** (4), 527-529 (2010).
29. J. Kost and R. Langer, *Advanced drug delivery reviews* **64**, 327-341 (2012).
30. J. R. Kumpfer and S. J. Rowan, *Journal of the American Chemical Society* **133** (32), 12866-12874 (2011).
31. A. Lendlein, H. Jiang, O. Jünger and R. Langer, *Nature* **434** (7035), 879 (2005).
32. K. C. Hribar, R. B. Metter, J. L. Ifkovits, T. Troxler and J. A. Burdick, *Small* **5** (16), 1830-1834 (2009).
33. U. N. Kumar, K. Kratz, W. Wagermaier, M. Behl and A. Lendlein, *Journal of Materials Chemistry* **20** (17), 3404-3415 (2010).
34. U. N. Kumar, K. Kratz, M. Heuchel, M. Behl and A. Lendlein, *Adv. Mater.* **23** (36), 4157-4162 (2011).
35. K. Yu, Z. Zhang, Y. Liu and J. Leng, *Applied Physics Letters* **98** (7), 074102 (2011).
36. Y. Liu, H. Lv, X. Lan, J. Leng and S. Du, *Compos. Sci. Technol.* **69** (13), 2064-2068 (2009).
37. J. Kennedy, G. Ter Haar and D. Cranston, *The British journal of radiology* (2014).
38. G. ter Haar and C. Coussios, *International journal of hyperthermia* **23** (2), 89-104 (2007).
39. S. Shahab and A. Erturk, *Smart Materials and Structures* **23** (12), 125032 (2014).
40. S. Shahab, M. Gray and A. Erturk, *Journal of Applied Physics* **117** (10), 104903 (2015).
41. S. Shahab and A. Erturk, presented at the ASME 2014 International Design Engineering Technical Conferences and Computers and Information in Engineering Conference, 2014.
42. M. B. Nejad, A. Elnahas, S. Jung and S. Shahab, presented at the SPIE Smart Structures and Materials+ Nondestructive Evaluation and Health Monitoring, 2017.
43. J. Kost, K. Leong and R. Langer, *Proceedings of the National Academy of Sciences* **86** (20), 7663-7666 (1989).

44. B. G. De Geest, A. G. Skirtach, A. A. Mamedov, A. A. Antipov, N. A. Kotov, S. C. De Smedt and G. B. Sukhorukov, *Small* **3** (5), 804-808 (2007).
45. H. Bruinewoud, 2005.
46. D. G. Shchukin, D. A. Gorin and H. Möhwald, *Langmuir* **22** (17), 7400-7404 (2006).
47. A. G. Skirtach, B. G. De Geest, A. Mamedov, A. A. Antipov, N. A. Kotov and G. B. Sukhorukov, *J. Mater. Chem.* **17** (11), 1050-1054 (2007).
48. G. A. Hussein, N. Y. Rapoport, D. A. Christensen, J. D. Pruitt and W. G. Pitt, *Colloids and Surfaces B: Biointerfaces* **24** (3), 253-264 (2002).
49. Y. Li, R. Tong, H. Xia, H. Zhang and J. Xuan, *Chem. Commun.* **46** (41), 7739-7741 (2010).
50. J. Wang, M. Pelletier, H. Zhang, H. Xia and Y. Zhao, *Langmuir* **25** (22), 13201-13205 (2009).
51. A. Marin, M. Muniruzzaman and N. Rapoport, *J. Controlled Release* **75** (1), 69-81 (2001).
52. B. Liu, H. Xia, G. Fei, G. Li and W. Fan, *Macromol. Chem. Phys.* **214** (22), 2519-2527 (2013).
53. J. Han, G. Fei, G. Li and H. Xia, *Macromolecular Chemistry and Physics* **214** (11), 1195-1203 (2013).
54. X. Lu, G. Fei, H. Xia and Y. Zhao, *Journal of Materials Chemistry A* **2** (38), 16051-16060 (2014).
55. G. Li, G. Fei, B. Liu, H. Xia and Y. Zhao, *RSC Advances* **4** (62), 32701-32709 (2014).
56. T. S. Hart and M. F. Hamilton, *The Journal of the Acoustical Society of America* **84** (4), 1488-1496 (1988).
57. A. Rozanova-Pierrat, (2006).
58. M. F. Hamilton and D. T. Blackstock, *Nonlinear acoustics*. (Academic press San Diego, 1998).
59. F. P. Curra, P. D. Mourad, V. A. Khokhlova, R. O. Cleveland and L. A. Crum, *IEEE transactions on ultrasonics, ferroelectrics, and frequency control* **47** (4), 1077-1089 (2000).

60. Y. Jing, D. Shen and G. T. Clement, IEEE transactions on ultrasonics, ferroelectrics, and frequency control **58** (5) (2011).
61. J. Tavakkoli, D. Cathignol, R. Souchon and O. A. Sapozhnikov, The Journal of the Acoustical Society of America **104** (4), 2061-2072 (1998).
62. M. Solovchuk, T. W. Sheu and M. Thiriet, The Journal of the Acoustical Society of America **134** (5), 3931-3942 (2013).
63. H. O'Neil, The Journal of the Acoustical Society of America **21** (5), 516-526 (1949).
64. J. E. Soneson, The Journal of the Acoustical Society of America **131** (6), EL481-EL486 (2012).
65. J. E. Soneson, R. Muratore and E. E. Konofagou, presented at the AIP Conf. Proc., 2012.
66. V. Khokhlova, S. Kashcheeva, M. Averkiou, L. Crum, W. Lauterborn and T. Kurz, presented at the AIP Conf. Proc., 2000.
67. B. Ystad and J. Berntsen, Acta acustica **3** (4), 323-330 (1995).
68. J. Huijssen and M. D. Verweij, The Journal of the Acoustical Society of America **127** (1), 33-44 (2010).
69. V. W. Sparrow and R. Raspet, The Journal of the Acoustical Society of America **90** (5), 2683-2691 (1991).
70. Y. S. Lee and M. F. Hamilton, The Journal of the Acoustical Society of America **97** (2), 906-917 (1995).
71. S. I. Aanonsen, *Numerical computation of the nearfield of a finite amplitude sound beam*. (University of Bergen, Department of Applied Mathematics, 1983).
72. M. F. Hamilton, J. N. Tjo/tta and S. Tjo/tta, The Journal of the Acoustical Society of America **78** (1), 202-216 (1985).
73. T. Kamakura, M. Tani, Y. Kumamoto and K. Ueda, The Journal of the Acoustical Society of America **91** (6), 3144-3151 (1992).
74. F. S. McKendree, 1981.
75. K. Frøysa, J. N. Tjøtta and J. Berntsen, Advances in nonlinear acoustics, 233-238 (1993).
76. F. Pestorius and D. Blackstock, Finite-Amplitude Wave Effects in Fluids, 24-29 (1974).

77. R. O. Cleveland, M. F. Hamilton and D. T. Blackstock, *The Journal of the Acoustical Society of America* **99** (6), 3312-3318 (1996).
78. K. R. Waters, M. S. Hughes, J. Mobley, G. H. Brandenburger and J. G. Miller, *The Journal of the Acoustical Society of America* **108** (2), 556-563 (2000).
79. N. Jiménez, F. Camarena, J. Redondo, V. Sánchez-Morcillo, Y. Hou and E. E. Konofagou, *Acta Acustica united with Acustica* **102** (5), 876-892 (2016).
80. L. Bjørnø, *Physics Procedia* **3** (1), 5-16 (2010).
81. G. B. Whitham, *Linear and nonlinear waves*. (John Wiley & Sons, 2011).
82. J. E. Soneson and E. S. Ebbini, presented at the AIP Conf. Proc., 2009.
83. J. E. Soneson and M. R. Myers, *IEEE Transactions on Ultrasonics, Ferroelectrics, and Frequency Control* **57** (11), 2450-2459 (2010).
84. M. Wang and Y. Zhou, *International Journal of Hyperthermia* **32** (5), 569-582 (2016).
85. W. F. Ames, *Numerical methods for partial differential equations*. (Academic press, 2014).
86. A. Ostermann and M. Roche, *Mathematics of Computation* **59** (200), 403-420 (1992).
87. C. R. Hill, J. C. Bamber and G. Ter Haar, *The Journal of the Acoustical Society of America* **116** (5), 2707-2707 (2004).
88. G. Ter Haar, *Prog. Biophys. Mol. Biol.* **93** (1), 111-129 (2007).
89. W. Summer and M. K. Patrick, *Ultrasonic therapy: A textbook for physiotherapists*. (Elsevier, 1964).
90. M. Khanolkar, J. Sodhi and I. J. Rao, (44151), 105-109 (2010).
91. G. Barot, I. J. Rao and K. R. Rajagopal, *International Journal of Engineering Science* **46** (4), 325-351 (2008).
92. L. V. Brent, C. L. Dimitris and C. Yi-Chao, *Smart Mater. Struct.* **19** (7), 075006 (2010).
93. H. J. Qi, T. D. Nguyen, F. Castro, C. M. Yakacki and R. Shandas, *Journal of the Mechanics and Physics of Solids* **56** (5), 1730-1751 (2008).
94. K. Yu and H. J. Qi, *Soft Matter* **10** (47), 9423-9432 (2014).

95. G. Barot, *Constitutive Modeling of the Thermo-mechanics Associated with Crystallizable Shape Memory Polymers*. (ProQuest, 2007).
96. A. Penttinen and M. Luukkala, *J. Phys. D: Appl. Phys.* **9** (10), 1547 (1976).
97. L. E. Kinsler, A. R. Frey, A. B. Coppens and J. V. Sanders, *Fundamentals of Acoustics*, 4th Edition, by Lawrence E. Kinsler, Austin R. Frey, Alan B. Coppens, James V. Sanders, pp. 560. ISBN 0-471-84789-5. Wiley-VCH, December 1999., 560 (1999).

Chapter 3 : Analysis of ultrasound actuated shape-memory polymer based drug delivery containers in heterogenous environments

Details of publication

Co-authors: Kaiyuan Peng, Reza Mirzaeifar, and Shima Shahab

Citation: Bhargava A, Peng K, Mirzaeifar R and Shahab S, 2018, Ultrasound actuated shape-memory polymer based drug delivery containers, Proc. SPIE **10595**, Active and Passive Smart Structures and Integrated Systems XII, 105952H (15 March 2018)

Abstract

Advancements in controlled drug delivery (CDD) technology still face major challenges in practice, including chemical issues with synthesizing biocompatible drug containers, releasing the pharmaceutical compounds at the targeted location in a controlled time rate, and using an effective and safe trigger for initiating the drug release. This work aims to overcome these challenges by employing biodegradable shape memory polymer (SMP) based drug-delivery containers. Besides biological safety, biodegradability ensures that no further surgery will be needed for the removal of the containers. Focused ultrasound (FU) is used as a trigger for noninvasively stimulating SMP-based drug capsules. FU has a superior capability to localize the heating effect, thus initiating a controlled shape recovery process only in selected parts of the

polymer. The current research uses a mathematical multiphysics model which performs an acoustic-thermoelastic analysis, to optimize the design of SMP containers. The proposed designs exploit various acoustic parameters such as nonlinearity, absorption, and diffraction effects, as well as input power and frequency of the propagating acoustic wave to attain the desired shape recovery. The acoustic-thermoelastic effects on the SMP containers are studied with the help of finite-element methods. Multilayer simulations are performed at a millimeter scale to mimic the *in vivo* conditions of a drug delivery container travelling inside an artery. It is shown that velocity of the drug particles can be controlled and directed towards a desired location by manipulating the shape recovery rate and consequent motion of the SMP containers. In order to realize the drug capsule designs, several geometrically simple 3d printed samples are tested to understand how 3d printed patterns affect the shape recovery behavior.

3.1. Introduction

The method of drug administration is of utmost importance as it affects drug pharmacokinetics inside the body. Conventional drug delivery mechanisms involved administration of drugs in the form of oral tablets or injecting intravenous/intramuscular solutions. Such delivery methods limit drug efficacy due to lack of targeted delivery, need of higher dosage, frequent drug administration, higher toxicity, and adverse side effects [1].

In order to achieve drug efficacy among patients, recent years have seen immense growth of drug delivery systems to achieve therapeutic specificity, localized and controlled delivery. Equally important is to suppress opsonization and prevent cytotoxicity due to the material of the device and its degradation products [2, 3]. Polymers are one such class of materials that have shown

immense potential for manufacturing controlled drug release systems because of their ease in manufacturing, availability, cost and tunable physical and chemical structure [4]. Increasing efforts are being made by scientists to use polymers for making biodegradable and biocompatible micro and nanoscale drug carriers.

Common categories of microscale CDD systems include matrix-based systems, reservoirs and chambers, chemically regulated degradable or erodible devices, microscale pumps, and valves among others [4]. Cell chambers which can manufacture drugs within the chambers, while remaining isolated from immune response show controllable release rates of the desired therapeutic compounds. However, such chambers have limitations on the continuity of the nutrient supply to the chamber cells after implantation [5]. Injectable CDD systems such as hydrogels regulate drug release by controlling the mesh size of the swollen polymer networks. Cellulose-based self-assembling hydrogels provide sustained release of proteins for up to 160 days [6]. Microspheres are another class of CDD which can transport drugs across blood-brain barrier and tumor cells due to their small size [7].

However, in the last decade, CDD systems have experienced a significant shift towards nanotechnology because of the advantage of smaller size and high surface to volume ratio. Polymer based nanoparticles, liposomes, and micelles are the dominant class of nano-range drug release mechanisms. PEG coatings and ligand based targeting have enhanced the stability [8] and the specificity of nanoparticles [9]. Effective penetration of neuroleptics across the blood brain barrier was achieved with poly(oxyethylene)-poly(oxypropylene) block copolymer micelles conjugated with antibodies [10]. N-(2-Hydroxyl) propyl-3-trimethyl ammonium chitosan

chloride nanoparticles sized 110-180 nm showed 90% encapsulation efficiency of bovine serum protein [11].

The above mentioned examples are only a handful of the extensive research done in the field of micro and nano drug delivery systems [12]. However, most of the research is still largely experimental and not in commercial use. Nano devices though promising, have only proved to be successful for targeted drug delivery to tumors. High initial burst release, low bioavailability [3], and premature release due to hostile environment are few of the hurdles limiting effective CDD devices. To overcome some of the challenges of the existing drug delivery systems, scientific community has increased its attention towards intelligent and combinatorial mechanisms.

Intelligent or smart devices provide an active and a more controllable form of drug delivery. Use of smart materials with properties sensitive to various stimuli in the surrounding environment, in combination with optimum sized micro and nano-scale devices, is the emerging trend in nanomedicine [13, 14]. pH-responsive multiblock polyurethane nanocarriers exhibited controlled release of paclitaxel with excellent antitumor activity in mice [15]. Ding *et al.* [16] prepared smart core-shell-corona hybrid nanogels by entrapping magnetic nanoparticles inside a silica shell and encapsulating the shell with thermo-responsive polymer.

This work aims to provide a novel alternative approach to make CDD systems by combining the shape memory properties of thermo-responsive polymers with a controllable and non-invasive stimulus; focused ultrasound (FU). Shape memory polymers (SMPs) are light-weight, inexpensive, able to undergo large deformations, have good mechanical strength, and have a controllable physical and chemical structure [17, 18]. These properties are some of the essential

attributes of drug delivery devices. Medical community is increasingly adopting biocompatible and biodegradable SMPs in medical applications such as stents for cardiovascular applications and scaffolds for tissue engineering among others [19-21]. In parallel, the use of FU has been well researched for biomedical purposes especially for drug delivery from polyelectrolyte microcontainers [22], polymer micelles [23, 24], and multi-layered capsules [25]. FU provides a non-invasive, biologically safe and a more flexible thermal trigger as compared to body heat. Focusing ultrasound in an area of approximately millimeter scale causes selective and localized heating of the target medium [26, 27]. Recently in our group, Bhargava *et al.* [26, 28] demonstrated the effect of various parameters such as geometric and material properties of SMPs, power and frequency of the applied acoustic pressure field on the shape recovery of a polymer filament, during 20s of FU actuation. By considering a polymer filament as a fundamental element for design of any SMP based drug delivery container, the authors demonstrated the controllability of FU on the thermally induced shape memory response and consequently the drug delivery rate from SMP containers. Thus, ultrasound actuated thermo-responsive shape memory polymers have significant potential as a more active and biocompatible method to non-invasively control the drug delivery rate.

In this chapter, we study the effects of FU on artery-scale SMPs in heterogenous environments. We use our previously built analytical acoustic-thermoelastic model [26] to analyze the *in vivo* shape memory response of biocompatible polymers. The model effectively predicts the influence of acoustic source, propagating medium and polymer geometric properties on the deformation behavior of a SMP inside a blood artery model. It is also shown that by varying the different FU

and SMP parameters, the desired drug delivery rate can be achieved from the drug carrying containers, solving some of the challenges of existing drug delivery mechanisms. Various drug delivery capsule designs are proposed based on the optimum conditions predicted by the analytical model. One of the proposed designs is of a container shape inspired from a flower as shown in Fig 3.1. Figure 3.1 depicts the cyclic shape recovery behavior where the first stage is to forcibly deform the permanent structure (open shape) of the container into a temporary closed shape on heating, thereby enclosing the drug particles inside the container. The second stage is fixing the temporary shape by cooling it while the drug particles remain inside it. At this stage, the container can be injected into the body. The third stage is exposing the container to ultrasound irradiation which results in the shape recovery of the container. The shape recovery mechanism is built on the idea of simultaneously opening the container and letting the drug particles out at a desired rate by pushing the diaphragm (bottom portion of the design) upwards at a desired speed determined by ultrasound induced thermal actuation. In order to realize different drug capsule geometries, different 3d printing patterns are looked at to assess how the printed patterns affect shape memory behavior.

3.2. Theory

The multiphysics theoretical model developed in this work studies the acoustic-thermoelastic interaction of SMP filaments with FU. The model is divided into three interconnected parts. The first part analyses the acoustic pressure field, p , using Khokhlov–Zabolotskaya–Kuznetsov (KZK) equation [29, 30] in a multilayer domain, starting from skin up to the deepest artery wall inside heart. The SMP is placed inside the artery to achieve maximum drug delivery to the target.

The equation takes into account the diffraction, attenuation and non-linear effects of the wave propagating medium and numerically solves it using operator-splitting method in a hybrid time-frequency domain. The second part evaluates the thermal field developed inside SMP due to absorbed acoustic energy, using Penne's Bioheat equation, Eq. 10 of chapter 2 [31]. The third part calculates the thermally induced mechanical strains inside the SMP. The subsequent shape recovery is estimated using a constitutive model (section 2.2.3) which is numerically implemented in a user material subroutine (UMAT) in ABAQUS. The equations below are a brief review and the complete analytical model is explained in detail in our previous works [26, 28]. The results from the analytical model are verified using COMSOL Multiphysics for a multilayer domain. The model is then used to optimize the complex 3D designs of drug delivery containers, which are then implemented in the finite-element method to study the controlled drug delivery behavior under biologically safe thresholds.

3.3. Results

3.3.1. Model validation for multi-medium environment

The analytical model developed in our previous work studied the acoustic-thermoelastic behavior of SMP submerged in a water domain and exposed to FU. The model was validated with finite-element methods and experiments to accurately predict the shape recovery behavior of a polymer filament [26]. To understand this behavior in an *in-vivo* environment, the SMP is considered to be placed inside a blood artery of a heart so that maximum drug delivery to the target (heart) can be achieved. The current work makes use of the previously built validated analytical model to show the effect of multiple domains (multiple layers between skin and artery)

on the acoustic and thermal fields of SMP exposed to FU. In order to emphasize the effect of multiple layers of tissues inside the body, a comparison is drawn between a SMP filament kept in water domain and a SMP filament kept inside the body (Figs. 3.2 and 3.3). The predicted values of acoustic and thermal fields from the analytical model are validated with finite-element simulations in COMSOL and a good agreement is observed. The acoustic and thermal properties for various tissues and polymer are taken from literature and our previous study, respectively [32].

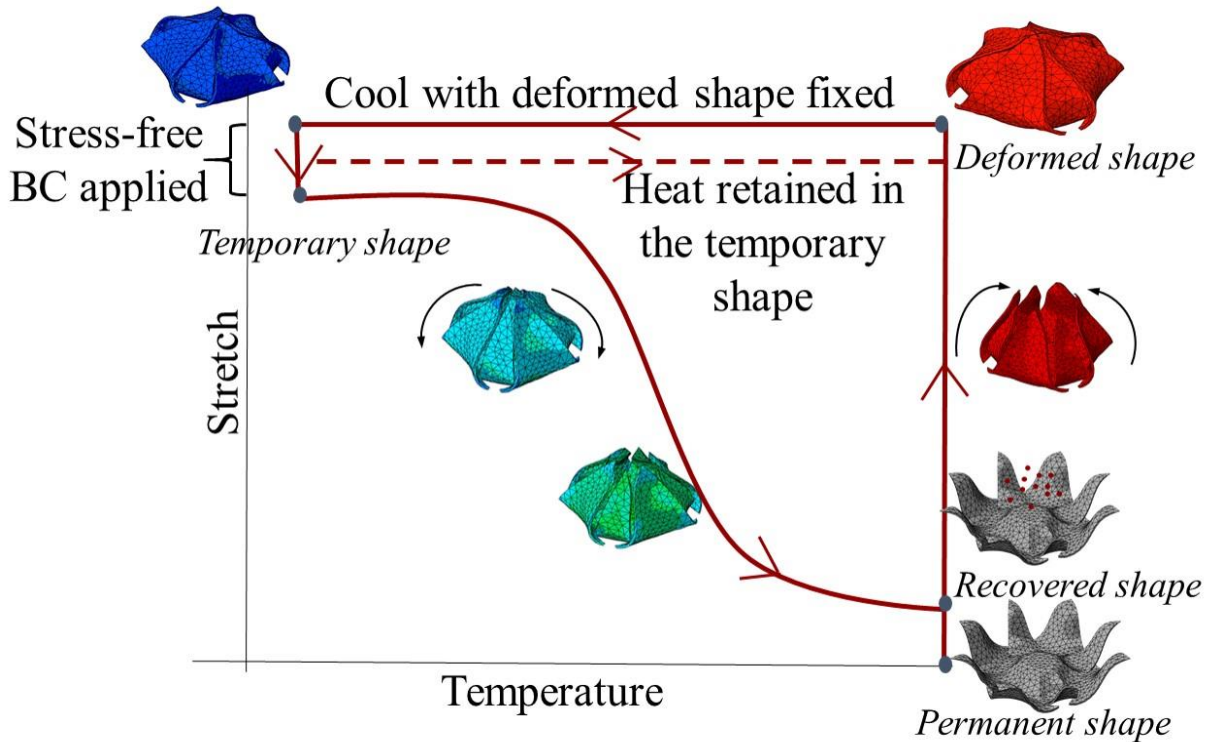


Fig. 3.1. The graph depicts the heating and cooling cycle of a flower shaped drug delivery container that undergoes ultrasound induced thermal actuation in the last stage, leading to release of the enclosed drug particles at the last stage.

Figure 3.2 shows the relative acoustic pressure field of the fundamental harmonic along axis of symmetry of the transducer at a source frequency (0.5 MHz) and 15 W input power of the transducer. The reduction in relative pressure amplitude in multi-layer domain is due to the high attenuation coefficients of tissues, particularly of fat. The amplified effects of diffraction and nonlinearity inside SMP as compared to surroundings cause a sudden jump in the pressure amplitude at the focal point of transducer ($z \cong 52$ mm). The oscillations in the pre-focal region are assumed to be due to standing waves, numerical dispersion and Gibb's phenomenon [33]. Figure 3.3 shows temperature rise of the polymer at the focal spot during 20 s of ultrasound exposure. The percentage of temperature reduction at focal point between single and multiple domain modelsthe is higher as compared to pressure reduction between the two models. This is due to the dominance of nonlinear effects over attenuation effects in the nearfield region which leads to significantly lower influence of absorption coefficient on pressure field as compared to thermal field in polymer, Eq. 10 of chapter 2 and Refs. [26, 34].

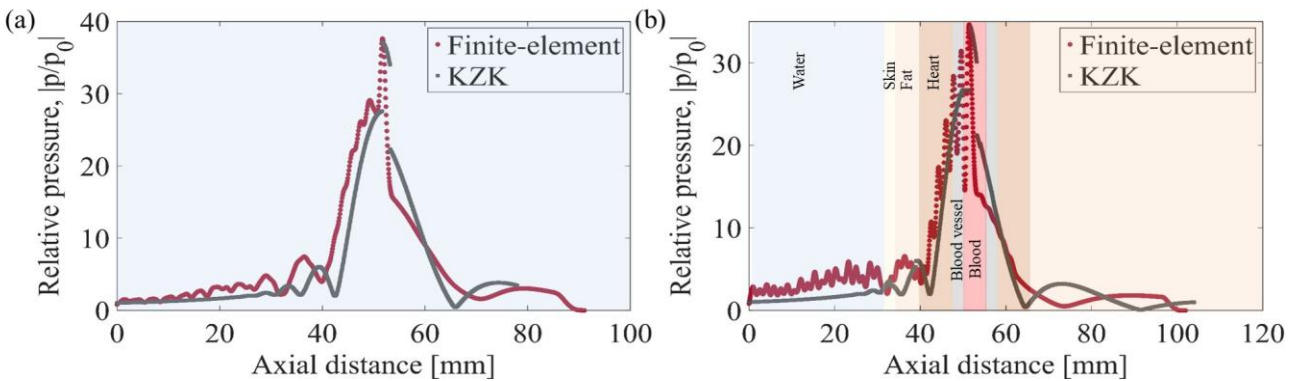


Fig. 3.2. Relative axial pressure along axis of symmetry of transducer in (a) water domain (b) blood artery inside heart. Both domains have SMP placed at the focal point. Normalization is done with respect to source pressure, p_0 .

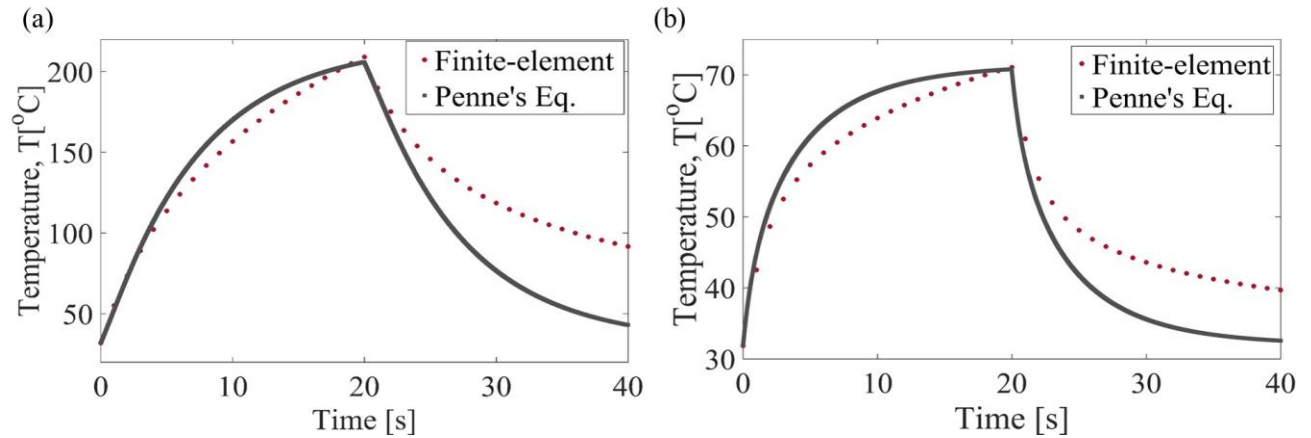


Fig. 3.3. Temperature rise at the focal point of transducer in (a) water domain (b) blood artery inside heart at 15W and 0.5 MHz. Both domains have SMP placed at the focal point.

3.3.2. Acoustic-thermal study of wave propagation in a multi-layer domain

One of the major concerns in the medical community related to the use of thermal trigger for effective drug delivery is of potential damage to the surrounding environment. The use of FU and a SMP is a promising solution to this problem. Figure 3.4 shows two-dimensional acoustic and thermal fields in a multi-layer domain calculated using finite element methods. It can be seen that most of the energy is concentrated in the focal region inside SMP, whereas the level of acoustic and thermal energy concentration in all tissues is well below the FDA approved threshold energy level (Spatial-Peak Pulse-Average Intensity =190 W/cm²) [35, 36]. This is further demonstrated in Fig. 3.4d which compares the temperature rise inside different tissues along the path of ultrasound actuation of SMP, for 20 s of sonication period. It is seen that the maximum temperature in blood and artery wall ($\cong 57^{\circ}\text{C}$) is attained for less than a second which is insufficient for causing thermal ablation [37]. Thus, it is inferred that FU actuated drug delivery containers can be operated at biologically safe conditions and are capable of producing localized responses.

3.3.3. Geometrical investigation of drug delivery capsules

The multi-domain acoustic-thermoelastic model is an efficient way of optimizing and customizing external properties such as FU power, source frequency and geometrical properties of the polymer. Having validated the thermal safety of using FU actuated SMPs inside the body, few designs of the drug delivery containers are proposed based on the analytical model, Fig. 3.5. In order to maintain brevity, only one of the designs is explained in detail in this work. The purpose of demonstrating these CDD container designs is to elaborate the ease and flexibility of designing at different length scales which SMPs offer as compared to other drug delivery mechanisms. The external FU induced shape recovery has an advantage of offering mechanical control on drug release over chemically controlled systems. Figure 3.6 shows the displacement and normalized velocity profiles of a 2 (diameter) x 2 mm flower shaped capsule at 15 W of power and 0.5 MHz. These geometrical dimensions enable the capsule to flow freely inside an artery having a lumen diameter of 6 mm. The simultaneous angular movement of valve with respect to upward displacement of diaphragm exhibits a quadratic relationship (Fig. 3.6a). This shows that the valve moves faster, thus pushing the drug particles (resting on the diaphragm initially) out of the container unhindered. This is further detailed in Fig. 3.5b where a higher normalized velocity of valve as compared to diaphragm insures a regulated and uniform passage of drug particles into the bloodstream. A small jump in the velocity profile at approximately 10 s can be seen. It is due to the method of implementing thermal data in ABAQUS to analyze mechanical stresses. The thermal data is divided into two halves from 0 to 10 s and 10 to 20 s

which results in a smooth response in these ranges but a discontinuous response between the two occurs.

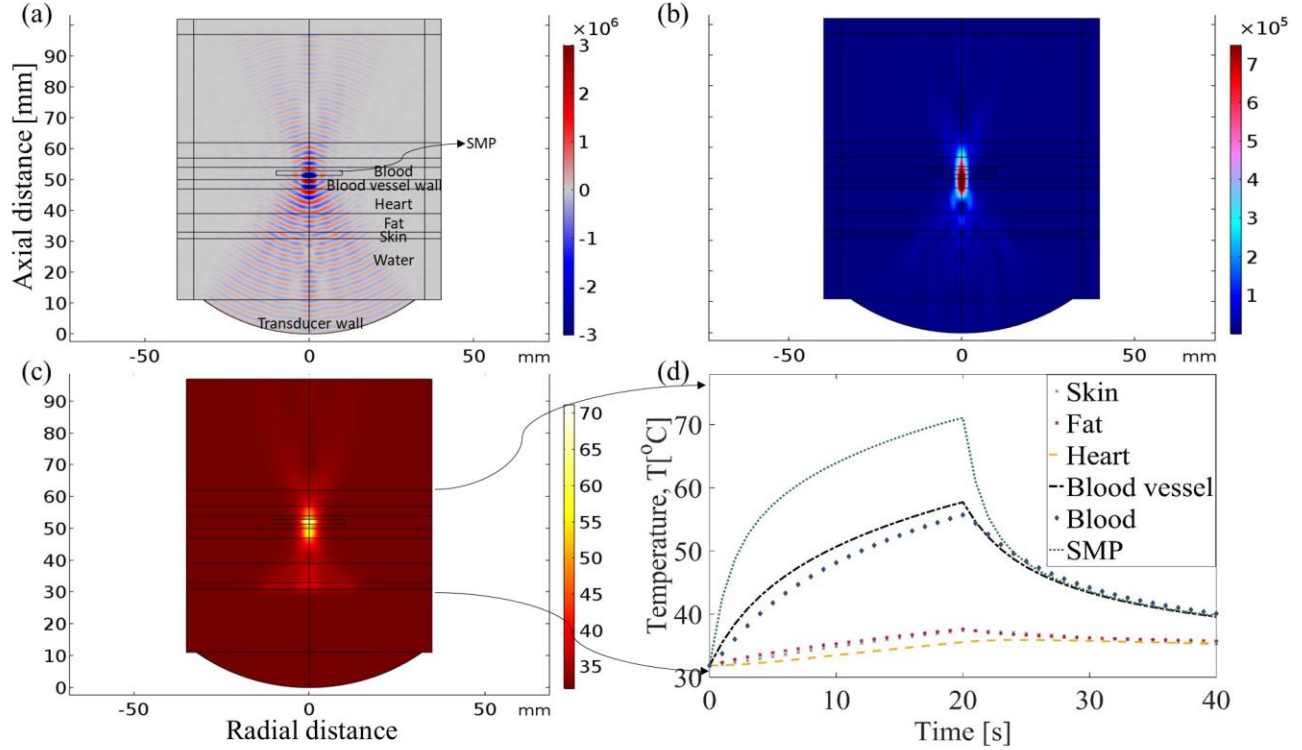


Fig. 3.4. 2D representations of (a) acoustic pressure field (Pa), (b) acoustic intensity (W/m²) and (c) Thermal field (°C) in a multilayer domain. (d) Temperature rise in different tissue layers during ultrasound actuation of SMP inside the artery.

3.3.4. Effects of acoustic parameters on drug delivery container's motion

To study the amount of controllability that FU offers on the drug release, simulations are performed for various power and source frequencies of the transducer (Fig. 3.7). It is observed in Fig. 3.7a and 3.7c that with an increase in power, the onset of shape recovery is accelerated and both angular and axial velocity increase by one order of magnitude for 250% increase in input power. This is expected as higher power leads to more energy deposition in the polymer [28],

leading to faster and more shape recovery. A similar behavior for axial velocity is observed with increase in acoustic wave frequency, however, its effect on the velocity magnitude is less than that of power (Fig. 3.7b and 3.7d). This is due to the increase in number of harmonics concentrated at the focal point leading to an increase in the cumulative heating rate of polymer (Eq. 21 of Ref. [26]) and consequently developing higher thermal stresses with increase in frequency. A higher normalized angular velocity is seen at 0.5 MHz as compared to 1 MHz in Fig. 3.7d. It is reasoned that this behavior is due to better uniform distribution of temperature at resonant frequency (0.5 MHz) as compared to 0.75 MHz and 1 MHz, thus giving higher angular velocity to the valve and better shape recovery. The variation in shape recovery with power and frequency can be exploited to choose the onset time and the amount of drug release as required. Figure 3.7 shows that by varying these two parameters, an efficient control on different parts of the container design can be achieved, which consequently influences the drug delivery rate, thus solving some of the challenges in CDD such as high initial burst release, maintaining the order of delivery rate, and bioavailability among others.

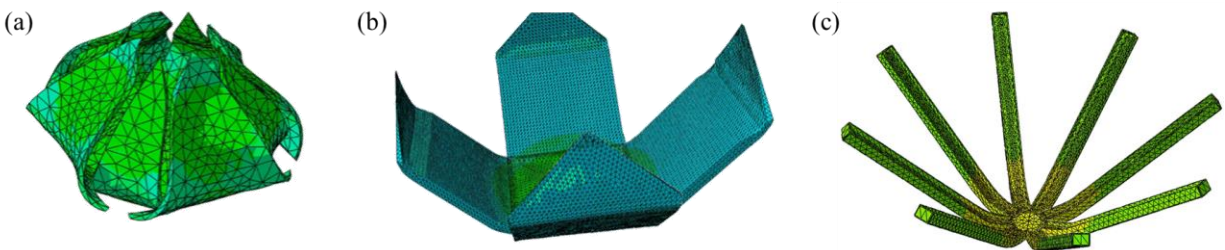


Fig. 3.5. Proposed capsule designs. (a) A flower shaped SMP capsule. (b) A box shaped capsule. (c) A star shaped capsule where drug particles are stored in the individual arms of the star and releases upon actuation of each arm separately.

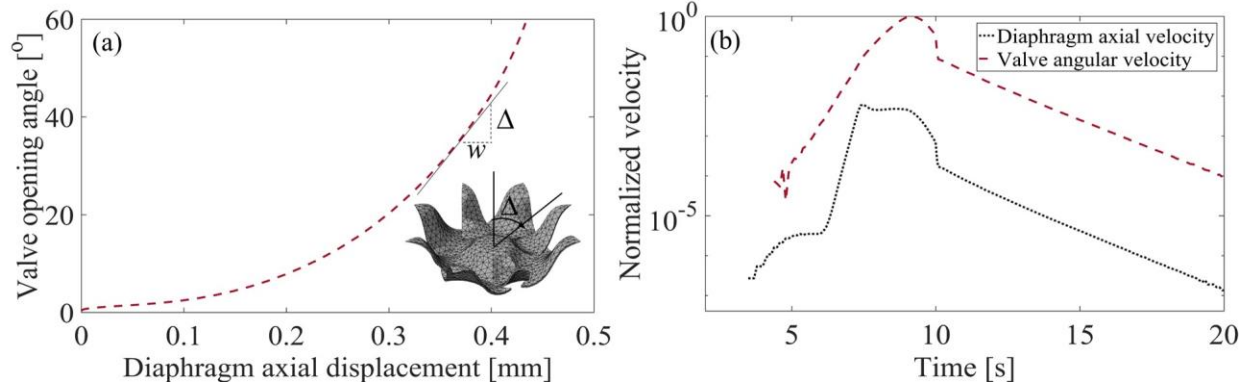


Fig. 3.6 (a) Angular displacement of valve with respect to diaphragm of the container (shown in inset) and (b) normalized velocity with respect to time in log scale, of the diaphragm and valve during shape recovery behavior. Normalization is done with respect to the maximum velocity. w is the diaphragm axial displacement.

3.4. 3d-printed SMPs

To realize the proposed drug capsule designs shown in Fig. 3.5, 3d printing technique is considered. 3d printing is a powerful technique with the capability of producing a wide variety of complex shapes with high accuracy. 3d printing of SMPs, also known as 4d printing, has recently gained attention due to reduced costs, ability to print multiple materials into one object, and simplicity of the printing procedure [38]. Many printing techniques such as fused-deposition modeling, direct ink writing, and stereolithography are currently being used to achieve 4d printing of polymers [39-41]. Ge *et al.* [42] used projection microstereolithography technique to photo-cure methacrylate based copolymers with highly tunable thermomechanical properties. In this work, extrusion based 3d printing using Ultimaker 3 is performed in collaboration with Medshape company. Various 3d printed patterns and shapes, as shown in Fig. 3.8, are composed of a thermoplastic polymer, Polyurethane. These samples have a transition temperature of approximately 60°C, as determined by the DMA analysis shown in appendix B. Out of these

patterns, various samples with different geometries are obtained from Medshape. Table 3.1 lists the geometrical properties of these samples. The table assigns a sample number to each unique sample with its corresponding shape and pattern shown in Fig. 3.8.

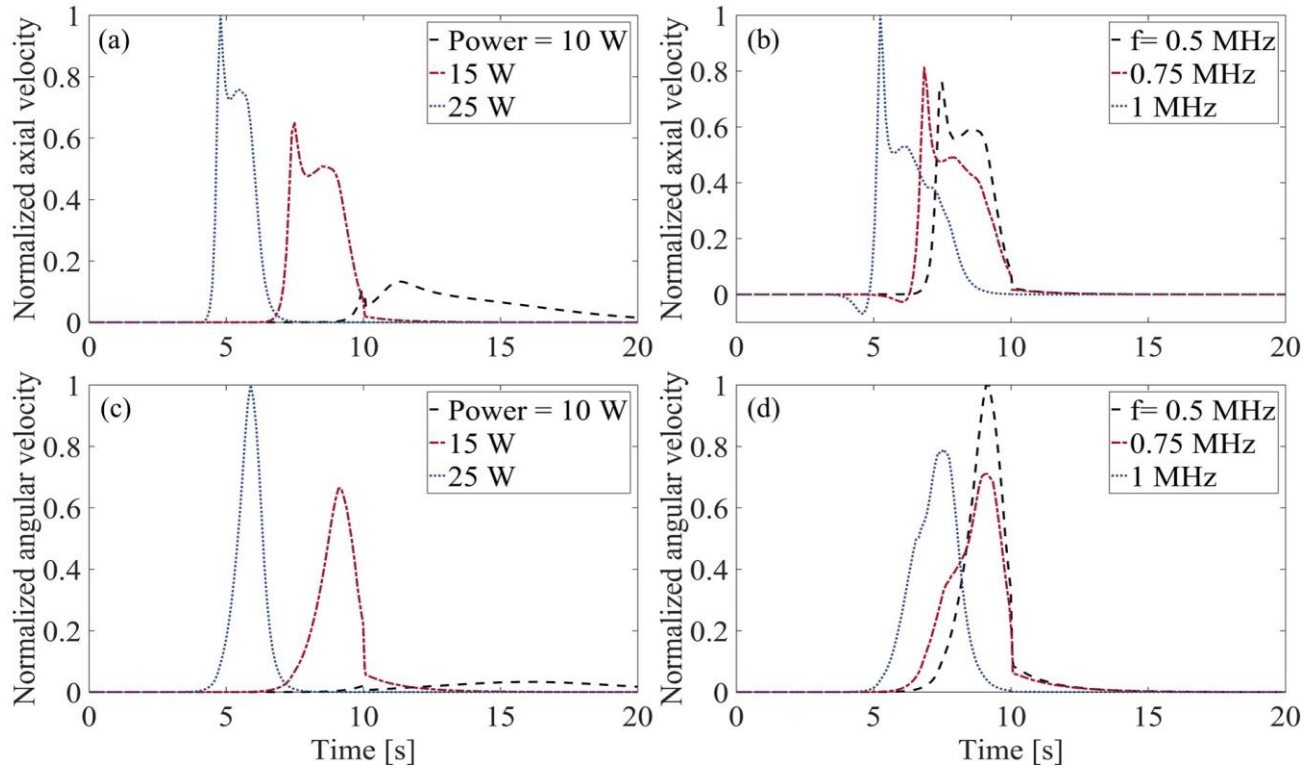


Fig. 3.7. Normalized axial velocity of diaphragm for various (a) input power and (b) source frequency. Normalized angular velocity of valve for various (c) input power and (d) source frequency, during 20 s of ultrasound actuation.

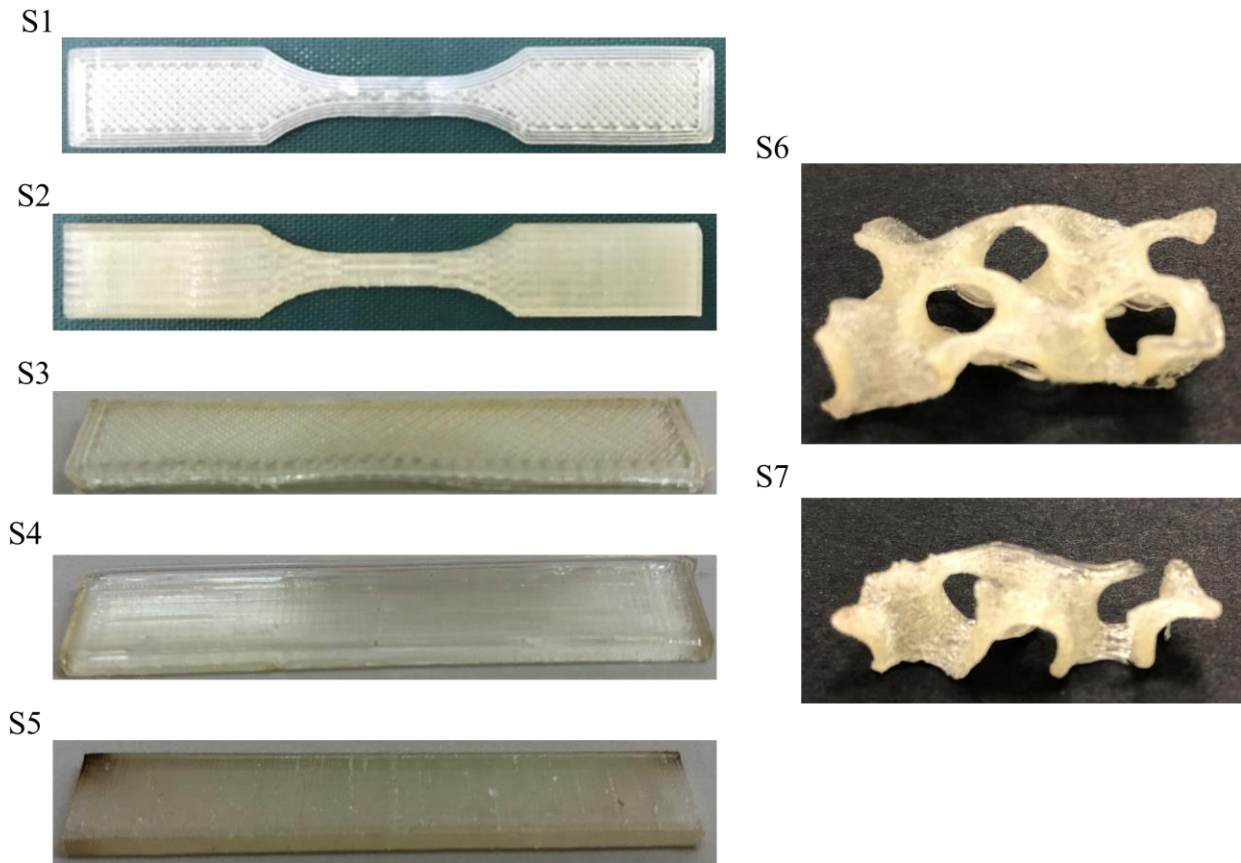


Fig. 3.8. Dogbone shape with (S1) criss-cross and (S2) longitudinal 3d printed patterns. Rectangular samples with (S3) criss-cross, (S4) longitudinal, and (S5) transverse 3d printed patterns. Hollow gyroidal shape samples with (S6) small width and (S7) large width.

To find the optimum 3d printed pattern and geometry for maximum shape recovery, experiments are conducted using the setup in our previous work [26]. The setup consists of a $61.5 \times 31.8 \times 32.5 \text{ cm}^3$ water tank lined with absorbing sheets to avoid sound reflection from the tank walls, Fig. 3.9a. Degassed water is used to avoid any bubble cavitation at high levels of ultrasound intensity. A H-104 SONIC Concepts high intensity focused ultrasound (HIFU) is placed at the bottom floor of the tank, Fig. 3.9a. The polymers are suspended at the focal point of the transducer as shown in Fig. 3.9b using a positioning system. The polymers are first deformed in

a V-shape by applying force under a heat gun. At high temperatures, the polymers are in amorphous phase and thus, easily deformable. Once cooled, the V-shape is fixed. The polymers are then suspended in the water tank to examine shape recovery under ultrasound exposure. Two sets of experiments are conducted; first, when polymer is mostly exposed to air (Fig. 3.9b1) and second, when the SMP is completely immersed in water (Fig. 3.9b2).

Table 3.1. Geometry of the samples used in experiments

Sample number (corresponding shape)	Length (mm) x width (mm) x thickness (mm)
1 (S1)	17.4 x 3.7 x 1.4 (middle neck)
2 (S2)	17.4 x 3.7 x 1.4 (middle neck)
3 (S3)	50 x 25 x 2
4 (S4)	50 x 25 x 2
5 (S5)	50 x 25 x 2
6 (S3)	50 x 9 x 2
7 (S4)	50 x 9 x 2
8 (S5)	50 x 9 x 2
9 (S6)	32 x 16 x 8
10 (S7)	32 x 9 x 8

Figure 3.10 shows the amount of shape recovery of the samples listed in Table 3.1 in terms of angle change. This angle change is the angle between the lines joining the red dot in Fig. 3.9b with the tip of the free polymer arm, at the beginning and the end of ultrasound actuation. For gyroidal shapes, it is difficult to measure the angle change due to the bulk expansion of the sample. Figure 3.11 shows the shape recovery graphically for wide and thin gyroidal samples in

air and underwater, as observed in experiments. It is seen that shape recovery is higher in air as compared to underwater for all samples.

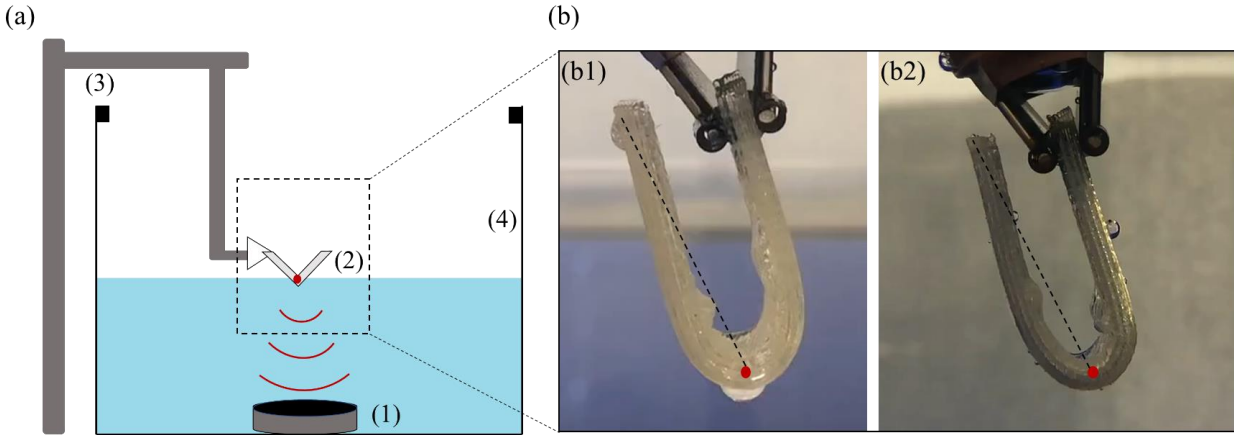


Fig. 3.9 (a) Schematic of the experimental setup consisting (1) FU transducer, (2) SMP filament, (3) positioning system, and (4) water tank. (b) Magnified images of a temporarily deformed SMP filament suspended in (b1) air and (b2) underwater. The polymer is kept such that the focal point lies inside the bent thickness of the filament.

Two possible reasons for this behavior are, first, fluid loading effects which provide added damping to the motion of the sample in dense fluids [43]. Since water is 1000 times denser than air, the former provides higher added damping and reduces the amplitude of recovery response more as compared to air. Second possible reason is the thermal cooling of water which leads to a lower temperature rise in water as compared to air. As the temperature rise is proportional to the amount of shape recovery, as seen from the mechanical constitutive model, the shape recovery reduces in water. It is also seen that samples with the least width show the maximum shape recovery. Here, dogbone samples 1 and 2 have the highest shape memory response. This is also in agreement with our previous results in chapter 2 where it was argued that large widths have

more area which has to undergo phase transformation. Thus, large widths show less recovery for a given duration of FU actuation. Among the various 3d printed patterns, criss-cross 3d patterning (sample 1,3, and 6) for the same width has shown the best shape recovery. Since 3d printed pattern directly determines several thermomechanical parameters, it is postulated that criss-cross pattern may be exhibiting higher heat capacity, better thermal conductivity, or lower elastic modulus. These parameters ultimately contribute to better shape memory behavior of the criss-cross polymer as compared to other 3d printed patterns.

Another interesting behavior is seen in gyroidal samples. It is observed that when these polymers are compressed, they do not show any recovery response for all levels of source input power. However, when these samples are somewhat bent, as shown in Fig. 3.11, the sharp angle allows strain concentration which enables the polymer to respond. This behavior agrees with our previous results where it was concluded that sharper bent angles exhibit better shape recovery. Since highly bent zones have a small zone of strain concentration, the size of the zone becomes comparable to the focal area of incident ultrasound. Thus, they tend to recover faster and by a higher amount as compared to the samples where the strains are distributed in a large area (such as in compressed samples). The overall performance in shape recovery of the gyroidal sample is the lowest as compared to dogbone and rectangular samples. It is hypothesized that the hollow pattern of the gyroidal samples doesn't allow uniform temperature distribution. As the polymer initiates shape recovery once all or most of the volume has transformed to amorphous phase, this irregular temperature distribution transforms the phase in random pockets, which hinders the shape recovery response.

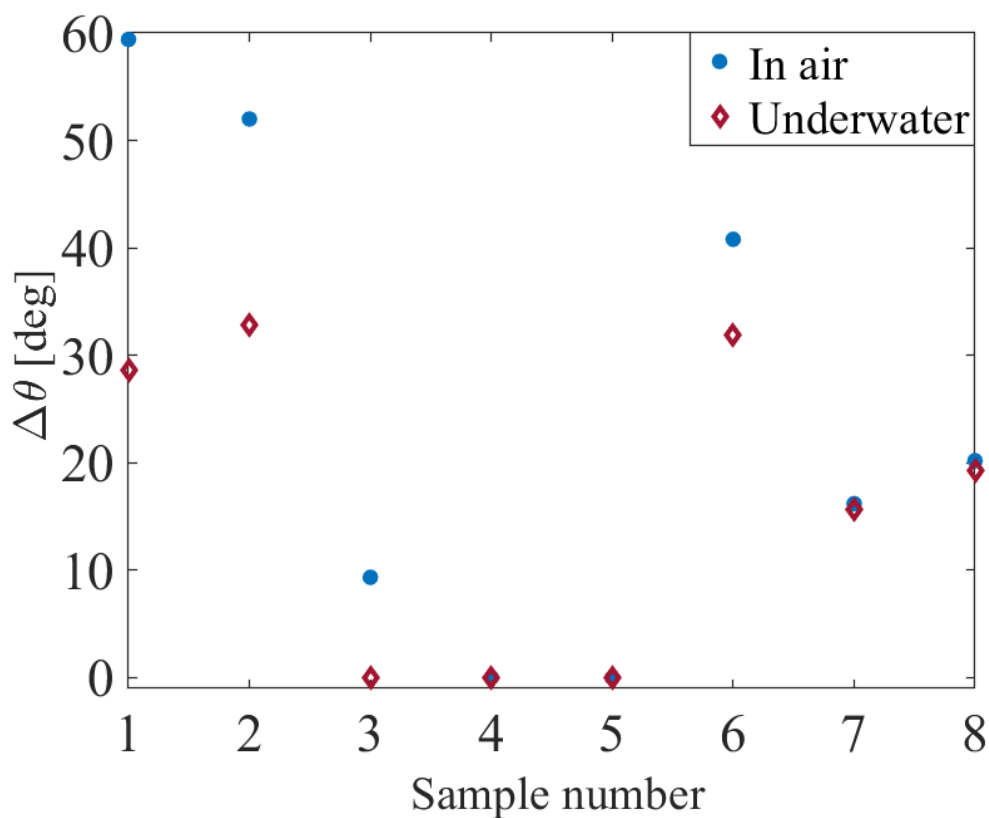


Fig. 3.10. The amount of ultrasound induced shape recovery for different samples in Table 3.1, when polymer is suspended in air (Fig. 3.9b1) and underwater (Fig. 3.9b2). The angle change is the angle between the lines joining the center of the bent area (red dot in Fig. 3.9b) with the tip of the free polymer arm at the beginning and end of shape recovery.

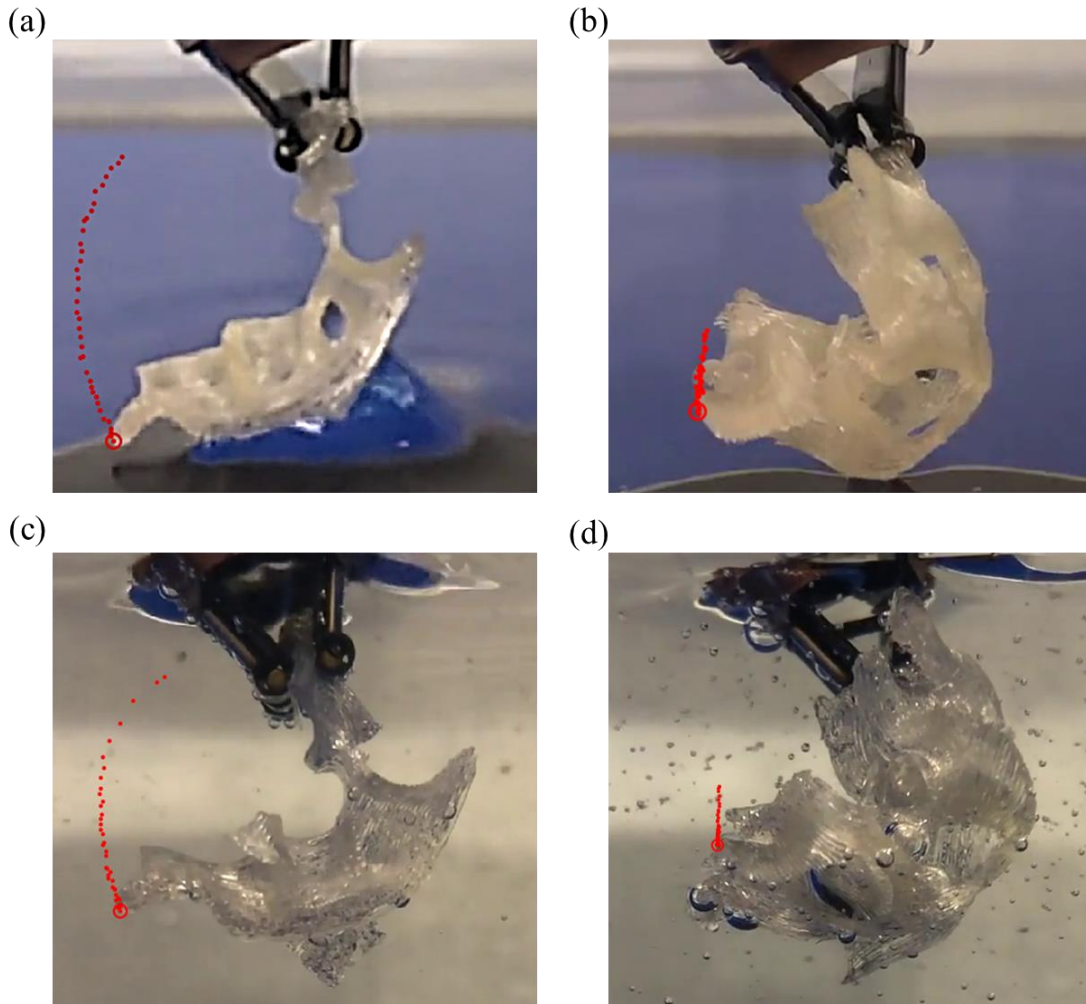


Fig. 3.11. Shape recovery for (a) thin and (b) wide gyroidal samples in air, and (c) thin and (d) wide gyroidal samples immersed in water. The red dot traces the movement of the tip (red circle) as the sample undergoes shape recovery due to ultrasound actuation.

3.5. Conclusions

This work aims to extend the previous work of the authors [26, 28] and to demonstrate the ability of FU actuated biocompatible SMPs to perform controlled drug delivery in *in-vivo* conditions.

The acoustic-thermoelastic model is used to analyse the drug delivery behaviour of SMP-based capsules inside an artery of a heart. Validation of the analytical model with COMSOL

multiphysics simulations shows good agreement for a multi-domain system. Comparisons between acoustic and thermal fields of SMP in single and multiple domains are performed to emphasize the attenuation and nonlinear effects of different tissue layers. Maximum concentration of ultrasound energy and localized temperature rise of the SMP shows that the usage of SMP based systems is biologically safe, without any thermal damage to the surrounding environment. Various artery-scale designs are proposed to emphasize the advantage of using mechanically controlled active drug delivery systems due to flexibility of design, ease of manufacturing, control on the order of drug release rate and availability of the drug at the target site. Variation in external parameters such as source power and frequency further elaborates that different desired drug release rates can be achieved with simple manipulation of FU. To realize the capsule designs further, 3d printing technique is examined. Various 3d printed samples are tested with geometrically simple shapes to examine the effect of the pattern of printing on shape recovery behaviour under FU, experimentally. Our work provides an efficient and potential alternative to the existing controlled drug delivery mechanisms and paves the way for intelligent microscale CDD devices.

Appendix B

DMA results of the dogbone samples obtained from Medshape shown in Figs. 3.8.S1 and 3.8.S2.

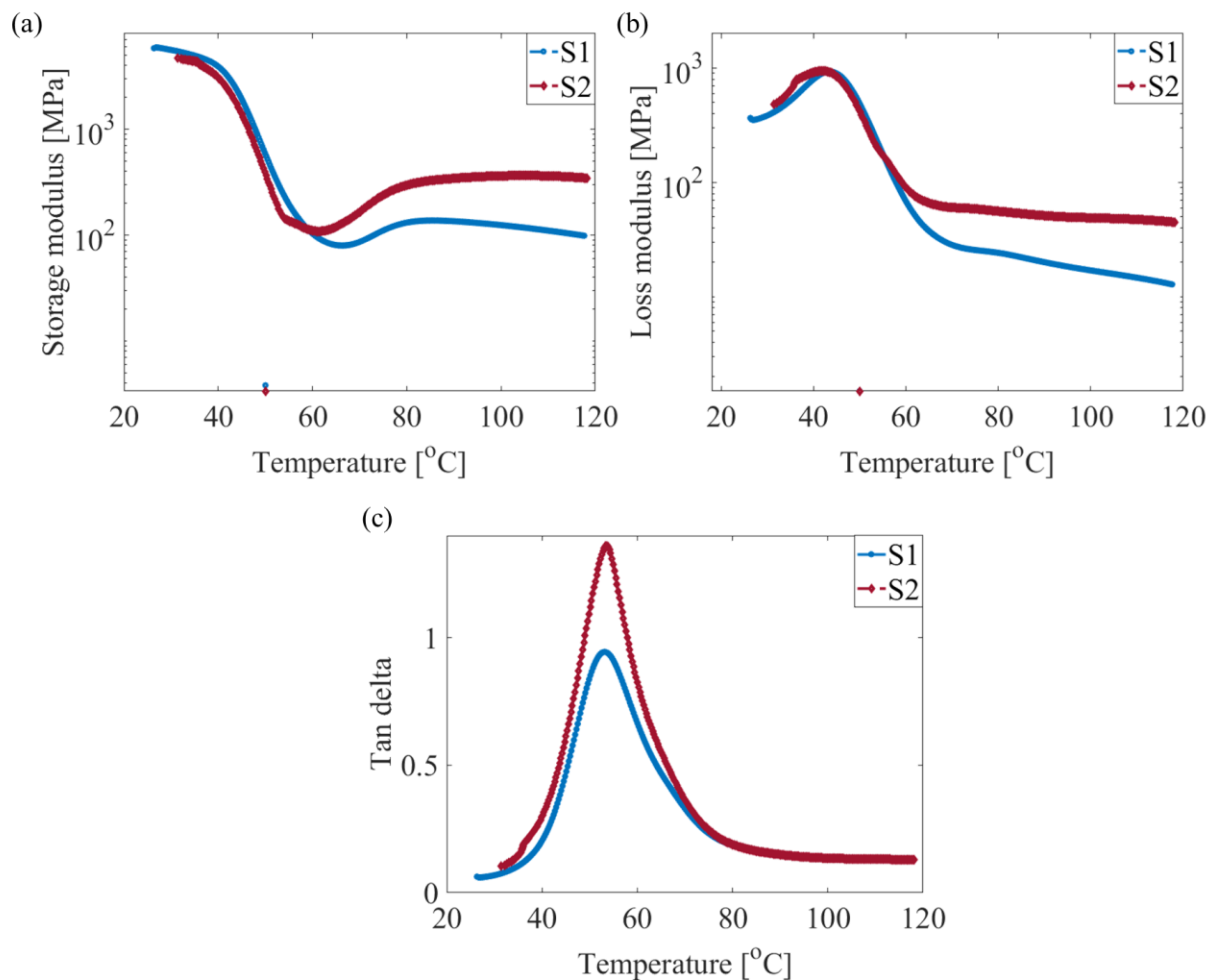


Figure B1. (a) Storage modulus, (b) Loss modulus, and (c) Tan delta of S1 and S2 samples obtained from DMA analysis

References

1. B. R. a. V. IS, *Int J Pharm Sci Res.* **4** (3), 970-982 (2013).
2. G. Tiwari, R. Tiwari, B. Sriwastawa, L. Bhati, S. Pandey, P. Pandey and S. K. Bannerjee, *International Journal of Pharmaceutical Investigation* **2** (1), 2-11 (2012).
3. E. Cukierman and D. R. Khan, *Biochemical Pharmacology* **80** (5), 762-770 (2010).

4. M. W. Tibbitt, J. E. Dahlman and R. Langer, *Journal of the American Chemical Society* **138** (3), 704-717 (2016).
5. T. A. Desai, W. H. Chu, J. K. Tu, G. M. Beattie, A. Hayek and M. Ferrari, *Biotechnol. Bioeng.* **57** (1), 118-120 (1998).
6. E. A. Appel, X. J. Loh, S. T. Jones, C. A. Dreiss and O. A. Scherman, *Biomaterials* **33** (18), 4646-4652 (2012).
7. K. K. Jain, in *Drug Delivery Systems*, edited by K. K. Jain (Humana Press, Totowa, NJ, 2008), pp. 1-50.
8. A. Akinc, M. Goldberg, J. Qin, J. R. Dorkin, C. Gamba-Vitalo, M. Maier, K. N. Jayaprakash, M. Jayaraman, K. G. Rajeev, M. Manoharan, V. Kotliansky, I. Rohl, E. S. Leshchiner, R. Langer and D. G. Anderson, *Mol. Ther.* **17** (5), 872-879 (2009).
9. J. K. Nair, J. L. Willoughby, A. Chan, K. Charisse, M. R. Alam, Q. Wang, M. Hoekstra, P. Kandasamy, A. V. Kel'in, S. Milstein, N. Taneja, J. O'Shea, S. Shaikh, L. Zhang, R. J. van der Sluis, M. E. Jung, A. Akinc, R. Hutabarat, S. Kuchimanchi, K. Fitzgerald, T. Zimmermann, T. J. van Berkel, M. A. Maier, K. G. Rajeev and M. Manoharan, *J. Am. Chem. Soc.* **136** (49), 16958-16961 (2014).
10. A. V. Kabanov, E. V. Batrakova, N. S. Melik-Nubarov, N. A. Fedoseev, T. Y. Dorodnich, V. Y. Alakhov, V. P. Chekhonin, I. R. Nazarova and V. A. Kabanov, *J. Controlled Release* **22** (2), 141-157 (1992).
11. Y. Xu, Y. Du, R. Huang and L. Gao, *Biomaterials* **24** (27), 5015-5022 (2003).
12. Y. Yun, B. K. Lee and K. Park, *Frontiers of Chemical Science and Engineering* **8** (3), 276-279 (2014).
13. D. a. P. R. Ramakrishna, *The J. Int. Federat. Clin. Chem. Lab. Med.* **22**, 1-10.
14. M. Akbulut, S. M. D'Addio, M. E. Gindy and R. K. Prud'homme, *Expert Review of Clinical Pharmacology* **2** (3), 265-282 (2009).
15. M. Ding, N. Song, X. He, J. Li, L. Zhou, H. Tan, Q. Fu and Q. Gu, *ACS Nano* **7** (3), 1918-1928 (2013).
16. T. M. Ruhland, P. M. Reichstein, A. P. Majewski, A. Walther and A. H. E. Müller, *Journal of Colloid and Interface Science* **374** (1), 45-53 (2012).
17. H. Meng and G. Li, *Polymer* **54** (9), 2199-2221 (2013).
18. D. Ratna and J. Karger-Kocsis, *Journal of Materials Science* **43** (1), 254-269 (2008).

19. S. S. Venkatraman, L. P. Tan, J. F. D. Joso, Y. C. F. Boey and X. Wang, *Biomaterials* **27** (8), 1573-1578 (2006).
20. T. Xie, *Polymer* **52** (22), 4985-5000 (2011).
21. C. M. Yakacki, R. Shandas, C. Lanning, B. Rech, A. Eckstein and K. Gall, *Biomaterials* **28** (14), 2255-2263 (2007).
22. D. G. Shchukin, D. A. Gorin and H. Möhwald, *Langmuir* **22** (17), 7400-7404 (2006).
23. G. A. Hussein, N. Y. Rapoport, D. A. Christensen, J. D. Pruitt and W. G. Pitt, *Colloids and Surfaces B: Biointerfaces* **24** (3), 253-264 (2002).
24. J. Wang, M. Pelletier, H. Zhang, H. Xia and Y. Zhao, *Langmuir* **25** (22), 13201-13205 (2009).
25. B. G. De Geest, A. G. Skirtach, A. A. Mamedov, A. A. Antipov, N. A. Kotov, S. C. De Smedt and G. B. Sukhorukov, *Small* **3** (5), 804-808 (2007).
26. A. Bhargava, K. Peng, J. Stieg, R. Mirzaeifar and S. Shahab, *RSC Advances* **7** (72), 45452-45469 (2017).
27. G. Li, G. Fei, B. Liu, H. Xia and Y. Zhao, *RSC Advances* **4** (62), 32701-32709 (2014).
28. A. Bhargava, K. Peng, J. Stieg, R. Mirzaeifar and S. Shahab, (58264), V002T004A014 (2017).
29. A. Rozanova-Pierrat, (2006).
30. M. F. Hamilton and D. T. Blackstock, *Nonlinear acoustics*. (Academic press San Diego, 1998).
31. F. P. Curra, P. D. Mourad, V. A. Khokhlova, R. O. Cleveland and L. A. Crum, *IEEE Transactions on Ultrasonics, Ferroelectrics, and Frequency Control* **47** (4), 1077-1089 (2000).
32. D. G. F. Hasgall PA, Baumgartner C, Neufeld E, Gosselin MC, Payne D, Klingenböck A, Kuster N, (September 01st, 2015), Vol. 3.0.
33. S. Ham and K.-J. Bathe, *Computers & structures* **94**, 1-12 (2012).
34. T. S. Hart and M. F. Hamilton, *The Journal of the Acoustical Society of America* **84** (4), 1488-1496 (1988).
35. T. R. Nelson, J. B. Fowlkes, J. S. Abramowicz and C. C. Church, *Journal of Ultrasound in Medicine* **28** (2), 139-150 (2009).

36. U. FDA, Rockville MD: FDA (2008).
37. G. Ter Haar, *Imaging in Medicine* **5** (6), 567 (2013).
38. S. Ma, Y. Zhang, M. Wang, Y. Liang, L. Ren and L. Ren, *Science China Technological Sciences* (2019).
39. X. Kuang, D. J. Roach, J. Wu, C. M. Hamel, Z. Ding, T. Wang, M. L. Dunn and H. J. Qi, *Advanced Functional Materials* **29** (2), 1805290 (2019).
40. J. Long, H. Gholizadeh, J. Lu, C. Bunt and A. Seyfoddin, *Curr Pharm Des* **23** (3), 433-439 (2017).
41. M. Habibi, S. H, T. V, S. S.D and B. Arezoo, *American Journal of Applied Sciences* **6** (2009).
42. Q. Ge, A. H. Sakhaei, H. Lee, C. K. Dunn, N. X. Fang and M. L. Dunn, *Scientific Reports* **6** (1), 31110 (2016).
43. J. Morison, J. Johnson and S. Schaaf, *Journal of Petroleum Technology* **2** (05), 149-154 (1950).

Chapter 4 : Coupling of nonlinear shape memory polymer cantilever dynamics with focused ultrasound field

Co-authors: Kaiyuan Peng, Reza Mirzaeifar, and Shima Shahab

Details of publication

Co-authors: Shima Shahab

Citation: Bhargava, A. and Shahab, S., 2019, Coupling of nonlinear shape memory polymer cantilever dynamics with focused ultrasound field, *Smart Mater. Struct.*, **28** 055002

Bhargava A., Peng K., and Shahab S., Dynamics of focused ultrasound actuated shape memory polymers," *Proc. SPIE 10967, Active and Passive Smart Structures and Integrated Systems XIII*, **1096720** (21 March 2019). (**Best Student Paper Award – honorable mention**).

Abstract

Research has found significant potential for ultrasound actuation of shape memory polymers (SMPs) in several fields such as biomedical equipment and electronic devices among others. Example applications range from controlled drug delivery containers to soft robotics and flexible electronics located in otherwise inaccessible places or hazardous environments, where direct external heating is not possible. SMPs can be manipulated into any temporary shape and later recover to their stress-free permanent shape when triggered with external stimuli such as heat. Focused ultrasound (FU) has the ability to induce localized heating and activate multiple

intermediate shapes and achieve complete shape recovery in the polymer, non-invasively and remotely. In addition, FU has a superior capability for temporal and spatial control of shape recovery by adjusting sample size, ultrasound frequency, exposure time and intensity as well as the position of ultrasound focusing. In this chapter, indirect actuation of the thermally-induced shape-memory effect of SMPs by FU is studied theoretically and experimentally with a focus on the acoustic field, medium, geometric and material properties. The changes in thermomechanical properties, during FU actuation, are studied through dynamic mechanical analyzer tests. Using these properties, an analytical acoustic-thermo-elastic dynamic model is developed to predict the shape memory response of a SMP cantilever beam, considering acoustic and geometric nonlinearities. The governing equations of motion are derived using reduced order modeling and solved by perturbation techniques. Having obtained an analytical expression for the shape recovery of the beam as a function of acoustic parameters, experimental validations for a cantilever SMP beam exposed to FU are performed. The model has the ability to successfully estimate the variation in the amount of shape recovery due to the change in source frequency of the transducer and peak acoustic pressure field inside SMP domain without the need of analyzing any intermediary acoustic/thermal/elastic behavior.

4.1. Introduction

Shape memory polymers (SMPs) are an emerging class of smart materials which have gained significant attention in both industry and academic research due to their ability to memorize their permanent shape. This ability enables them to be manipulated into any temporary shape and later return to their stress-free permanent shape when triggered with different environmental factors

such as heat. Being polymers, they offer a wide variation in their mechanical properties in addition to being cheap, light-weight, biodegradable and easily process-able [1]. Last decade has observed an increasing use of SMPs in aerospace, biomedical, textile, structural and flexible electronic applications [2-4]. SMP-based controlled drug delivery devices, biodegradable sutures, catheters, cardiovascular stents actuated at body temperatures and microactuators are some of the emerging applications of SMPs in the biomedical industry [5-10].

The choice of environmental trigger for actuating SMPs is one of the key factors in attaining efficient shape recovery. Although, direct heat is one of the most commonly used trigger for shape memory behavior, it is not always practical and safe, especially for heat-sensitive applications [11]. Consequently, other forms of actuating mechanisms such as irradiation (UV, IR and solar), magnetic field, electric current among others have come to forefront [12-17]. Chen *et. al* [18] processed chitosan/PEG-based spiral coils as vascular stents which showed rapid shape recovery on hydration. Small *et al.* [7, 19] studied the use of shape memory polyurethanes doped with light absorbing dyes for use as stents and foams. Sahoo *et al.* [20, 21] used electric current to actuate shape memory polyurethanes coated with conductive polymer (PPy) and achieved 85%-90% of shape recovery. Thermomagnetically and electromagnetically induced shape memory effects can be achieved through fillers such as metal particles, iron (III) oxide [22, 23] and ferromagnetic particles [24]. Razzaq *et al.* [25] actuated shape memory polyurethanes at lower field frequencies through micro-sized magnetite fillings. They achieved a considerable decrease in electrical resistivity and an increase in thermal conductivity with 40 vol% magnetite, and demonstrated a full shape recovery of SMP under magnetic field. Most of the triggers

mentioned above require filler particles to induce shape memory behavior, which can compromise the structural/thermal integrity or biocompatibility of the polymer. A possible solution to overcome this challenge is the use of focused ultrasound (FU) as a safer, non-invasive remote trigger. An increased focus on ultrasound actuation is seen especially in biomedical applications where the need of a non-invasive and controllable trigger is of utmost importance [26-28]. FU enables selective, spatially and temporally controlled heating of SMP without the need of any filler particles. The underlying mechanism involves inducing heat generation due to viscous shearing oscillation of molecules under ultrasound exposure [29, 30], resulting in shape recovery. FU also offers significant advantage over other methods for actuation in applications requiring remote access. The limited literature of ultrasonic actuation of SMPs is mainly centered on proof-of-concept experiments demonstrating the feasibility of this method, lacking experimentally-validated modeling efforts for the resulting multiphysics problem that couples the domain acoustics with polymer dynamics. In this work, we present a coupled analytical and experimental multiphysics investigations for FU induced thermal actuation of a SMP cantilever, considering acoustic and weak geometric nonlinearities.

The use of thermally actuated SMPs in every application requires a comprehensive understanding of the thermomechanical process of shape recovery. Thus, the past two decades have observed several constitutive models to capture the shape memory behavior [31-34]. Liu *et al.* [35] developed one of the first phenomenological constitutive models which considered SMPs as a mixture of two phases: the frozen phase (hard phase) and active phase (soft phase). The model describes the structural transformation of SMPs as being dependent on two internal

state variables (the frozen phase volume fraction and stored strain). Several others improved this model by eliminating his model's assumptions [36-38]. This chapter presents dynamic equations governing the motion of an ultrasound actuated SMP cantilever in heating, cooling and shape recovery stages, following the constitutive model developed by Liu *et al.* [35] combined with acoustic-thermal equations. The FU nonlinear acoustic field and induced thermal energy are obtained using Khokhlov–Zabolotskaya–Kuznetsov (KZK) [39, 40] and Penne's Bioheat [41] equations, respectively [42]. The behavior of temperature dependent mechanical properties of SMP is studied using dynamic mechanical analyzer (DMA) tests. A model is built to predict the shape memory behavior of a SMP based cantilever beam subjected to pure bending and the governing equations of motion for the shape fixation and shape recovery stages are derived, using reduced order mathematical modeling. An analytical dynamic solution is then developed using perturbation techniques for a weakly geometric nonlinear SMP cantilever to estimate the acoustically driven recovery of the beam. The experimentally-validated analytical solution is then used to characterize the acoustic parameters and their effects on ultrasound induced shape recovery of the beam. The scope of this work encompasses all applications of thermally actuated SMPs requiring shape recovery such as SMP based switches and drug delivery containers among others. In section 4.2, we develop the theoretical background and acoustic-thermo-elastic model for an ultrasound-SMP actuation system. Experimental results and model validation are presented in section 4.3. A summary and conclusions are presented in section 4.4.

4.2. Theory

In order to understand the nonlinear dynamics of FU induced thermal actuation of SMPs, a robust model which predicts the acoustic and thermal fields and subsequent shape recovery is essential. The model is divided into three interconnected parts. The first part uses KZK equation [39, 40] to estimate the focused acoustic pressure field inside an SMP submerged in water [30]. The equation is numerically solved in a hybrid time-frequency domain taking into account the effects of absorption, diffraction and nonlinearity in the medium. The second part solves Penne's Bioheat equation [41] to calculate the FU induced temperature rise inside the polymer. The third part predicts the shape recovery of SMP using a constitutive model developed by Liu *et al.* [35]. The dynamic response of a SMP cantilever beam is studied using reduced order mathematical modeling and solved using perturbation techniques. The advantages of such techniques over numerical methods is the flexibility to study the characteristics of the nonlinear response and determine the effect of various acoustic and SMP geometric and material parameters individually on the shape recovery. The governing equations of motion are developed using Generalized Hamilton's Principle [43], assuming an SMP filament as an Euler-Bernoulli beam. We use Galerkin weighted residual method [43] to convert the partial differential governing equations into n modal ordinary differential equations. The method of multiple scales [44] is then used to develop an analytical solution to predict the shape recovery of SMP as a function of acoustic and thermal parameters.

4.2.1. Multiphysics acoustic-thermal-elastic modeling

KZK equation is used to predict the nonlinear FU generated acoustic pressure field in SMP and fluid domains. The non-dimensional form of the equation is stated in Eq. 2 of chapter 2 and Ref. [40]. The parameters \bar{A} , G and \bar{B} represent the attenuation, gain and nonlinearity of the medium respectively. A detailed explanation of the equation and solving technique is given by Bhargava *et al.* [30]. This acoustic framework can also be used for ultrasonic energy systems using FU sources [45-48]. The calculated pressure field is then used as an input to Penne's Bioheat equation [41] which predicts the thermal field generated due to viscous shearing exerted by FU waves inside the polymer. The equation is given by Eq. 10 of chapter 2.

The temperature rise in the polymer results in a mechanical response which subsequently causes shape recovery of the polymer. A constitutive model developed by Liu *et al.* [35] is used to capture the thermomechanical response. The model uses the glass transition temperature, T_g , to define the relationship between the final recoverable stress and strain. The shape recovery process involves four stages with the first stage as the loading stage where the polymer is heated above its T_g and deformed to a temporary shape by an external force. The second stage is cooling the polymer below its T_g to fix the temporary deformed shape. The third stage is unloading of the external forces and the fourth stage is re-heating the polymer to attain shape recovery. The model quantifies the storage and release of entropic deformation in the form of "frozen" strains which are equal to the strains in the pre-deformed body at the end of loading stage, in our study. During cooling, the pre-deformed strains freeze in the polymer and are

released upon ultrasound actuation and the body returns to its original shape. The model is derived using the evolution of storage strains during the cooling process only, but is assumed to hold true for both cooling and re-heating stages of the shape recovery process under monotonous decreasing and increasing temperature profiles, respectively. The model has shown reasonable agreements with experiments for both these stages [35]. However, in case of repeated cooling/heating intermediary cycles, a net cooling history needs to be incorporated in the model to account for any partial storage/release of stored strains [49, 50]. Since, in this work, temperature profiles of cooling and heating due to ultrasound actuation are strictly decreasing and increasing respectively, Liu's model [35] is used. The model defines the 1-D constitutive equation and temperature derivative of stored strain for the SMP, as Eqs. (1) and (2), respectively [35].

$$\sigma = \frac{\varepsilon - \varepsilon_s - \int_{T_h}^T \alpha dT}{\frac{\phi_f}{E_i} + \frac{1 - \phi_f}{E_e}} = E \left(\varepsilon - \varepsilon_s - \int_{T_h}^T \alpha dT \right) \quad (1)$$

$$\frac{d\varepsilon_s}{dT} = \frac{E}{E_e} \left(\varepsilon - \varepsilon_s - \int_{T_h}^T \alpha dT \right) \left(\frac{d\phi_f}{dT} \right) \quad (2)$$

where ε is the total strain and σ is the total stress in the body. The parameters ε_s , α and T_h represent the temperature, T , dependent storage strain, thermal expansion coefficient and maximum temperature up to which SMP is heated in loading stage before deformation, respectively. The frozen fraction ϕ_f represents the fraction of the volume in the frozen (stiffer)

phase and is given as $\phi_f = 1 - [1 + c_f(T_h - T)^n]^{-1}$, where c_f and n are variables which can be experimentally found by curve fitting method. The Young's modulus E is related to temperature by the relation, $E = [(\phi_f / E_i) + (1 - \phi_f / E_e)]^{-1}$ where E_i is the modulus of the internal energetic deformation and E_e is the modulus of the entropic deformation calculated using the formulae, $E_e = 3NkT$. The parameters N and k denote the cross-link density and Boltzmann's constant ($k = 1.38 \times 10^{-23}$ Nm/K) respectively. The model given by Eqs. (1) and (2) exhibits a linear stress-strain relationship and assumes rubbery elasticity to hold true as long as the strains and cross-linking density fall in the domain of small-moderate (40–50%) [35, 51-56]. Note that the strains in this work are not small, but lie in the domain such that rubbery linear elasticity assumption gives good approximation with experimental data.

To develop a comprehensive understanding of the dynamic response of SMP during shape recovery process, we develop governing equations of motions for each stage of shape recovery process for an Euler-Bernoulli SMP cantilever beam using Generalized Hamilton's principle. We then solve these equations using Galerkin's weighted residual method and method of multiple scales and validate the results with experiments and numerical solution of the governing equation. The main aim is to express the dynamic shape recovery of the SMP cantilever as a function of the FU parameters through an analytical expression.

4.2.2. Nonlinear SMP cantilever dynamics: loading, cooling, shape fixation and shape recovery

A SMP cantilever beam with length l , width b and thickness h is shown in Fig. 4.1. The beam's response is derived under the assumptions of Euler-Bernoulli beam which considers the beam to have a higher length to thickness ratio, such that the rotational effects and angular distortion of the differential element are ignored. As per the Euler-Bernoulli beam theory, shear effects in beams with large aspect ratio are neglected. However, they can be incorporated to obtain better approximation. In this work, for simplification, shear effects are neglected for a cantilever beam with large aspect ratio in order to obtain an analytical solution of the complicated dynamics of acoustic-thermoelastic coupling in SMPs with sufficient accuracy (shown in section 3). Linear elasticity is assumed for the range of strains $\leq 40\%$. The beam is subjected to pure bending such that deflections are large but curvature remains small, i.e. curvature is proportional to bending moment. In this work, we used the nonlinear 2-D Euler-Bernoulli beam theory with allowance for damping, following the theory developed by Nayfeh and Pai [57]. The condition of inextensibility is assumed for simplification and to obtain an analytical solution with good approximation [58].

The generalized Hamilton's principle is stated as

$$\int_{t_1}^{t_2} (\delta T_E - \delta U_E + \delta W_{nc}) dt = 0 \quad (3)$$

where δT_E , δU_E and δW_{nc} are the variations in kinetic energy, potential energy and the work done by non-conservative forces.

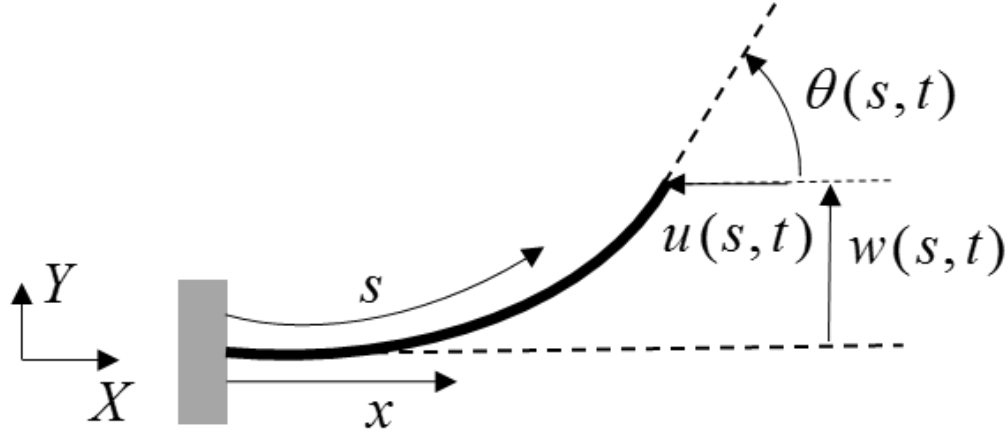


Fig. 4.1. Schematic of deformation of cantilever beam in pure bending due to end point force (positive Y direction) at the free end. The dashed line represents the original position of the beam. X and Y are the global coordinates of the system.

The potential energy of a cantilever beam in pure bending with no gravitational effects, is given by

$$U_E = \frac{1}{2} \int_V E y^2 \gamma^2 dA ds = \frac{1}{2} \int_0^l EI \gamma^2 ds \quad (4)$$

where γ is the curvature denoted by $\gamma = \partial\theta(s,t) / \partial s$ (inextensible), $\theta(s)$ is the angle of the perpendicular to the cross-section, dA , of the beam with the horizontal axis X , s is the curvilinear coordinate along the length of the beam and E is the Young's modulus. The parameter $I = \int_A y^2 dA$ is the area moment of inertia of the beam where y is the distance from the neutral axis. By defining w as the vertical deflection of the beam (Fig. 4.1) and realizing that

$\theta(s,t) = \sin^{-1}[w'(s,t)] = w'(s,t) + w'(s,t)^3/6$, the potential energy till fourth order

i.e. $O([]^{n>4}) = 0$, can be expressed as $U_E = \frac{1}{2} EI \int_0^l (w''(s,t)^2 + w'(s,t)^2 w''(s,t)^2) ds$. The kinetic

energy T_E is given by

$$T_E = \frac{1}{2} \rho A \int_0^l (\dot{u}(s,t)^2 + \dot{w}(s,t)^2) ds + \frac{1}{2} \int_0^l \rho I \dot{\theta}(s,t)^2 ds \quad (5)$$

where ρ is the density of the SMP, A is the area, u is the horizontal displacement of the beam and $(\dot{})$ is the time derivative of a quantity. The second term on the right hand side of Eq. 5 accounts for rotational inertia effect and will be ignored in the rest of this study due to its negligible contribution. From geometry (Fig. 4.1), using the relation $\cos[\theta(s,t)] = 1 - u'(s,t)$, expressing it in terms of w and substituting in Eq. 5, gives the expression for kinetic energy as

$$T_E = \frac{1}{2} \rho A \int_0^l \left(\left(\int_0^s (w'(s,t)\dot{w}(s,t) + \frac{w'(s,t)^3 \dot{w}(s,t)}{2}) d\xi \right)^2 + \dot{w}(s,t)^2 \right) ds. \text{ The virtual work done by}$$

non-conservative forces is

$$\delta W_{nc} = \frac{1}{2} \int_0^l EI \delta(\gamma_s(s,t)^2) ds - \int_0^l F \delta w(s,t) ds - \int_0^l d_1 \dot{w}(s,t) \delta w(s,t) ds \quad (6)$$

where F is a distributed external force per unit length and damping coefficient is denoted by d_1 .

The first term in Eq. 6 is a contribution of the energy due to frozen strains, $\varepsilon_s(s,T)$ obtained from Eq. 2 and thermal strains, $\varepsilon_T(t)$. This approach arises from the understanding that all

mechanical, frozen and thermal strains contribute to the overall stress of the system through the relation given by Eq. 1. Therefore, the energy contribution due to this stress can be expressed as the energy contribution from each of the mechanical, frozen and thermal strains individually, as the stress-strain relation is linear [51]. To accomplish this, the mechanical strains are assumed to contribute to the potential energy of the system (similar to any beam system) and the rest of the strains are assumed to contribute to the external work done. Since ε_s is a function of spatial variable s and temperature T , which is a function of time t from Eq. 10 of chapter 2, ε_s can be represented as, $\varepsilon_s(s,t)$. The parameter $\gamma_s(s,t)$ in the first term of Eq. 6 is the curvature associated with $\varepsilon_s(s,t)$ and $\varepsilon_T(t)$, and is expressed as $\gamma_s(s,t) = w_s''(s,t) + w_s'(s,t)^2 w_s''(s,t) / 2 + \text{higher order terms}$. Taking the variation of Eqs. 4 and 5 and substituting them in Eq. 3 along with Eq. 6 yields the governing equation of motion as

$$\rho A \left(\left(\frac{w'(s,t)}{2} \int_0^s \int_0^s \frac{\partial^2 w'(s,t)^2}{\partial t^2} d\xi ds \right)' - \ddot{w}(s,t) \right) - EI \left(w''''(s,t) - w_s''''(s,t) \right) - EI \left(\left(w'(s,t) (w'(s,t) w''(s,t))' \right)' - \left(w_s'(s,t) (w_s'(s,t) w_s''(s,t))' \right)' \right) - d_1 \dot{w}(s,t) - F = 0 \quad (7)$$

with geometric boundary conditions at $s = 0$ as

$$w(s,t)|_{s=0} = 0 \quad (8)$$

$$w'(s,t)|_{s=0} = 0 \quad (9)$$

And natural boundary conditions from moment and shear at $s = l$ as

$$w''(s,t) + w'^2(s,t)w''(s,t) - w_s''(s,t) - w_s'^2(s,t)w_s''(s,t) \Big|_{s=l} = 0 \quad (10)$$

$$\begin{aligned} w'''(s,t) + w'''(s,t)w'(s,t)^2 + w'(s,t)w''(s,t)^2 - w_s'''(s,t) - w_s'''(s,t)w_s'(s,t)^2 \\ - w_s'(s,t)w_s''(s,t)^2 \Big|_{s=l} = 0 \end{aligned} \quad (11)$$

The time dependency in equation of motion arises during the shape recovery process. This time dependency is due to the rise in temperature with time during ultrasound actuation, Eq. 10 of chapter 2. Since stored strains are a function of temperature, Eq. 2, the release of storage strains become time dependent during shape recovery stage. As the material is elastic for the range of strains $\leq 40\%$ [51], the stored strains are instantaneously released when the temperature reaches the glass transition temperature.

4.2.2.1. Loading and cooling. In this stage, the SMP is heated to an elevated temperature T_h such that the SMP is in rubbery phase and the frozen fraction is zero. After heating, SMP is deformed to a temporary shape in the upward direction by a force P_y applied at the tip end (Fig. 4.1). Due to static loading, time derivative terms are zero and with no contribution of frozen energy, the terms with variable w_s are zero in Eqs. (7)-(11). Equation 7 for this stage in terms of

$\theta(s)$ with $F = \int_0^l P_y \delta^*(s-l) ds$ becomes [59]

$$E_h I \theta''(s) + P_y \cos[\theta(s)] = 0 \quad (12)$$

with boundary conditions $\theta(0) = 0$ and $\theta'(l) = 0$. In Eq. 12, E_h is the elastic modulus at T_h . The equation of motion for static loading, Eq. 12 is expressed in $\theta(s)$ due to ease of solving as compared to solving in terms of transverse displacement $w(s)$. A detailed derivation of this equation is given in [60]. Wang *et al.* [61] derived the solution of Eq. 12 for large deflections using homotopy analysis method. In this study, we used a similar approach to estimate the deflection of the beam in the loading stage. The strains at the end of this stage are denoted by ε_{pre} .

The SMP cantilever beam is cooled to a temperature below T_g under the pre-strain constraint [35] i.e. maintaining the deformed shape. This results in freezing of the thermally reversible molecular chains and the deformation history is stored in the form of frozen energy which can be released by heating the SMP again.

4.2.2.2. Fixation and shape recovery. After cooling, the external forcing is removed and the deformed shape of the cantilever beam is fixed. Setting $\varepsilon = \varepsilon_{pre}$ in Eq. 2 and using Eq. 10 of chapter 2, $\varepsilon_s(s, t)$ is obtained which leads to $\gamma_s(s, t)$ in Eq. 6. Equations 7-11 are discretized

using $w(s, t) = \sum_{i=1}^{\infty} \varphi_i(s) \eta_i(t)$ where $\varphi_i(s)$ represents mode shape associated with i^{th} natural

frequency, $\eta_i(t)$ is the i^{th} modal coordinate. Setting external force distribution $F = 0$, applying

Galerkin's weighted residual method to Eq. 7 [57] and considering only one mode, equation of motion for shape recovery is,

$$\psi\eta(\eta\dot{\eta} + \dot{\eta}^2) + \dot{\eta} + \eta\omega^2 + 2\mu\dot{\eta} + \bar{\zeta}\eta^3 - \xi(t) - \bar{\xi}(t) = 0 \quad (13)$$

where $\psi = \rho A \int_0^l \varphi'^2 \left(\int_s^l \int_0^s \varphi'^2 d\xi dh \right) ds$, $\mu = \frac{d_1}{2} \int_0^l \varphi^2 ds$, $\bar{\zeta} = EI \int_0^l (\varphi'^2)' (\varphi' \varphi'') ds$,

$$\xi(t) = EI \int_0^l \varphi'' w_s''(s,t) ds, \quad \bar{\xi}(t) = EI \int_0^l \left(\varphi' w_s'(s,t) \right)' \left(w_s'(s,t) w_s''(s,t) \right) ds$$
 and ω is the natural

circular frequency (rad/s) such that $\omega^2 = \beta^4 EI / \rho A$ with β being the eigen value obtained from the characteristic equation of the undamped and unforced linear system, obtained by reducing Eqs. 7-11 [43].

Here $\xi(t)$ and $\bar{\xi}(t)$ are functions of w_s , which changes with time as the SMP is heated. For fixation, the beam is below the T_g and is in static position when the external forces are removed. It is assumed that the entire polymer has transformed to glassy state and has completely stored the energy due to strains developed in loading stage. Therefore, the equation for the deformation of the beam in this stage is obtained by setting time derivative terms to zero and taking $\xi(t)$ and $\bar{\xi}(t)$ at time $t = 0$ in Eq. 13. The governing equation thus becomes,

$$\eta\omega^2 + \bar{\zeta}\eta^3 - \xi(0) - \bar{\xi}(0) = 0 \quad (14)$$

The above stated approach gives an approximate solution for these shape recovery stages, however, the error is minimized by using Galerkin's weighted residual method [62].

4.2.3. Solution approach using method of multiple scales

During ultrasound actuation, the thermal field developed inside SMP leads to shape recovery due to release of temperature dependent frozen energy. Equation 13 represents the equation of motion in this stage where time t is the duration of ultrasound actuation. To obtain the magnitude of the shape recovery, method of multiple scales [44, 63] is used to find an approximate solution of Eq. 13 in case of weak nonlinearities. A technique similar to Meesala *et al.* [64] is followed where a bookkeeping parameter, $\tilde{\varepsilon}$ is introduced which signifies the effect of each term in Eq. 13 on the final response. Equation 13 is re-written as

$$\tilde{\varepsilon}\psi\eta(\eta\ddot{\eta} + \dot{\eta}^2) + \ddot{\eta} + \eta\omega^2 + 2\tilde{\varepsilon}\mu\dot{\eta} + \tilde{\varepsilon}\bar{\zeta}\eta^3 - \xi(t) - \bar{\xi}(t) = 0 \quad (15)$$

where η depends on t and $\tilde{\varepsilon}$. During heating, the temperature dependent elastic modulus E changes with time, since $T = T(t)$. To account for this variation in E , the process of re-heating in fourth stage is divided into multiple stages of small time intervals, with each stage having a constant modulus. This multi-stage division is necessary to have constant coefficients of nonlinearities in Eq. 15 and to derive an approximate analytical solution. Equation 17 is thus applied to each of these stages to obtain the response of the beam till the nonlinear terms become negligible and the response can be accurately predicted by linear equation

$$\ddot{\eta} + \eta\omega^2 + 2\mu\dot{\eta} - \xi(t) - \bar{\xi}(t) = 0 \quad (16)$$

An approximate solution for Eq. 15 is expressed in the form of power series in η given by

$$\eta(t; \tilde{\varepsilon}) = \eta_0(t) + \tilde{\varepsilon}\eta_1(t) + \tilde{\varepsilon}^2\eta_2(t) + \text{higher order terms} \quad (17)$$

Retaining up to $O(\tilde{\varepsilon}^1)$ terms, the dependence of η on t and $\tilde{\varepsilon}$ occurs on different time scales,

T_0 and T_1 such that $T_n = \tilde{\varepsilon}^n t$ for $n = 0, 1$. Using chain rule, the differentiation terms with respect

to t can be expressed as $\frac{D}{Dt} = \frac{\partial}{\partial T_0} + \tilde{\varepsilon} \frac{\partial}{\partial T_1} \equiv D_0 + \tilde{\varepsilon} D_1$ and

$\frac{D^2}{Dt^2} = \frac{\partial^2}{\partial T_0^2} + 2\tilde{\varepsilon} \frac{\partial^2}{\partial T_0 \partial T_1} + \tilde{\varepsilon}^2 \frac{\partial^2}{\partial T_1^2} \equiv D_0^2 + 2\tilde{\varepsilon} D_0 D_1 + \tilde{\varepsilon}^2 D_1^2$. The solution form, Eq. 17 now

becomes a function of new time scales, given by

$$\eta(t; \tilde{\varepsilon}) = \eta_0(T_0, T_1) + \tilde{\varepsilon}\eta_1(T_0, T_1) + \tilde{\varepsilon}^2\eta_2(T_0, T_1) + \text{higher order terms} \quad (18)$$

Expressing Eq. 15 using Eq. 18, and retaining up to $O(\tilde{\varepsilon}^1)$ terms, equations for each order of $\tilde{\varepsilon}$ are given as,

$$O(\tilde{\varepsilon}^0): \omega^2 \eta_0 + D_0^2 \eta_0 = -\bar{F} \quad (19)$$

where \bar{F} is used to denote combined stored energy effect, $\bar{F} = -\xi(T_0) - \bar{\xi}(T_0)$.

$$O(\tilde{\varepsilon}^1): D_0^2 \eta_1 + \eta_1 \omega^2 = \bar{\zeta} \eta_0^3 - \psi \eta_0 (D_0 \eta_0)^2 - 2D_0 D_1 \eta_0 - \psi \eta_0^2 D_0^2 \eta_0 - 2\mu D_0 \eta_0 \quad (20)$$

The solution of Eq. 19 is of the form

$$\eta_0 = \frac{-\bar{F}}{\omega^2} + e^{i\omega T_0} A(T_1) + e^{-i\omega T_0} \bar{A}(T_1) \quad (21)$$

where the second and the third terms on the right hand side of Eq. 21 are complex conjugates and i denotes imaginary number. Using Eq. 21 in Eq. 20,

$$\begin{aligned}
D_0^2 \eta_1 + \eta_1 \omega^2 = & -\frac{\bar{F}^3 \bar{\zeta}}{\omega^6} + \frac{3e^{i\omega T_0} \bar{F}^2 \bar{\zeta} A}{\omega^4} + \frac{e^{i\omega T_0} \bar{F}^2 \psi A}{\omega^2} - 3e^{2i\omega T_0} \bar{F} \psi A^2 - \frac{3e^{2i\omega T_0} \bar{F} \bar{\zeta} A^2}{\omega^2} \\
& + e^{3i\omega T_0} \bar{\zeta} A^3 + 2e^{3i\omega T_0} \omega^2 \psi A^3 - 2\psi \bar{F} A \bar{A} - \frac{6\bar{F} \bar{\zeta} A \bar{A}}{\omega^2} + 3e^{i\omega T_0} \bar{\zeta} A^2 \bar{A} \\
& + 2e^{i\omega T_0} \omega^2 \psi A^2 \bar{A} - 2ie^{i\omega T_0} \omega A \mu - 2ie^{i\omega T_0} \omega D_1 A + \text{complex conjugates}
\end{aligned} \tag{22}$$

For a bounded solution, secular terms should be eliminated and are therefore set to zero.

$$-\frac{3e^{i\omega T_0} \bar{F}^2 \bar{\zeta} A}{\omega^4} - \frac{e^{i\omega T_0} \bar{F}^2 \psi A}{\omega^2} - 3e^{i\omega T_0} \bar{\zeta} A^2 \bar{A} - 2e^{i\omega T_0} \omega^2 \psi A^2 \bar{A} + 2ie^{i\omega T_0} \omega A \mu + 2ie^{i\omega T_0} \omega D_1 A = 0 \tag{23}$$

$$-\frac{3e^{-i\omega T_0} \bar{F}^2 \bar{\zeta} \bar{A}}{\omega^4} - \frac{e^{-i\omega T_0} \bar{F}^2 \psi \bar{A}}{\omega^2} - 3e^{-i\omega T_0} \bar{\zeta} \bar{A}^2 A - 2e^{-i\omega T_0} \omega^2 \psi \bar{A}^2 A - 2ie^{-i\omega T_0} \omega \bar{A} \mu - 2ie^{-i\omega T_0} \omega D_1 \bar{A} = 0 \tag{24}$$

Equations 23 and 24 are complex conjugates and satisfying one consequently satisfies the other.

Substituting $\frac{1}{2}ae^{i\beta}$ for A and $\frac{1}{2}ae^{-i\beta}$ for \bar{A} and making real and imaginary terms equal to zero,

we obtain

$$a = A_0 e^{-T_1 \mu} \text{ and } \beta = \frac{-4\bar{F}^2(3\bar{\zeta} + \psi\omega^2)T_1 + \frac{e^{-2T_1\mu}\omega^4(3\bar{\zeta} + 2\psi\omega^2)A_0^2}{2\mu}}{8\omega^5} + \beta_0 \tag{25}$$

where A_0 and β_0 are constants and depend on initial conditions of the SMP system. Eliminating secular terms from Eq. 22, the solution is derived as

$$\eta_1 = -\frac{\bar{F}^3 \bar{\zeta}}{\omega^8} + \frac{e^{2i\omega T_0} \bar{F} \bar{\zeta} A^2}{\omega^4} + \frac{e^{2i\omega T_0} \bar{F} \psi A^2}{\omega^2} - \frac{1}{4} e^{3i\omega T_0} \psi A^3 - \frac{e^{3i\omega T_0} \bar{\zeta} A^3}{8\omega^2} - \frac{6\bar{F} \bar{\zeta} A \bar{A}}{\omega^4} - \frac{2\bar{F} \psi A \bar{A}}{\omega^2} + A e^{i\omega T_0} + \text{complex conjugates} \quad (26)$$

Substituting Eqs. 21, 25 and 26 in Eq. 17 gives the approximate solution of $\eta(t)$ upto $O(\tilde{\varepsilon}^1)$. We use this approximate solution to calculate the shape recovery of the beam for multiple stages and verify with numerical solution of Eq. 13.

4.3. Experimental results and model validation

4.3.1. Experimental setup and DMA tests' results

A 25 mm long, 3mm wide and 1.5 mm thick SMP filament is used for the experimental setup in Fig. 4.2 to study FU generated thermally induced shape recovery of SMP cantilever beam. The filament composed of 95% TBA and 5% DEGMA, is exposed to harmonic acoustic pressure field generated by a H-104-4A SONIC Concepts high intensity focused ultrasound (HIFU) transducer for 20 continuous seconds, Figs. 4.2a and 4.2b. The SMP is mounted with a fixed-free boundary condition to mimic a cantilever beam using a positioning system. The water level in the tank is maintained such that the bottom part of the filament is submerged in water and the focal point of the FU transducer lies inside the submerged portion of the filament. Special care is taken to maintain the power of the transducer below a threshold level to prevent degradation of the sample [30]. A FLIR C2 infrared camera is used to capture thermal images during 20 seconds of ultrasound actuation with additional 20 seconds to capture cool down (Fig. 4.2a). Experiments are conducted for pressure measurement from FU transducer as shown in Fig. 4.2c. A Precision

Acoustics 1mm needle hydrophone is used to acquire pressure measurements using NI SignalExpress[®] software through a National Instrument data acquisition device (PCI-6115). The hydrophone is mounted using a positioning system and measures pressure data in axial and radial directions of the transducer to capture the exact location of the focal point. The pressure measured at the focal point is then used for analysis and model validation. Figures 4.3a and 4.3b show the storage modulus and tan delta curves obtained from DMA tests for 95% TBA-5% DEGMA, respectively. While storage modulus gives insight into the material's elastic behavior, tan delta is a measure of energy dissipation when the material is subjected to sinusoidal force and varying temperature. A detailed explanation of the fabrication of the SMP filament, DMA tests and thermal experiments for its characterization is given in our previous work [30] as well as in the Supplementary Material. Figure 4.3 shows the variation of mechanical properties with temperature which forms the basis of the shape recovery response and will be used in our analysis, as explained in later sections. It is important to note that the heating rate shifts the transition temperature [65]. Since the actuation with FU has a varying heating rate, the transition temperature in our experiments is different from the transition temperature obtained from DMA.

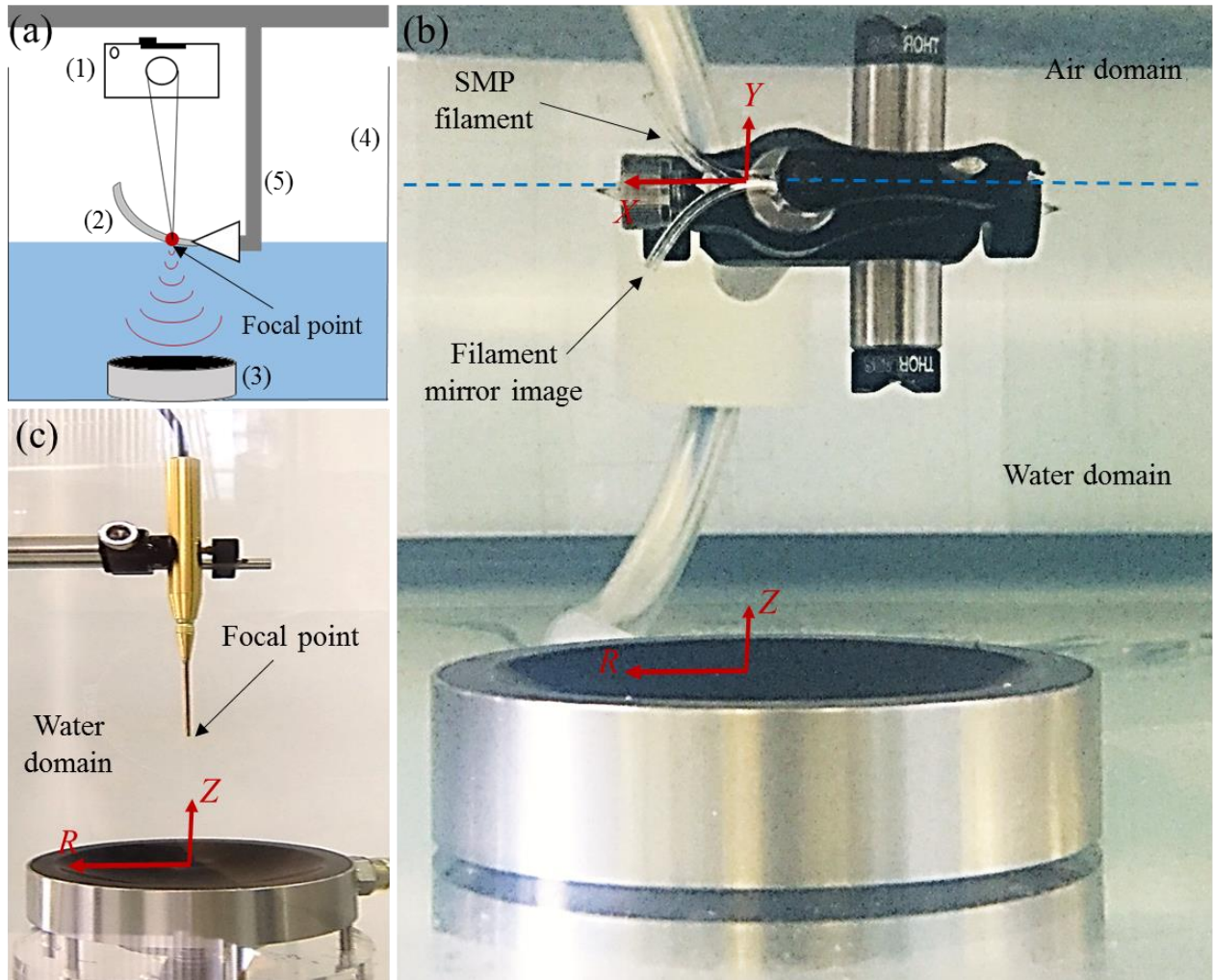


Fig. 4.2. (a) Illustration of the experimental setup; (1) thermal imaging camera directed at the focal point, (2) SMP cantilever filament exposed to FU, (3) HIFU transducer, (4) water tank and (5) positioning system. (b) Experimental setup of an SMP filament with fixed-free boundary conditions deformed in a temporary shape. (c) Experimental setup of a needle hydrophone mounted on the positioning system and exposed to FU. The tip of the needle lies at the focal point of the transducer. R and Z are the radial and axial coordinate axis for the transducer setup, respectively.

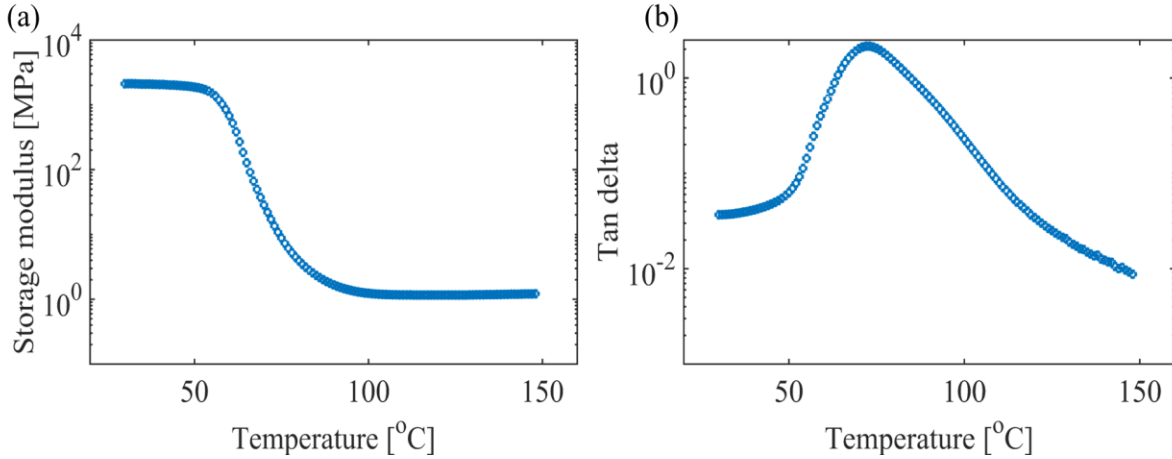


Fig. 4.3. (a) Storage modulus and (b) tan delta obtained from DMA tests for 95% TBA-5% DEGMA composition.

4.3.2. Acoustic-thermal model validation

The developed analytical-numerical model [30], explained in section 2, is used to study the acoustic and thermal fields of the FU actuated cantilever beam. The thermal energy induces shape recovery behavior modelled through the constitutive equations in section 2 (Eqs. 1, 2 and 7). To study sound wave propagation in SMP, the model predicted acoustic field is first validated through experiments only in water domain, using hydrophone (Fig. 4.2). Figure 4.4a shows the normalized sound pressure along the axial axis measured by the hydrophone at 10 W input power and 0.5 MHz source frequency. A good agreement is observed between the waveform obtained from KZK model and experiments for the normalized pressure wave at the focal point as shown in Fig. 4.4b. The pressure is normalized with respect to the maximum pressure at the focal point, P_{\max} .

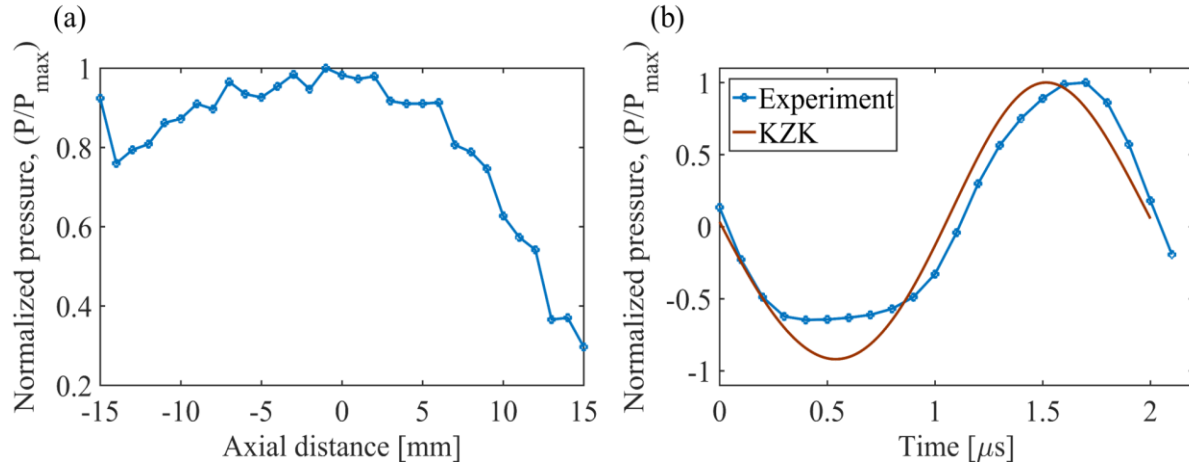


Fig. 4.4. (a) Normalized pressure along axial axis and (b) normalized pressure waveform at focal point (0 mm) at 10 W and 0.5 MHz source frequency in water domain.

The acoustic model is now used to calculate the pressure field at the focal point inside SMP. A numerical validation of the model estimated acoustic behavior in SMP upon FU exposure, is done with finite element method in our previous work with good agreement [30]. Our previous study [42] also discusses in-depth, the influence of medium parameters such as diffraction, attenuation and nonlinearity of the medium, and input parameters such as input power and source frequency on the nonlinearity of the propagating sound wave in the SMP. It is known that an increase in the number and amplitude of the higher harmonics increases the nonlinearity and the total acoustic energy of the pressure wave at a point. Our previous study [42] observed that a higher coefficient of nonlinearity of the SMP as compared to water, increase in source frequency and input power have a nonlinearly proportional influence on the nonlinearity of the acoustic wave. It was shown that the wave nonlinearity is an important parameter to consider since the absorption of the acoustic energy in SMP is proportionally correlated to the amplitude and number of the higher harmonics. Due to the absorption of the ultrasound waves in the polymer, a

viscous shearing effect on the molecules is created which causes a release of energy in the form of heat. Therefore, it was concluded that the higher the nonlinearity of the propagating wave, the more is the absorption and an increase in the temperature of the polymer which increases the shape recovery of the SMP. Consequently, in this work, we use 10 W of input power at 0.5 MHz frequency to achieve shape recovery at a reasonable spatial scale.

Using Eq. 10 of chapter 2, the absorbed pressure field in SMP predicts the temperature rise in the filament during ultrasound actuation. Figure 4.5a shows the thermal image of ultrasound actuated SMP at 20 seconds with 10 W input power and 0.5 MHz source frequency. The circle in the image shows the region of highest energy concentration. As can be seen, the temperature of the surrounding water is approximately at room temperature which emphasizes the localized heating effect of FU actuation. Figure 4.5b shows the corresponding temperature rise at the focal point for the experimental setup depicted in Fig. 4.2. A good agreement is observed between the temperature predicted by the model and the experiment.

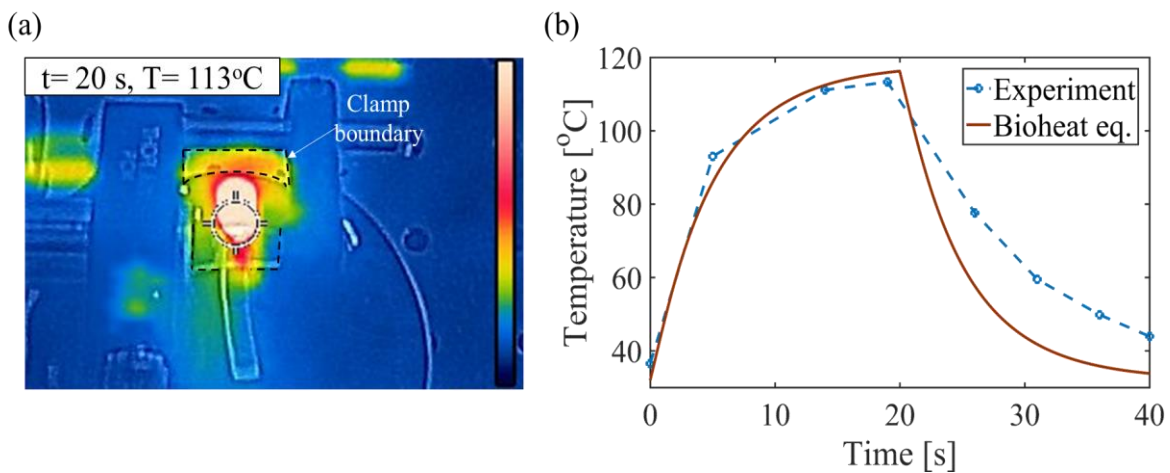


Fig. 4.5. (a) Thermal image of SMP cantilever during ultrasound actuation at 20 s and (b) temperature rise with actuation time at the focal point in SMP.

To study the dynamic response of SMP during the four stages of shape recovery, it is important to account for the temperature dependent mechanical properties of SMP. Figure 4.3 shows the change in the stiffness of the SMP used in this study, with temperature through DMA experiments. It is seen that, at high temperatures, the stiffness of the polymer is low and the elastic deformation produces a change in the conformational entropic state of the polymer chains resulting in a ductile, rubbery behavior of the polymer. At low temperatures below glass transition temperature, $T \cong 72^{\circ}C$ (for SMP in this study), the polymer is in a glassy state and behaves as an elastic solid [35]. To understand the shape memory behavior, the dynamic analytical model is divided into the following four stages.

4.3.3. Dynamics of SMP shape recovery under focused ultrasound actuation; analytical approach

4.3.3.1. Loading, cooling and shape fixation model validation. In the loading stage, the SMP filament (initial straight shape) is mounted with one end fixed using a clamp. The material is then heated to a temperature T_h such that it becomes amorphous. A pre-determined end-point deflection of approximately 15 mm is applied at the free end of the cantilever. The deflection is calculated from the horizontal axis, X in the vertical direction, Y . This gives an end-point vertical force of approximately 6 mN for static deflection of beam as calculated by Eq. 12 of the revised manuscript. The force is maintained until the filament cools down. Figure 4.2b shows the temporary shape of the beam in this stage. Bergman *et al.* [59] solved the loading stage behavior to mimic an Euler-Bernoulli beam under static loading, given by Eq. 12 using numerical methods. In this study, we use homotopy analysis method [61] to derive an analytical solution of

Eq. 12 to predict the deflection of the beam. The analytical solution gives us the advantage of estimating the resulting strains, ε_{pre} which are used as a boundary condition in Eq. 2 by setting $\varepsilon = \varepsilon_{pre}$ to predict the frozen strains in cooling stage. Figures 4.6a and 4.6b show the strains developed and angular displacement of the beam respectively. Figure 4.6c shows the transverse (upward) deflection of the beam upon application of end point force at $T > T_g$.

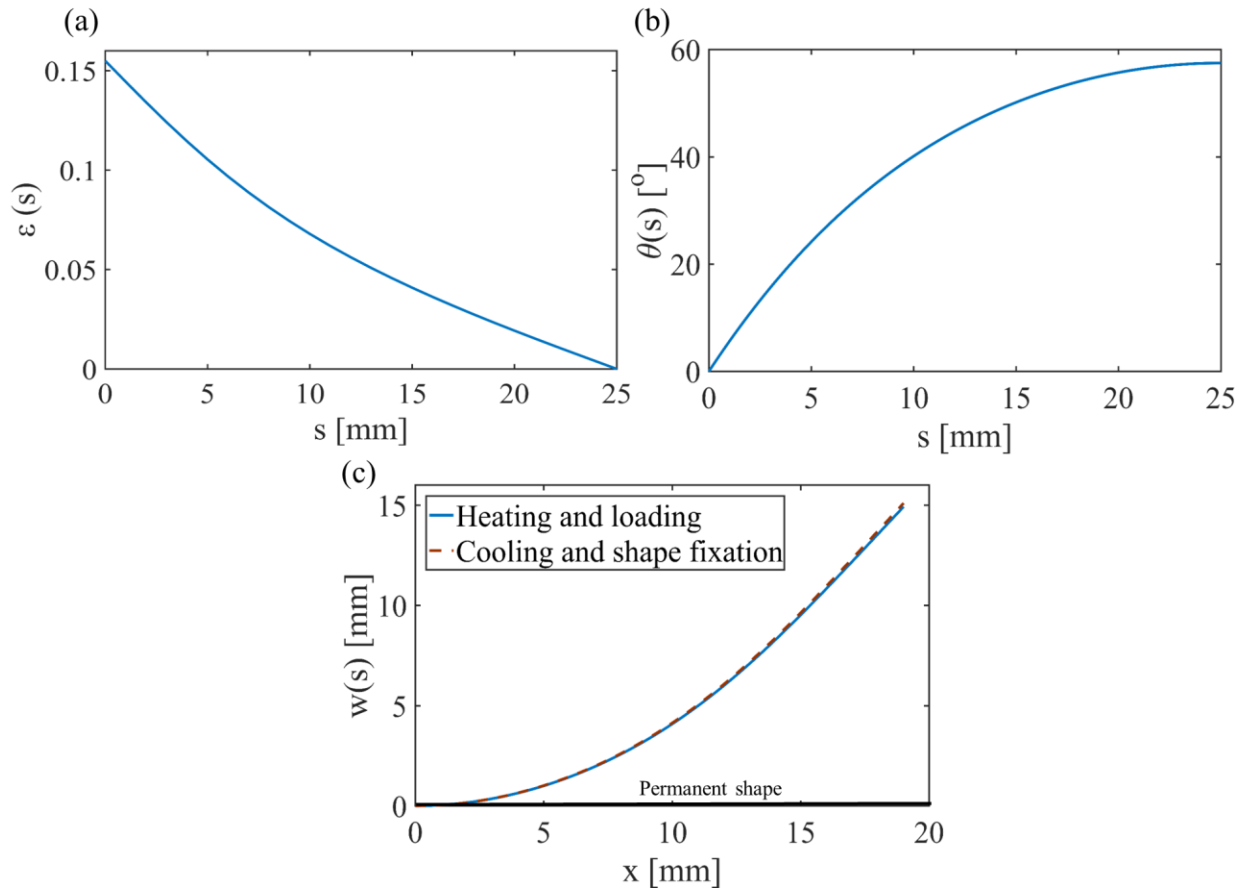


Fig. 4.6. Static loading of cantilever beam showing (a) strain and (b) angular displacement of the beam upon loading. (c) Transverse displacement of the beam at loading stage (force applied), $T > T_g$ and at unloading (no force applied), $T < T_g$.

During cooling, the external force is maintained as the temperature of the beam decreases. With lowering of temperature, the polymer becomes stiffer with increase in the elastic modulus and stores the elastic strains developed due to static loading, in the form of internal “frozen” strains (Eq. 2). It is assumed that at $T < T_g$, the complete filament transitions from amorphous to glassy state and $\phi_f = 1$. After cooling down in the fixation stage, the external forces are removed and due to high elastic modulus and stored energy, the beam remains fixed in its deformed “fixed” position. To analytically formulate the temporary deflection of the beam in the absence of external forces and account for the frozen energy, Generalized Hamilton’s principle is used along with Eqs. 2 and 7 to derive Eq. 14 in section 2.2.2. Figure 4.6c shows that the beam remains approximately at the same position before and after the removal of the external forces at cool down since all the strains applied during loading are frozen. Similar observations were made during our experiments. At this stage, the beam is mounted in the experimental setup, Fig. 4.2b, to study ultrasound induced shape recovery behavior.

4.3.3.2. Shape recovery model validation and the effects of peak pressure. In the shape recovery stage, ultrasound-induced thermal energy increases the temperature of the SMP filament which results in a decrease of the temperature dependent stiffness of the polymer and the polymer transitions into rubbery state. Since, the temperature rise occurs during 20 seconds of ultrasound actuation, it is important to formulate the changing stiffness with actuation time. As a first step, a phenomenological relation of temperature, T variation with time, t , is obtained at different peak pressures in SMP, P_{\max} and source frequency, f_0 , and is given by

$$T = ae^{bt} + ce^{dt} \quad (27)$$

where parameters a , b , c and d are non-dimensional second order polynomials in P_{\max} and third order polynomials in f_0 , Figs. C1 and C2, respectively. Tables C2 and C3 list the value of the coefficients of the polynomials in f_0 and P_{\max} , respectively. In the second step, using Eq. 27 and the relation of E with temperature from DMA analysis as shown in Fig. 4.3a [30], an FU actuation time dependent Young's modulus is obtained as a function of P_{\max} and f_0 , which is used in the equation of motion for shape recovery of the SMP beam, Fig. C3. For FU actuation of SMPs, the heating rate is not constant and changes from high to low as the actuation time increases, Fig. 4.5b. Many works have incorporated the effects of heating rate through a phenomenological relation by expressing frozen fraction as $\phi(T, \dot{T})$ or frozen strains as $\varepsilon_s(T, t)$ or $\varepsilon_s(T, \dot{T})$ [38, 66, 67]. However, since the FU actuation can be controlled through source power and source frequency only, instead of directly manipulating heating rate, Eq. 27 is formulated which captures the changing heating profile with change in P_{\max} (function of source power) and f_0 . This intrinsically incorporates the changing heating rate profile which affects the release rate of temperature dependent frozen strains, since $T = T(P_{\max}, f_0, t)$ from Eq. 27.

To model the equation of motion of the cantilever SMP beam during shape recovery, the derivation in section 2.2.2 is used. Applying modal analysis and Galerkin's weighted residual method to distributed parameter governing Eq. 7, Eq. 13 is obtained which accounts for the time variation of material properties during ultrasound exposure. The frozen internal energy given by Eq. 6, releases nonlinearly with actuation time as the beam heats and recovers. A constant value

of damping ratio at $T = T_g$ is considered and is obtained from the DMA analysis (Fig. 4.3). The material properties used in the analytical model are derived from experiments and are listed in table 1.

In order to derive an analytical expression for the shape recovery of the beam, method of multiple scales is applied to Eq. 13. However, since the method of multiple scales is limited to weak nonlinearities in the system [57], the forcing applied on the system during loading stage is small enough such that the geometric nonlinearities in Eq. 13 are weak. The equation is then scaled with a book-keeping parameter, $\tilde{\epsilon}$ to obtain Eq. 15. Since, the internal frozen energy and the elastic modulus is changing with time, the process of shape recovery is divided into multiple stages of constant coefficients of geometric nonlinearities where the initial conditions of each stage depend on the behavior of the beam in the previous stage. For each stage accounting for a fraction of the total time, Eq. 15 is used to obtain the response of the beam. This iterative process is followed until the nonlinear terms become negligible ($>O(\tilde{\epsilon})$) and the response at that stage is predicted by the linear Eq. 16 accurately. Figure 4.7a shows the influence of individual terms in Eq. 13 on the response of the beam based on which scaling is done. A validation of the method of multiple scales for weak nonlinearities is done with numerical solution of Eq. 13 using NSolve in Mathematica[®], Fig. 4.7b with good agreement. It was observed that the agreement with numerical solution is good when the weakness of the geometric nonlinearities' is of the order of .1 or smaller i.e. $\tilde{\epsilon} \leq 0.1$. The maximum error between the two solutions for the transverse displacement of the free end is 8.5% and can be considered negligible for practical applications. The increasing difference in the intermediate time intervals in Fig. 4.7b is because of the change

in the order of the geometric nonlinearities from $\tilde{\varepsilon}$ to $\tilde{\varepsilon}^2$. However, in this work, the solution until $O(\tilde{\varepsilon})$ is obtained. Figure 4.7b shows an approximately 20% shape recovery upon 20 seconds of actuation time at 10 W power and 0.5 MHz of source frequency. In order to achieve full shape recovery, repeated cycles of HIFU exposure are needed due to the slow response time of SMPs. Similar observations of repeated actuation were observed in experiments and by Lu *et al.* [68]. Another reason for partial shape recovery is the geometry of the exposed SMP which plays a significant role in the temperature distribution of the exposed area [30]. Bhargava *et al.* [30] observed that a sharpness of the deformed angle exposed to FU leads to higher temperature concentration and faster shape recovery.

Figure 4.8 shows the experimental validation of the numerical solution of Eq. 13 with good agreement at 10 W of input power and 0.5 MHz of source frequency. The numerical solution is used for experimental validation in order to obtain the deformation at a large spatial scale which leads to strong geometric nonlinearities in the temporary shape. Since method of multiple scales is only applicable for weak non-linearities, numerical solution of Eq. 13 is used for comparison with experiments. Figure 4.8a shows the initial and final positions of the beam obtained from model and experiments, plotted against horizontal displacement, x , calculated as

$$x = \int_0^s \cos[\theta(s,t)] ds .$$

It is noted that for the cantilever beam in this study, the recovery starts at 7

seconds post initiation of ultrasound exposure, Fig. 4.8b.

Table 4.1. Thermomechanical properties of SMP in this study

Parameters	Value
Modulus at $T < T_g$	1.23 MPa
Modulus at $T > T_g$	2.1 GPa
c_f	2.84×10^{-15}
n	11
N	8.04×10^{25} molecules/m ³
$\alpha(T)$	$-6.47 \times 10^{-4} + 2.35 \times 10^{-6} T \text{ K}^{-1}$ [69]
T_h	373 K

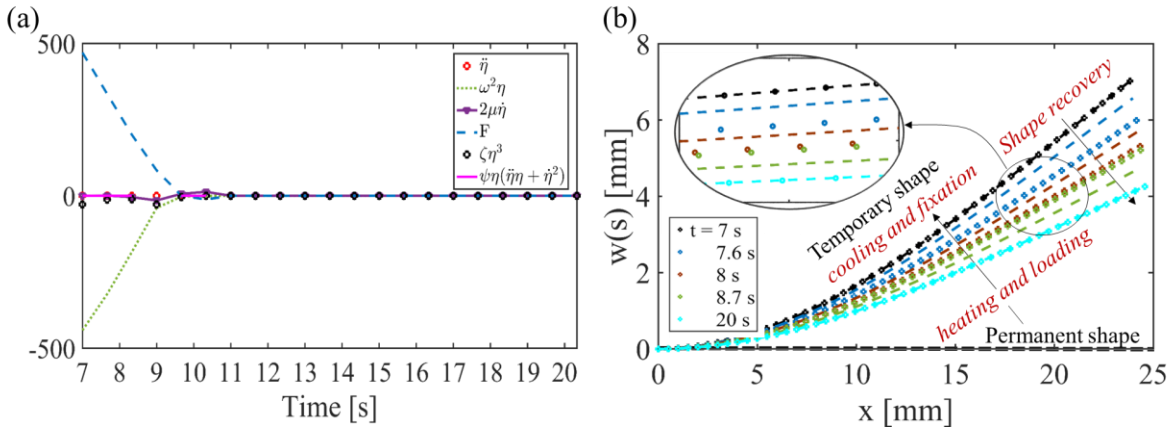


Fig. 4.7. (a) Time history of the individual terms in Eq. 13 starting at the onset of the shape recovery at 7 s. Here F is the term defined in Eq. 19 at the corresponding time. (b) Beam deflection at various instances of time during shape recovery obtained from numerical solution of Eq. 13, hollow circle symbols, and method of multiple scales, dashed lines; the inset shows a magnified image where change in color represents the change in time.

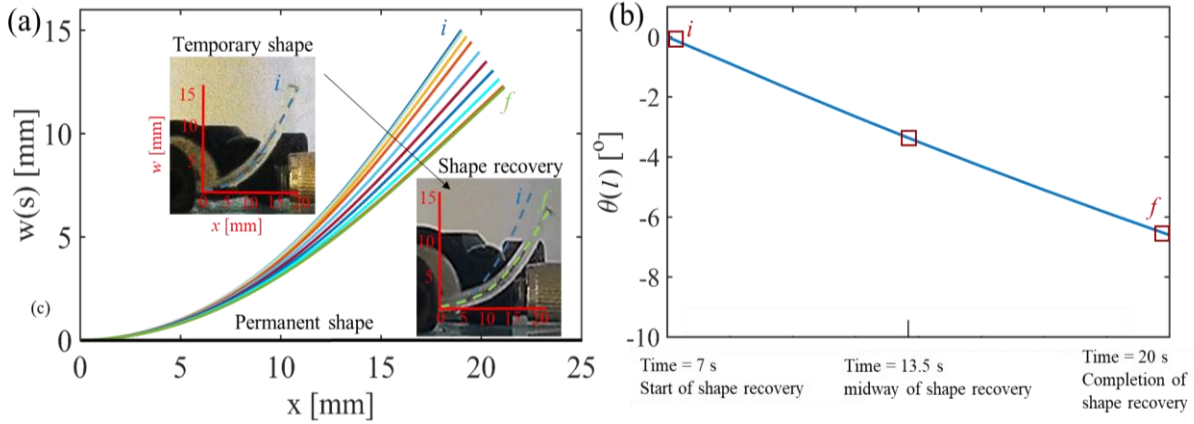


Fig. 4.8. (a) Transverse displacement during shape recovery. The insets show the deformed shape as well as the initial and final position of the beam. (b) Time history of the deformation angle of the free end of the beam. The square markers show the experimentally observed deformation angle at the corresponding time during shape recovery. Here i denotes the initial angle at temporary shape and f denotes the final angle after shape recovery.

To study the effect of acoustic parameters on shape recovery response using the developed analytical model, peak acoustic pressure inside the SMP, P_{\max} is varied. It is observed that the strain release due to the release of internal frozen energy inside the SMP varies with variation in P_{\max} . Since the release of the frozen energy is dependent on the rate and amount of temperature rise inside the SMP, the energy release and thus the resulting strain release for recovery varies with temperature rise rate and amount, which depends on P_{\max} as shown in Fig. 4.9a (Eq. 10 of chapter 2). Figure 4.9b shows the experimental validation of the deformation of the SMP cantilever beam at 0.5 MHz obtained from analytical model at different P_{\max} . It is observed that with increase in peak pressure inside SMP, the temperature at the focal point at 20 seconds increases, increasing the temperature dependent frozen energy release and giving more shape

recovery. The shape recovery in transverse direction, w , is approximately 1.5 mm at 2.7 MPa and approximately 3 mm at 3.5 MPa.

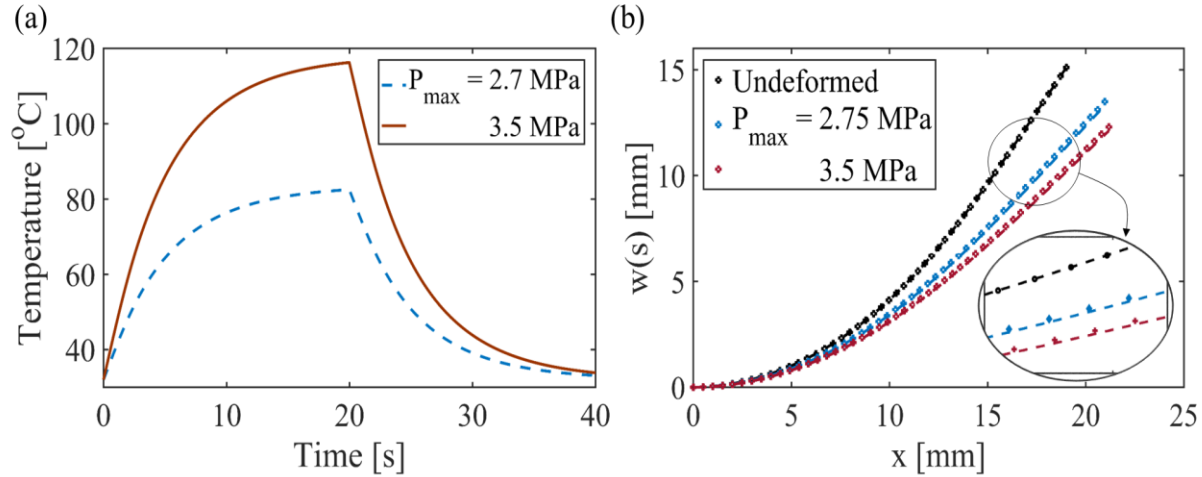


Fig. 4.9. (a) Time history of temperature rise inside SMP at focal point and (b) transverse beam deformation from experiment (dashed) and analytical model (circular symbols) at different P_{\max} ; the inset shows a magnified image where change in color shows the change in P_{\max} .

4.4. Conclusions

As an alternative to relatively well-studied methods of external stimulus to trigger the shape recovery of SMPs, namely light and magnetic field, FU is used to actuate the thermal-responsive SMPs in this study. The underlying mechanism of FU actuation is that the induced thermal energy is a result of selective, localized and controllable heating by FU, which influences the mechanical behavior of SMP. FU actuation offers advantage of temporal and spatial control through flexible selection of the acoustic intensity, frequency, exposure time, sample size as well as the ease in positioning of the acoustic source. While non-contact ultrasound triggering has been used to achieve broad utilization of SMPs, to the best of our knowledge, no report involved

an analytical solution to analyze the acoustic-thermo-elastic dynamics of ultrasound-responsive SMPs. This chapter presents a fundamental research focusing on ultrasound actuation of SMPs considering acoustic, mechanical and geometric nonlinearities and aims to show the dynamical behavior of SMPs during the four stages of shape recovery process. The FU induced thermal energy inside SMP causes a nonlinear change in thermomechanical properties namely elastic modulus and thermal expansion coefficient, with respect to actuation time. A model is developed which accounts for this nonlinear temporal variation of material properties and uses method of multiple scales to derive a solution of the governing equations of motion of an Euler-Bernoulli SMP cantilever beam assuming weak geometric nonlinearities. The analytical solution is successfully validated with numerical solutions and experiments. While the solution of method of multiple scales can give accurate shape recovery response for temporary deformations with weak geometric nonlinearities such as electrical switches, the semi-numerical modal analysis solution can predict shape memory behavior with strongly geometrically nonlinear temporary shapes. In both the cases, the shape recovery response is expressed as a function of acoustic and thermal parameters, thus eliminating the need of calculating any intermediary or internal acoustic/thermal/elastic effects on SMP.

Appendix C

C.1. SMP material preparation

The monomer and the crosslinker that are utilized for fabrication of the SMP filament during the experiments are Tert-Butyl acrylate (TBA) and Di (ethylene glycol) dimethacrylate (DEGMA) (molecular weight 550) respectively. The photo-initiator used for the UV curing process is 2,2-

Dimethoxy-2phenyl-acetophenone. All chemicals are purchased from Sigma-Aldrich, and are not altered prior to use. Molds are created with dimensions of 150 mm x 100 mm from clear ultra-scratch resistant acrylic, and sealed with Loctite silicon sealant. Thickness of polymer filaments developed is varied as per the needs of the experiment, but is typically 1.5 mm. Curing is completed with a 100 W Blak-Ray B-100 AP High Intensity UV Lamp.

TBA is mixed with DEGMA in a volumetric ratio of 95-5%. The crosslinker-monomer combination is mixed well for ten minutes with a stir plate after adding 1 wt% photo-initiator. The mixture is then transferred to the acrylic molds for curing. The UV light exposure lasts 20 minutes for each mold. The prepared SMP is then removed from the mold. All SMP samples have a permanent shape of a flat rectangle. The SMP film is cut to the desired geometry by either scoring the material or use of a rotary tool.

C.2. Thermo-mechanical tests

Dynamic mechanical analysis (DMA) is done using a TA Instruments-Q800 DMA with an oscillation rate of 1 Hz. The data is collected in 0.5°C steps, and the temperature is ramped at a rate of 2°C per minute. A hot disk thermal constants analyzer is utilized for evaluating thermal properties of the SMP filament. The hot disk hardware consists of a Keithley 2000 voltmeter, a Keithley 2400 sourcemeter, a Hot-disk bridge, and a computational device. After fabrication of SMP films, 14 disks of 15 mm diameter and 1 mm thickness are cut with a rotary tool. These sheets are clamped tightly in the sample holder for testing. The measurement method is verified with solid porcelain and sheets of PMMA with known thermal properties. The values of

mechanical and thermal properties extracted from DMA analysis and hot disk experiment for 95%TBA-5%DEGMA are reported in Table C1.

Table C4.2. Mechanical and thermal properties of 95%TBA-5% DEGMA polymer

Property	Value
T_g	72 °C
Density, ρ_m	1100 Kg/m ³
Amorphous phase elastic modulus, E_a	1.66 MPa
Glassy phase elastic modulus, E_g	2100 MPa
Thermal conductivity, κ	0.175 W/m/K
Specific heat capacity, C_{hm}	1050 J/kg/K

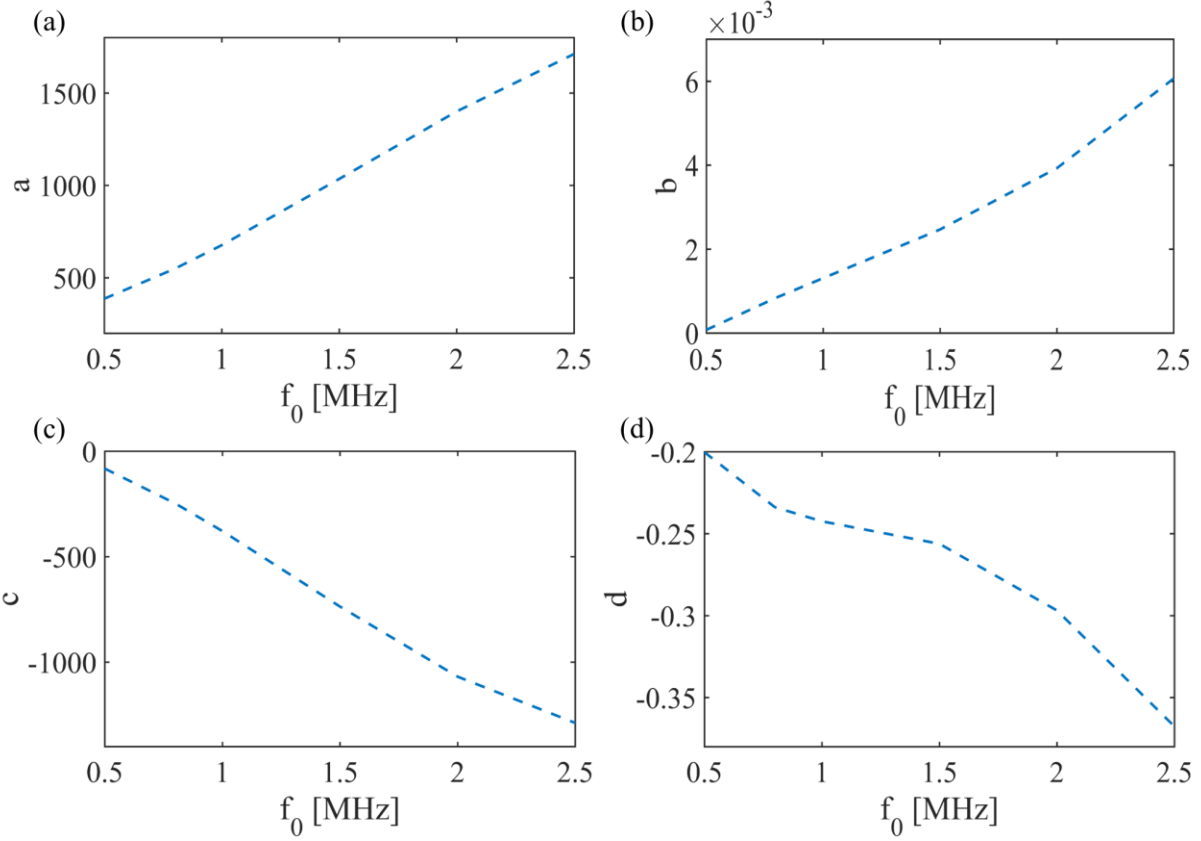


Fig. C1. Variation of non-dimensional parameters in Eq. (27) with f_0 . Parameters a, b, c and d are third order polynomial and d is a fourth order polynomial in f_0

Table C2. Dependency of parameters in Eq. (27) on f_0

Parameter	$\times f_0^4$	$\times f_0^3$	$\times f_0^2$	$\times f_0^1$	$\times f_0^0$
a		-82.21	384	147.1	227.8
b		0.0004987	-0.001642	0.004054	-0.001603
c		116.3	-472.1	-87.89	65.11
d	0.03484	-0.2481	0.5835	-0.5908	-0.0219

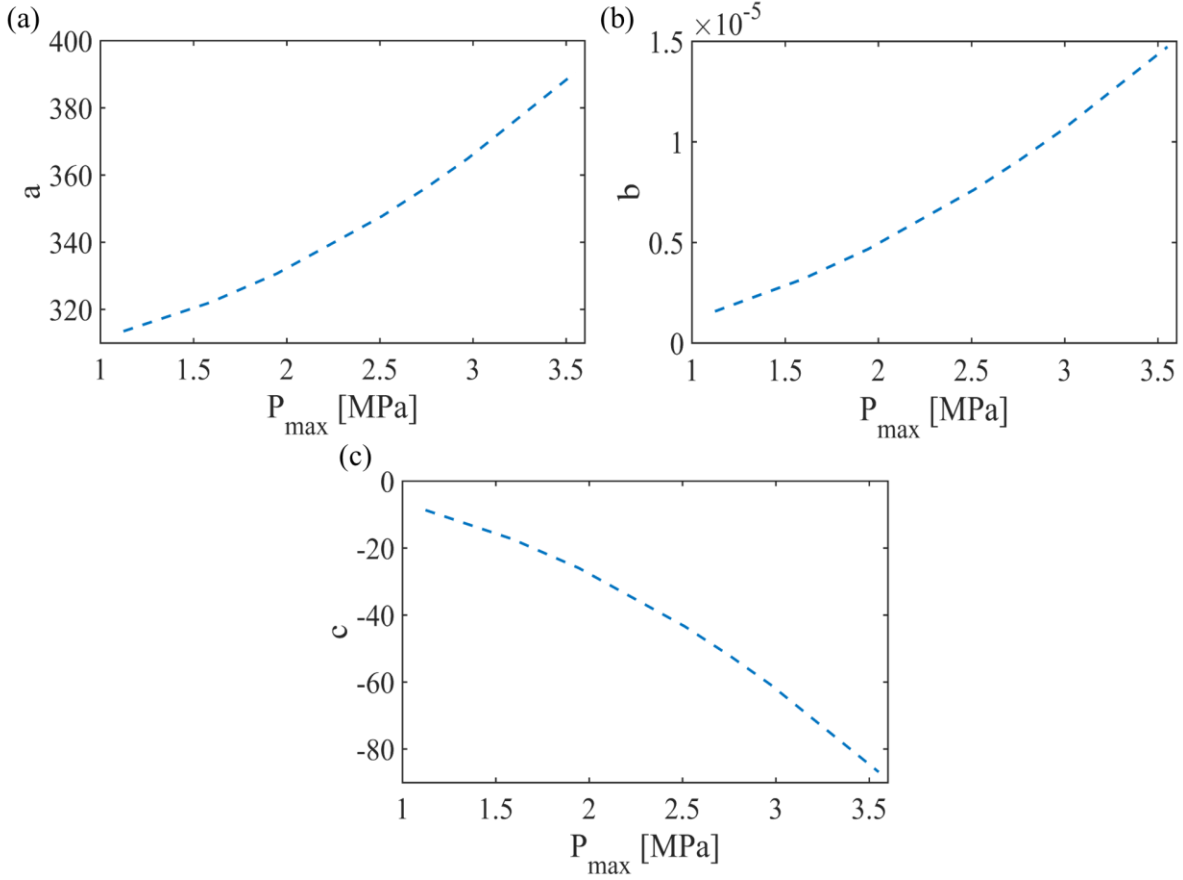


Fig. C2. Variation of non-dimensional parameters in equation (27) with P_{\max} during FU exposure. Parameters a, b and c are second order polynomial in peak pressure and d is a constant.

Table C3. Dependency of parameters in equation (27) on P_{\max}

Parameter	$\times P_{\max}^2$	$\times P_{\max}^1$	$\times P_{\max}^0$
a	6.815	-0.09395	305
b	1.028×10^{-6}	6.13×10^{-7}	-4.153×10^{-7}
c	-6.939	0.2215	-0.1595
d			-0.2005

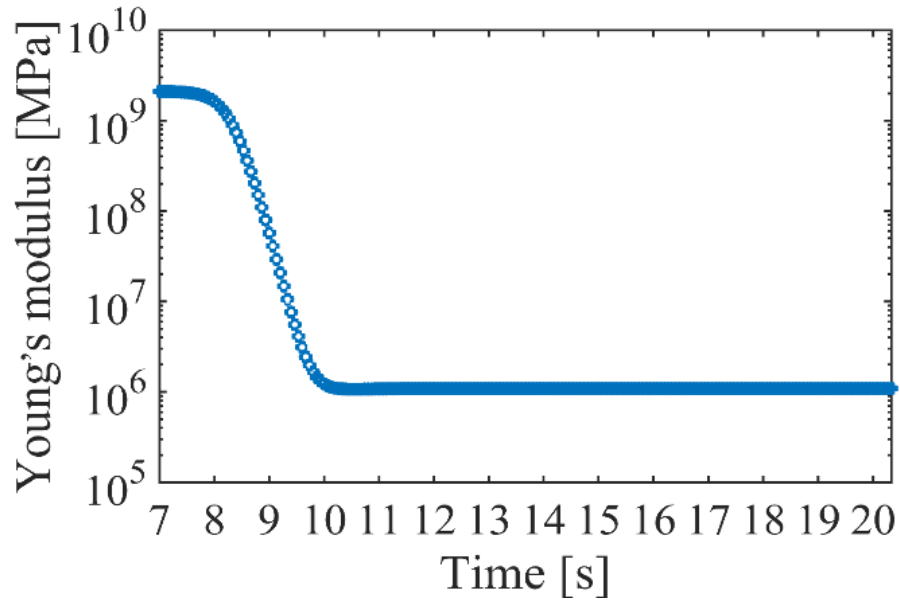


Fig. C2: Variation of Young's modulus with actuation time during shape recovery

References

1. D. Ratna and J. Karger-Kocsis, *Journal of Materials Science* **43** (1), 254-269 (2008).
2. M. Zarek, M. Layani, I. Cooperstein, E. Sachyani, D. Cohn and S. Magdassi, *Advanced Materials* **28** (22), 4449-4454 (2016).
3. B. Dietsch and T. Tong, *Journal of advanced materials* **39** (2), 3-12 (2007).
4. C. Liu, H. Qin and P. Mather, *Journal of materials chemistry* **17** (16), 1543-1558 (2007).
5. A. Metcalfe, A.-C. Desfaits, I. Salazkin, L. H. Yahia, W. M. Sokolowski and J. Raymond, *Biomaterials* **24** (3), 491-497 (2003).
6. A. A. Sharp, H. V. Panchawagh, A. Ortega, R. Artale, S. Richardson-Burns, D. S. Finch, K. Gall, R. L. Mahajan and D. Restrepo, *Journal of neural engineering* **3** (4), L23 (2006).
7. W. Small, M. F. Metzger, T. S. Wilson and D. J. Maitland, *IEEE Journal of selected topics in quantum electronics* **11** (4), 892-901 (2005).

8. D. J. Maitland, M. F. Metzger, D. Schumann, A. Lee and T. S. Wilson, *Lasers Surg. Med.* **30** (1), 1-11 (2002).
9. C. M. Yakacki, R. Shandas, C. Lanning, B. Rech, A. Eckstein and K. Gall, *Biomaterials* **28** (14), 2255-2263 (2007).
10. A. Lendlein and R. Langer, *Science* **296** (5573), 1673-1676 (2002).
11. P. T. Mather, X. Luo and I. A. Rousseau, *Annual Review of Materials Research* **39**, 445-471 (2009).
12. Y. Amamoto, H. Otsuka, A. Takahara and K. Matyjaszewski, *Advanced Materials* **24** (29), 3975-3980 (2012).
13. B. Ghosh and M. W. Urban, *Science* **323** (5920), 1458-1460 (2009).
14. L. Fang, T. Fang, Z. Fang, C. Lu and Z. Xu, *Macromolecular Materials and Engineering* **301** (3), 267-273 (2016).
15. H. Meng and G. Li, *Polymer* **54** (9), 2199-2221 (2013).
16. K. C. Hribar, R. B. Metter and J. A. Burdick, presented at the Engineering in Medicine and Biology Society, 2009. EMBC 2009. Annual International Conference of the IEEE, 2009.
17. Y. Bai, J. Zhang and X. Chen, *ACS Applied Materials & Interfaces* **10** (16), 14017-14025 (2018).
18. M.-C. Chen, H.-W. Tsai, Y. Chang, W.-Y. Lai, F.-L. Mi, C.-T. Liu, H.-S. Wong and H.-W. Sung, *Biomacromolecules* **8** (9), 2774-2780 (2007).
19. W. Small, P. R. Buckley, T. S. Wilson, W. J. Benett, J. Hartman, D. Saloner and D. J. Maitland, *IEEE Transactions on Biomedical Engineering* **54** (6), 1157-1160 (2007).
20. N. G. Sahoo, Y. C. Jung, N. S. Goo and J. W. Cho, *Macromolecular Materials and Engineering* **290** (11), 1049-1055 (2005).
21. N. G. Sahoo, Y. C. Jung and J. W. Cho, *Mater. Manuf. Processes* **22** (4), 419-423 (2007).
22. X. Yu, S. Zhou, X. Zheng, T. Guo, Y. Xiao and B. Song, *Nanotechnology* **20** (23), 235702 (2009).
23. U. N. Kumar, K. Kratz, M. Behl and A. Lendlein, *Express Polymer Letters* **6** (1) (2012).
24. J. Cuevas, J. Alonso, L. German, M. Iturrondobeitia, J. Laza, J. Vilas and L. León, *Smart Materials and Structures* **18** (7), 075003 (2009).

25. M. Y. Razzaq, M. Anhalt, L. Frormann and B. Weidenfeller, *Materials Science and Engineering: A* **444** (1-2), 227-235 (2007).
26. J. Kost, K. Leong and R. Langer, *Proceedings of the National Academy of Sciences* **86** (20), 7663-7666 (1989).
27. B. G. De Geest, A. G. Skirtach, A. A. Mamedov, A. A. Antipov, N. A. Kotov, S. C. De Smedt and G. B. Sukhorukov, *Small* **3** (5), 804-808 (2007).
28. G. A. Hussein, N. Y. Rapoport, D. A. Christensen, J. D. Pruitt and W. G. Pitt, *Colloids and Surfaces B: Biointerfaces* **24** (3), 253-264 (2002).
29. A. Bhargava, K. Peng, R. Mirzaeifar and S. Shahab, presented at the Active and Passive Smart Structures and Integrated Systems XII, 2018.
30. A. Bhargava, K. Peng, J. Stieg, R. Mirzaeifar and S. Shahab, *RSC Advances* **7** (72), 45452-45469 (2017).
31. H. Tobushi, T. Hashimoto, S. Hayashi and E. Yamada, *Journal of intelligent material systems and structures* **8** (8), 711-718 (1997).
32. H. Tobushi, K. Okumura, S. Hayashi and N. Ito, *Mechanics of materials* **33** (10), 545-554 (2001).
33. J. Morshed, H. A. Khonakdar and S. Rasouli, *Macromolecular theory and simulations* **14** (7), 428-434 (2005).
34. Y. Li, S.-S. Guo, Y. He and Z. Liu, *International Journal of Computational Materials Science and Engineering* **4** (01), 1550001 (2015).
35. Y. Liu, K. Gall, M. L. Dunn, A. R. Greenberg and J. Diani, *Int. J. Plast.* **22** (2), 279-313 (2006).
36. H. J. Qi, T. D. Nguyen, F. Castro, C. M. Yakacki and R. Shandas, *Journal of the Mechanics and Physics of Solids* **56** (5), 1730-1751 (2008).
37. K. Rajagopal and A. Srinivasa, *Int. J. Plast.* **14** (10-11), 945-967 (1998).
38. Y. Li, J. Hu and Z. Liu, *International Journal of Solids and Structures* **124**, 252-263 (2017).
39. A. Rozanova-Pierrat, (2006).
40. M. F. Hamilton and D. T. Blackstock, *Nonlinear acoustics*. (Academic press, San Diego, 1998).

41. F. P. Curra, P. D. Mourad, V. A. Khokhlova, R. O. Cleveland and L. A. Crum, *IEEE Transactions on Ultrasonics, Ferroelectrics, and Frequency Control* **47** (4), 1077-1089 (2000).
42. A. Bhargava, K. Peng, J. Stieg, R. Mirzaeifar and S. Shahab, presented at the Smart Materials, Adaptive Structures and Intelligent Systems, 2017.
43. S. S. Rao, *Vibration of continuous systems*. (John Wiley & Sons, 2007).
44. A. H. Nayfeh, *Introduction to perturbation techniques*. (John Wiley & Sons, 2011).
45. S. Shahab, M. Gray and A. Erturk, *Journal of Applied Physics* **117** (10), 104903 (2015).
46. S. Shahab and A. Erturk, *Smart Materials and Structures* **23** (12), 125032 (2014).
47. M. Bakhtiari-Nejad, A. Elnahas, M. R. Hajj and S. Shahab, presented at the Active and Passive Smart Structures and Integrated Systems XII, 2018.
48. V. C. Meesala, M. R. Hajj and S. Shahab, presented at the Active and Passive Smart Structures and Integrated Systems XII, 2018.
49. Y.-C. Chen and D. C. Lagoudas, *Journal of the Mechanics and Physics of Solids* **56** (5), 1752-1765 (2008).
50. Y.-C. Chen and D. C. Lagoudas, *Journal of the Mechanics and Physics of Solids* **56** (5), 1766-1778 (2008).
51. M. C. Boyce and E. M. Arruda, *Rubber Chemistry and Technology* **73** (3), 504-523 (2000).
52. R. B. Dupaux and M. C. Boyce, *Mechanics of Materials* **39** (1), 39-52 (2007).
53. C. Buckley and D. Jones, *Polymer* **36** (17), 3301-3312 (1995).
54. C. Buckley, D. Jones and D. Jones, *Polymer* **37** (12), 2403-2414 (1996).
55. I. Ward, *Polymer Engineering & Science* **24** (10), 724-736 (1984).
56. L. R. G. Treloar, *The physics of rubber elasticity*. (Oxford University Press, USA, 1975).
57. A. H. Nayfeh and P. F. Pai, *Linear and nonlinear structural mechanics*. (John Wiley & Sons, 2008).
58. D. Tang, M. Zhao and E. H. Dowell, *Journal of Applied Mechanics* **81** (6), 061009-061009-061010 (2014).

59. D. Bergman, B. Yang and H. Fang, presented at the The 14th AIAA Gossamer Spacecraft Forum, Boston, 2013.
60. J. M. Gere and S. P. Timoshenko, *Mechanics of materials*, 4th edition ed. (PWS Publishing Company, Boston, 1997).
61. J. Wang, J.-K. Chen and S. Liao, *Journal of Computational and Applied Mathematics* **212** (2), 320-330 (2008).
62. L. Meirovitch and R. Parker, *Applied Mechanics Reviews* **54**, B100 (2001).
63. A. H. Nayfeh and D. T. Mook, *Nonlinear oscillations*. (John Wiley & Sons, 2008).
64. V. C. Meesala and M. R. Hajj, *J. Appl. Phys.* **124** (6), 065112 (2018).
65. K. Yu and H. J. Qi, *Soft Matter* **10** (47), 9423-9432 (2014).
66. Q. Yang and G. Li, *Int. J. Plast.* **80**, 168-186 (2016).
67. M. Baghani, R. Naghdabadi, J. Arghavani and S. Sohrabpour, *Int. J. Plast.* **35**, 13-30 (2012).
68. X. Lu, G. Fei, H. Xia and Y. Zhao, *Journal of Materials Chemistry A* **2** (38), 16051-16060 (2014).
69. C. Yuan, Z. Ding, T. Wang, M. L. Dunn and H. J. Qi, *Smart Mater. Struct.* **26** (10), 105027 (2017).

Chapter 5 : Comparison of hydroelastic and thermal effects in fluid-loaded shape memory polymers in acoustic fields

Abstract

Shape memory polymers are intelligent structures that have the ability to remember and revert to their permanent shape irrespective of their temporary deformed form, in presence of an external stimulus. In this work, high intensity focused ultrasound (HIFU) is used to trigger the shape memory response. HIFU has a superior capability of being remote, biomedically safe, and highly efficient with its property of focusing all input energy into a tight focal spot. While few works have studied the multiphysics of HIFU-actuated shape recovery behavior, this work aims to extend the previous studies by investigating the shape memory behavior in dense fluid mediums, for the first time. The need for this investigation arises with the increase of many applications using SMPs in biomedical, underwater robotic, and MEMS devices. In the operation of such devices, the surrounding medium may affect the SMP response differently as compared to in-vacuo conditions. By conducting experiments for FU actuation of SMPs in air and water, this study finds that the amount of shape recovery is significantly lower in water, as compared to air. Analysis of the effects of fluid loading and thermal cooling on shape memory behavior of polymers immersed in water is performed using a mathematical framework and finite element simulations. The analysis reveals that while additional damping due to surrounding fluid negligibly affects the polymer response, the magnitude and the rate of temperature rise inside the polymer makes a significant difference in SMP recovery in air and water. This work aims to fill

the gaps in the existing mathematical frameworks and provide a groundwork for building complex FU-actuated SMP systems operating in dense fluid environments.

5.1. Introduction

Shape memory polymers (SMPs) are a class of smart materials that have the ability to change shape when subjected to external stimuli such as light and heat [1-4]. These polymers store their temporary shape, unless an external trigger actuates them to go back to their permanent or original shape. Due to several advantages including being light-weight, inexpensive, easy to manufacture, flexibility in composition, bio-compatibility, and ability to undergo large deformations, SMPs are widely used in many applications ranging from aerospace, biomedical, and soft robotics [5-7]. SMPs fall broadly in three categories namely, chemo-responsive, thermo-responsive, and photo-responsive [8, 9]. While chemo-responsive SMPs undergo a phase-transition from stiff to amorphous phase, which initiates shape recovery, due to interaction with a solvent, thermo-responsive polymers undergo a change in elastic modulus due to temperature change. Shape memory of photo-responsive polymers depends on the changes in the properties of the crosslinker content (responsible for holding the polymer molecules together) due to change in incident light characteristics. In this study, thermo-responsive SMPs are considered which undergo phase transformation from glassy (stiff) phase to amorphous (soft) phase above a glass transition temperature [10, 11]. A typical shape recovery process for thermo-responsive polymers involves four stages, the loading (polymer is deformed into temporary shape in amorphous phase), cooling (phase transition from amorphous to glass phase), unloading (

removal of external forces in glassy phase), and heating (shape recovery due to phase transition to return to original shape) [12].

The extent of the response of SMPs relies on the nature of the external trigger. Direct heat has often been used to trigger the shape memory effect, particularly in in-vivo applications using body heat. However, for sensitive and remote applications, there is a need of a more flexible, non-invasive, and controllable trigger. Thus, remote stimulus from light, magnetic fields, and electrical fields are increasingly being used [13-16]. However, these triggers require incorporation of responsive fillers such as magnetic or conductive particles in the polymer matrix to respond to external stimuli. These fillers can compromise the biological or structural integrity of the material. Thus, a trigger which is remote and maintains the polymer's compatibility with its surrounding is needed. To fulfill this requirement, this study proposes the use of focused ultrasound (FU) to actuate the SMPs.

Ultrasound has been used in biomedical field for many years in various applications including tissue necrosis, imaging, and drug delivery [17-19]. Due to high penetration depth and biological safety, ultrasound has also been used for wireless acoustic power transfer applications to charge biomedical implants, remote sensors in oceans and automobiles [20, 21]. FU has a unique capability of concentrating the entire input energy in a tight spot at the desired location. In this work, the localized energy deposition is used to heat the polymer due to viscous shear oscillation of its molecules under ultrasound exposure. The consequent temperature increase initiates the shape recovery. Bhargava *et al.* [12] developed a SMP-based drug delivery container to achieve controlled drug delivery through controlled FU excitation. The study developed a drug container

which can be inserted into the body with SMP in its temporary shape, and contained trapped drug particles inside it. Upon reaching the target location, the SMP can be exposed to FU to undergo shape recovery and release the entrapped drug. The authors in a later work also developed a comprehensive multiphysics mathematical framework to quantify the FU-induced shape memory effect in a simple Euler-Bernoulli cantilever beam analytically using perturbation techniques [22]. This study aims to extend this framework for applications employing such simple SMP systems (cantilevers) in underwater or fluid-surrounded environments.

Fluid-loading effects have been extensively studied on forced vibration of slender structures immersed in oscillating or quiescent flows. The interest in this research arises from the widespread applications in MEMS, bio-inspired robots, energy-harvesting, atomic force microscopy, and off-shore engineering [23-27]. It is conventionally accepted that the hydrodynamic interactions with a moving structure in a fluid can be decomposed in two major forces, namely added mass effect, and added damping effect. The added mass is in-phase with the acceleration of the body and lowers the resonant frequency of the oscillating structure, while added damping is out-of-phase forcing with respect to the acceleration of the body. The added damping increases the damping effects in an oscillating system [24, 28]. Sader developed a linear hydrodynamic function to model the response of an oscillating cantilever beam in an incompressible fluid for small-amplitude vibrations [24]. However, this model fails to account for cantilevers undergoing large deformations, where vortex shedding and convection phenomena define the flow [23, 29]. Various studies have used a semi-empirical approach based on experimental data to model large deformations, known as Morison's formulae [23, 30]. Many

works also extended Sader's theory to include a correction to the hydrodynamic function for a wide range of aspect ratios, operating frequencies, and vibration amplitudes [28, 31, 32]. A nonlinear form of Morison's equation has also been studied for analyzing large amplitude and high frequency oscillations for rigid cylinders and beams [33-35]. Shahab *et al.* [36] investigated the underwater electrohydroelastic actuation of MFC cantilevers for different aspect ratios and two mode shapes using Morison's nonlinear equation. The drag and inertia coefficients for Morison's formulae were extracted from experimental data and verified with literature.

In this work, we use the nonlinear Morison's equation using the hydrodynamic coefficients given by Shahab *et al.* [36] to understand the effect of fluid-loading on SMP cantilever beam placed in quiescent fluid. This study is organized as follows. Section 2 gives a brief summary of our previous work [22, 37] to describe the multiphysics mathematical framework for ultrasound actuation of SMP cantilever beams. The equation of motion for the shape recovery stage is extended in this work, to incorporate the fluid loading effects. Section 3 presents an experimental study in air and underwater. This section compares the experimental observations with the theoretical model and finite element simulations. Detailed discussion of the possible factors contributing to the shape recovery response of the beam in two fluid mediums is done. Section 4 reports the conclusions of this study.

5.2. Theory

To understand the acoustic-thermoelastic response of SMPs, a comprehensive framework to predict the dynamics of acoustic wave propagation in different mediums, its role in heating SMPs, and the subsequent elastic response of polymers is important. Bhargava *et al.* [12, 22]

introduced a multiphysics model which examines the FU-induced SMP response in three interconnected stages. The first stage uses the Khokhlov–Zabolotskaya–Kuznetsov (KZK) equation to predict the acoustic wave field in the fluid as well as polymer medium [38]. The second stage uses the calculated pressure field to estimate the temperature rise inside the SMP using Penne’s Bioheat equation [39]. The third stage predicts the thermally-induced phase transformation of SMP and its subsequent shape recovery [40]. The following subsections provide a brief summary of this previously developed model.

5.2.1. Acoustic-thermoelastic model

This model divides the acoustic-polymer interaction phenomena into three interconnected stages. The first stage predicts the acoustic pressure field using the KZK equation in the SMP and the surrounding fluid medium. The non-dimensional form of this equation is given by Eq. 2 of chapter 2 and Ref. [38]. The first term on the right-hand side of this equation represents diffraction with gain in the pressure field due to focusing effects. The second term on the right side of Eq. 2 of chapter 2 denotes absorption effects. Lastly, the third term represents nonlinearity effects in the medium [41].

Nonlinearity arises due to variation of acoustic wave pressure with the density of the medium. Due to this variation, the peaks of a wave may travel faster than troughs, thus giving a distorted shape to the pressure waveform [42]. This nonlinearity is represented as the generation of higher harmonics in the wave with frequencies equal to the integer multiples of the excitation frequency. Since the nonlinearity is cumulative and grows with distance, it leads to a nonlinear increase in pressure amplitude as the distance from the source increases, particularly at focus. On

the other hand, absorption leads to attenuation of the pressure amplitude. The attenuation parameter follows a linear and a squared power-law dependence with harmonic frequency in water and polymers, respectively. Thus, attenuation is higher for higher harmonics [12].

An operator splitting method is used to solve Eq. 2 of chapter 2, which calculates each of the diffraction, attenuation, and nonlinear effects separately at each integration step. A detailed description of the solving technique and the boundary conditions for the whole domain are given in Ref. [12]. The pressure field developed inside the SMP that is kept at the focal point of the FU transducer, is predicted by this equation. This pressure is treated as an external input heat source that leads to temperature rise of the polymer. The temperature, T , in SMP is calculated using Penne's Bioheat equation, given by Eq. 10 of chapter 2 and Ref. [39].

The temperature rise predicted by Penne's equation induces thermal stresses inside the SMPs. These stresses result in the phase transformation behavior of SMPs from glassy to amorphous phase, above the glass transition temperature, T_G . The entire process is divided into four stages as follows. The first stage involves heating the polymer into amorphous phase and deforming it through external forces. In the second stage, the polymer is cooled to glassy phase without removing the external forces. This phase transformation results in storage of the entropic deformation of the SMP in the form of "frozen" strains [40]. The third stage involves removal of external forces. Since the strains are already stored by this stage, the deformed shape of the SMP persists. Lastly, in the fourth stage, the stored entropy is released under FU-induced heating and shape recovery occurs due to phase change from glassy to amorphous phase. The estimation of stresses and consequent shape recovery during this process is done using the constitutive model

proposed by Liu *et al.* [40] The 1D equations relating the stresses to total strains, ε_t , in the SMP are given by Eqs. 1 and 2 of chapter 4 [40]. In this chapter, variables ε_{st} , $\bar{\alpha}$, and ϕ_s represent frozen strains, thermal expansion coefficient, and the fraction of the SMP volume in frozen phase, used in the constitutive model (chapter 4), respectively. The variable T_h is the maximum temperature upto which SMP is heating in the loading stage of the shape recovery process. The frozen fraction is related to temperature through the relation, $\phi_s = 1 - \left[1 + c_f (T_h - T)^n \right]^{-1}$, where T is the temperature, c_f and n are constants that are experimentally determined. The variables E_i and E_e are the modulus of internal energetic deformation and modulus of entropic deformation, respectively. They are related to the Young's modulus, E , as $E = \left[(\phi_s / E_i) + (1 - \phi_s / E_e) \right]^{-1}$, with $E_e = 3NkT$ where N denotes the cross-link density and k is the Boltzmann's constant [40].

5.2.2. Hydroelastic dynamic analysis

To understand the thermomechanical behavior and the dynamics of motion of the SMP for each stage in the shape recovery process, equations of motion are derived for a simple case of Euler-Bernoulli cantilever beam assuming large deformations, using Eqs. 1 and 2 of chapter 4. The Generalized Hamilton's principle along with Galerkin's weighted residual method is used to develop these equations for the first mode shape of the beam [43].

Figure 5.1 shows the schematic of a cantilever beam of length l_c , width w_c , and thickness h_c . Under the assumptions of Euler-Bernoulli beam with a high length-to-thickness ratio, pure bending is assumed without any shear effects.

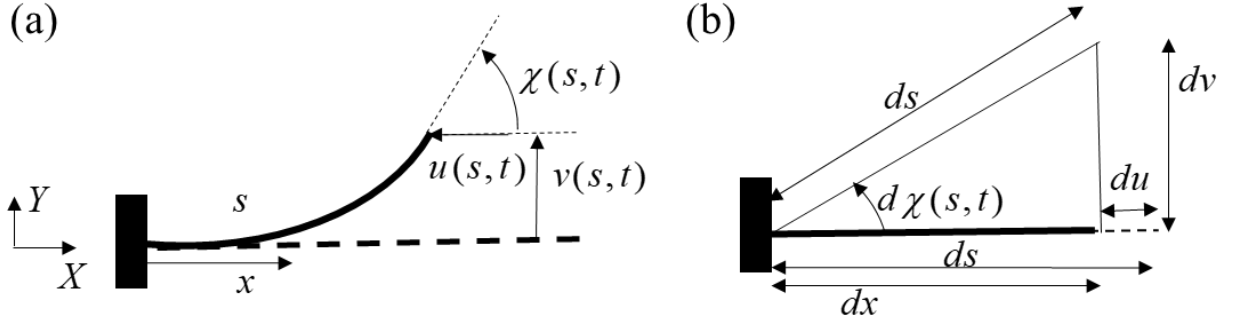


Fig. 5.1. (a) Schematic of a cantilever beam under point force applied at $s = l_c$. (b) A schematic of the deformation of a differential element of length ds of the beam. The dashed lines represent original position of the beam.

The generalized Hamilton's principle is stated as [43, 44]

$$\int_{t_1}^{t_2} (\delta \widehat{K} - \delta \widehat{U} + \delta \widehat{W}_{nc}) dt = 0 \quad (1)$$

where $\widehat{\delta}$ is the variational parameter applied to kinetic energy, K , potential energy, U , and non-conservative work done on SMP, W_{nc} , in a time interval $[t_1, t_2]$. Taking

$$\chi(s, t) = \sin^{-1} [v'(s, t)] = v'(s, t) + v'(s, t)^3 / 6 \quad (2)$$

where v is the vertical displacement in the Y direction, and s is the curvilinear axis along the length of the beam, Fig. 5.1. Neglecting all terms greater than fourth order, and substituting expressions for the energy terms in Eq. 1 in terms of v , the equation becomes

$$\begin{aligned} & \rho_s A \left(\left(\frac{v'(s,t)}{2} \int_s^{l_c} \int_0^s \frac{\partial^2 v'(s,t)^2}{\partial t^2} d\xi ds \right)' - \ddot{v}(s,t) \right) - EI \left(v''''(s,t) - v_f''''(s,t) \right) \\ & - EI \left(\left(v'(s,t)(v'(s,t)v''(s,t))' \right)' - \left(v_f'(s,t)(v_f'(s,t)v_f''(s,t))' \right)' \right) - c_1 \dot{v}(s,t) - F_{ex} = 0 \end{aligned} \quad (3)$$

with boundary conditions similar to Eqs. (8-11) of chapter 4. The operators $(\dot{})$ and $()'$ denote time and spatial derivatives of a quantity, respectively. The area moment of inertia of the beam, I , is defined as $I = \int_A \tilde{k}^2 dA$, where \tilde{k} is the vertical distance from the beam's neutral axis. The variables c_1 and F_{ex} represent the damping coefficient and external distributed force per unit length, respectively. The vertical displacement, v_f , is the displacement occurring due to the release of “frozen” strains, ε_{st} (Eq. 2 of chapter 4). A detailed derivation of these equations is given in Ref. [22].

5.2.2.1. Loading and cooling stages for SMPs immersed in fluid domain

For the loading stage, SMP is heated above the transition temperature upto T_h , such that the complete polymer transitions into the amorphous stage. A static point force, F_y , at $s = l_c$ is applied in the Y direction to deform the cantilever as shown in Fig. 5.1. Using Eq. 2 to express displacement $v(s,t)$ in terms of angle of the perpendicular to the cross-section of the beam with

the horizontal axis X , $\chi(s,t)$, ignoring all time derivative terms due to static deformation, and in the absence of frozen strains, Eq. 3 transforms to

$$E_m I \chi''(s) + F_y \cos[\chi(s)] = 0 \quad (4)$$

with $\chi(0) = 0$ and $\chi'(l_c) = 0$. In Eq. 4, E_m is the Young's modulus in the amorphous phase at T_h . Equation 4 is solved using homotopy analysis method [45] to obtain an analytical expression for strains at the end of loading stage, denoted by ε_a .

In the cooling stage, the polymer is cooled to a temperature below T_G such that the entire polymer becomes stiff and transforms into glassy phase. The cooling is performed while maintaining the external forces on the polymer.

5.2.2.2. Fixation and shape recovery stages for SMPs immersed in fluid domain

After cooling, all the strains induced by the external forcing are stored in the polymer due to freezing of the molecular chains in the glassy phase. To further analyze the dynamic motion of the cantilever beam, modal analysis along with Galerkin's weighted residual method is applied to obtain the equations of motion in reduced order.

Modal analysis

Modal analysis is used to derive the mode shapes and orthogonality conditions of the system [43]. Accordingly, Eq. 3 is reduced to linear, undamped and unforced system and is expressed as

$$EIv'''' + \rho_s A \ddot{v} = 0 \quad (5)$$

with boundary conditions

$$v(s,t)|_{s=0} = v'(s,t)|_{s=0} = v''(s,t)|_{s=l_c} = v'''(s,t)|_{s=l_c} = 0 \quad (6)$$

Eq. 5 can be decomposed into ordinary differential equations by expressing $v(s,t)$ as a product of spatial and temporal functions as

$$v(s,t) = \widehat{\varphi}(s)\overline{\eta}(t) \quad (7)$$

Rearranging Eq. 5 using Eq. 7 and using ω_n as the natural frequency, we obtain

$$-\frac{\ddot{\overline{\eta}}}{\overline{\eta}} = \frac{c^2 \widehat{\varphi}''''}{\widehat{\varphi}} = \omega_n^2 \quad (8)$$

where $c^2 = \frac{EI}{\rho_s A}$. Using $\beta^4 = \frac{\omega_n^2}{c^2}$, Eq. 8 can be written in two forms

$$\ddot{\overline{\eta}} + \omega_n^2 \overline{\eta} = 0 \quad (9)$$

$$\widehat{\varphi}'''' - \beta^4 \widehat{\varphi} = 0 \quad (10)$$

$$\text{with } \widehat{\varphi}(s)|_{s=0} = \widehat{\varphi}'(s)|_{s=0} = \widehat{\varphi}''(s)|_{s=l_c} = \widehat{\varphi}'''(s)|_{s=l_c} = 0 \quad (11)$$

The general solution of Eq. 9 is

$$\begin{aligned} \overline{\eta}(t) = & C_1 (\cos(\beta s) + \cosh(\beta s)) + C_2 (\cos(\beta s) - \cosh(\beta s)) + C_3 (\sin(\beta s) + \sinh(\beta s)) \\ & + C_4 (\sin(\beta s) - \sinh(\beta s)) \end{aligned} \quad (12)$$

Using Eq. 12 along with the boundary conditions (Eq. 11) gives a system of equations in the unknowns C_2 and C_4 . For a nontrivial solution of these two unknowns, the determinant of the system should be zero. This gives the characteristic equation

$$\cos(\beta l_c) \cosh(\beta l_c) + 1 = 0 \quad (13)$$

Eq. 13 has infinite number of solutions and thus infinite number of modes. The n th mode shape is expressed as

$$\widehat{\varphi}_n(s) = C_2 \left((\cos(\beta_n s) - \cosh(\beta_n s)) - \frac{\cos(\beta_n l_c) + \cosh(\beta_n l_c)}{\sin(\beta_n l_c) + \sinh(\beta_n l_c)} (\sin(\beta_n s) - \sinh(\beta_n s)) \right) \quad (14)$$

For two distinct modes, i and j , the orthogonality conditions are

$$\rho_s A \int_0^{l_c} \widehat{\varphi}_i(s) \widehat{\varphi}_j(s) ds = \delta_{ij}^* \quad (15)$$

$$EI \int_0^l \widehat{\varphi}_i''(s) \widehat{\varphi}_j''(s) ds = \omega_{n,i}^2 \delta_{ij}^* \quad (16)$$

where $\delta^*(.)$ is the Kronecker delta operator. The natural frequency associated with i th mode is

given as $\omega_{n,i} = \beta_i^2 \sqrt{\frac{EI}{\rho_s A}}$. In this system of a vibrating beam, the transverse displacement is a

sum of infinite number of modes, and thus, Eq. 7 becomes

$$v(s, t) = \sum_{n=1}^{\infty} \widehat{\varphi}_i(s) \bar{\eta}_i(t) \quad (17)$$

where $\widehat{\varphi}_i(s)$ represents mode shape associated with i th natural frequency, $\widehat{\eta}_i(t)$ is the i th modal coordinate. For this study, we consider finite number of modes upto M for analysis.

Discretized Non-linear Equation of Motion

Using Eq. 17 with limited number of modes, Eq. 3 is expressed as

$$\begin{aligned} & \rho_s A \left(\sum_{i,j,k=1}^M \left(\frac{\widehat{\varphi}_i' \bar{\eta}_i}{2} \int_0^s \int_0^{\xi} \widehat{\varphi}_j' \widehat{\varphi}_k' \frac{\partial^2 (\bar{\eta}_j \bar{\eta}_k)}{\partial t^2} d\xi ds \right)' - \sum_{i=1}^M \widehat{\varphi}_i \ddot{\eta}_i \right) - EI \sum_{i=1}^M \widehat{\varphi}_i'''' \bar{\eta}_i + EI v_f''''(s,t) \\ & - EI \sum_{i,j,k=1}^M \bar{\eta}_i \bar{\eta}_j \bar{\eta}_k \left(\widehat{\varphi}_i' \left(\widehat{\varphi}_j' \widehat{\varphi}_k'' \right)' \right)' - c_1 \sum_{i=1}^M \widehat{\varphi}_i \dot{\eta}_i - F_{ex} + EI \left(v_f'(s,t) \left(v_f'(s,t) v_f''(s,t) \right)' \right)' = 0 \end{aligned} \quad (18)$$

In order to minimize the error due to consideration of only M modes, Galerkin's weighted residual method is used [43]. Since the base functions i.e. mode shapes are orthogonal, orthogonality conditions are used. The weight functions are set as mode shapes to make the residue orthogonal to the weight functions. The weighted integral of residue can be then set to zero to find modal coordinates. Therefore, Eq. 18 is multiplied with a mode shape $\widehat{\phi}_n(s)$ and integrated over the length of the beam to derive the governing equation of modal coordinates. Considering only one mode, $M = 1$ and using orthogonality conditions, Eq. 18 becomes

$$\begin{aligned}
& \rho_s A \bar{\eta}_1 \left(\bar{\eta}_1 \ddot{\eta}_1 + \dot{\eta}_1^2 \right) \int_0^{l_c} \bar{\varphi}_1^2 \left(\int_s^{l_c} \int_0^s \bar{\varphi}_1'^2 d\lambda dg \right) ds + \ddot{\eta}_1 + \bar{\eta}_1 \omega_{n,1}^2 \\
& + EI \bar{\eta}_1^3 \int_0^{l_c} \left(\bar{\varphi}_1^2 \right)' \bar{\varphi}_1' \bar{\varphi}'' ds + c_1 \dot{\eta}_1 \int_0^{l_c} \bar{\varphi}_1^2 ds + \int_0^{l_c} F_{ex} \bar{\varphi}_1(s) ds - EI \int_0^{l_c} \bar{\varphi}'' v_f'' ds \\
& - EI \int_0^{l_c} \left(\bar{\varphi}_1' v_f'(s,t) \right)' v_f'(s,t) v_f''(s,t) ds - EI \bar{\eta}_1 \left| \bar{\varphi}_1 \bar{\varphi}_1''' \right|_{s=l_c} + EI \bar{\eta}_1 \left| \bar{\varphi}_1' \bar{\varphi}_1'' \right|_{s=l_c} - EI \bar{\eta}_1^3 \left| \bar{\varphi}_1 \bar{\varphi}_1'^2 \bar{\varphi}_1''' \right|_{s=l_c} \\
& - EI \bar{\eta}_1^3 \left| \bar{\varphi}_1 \bar{\varphi}_1' \bar{\varphi}_1''^2 \right|_{s=l_c} + EI \bar{\eta}_1^3 \left| \bar{\varphi}_1'' \bar{\varphi}_1'^3 \right|_{s=l_c} + EI \left| \bar{\varphi}_1 v_f'(s,t) v_f''(s,t)^2 \right|_{s=l_c} + EI \left| \bar{\varphi}_1 v_f'(s,t)^2 v_f'''(s,t) \right|_{s=l_c} \\
& - EI \left| \bar{\varphi}_1 v_f'(s,t)^2 v_f''(s,t) \right|_{s=l_c} + EI \left| \bar{\varphi}_1 v_f'''(s,t) \right|_{s=l_c} - EI \left| \bar{\varphi}_1' v_f''(s,t) \right|_{s=l_c} = 0
\end{aligned} \tag{19}$$

Using η and φ for η_1 and φ_1 respectively for convenience of notation and discretizing shear boundary conditions using Eq. 17 for only $M = 1$, the governing equation of motion, Eq. 19, becomes

$$\ddot{\eta} + \bar{\eta} \omega_n^2 + \xi \bar{\eta} \left(\bar{\eta} \ddot{\eta} + \dot{\eta}^2 \right) - \zeta \bar{\eta}^3 + 2\mu \dot{\eta} + \tilde{F} = 0 \tag{20}$$

$$\text{where} \quad \xi = \rho_s A \int_0^{l_c} \bar{\varphi}^2 \left(\int_s^{l_c} \int_0^s \bar{\varphi}'^2 d\lambda dg \right) ds, \quad \zeta = EI \int_0^{l_c} \bar{\varphi}'^2 \left(\bar{\varphi}' \bar{\varphi}'' \right)' ds, \quad \mu = \frac{c_1}{2} \int_0^{l_c} \bar{\varphi}^2 ds \quad \text{and}$$

$$\tilde{F} = \int_0^{l_c} F_{ex} \bar{\varphi}_1(s) ds - EI \int_0^{l_c} \bar{\varphi}'' v_f'' ds - EI \int_0^{l_c} \left(\bar{\varphi}_1' v_f'(s,t) \right)' v_f' v_f'' ds.$$

Fixation

In this stage after cooling, the external forces are removed and the deformed shape remains fixed due to freezing of internal molecular chains. Thus, the beam is in a static position with all the frozen strains stored. The total strains in Eq. 2 of chapter 4 become equal to strains applied,

$\varepsilon_t = \varepsilon_a$. Substituting this expression in Eq. 2 of chapter 4, the corresponding displacement due to frozen strains, v_f are obtained. Consequently, Eq. 20 reduces to

$$\bar{\eta}\omega_n^2 - \zeta\bar{\eta}^3 + \hat{F}\Big|_{t=0} = 0 \quad (21)$$

where $\hat{F}\Big|_{t=0} = -EI \int_0^{l_c} \hat{\phi}'' v_f''(s,0) ds - EI \int_0^{l_c} (\hat{\phi}' v_f'(s,0))' v_f'(s,0) v_f''(s,0) ds$.

Shape recovery

During this stage, the frozen strains are released as a function of temperature rise due to the ultrasound exposure, in the absence of external forcing. As a result of heating, glassy phase transforms to amorphous phase and the polymer returns to its straight (parallel to X axis) shape.

The equation of motion for in-vacuo shape recovery is given as

$$\ddot{\bar{\eta}} + \bar{\eta}\omega_n^2 + \xi\bar{\eta}(\bar{\eta}\ddot{\bar{\eta}} + \dot{\bar{\eta}}^2) - \zeta\bar{\eta}^3 + 2\mu\dot{\bar{\eta}} + \hat{F} = 0 \quad (22)$$

5.2.3. Fluid-loading effects on shape recovery

Morison *et al.* [34] investigated the hydrodynamic loading effects on an oscillating structure where the fluid load per unit length, H_l , is expressed in the form a semi-empirical relation [34, 36]

$$H_l = \frac{\pi}{4} \rho w_c^2 h_m \frac{\partial^2 v(s,t)}{\partial t^2} + \frac{1}{2} \rho w_c h_d \frac{\partial v(s,t)}{\partial t} \left| \frac{\partial v(s,t)}{\partial t} \right| \quad (23)$$

where ρ is the density of water. The variables h_m and h_d are inertial and drag coefficients, respectively. These coefficients depend on the geometry of the beam and are experimentally determined. Using Eq. 17, applying Galerkin's weighted residual method, and considering only one mode, Eq. 22 modifies to

$$(1 + \hat{h}_m)\ddot{\bar{\eta}} + \bar{\eta}\omega_n^2 + \xi\bar{\eta}(\ddot{\bar{\eta}} + \dot{\bar{\eta}}^2) - \zeta\bar{\eta}^3 + (2\mu + \hat{h}_d|\dot{\bar{\eta}}|)\dot{\bar{\eta}} + \hat{F} = 0 \quad (24)$$

where $\hat{h}_m = \frac{\pi}{4}\rho w_c^2 h_m \int_0^{l_c} \bar{\varphi}^2 ds$ and $\hat{h}_d = \frac{1}{2}\rho w_c h_d \int_0^{l_c} \bar{\varphi}^2 |\dot{\bar{\varphi}}| ds$ for underwater shape recovery.

5.3. Experimental results and discussion

Experiments are conducted to examine the effects of the dense fluid medium environment on the shape recovery behavior of a SMP filament under FU exposure. A 63 mm long, 3.8 mm wide, and 1.5 mm thick polymer filament composed of polyurethane is obtained from the company Medshape, with a $T_G \cong 60^\circ\text{C}$. The original straight beam shape is deformed into a V-shape by heating the polymer under a heat gun. After cooling and shape fixation, the polymer is exposed to ultrasound using the experimental setup given in Fig. 3 of Ref [12]. The experimental setup consists of a $61.5 \times 31.8 \times 32.5 \text{ cm}^3$ water tank containing deionized water and lined with Aptflex F28 absorber sheets to avoid reflections from the tank walls. A H-104-4A SONIC Concepts high intensity focused ultrasound (HIFU) transducer is kept at the bottom of the tank. The polymer filament is suspended in the tank using a positioning system, Fig. 5.2. This figure shows two experimental setups where the polymer is suspended in-air, Fig. 5.2a and underwater, Fig. 5.2b. In air, the polymer is suspended such that the focal point always lies in the submerged

portion of the polymer filament. The polymer is exposed to 20 seconds of ultrasound with additional 10-20 seconds to enable cool down, for both setups. Fig. 5.2c shows a significant change in the angle of the free arm of the polymer due to thermally induced shape recovery in air as compared to water, during FU actuation. Figure 5.3 shows the corresponding vertical and horizontal displacements of the tip of the free polymer arm, emphasizing that the shape recovery is much higher in air as compared to water. All the displacements are measured relative to the initial position, i marked in Fig. 5.2. Two possible reasons to account for the difference in shape memory behavior in the two mediums are, first, the fluid loading effects which provide additional damping to the system, and second, faster thermal cooling due to surrounding water as compared to air. These reasons are investigated in detail in following sections to justify this difference.

5.3.1. Investigation of fluid loading on shape recovery

To segregate the influence of fluid loading effects from thermal cooling on shape recovery, the multiphysics model developed by Bhargava *et al.* [22] is used. The model has been shown to predict the acoustic pressure field, temperature rise of polymer, and estimate motion for different stages of the shape recovery process in good agreement with experimental results for an Euler-Bernoulli cantilever beam suspended in air. In this study, the model is modified by incorporating the hydrodynamic loading function (Morison's formulae) in the equation for shape recovery stage during underwater FU actuation, section 2.2.3. The modified model is used to predict the shape recovery of a 25 mm long, 3 mm wide, and 1.5 mm thick SMP filament with similar properties as specified in Ref. [22].

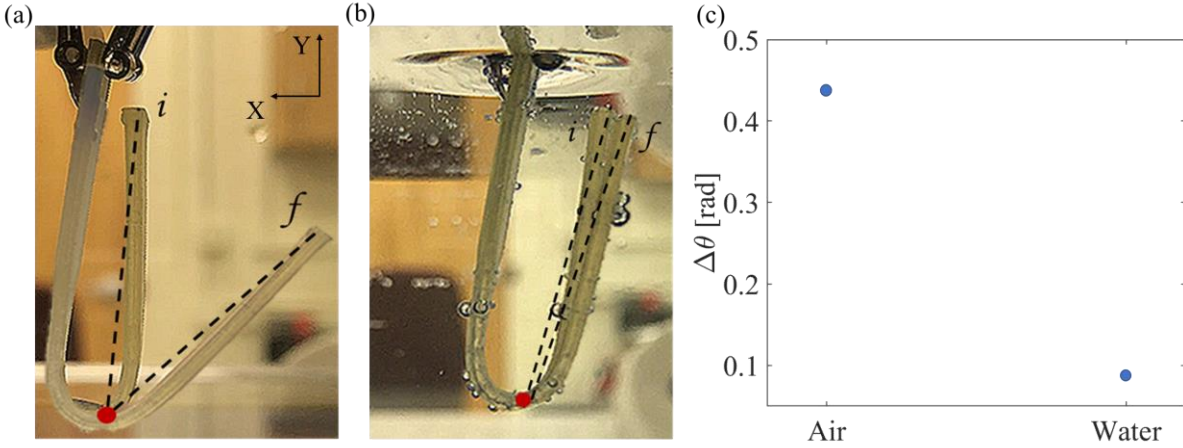


Fig. 5.2. Experimental setup with a V-shaped SMP filament suspended in (a) air and (b) water with the help of a positioning system. The letters i and f denote the initial and final position of the polymer arm at the start and end of ultrasound exposure, respectively. The red dot denotes the origin which is connected with the tip of the polymer arm through dotted lines. (c) Change in the angle of the dotted line as the polymer recovers from initial temporary shape to final shape, under ultrasound exposure.

The pressure and thermal fields due to HIFU transducer operation at 10W power and 0.5 MHz for 20 seconds are considered for estimating shape recovery, similar to the acoustic-thermal fields specified in the previous study [22]. The inertial and drag coefficients in Eq. 24 are taken as $\hat{h}_m = 1$ and $\hat{h}_d = 22$, based on the filament geometry, and experimental observations of Shahab *et al.* [36] Figure 5.4a shows the final position of the cantilever beam after FU-induced shape recovery for air and underwater, calculated from Eqs. 22 and 24, respectively. It is seen that the angle recovered and thus, the final position of the beam is identical in air and underwater. This behavior is contrary to the shape recovery behavior observed in experiments for a slightly different geometry of the beam as compared to one used in the theoretical model. Experimental observations show that the vertical displacement of the tip of the free polymer arm is

significantly high in air as compared to polymer immersed in water. Figure 5.4b further shows how each term in Eq. 24 varies with time and consequently affect the shape recovery. The shape recovery only initiates after the temperature is above T_G in significant portion of the polymer, i.e. after 7 seconds in this case. It is observed from Fig. 5.4b that the added damping term is negligible in magnitude (two orders lower) as compared to the structural damping term. Since the added damping affects the beam vibration amplitude in different fluids, a small magnitude means that added damping does not play a role in shape recovery of the SMP. Consequently, the fluid loading effects are not the cause of the difference in shape memory behavior in the two mediums.

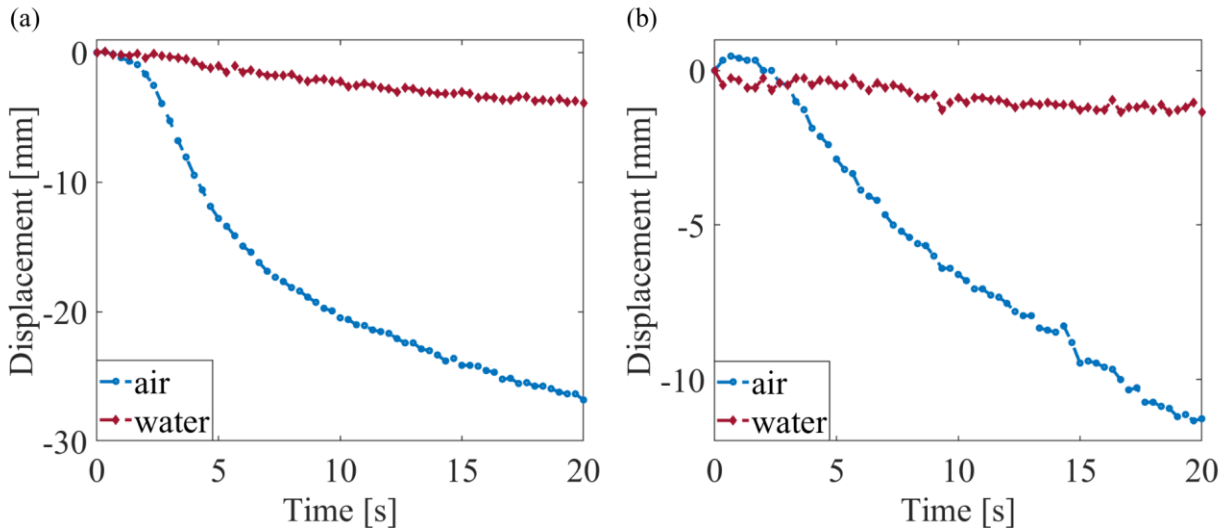


Fig. 5.3. Displacement of the tip of the free polymer arm in (a) Y axis and (b) X axis during shape recovery under FU exposure in air and underwater experiments, Fig. 5.2.

The predictions of the theoretical model are further verified with finite element simulations. The simulations analyze the deflection of the SMP cantilever beam subjected to constant end point force. The magnitude of the force is such that the vertical deflection of $s = L$ end obtained after

20 seconds is similar to the vertical tip displacement of the free arm of the polymer filament in experiments in air, Fig. 5.3a. It is postulated that if fluid loading effects particularly the added damping effects were significant, the same point force on the beam would produce a different amount of displacement in water as compared to air. Figure 5.5 shows the simulation results for vertical and horizontal displacement of the cantilever tip in air and underwater. It is seen that the tip undergoes same amount of deflection under equal amount of force in two different fluid mediums. This behavior is similar to the predictions of the theoretical model, where stored or frozen energy provide external forcing. Aureli *et al.* [28] demonstrated that added damping effects arise from convection and vortex shedding effects at large amplitude vibration and oscillation frequency. While in this study, the deflection amplitude of the beam is high, the average velocity of the beam bending is small (<0.3 mm/s) for both air and water, as calculated from finite element simulations and the theoretical model in section 2.2.3. Thus, the added damping effect which is proportional to the square of the velocity of the cantilever beam (Eq. 24), is negligible and does not affect the shape recovery behavior in water. From the mathematical model and finite element simulations predictions, it can be inferred that out of the two possible reasons for the significant difference in shape recovery behavior in the two fluid mediums observed in experiments, fluid loading effects play a negligible role. The following section analyzes the role of thermal cooling on SMP shape recovery behavior.

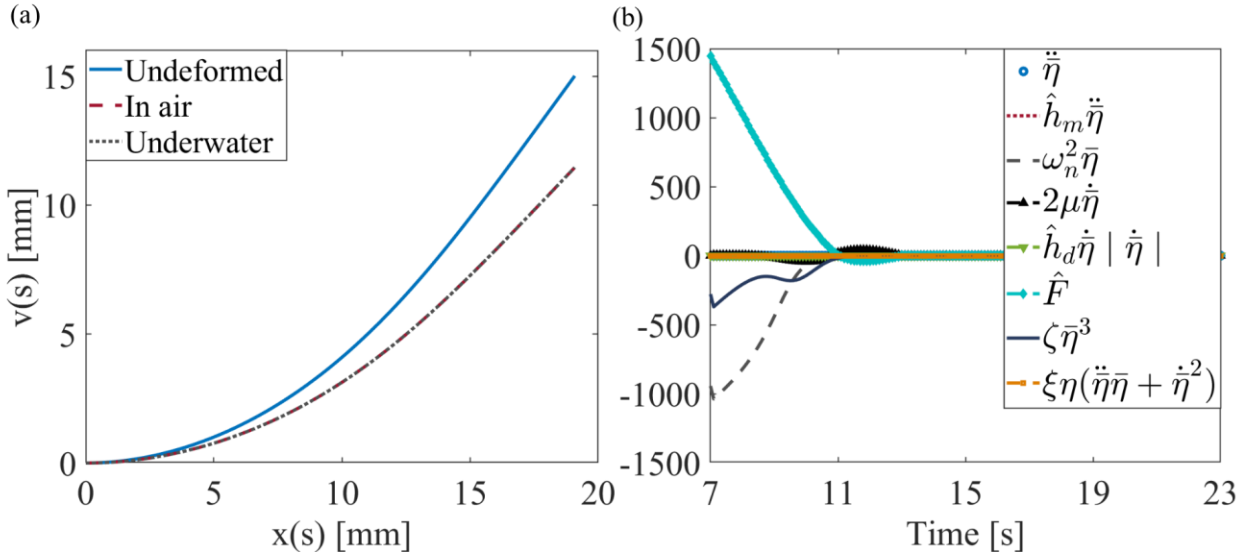


Fig. 5.4. (a) Shape recovery behavior of a SMP Euler-Bernoulli cantilever beam calculated using Eqs. 22 and 24 for air and underwater experiments, respectively. The variable $x(s)$ represents the distance in the X coordinate, Fig. 5.1. (b) Variation of each term in Eq. 24 with time after the onset of shape recovery at 7 seconds.

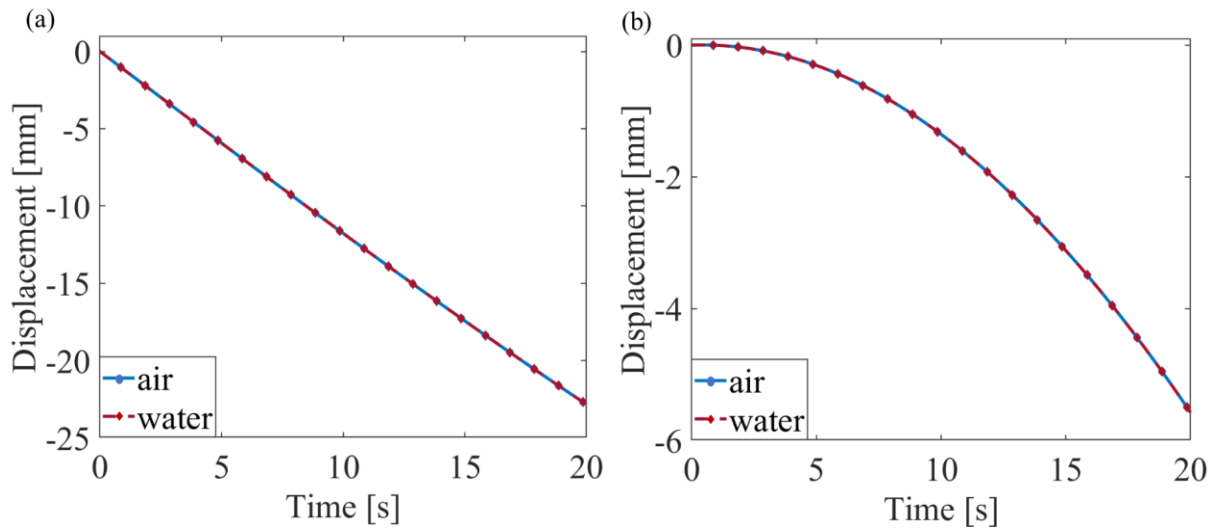


Fig. 5.5. Finite element predictions of the displacement of the free tip of the SMP cantilever beam in (a) vertical Y axis and (b) horizontal X axis, due to constant end point force in air and underwater.

5.3.2. Thermal cooling effect on shape recovery

With the understanding of negligible role of fluid-loading effects on shape memory behavior in different fluid mediums, thermal cooling due to surrounding medium is investigated. Finite element simulations are performed for the SMP filament exposed to HIFU for 20 seconds at 0.5 MHz and 10W of source power, using COMSOL Multiphysics. The simulation setup is divided into two domains for simulating in-air shape recovery behavior. The interface of the two domains lies approximately at the top surface of the polymer filament. The polymer is kept at the focal point of the HIFU transducer. The bottom domain closer to the HIFU source is water, while the upper domain is air. For underwater shape recovery behavior simulation, both domains have water as the wave propagation medium. Figure 5.6 shows pressure fields for the two simulation setups. It is seen that due to mismatch in the acoustic impedance of air and water, almost all the pressure waves are reflected in air-water domain simulation, Fig. 5.6a. Whereas in a complete water domain, only the reflection due to SMP filament in the focal region exists, Fig. 5.6b. The reflected waves are out-of-phase, while the transmitted waves are in-phase with the incident pressure waves [46]. Thus, the pressure field in the bottom water domain lowers in magnitude due to the superposition of incident and reflected waves. The amount of lowering is higher in air-water simulation as the number of reflected waves due to impedance mismatch is higher, Fig. 5.6a, as compared to underwater simulation, Fig. 5.6b. Since, the amplitude of the pressure field is proportional to the temperature in the SMP filament, Eq. 10 of chapter 2, the SMP in air-water setup, Fig. 5.6a, should experience a lower thermal heating as compared to complete water setup. Figs. 5.7a and 5.7b show the heat generated inside the polymer due to absorption of ultrasound

pressure waves and corresponding temperature rise for the two simulation setups, respectively. As expected, the heat deposition with SMP exposed to air-water interface is significantly lower than SMP placed in complete water domain, due to reduced pressure field from reflected pressure waves. Thus, the temperature rise is lower for the former as compared to the latter case. According to the expression of frozen fraction ϕ_s in section 2.1, a high temperature field leads to lower volume fraction of the polymer in glassy phase, producing more thermal stresses and a higher shape recovery response, Eqs. 1 and 2 of chapter 4.

However, the shape recovery response in a complete water domain experiment is lower as compared to the case when SMP is exposed to air, Fig. 5.2, in spite of having a higher temperature rise in the former setup, Fig. 5.7b. A possible explanation of this contrary behavior can be given by looking at the observations made by Yu *et al.* in section 4.3 (Fig. 5.7) of Ref. [47]. The authors looked at the role of heating rate, i.e. the rate of temperature rise with time, on the shape recovery response. Their study showed that by increasing the heating rate, the temperature needed for achieving the same amount of shape recovery response increases. The authors explained this behavior in terms of a unified parameter known as reduced time that depends on internal stress conditions of different molecular chains. This parameter determines the shape fixation and recovery response of SMPs. A higher heating rate reduces the recovery reduced time and thus, decreases the shape recovery response of the SMP. An alternative way of explaining the consequence of variation in heating rate. A gradual heating rate allows the thermal field to spread more uniformly with sufficient time to undergo a phase change from glassy to amorphous phase in a larger volume of polymer filament. On the contrary, a higher heating rate

allows the transformation in a smaller section of the polymer due to limited time. Thus, although the temperature field in the SMP in a complete water domain is high, it requires more time to recover the same amount as the polymer exposed to air, due to the difference in heating rates. Similarly, if the actuation time and input power are same, the former will show lesser shape recovery as compared to the latter case. However, if the input power is manipulated such that the temperature field inside the complete water domain setup follows the same trend as the field inside polymer exposed to air, one may observe same amount of shape recovery for the two setups.

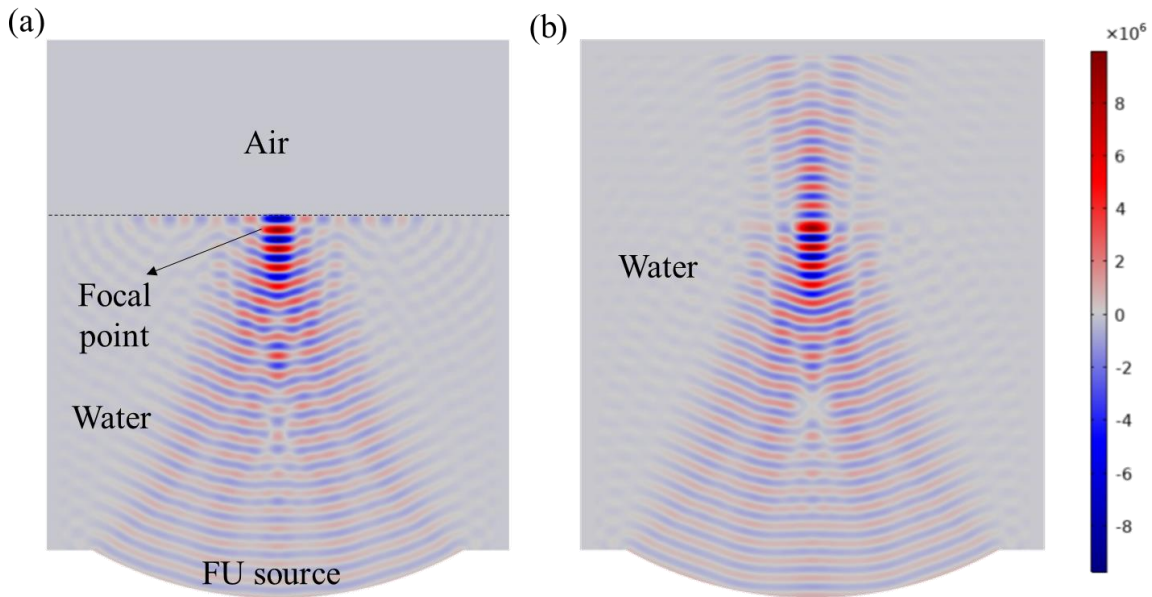


Fig. 5.6. (a) Finite element simulations showing the pressure field in setup where (a) SMP is exposed to both air and water mediums such that the top surface of polymer filament (farther from FU source) lies at the air-water interface. This situation is similar to the surrounding environment for the bent area of the V-shape filament in Fig. 5.2a, and (b) where SMP filament is immersed in a complete water domain. In both scenarios, the SMP is placed such that the focal point lies inside the polymer thickness. The color bar on the right side tells the magnitude of the total acoustic pressure.

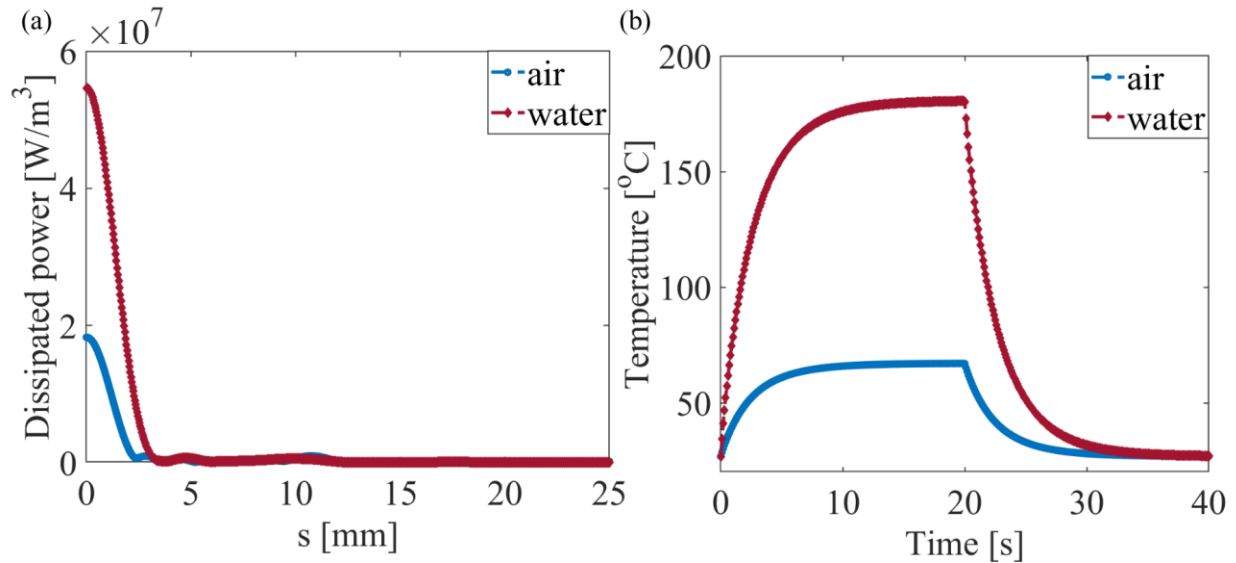


Fig. 5.7. (a) Dissipated acoustic power acting as the heat source and (b) corresponding temperature rise in the SMP for the two simulation setups, where the polymer top surface is exposed to air in one setup and to water in the second, Fig. 5.6.

5.4. Conclusions

This study investigates the shape recovery response of SMPs due to ultrasound exposure in underwater applications. The need for investigating the hydrodynamic loading on shape memory behavior arises from the widespread use of SMPs in dense fluid mediums, including biomedical and robotic applications. Our previously built experimentally-validated mathematical model is extended in this chapter to include the fluid loading effects on the deformation of an Euler-Bernoulli cantilever beam, using Morison's equation. The multiphysics framework is divided into three interconnected stages. The first stage uses KZK equation to predict the pressure field inside the polymer filament. The second stage uses this pressure field as a heating source to

estimate the temperature rise of the polymer, using Pennes's Bioheat equation. The third stage uses this thermal field to estimate the phase transformation of SMPs and consequent thermal stresses that initiate shape recovery. The governing equations for the shape recovery stage are derived using the previous framework that is modified to include hydrodynamic loading. Experiments conducted to investigate the shape recovery response when SMP is exposed to two different fluid mediums, air and water, show that shape recovery is less in water as compared to air for same duration and intensity of ultrasound exposure. The difference in the shape memory behavior is attributed to two possible reasons, fluid loading and thermal cooling in water. The fluid loading effects are first examined using the theoretical model and finite element simulations. It is seen that due to the slow rate of shape recovery i.e. low velocity of beam motion, the velocity dependent fluid damping effects are negligible and thus cannot account for the difference in shape recovery between water and air. Investigation of the FU induced thermal effects show that the temperature rise in the SMPs exposed to air is slower and lower in magnitude as compared to SMPs completely immersed in water. This is due to the higher reflection of pressure waves due to impedance mismatch at the air-water interface, leading to lower total pressure fields inside SMPs exposed to air. Due to the low rate of temperature rise in SMPs, the heating rate is low which allows the temperature field to spread more uniformly giving sufficient time to the molecular chains to undergo phase transformation. Thus, the shape recovery of SMPs in air is higher as compared to SMPs in water, as seen in the experiments. This study opens the door for understanding the fluid loading and thermal effects of shape memory behavior in different fluid mediums, thus, providing fundamental insights into building more complex systems.

References

1. X. Chen, M. A. Dam, K. Ono, A. Mal, H. Shen, S. R. Nutt, K. Sheran and F. Wudl, *Science* **295** (5560), 1698 (2002).
2. C. e. Yuan, M. Z. Rong, M. Q. Zhang, Z. P. Zhang and Y. C. Yuan, *Chemistry of Materials* **23** (22), 5076-5081 (2011).
3. K. E. Uhrich, S. M. Cannizzaro, R. S. Langer and K. M. Shakesheff, *Chemical reviews* **99** (11), 3181-3198 (1999).
4. R. Bogue, *Assembly Automation* **32** (1), 3-7 (2012).
5. H. Meng and G. Li, *Polymer* **54** (9), 2199-2221 (2013).
6. C. Liu, H. Qin and P. Mather, *Journal of materials chemistry* **17** (16), 1543-1558 (2007).
7. S. S. Venkatraman, L. P. Tan, J. F. D. Joso, Y. C. F. Boey and X. Wang, *Biomaterials* **27** (8), 1573-1578 (2006).
8. W. M. Huang, Y. Zhao, C. C. Wang, Z. Ding, H. Purnawali, C. Tang and J. Zhang, *Journal of Polymer Research* **19** (9), 9952 (2012).
9. Y. Amamoto, H. Otsuka, A. Takahara and K. Matyjaszewski, *Advanced Materials* **24** (29), 3975-3980 (2012).
10. G. Barot, I. Rao and K. Rajagopal, *International Journal of Engineering Science* **46** (4), 325-351 (2008).
11. H. J. Qi, T. D. Nguyen, F. Castro, C. M. Yakacki and R. Shandas, *Journal of the Mechanics and Physics of Solids* **56** (5), 1730-1751 (2008).
12. A. Bhargava, K. Peng, J. Stieg, R. Mirzaeifar and S. Shahab, *RSC Advances* **7** (72), 45452-45469 (2017).
13. A. Lendlein, H. Jiang, O. Jünger and R. Langer, *Nature* **434** (7035), 879 (2005).
14. K. C. Hribar, R. B. Metter, J. L. Ifkovits, T. Troxler and J. A. Burdick, *Small* **5** (16), 1830-1834 (2009).
15. U. N. Kumar, K. Kratz, M. Heuchel, M. Behl and A. Lendlein, *Advanced Materials* **23** (36), 4157-4162 (2011).
16. K. Yu, Z. Zhang, Y. Liu and J. Leng, *Applied Physics Letters* **98** (7), 074102 (2011).

17. G. ter Haar and C. Coussios, *International journal of hyperthermia* **23** (2), 89-104 (2007).
18. J. Kost, K. Leong and R. Langer, *Proceedings of the National Academy of Sciences* **86** (20), 7663-7666 (1989).
19. B. G. De Geest, A. G. Skirtach, A. A. Mamedov, A. A. Antipov, N. A. Kotov, S. C. De Smedt and G. B. Sukhorukov, *Small* **3** (5), 804-808 (2007).
20. S. Ozeri and D. Shmilovitz, *Ultrasonics* **50** (6), 556-566 (2010).
21. S. Shahab and A. Erturk, *Smart Materials and Structures* **23** (12), 125032 (2014).
22. A. Bhargava and S. Shahab, *Smart Materials and Structures* **28** (5), 055002 (2019).
23. T. Sarpkaya, *Journal of Fluid Mechanics* **165**, 61-71 (1986).
24. J. E. Sader, *Journal of applied physics* **84** (1), 64-76 (1998).
25. H. Hosaka, K. Itao and S. Kuroda, *Sensors and Actuators A: Physical* **49** (1-2), 87-95 (1995).
26. M. Kimber, R. Lonergan and S. Garimella, *Journal of Fluids and Structures* **25** (8), 1334-1347 (2009).
27. Z. Chen, S. Shatara and X. Tan, *IEEE/ASME transactions on mechatronics* **15** (3), 448-459 (2009).
28. M. Aureli, M. Basaran and M. Porfiri, *Journal of sound and vibration* **331** (7), 1624-1654 (2012).
29. R. Gabbai and H. Benaroya, *Journal of Sound and Vibration* **282** (3-5), 575-616 (2005).
30. P. Bearman, M. Downie, J. Graham and E. Obasaju, *Journal of Fluid Mechanics* **154**, 337-356 (1985).
31. C. N. Phan, M. Aureli and M. Porfiri, *Journal of Fluids and Structures* **40**, 52-69 (2013).
32. G. Falcucci, M. Aureli, S. Ubertini and M. Porfiri, *Philosophical Transactions of the Royal Society A: Mathematical, Physical and Engineering Sciences* **369** (1945), 2456-2466 (2011).
33. V. Kopman and M. Porfiri, *IEEE/ASME Transactions on mechatronics* **18** (2), 471-483 (2012).
34. J. Morison, J. Johnson and S. Schaaf, *Journal of Petroleum Technology* **2** (05), 149-154 (1950).

35. J. Graham, *Journal of Fluid Mechanics* **97** (2), 331-346 (1980).
36. S. Shahab and A. Erturk, *Smart Materials and Structures* **25** (10), 105007 (2016).
37. A. Bhargava, K. Peng and S. Shahab, presented at the SPIE Smart Structures + Nondestructive Evaluation, 2019.
38. M. F. Hamilton and D. T. Blackstock, *Nonlinear Acoustics*. (Academic Press, 1998).
39. F. P. Curra, P. D. Mourad, V. A. Khokhlova, R. O. Cleveland and L. A. Crum, *IEEE transactions on ultrasonics, ferroelectrics, and frequency control* **47** (4), 1077-1089 (2000).
40. Y. Liu, K. Gall, M. L. Dunn, A. R. Greenberg and J. Diani, *International Journal of Plasticity* **22** (2), 279-313 (2006).
41. T. S. Hart and M. F. Hamilton, *The Journal of the Acoustical Society of America* **84** (4), 1488-1496 (1988).
42. M. S. Canney, M. R. Bailey, L. A. Crum, V. A. Khokhlova and O. A. Sapozhnikov, *The Journal of the Acoustical Society of America* **124** (4), 2406-2420 (2008).
43. S. S. Rao, *Vibration of Continuous Systems*. (Wiley, 2007).
44. A. H. Nayfeh and P. F. Pai, *Linear and Nonlinear Structural Mechanics*. (Wiley, 2008).
45. J. Wang, J.-K. Chen and S. Liao, *Journal of Computational and Applied Mathematics* **212** (2), 320-330 (2008).
46. L. E. Kinsler, A. R. Frey, A. B. Coppens and J. V. Sanders, *Fundamentals of Acoustics*, 4th Edition, by Lawrence E. Kinsler, Austin R. Frey, Alan B. Coppens, James V. Sanders, pp. 560. ISBN 0-471-84789-5. Wiley-VCH, December 1999., 560 (1999).
47. K. Yu and H. J. Qi, *Soft Matter* **10** (47), 9423-9432 (2014).

Chapter 6 : Contactless acoustic power transfer using high-intensity focused ultrasound

Details of publication

Co-authors: Shima Shahab

Citation: Bhargava, A. and Shahab, S., 2019, Contactless acoustic power transfer using high-intensity focused ultrasound (**submitted**)

Abstract

Contactless ultrasound power transfer (UPT) has emerged as one of the promising techniques for wireless power transfer due to several advantages over other known techniques. Physical processes supporting UPT include the vibrations at a transmitting/acoustic source element, piezoelectric transduction of elastic vibrations at a receiving element, acoustic wave propagation, and acoustic-structure interactions at the surfaces of the transmitting and receiving elements. In this chapter, a novel mechanism using a high-intensity focused ultrasound (HIFU) transmitter is proposed for enhanced power transfer in UPT systems. By focusing the transmitted energy in space, the HIFU strongly excites the receiver with dramatically reduced levels of energy input to the source, in comparison to the case of unfocused power transmission. The HIFU source is used for actuating a finite-size piezoelectric disk receiver. The underlying physics of the proposed system includes the coupling of the nonlinear acoustic field with structural responses of the receiver, which lead to spatial resonances and the appearance of higher harmonics during wave

propagation in a nonlinear dispersive medium. Acoustic nonlinearity due to wave kinematics in the HIFU-UPT system is modeled by taking into account the effects of diffraction, absorption, and nonlinearity in the medium. The experimentally-validated acoustic-structure interaction formulation is employed in a finite element based multiphysics model. The results show that the existence of the HIFU high-level excitation can cause disproportionately large responses in the piezoelectric receiver if the frequency components in the nonlinear acoustic field coincide with the resonant frequencies of the receiver. This research aims to give a comprehensive view of modeling and to serve as a basis for designing UPT systems where piezoelectric disks of finite aspect ratios are operating in a nonlinear acoustic field.

6.1. Introduction

Ultrasound power transfer (UPT) has emerged as one of the more promising of all the other practiced techniques, namely inductive, capacitive, and microwave-based techniques, to wirelessly transfer power [1]. The underlying mechanism of UPT involves vibration-induced acoustic wave propagation from a piezoelectric transmitter to generate an elastic vibration-induced electrical response in a piezoelectric receiving element. The preference for UPT over other methods is due to shorter wavelengths enabling the use of smaller sized receiver/transmitter, lower attenuation, higher penetration depth, no electromagnetic interference/losses, high directionality, and biological safety [1-4]. In recent years, UPT has found increasing applications in biomedical technology [5-8], data delivery [9, 10], and through-wall transmission [11-13]. Recent studies have explored the use of UPT to supply low electrical power (e.g. $1\mu\text{W} - 10\text{mW}$ [14-16]) to biomedical implants in order to eliminate battery

replacement issues and reduce the risks/maintenance costs for devices in inaccessible areas. For example, Cochran *et al.* [8] excited piezoelectric elements embedded in a fixation plate to provide current to electrodes placed at fracture sites to promote bone healing. Shi *et al.* [17] developed a MEMS-based piezoelectric ultrasonic energy harvester (PUEH) to power implants inside the body. By adjusting the frequency of the PUEH, they aimed to minimize the standing wave effect which can reduce the efficiency of the UPT system. Ozeri *et al.* [6, 7] demonstrated ultrasonic transcutaneous energy transfer from plane disc transducers to power implants in a pig muscle tissue up to 50 mm depth. Coupling of the low-power receivers with UPT and backscatter communication has also been used as a tool to build reliable neural recording systems [18].

In UPT, the power transfer efficiency is sensitive to the orientation of the receiver [19], depth of the transducer [20, 21], and acoustical scattering from the receiver [22]. Various concepts can be considered for UPT, as summarized by Shahab *et al.* [21]. These concepts include excitation of an array of receivers by a spherical source in the same domain [23], excitation of a receiver in a separate domain (e.g., as in transcutaneous UPT [6]), and enhanced power transfer by focusing of the source transmitted energy using high-intensity focused ultrasound (HIFU) transducer. The focusing of acoustic waves can also be achieved using passive acoustic holograms (lenses) to generate a multifocal pressure pattern [24, 25]. In this work, for the first time, a HIFU source is used for actuating a finite-size piezoelectric disk, i.e., the diameter-to-thickness ratio is higher than 0.1 and less than 20, in a UPT system.

HIFU has been used in the biomedical field for several years in various applications, such as drug delivery, therapeutic applications, and neurostimulation of muscles [26-30]. The two main

advantages which support the usage of HIFU in UPT are: (1) its capability of focusing acoustic energy in a tight spot resulting in a localized, selective and controlled actuation; and (2) the increased pressure obtained at the focal spot as compared to spherical or planar waves, thus increasing the efficiency of the system [31]. Consequently, the use of HIFU in UPT systems will enable a significant increase in power transfer efficiency as well as target the energy transfer to the desired receiver. The localization ability of HIFU also provides flexibility to use small-sized receivers for UPT applications. This energy concentration ability is particularly required in the powering of devices placed in sensitive environments where the thermal effects associated with ultrasound are undesirable in the surrounding areas, such as the wireless powering of small-size implants in bodies or neural dust motes in the brain [18]. Our previous work of actuating polymer-based drug delivery containers inside the body, also demonstrates that the use of HIFU can achieve targeted response by localizing the thermal effect inside the polymers while maintaining the thermal intensity in surrounding tissues below the FDA prescribed levels [32, 33].

The limited existing models on UPT cannot be applied to predict acoustic pressure fields from HIFU, as they do not model focusing of waves and its associated effects on the HIFU-UPT system. Moreover, detailed and systematic investigations on understanding the physics of each of the individual entities involved in UPT are limited and assume linear acoustic wave propagation [34]. Shahab *et al.* [23] proposed a multiphysics model to demonstrate energy transfer from a spherical acoustic source to a piezoelectric disk in fixed-free boundary conditions. The linear model was validated with finite element (FE) simulations and later experimentally validated for

free-free boundary conditions [21]. Ozeri *et al.* [6] also used a linear acoustic model to estimate the power transfer through acoustic waves propagating from planar transducers, and traveling in tissue at 673 kHz to actuate a piezoelectric disk. While most of the works in UPT have studied the acoustic-electroelastic behavior of piezoelectric disks in the linear range, the assumptions of the linear model fail to hold when acoustic nonlinearities, and/or piezoelectric geometric and material nonlinearities are triggered. Operating with focused sources at practical high acoustic intensities (such as in HIFU), high acoustic frequencies or in mediums having a high coefficient of nonlinearity such as tissues, makes the propagating acoustic waves nonlinear. On the other hand, piezoelectric geometric and material nonlinearities become dominant under large strains. In such cases, it becomes necessary to account for acoustic and structural nonlinearities for accurate predictions of the receiver responses. This work focuses on acoustic nonlinearities by taking into account the effects of diffraction, absorption, and nonlinearity in the medium on the propagating waves. To model acoustic nonlinearities from a focusing source, Khokhlov-Zabolotskaya-Kuznetsov (KZK) equation is used [35]. The equation is based on parabolic approximation and is applicable for directional sound beams and focused transducers with limited aperture angles [36, 37]. This equation models forward wave propagation and accounts for nonlinear wave distortion in a direction normal to the propagation plane.

Another limitation of the current UPT modeling efforts arises due to the finite aspect ratio (diameter-to-thickness ratio) of the receiver/transmitter disks. Studies have reported that the assumption of piston-like vibration mode where the disk vibrates only in the thickness direction, does not hold for disks with aspect ratios between 0.1-20 [38]. This is primarily due to the

motion of the disks occurring both in radial and thickness directions, as compared to the conventional assumption of only thickness direction motion. Thus, the derivation of a closed-form solution for a finite-size piezoelectric disk acting as a transmitter or a receiver becomes very complicated. Various works have used different approaches based on elasticity theory, plate theory, and numerical methods to study the structural response of transmitter disks under electrical excitation [38-40]. However, these modeling efforts remain limited for disks acting as receivers in an acoustic field. For the case of finite-size receivers, acoustic-structure interaction effects arising from the reflected and scattered acoustic field also need to be accounted for by the existing models, since these effects influence the non-planar motion of the disk and vice-versa. Consequently, this issue is addressed in this work using an FE based approach to formulating the acoustic-piezoelectric structure interaction problem.

Based on the above-mentioned limitations/challenges in the current UPT modeling efforts, this study aims to demonstrate a novel concept involving the acoustic-structure interaction effects of the HIFU nonlinear acoustic field on the response of a finite-size piezoelectric receiver. It is assumed that the strains produced in the receiver due to acoustic excitation are small such that structural or geometrical nonlinearities in the disk are not triggered. Following this, in section 2, the KZK equation is used to estimate sound pressure on a piezoelectric disk. The structural response of the disk is formulated using an FE approach. Based on boundary conditions, the acoustic-structure interaction is quantified through a coupling matrix, which gives information about the reflection and scattering effects of the pressure field in the presence of the disk. The FE model is implemented through COMSOL Multiphysics[®]. Experimental results and model

validation are presented in section 3. Characteristics of the nonlinear acoustic field and the response of a finite-size receiver are first investigated individually, and then the combined system is analyzed to understand the interaction of the two physics. A summary of the power output characteristics and conclusions is given in section 4.

6.2. Theory

6.2.1. Nonlinear acoustic-electroelastic theory

The coupled acoustic-electroelastic multiphysics of high-intensity focused UPT involves the estimation of the focused ultrasound (FU) field from a HIFU transducer, and its interaction with the receiver to predict the mechanically induced vibrational and electrical responses. First, to understand the wave kinematics, KZK equation is used to estimate the acoustic pressure field on a piezoelectric disk submerged in a fluid domain. The disk is placed in a way such that the excitation is along the polarity direction, i.e., thickness direction, as shown in Fig. 6.1. Although in this work, the KZK equation predicts the pressure field only in the fluid domain, it can be easily extended to study the acoustic pressure field in a multi-domain environment, as demonstrated in [32]. The multi-domain approach is particularly useful when the receiver disk is placed in a heterogeneous domain such as inside the human body, where acoustic waves pass through multiple layers of skin, tissue, and muscles.

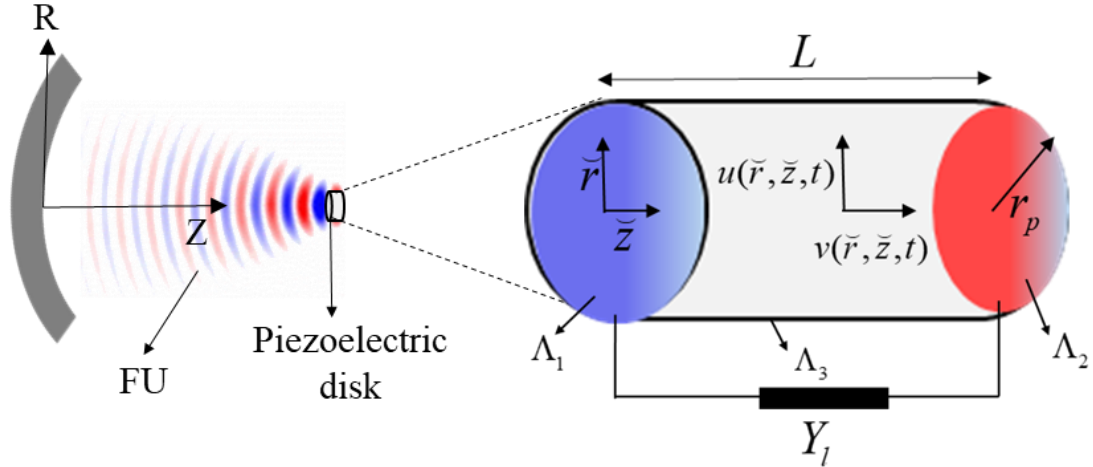


Fig. 6.1. Schematic representation of FU actuated piezoelectric receiver in a UPT system; the receiver is located in the focal area of the transducer in free-free boundary conditions.

The KZK equation incorporates the effects of absorption, diffraction, and nonlinearity of the medium on the wave propagation. It is expressed by Eq. 1 of chapter 2 and Refs. [35, 41, 42]. In this chapter, variables p , t and z are used to represent the sound pressure at the observation point, the time, and the wave propagation distance in the axial direction Z , respectively. The parameters ρ and c are used to denote the density and speed of sound in the acoustic medium, respectively. The first, second and third terms on the right-hand side of Eq. 1 of chapter 2 represent diffraction, absorption, and nonlinearity effects of the medium on the wave, respectively. The parameter β in this equation is the coefficient of the nonlinearity of the medium.

In Eq. 1 of chapter 2, absorption refers to the thermoviscous attenuation leading to loss of energy in a propagating wave. This equation also accounts for nonlinearity in the medium that leads to the generation of higher harmonics and make the wave distorted as it moves through the

medium. The coefficient of nonlinearity is defined as $\beta=1+B/2A$ where B/A is the nonlinearity parameter [35]. An operator splitting method is used to numerically solve Eq. 2 of chapter 2, which involves solving for each of the three terms in the right-hand side of the equation separately at each integration step [43]. A hybrid time-frequency domain method is used where the linear terms are solved in the frequency domain using second-order finite difference methods. The nonlinear term is solved in the time domain using the upwind method [44]. For accurate modeling of the nonlinear pressure field, up to 128 harmonics are considered. A detailed explanation of the solving technique is given in Ref. [45].

The acoustic pressure predicted by the KZK equation exerts a force on a piezoelectric disk, located at the focal point of the transducer, in the direction of wave propagation, as illustrated in Fig. 6.1. To model the electroelastic response, a disk of thickness L , density ρ_p , and radius r_p connected to a circuit with load resistance R_l ($Y_l = 1/R_l$ for purely resistive load in Fig. 6.1) is considered in free-free boundary conditions. The variable \tilde{r} represents the radial distance from the center of the disk in the radial direction, R and, \tilde{z} is the distance along the thickness of the disk in the axial direction, Z (Fig. 6.1). The receiver is assumed to be transversely isotropic. Thus, it has an axisymmetric response with $d\varphi = 0$. The displacements of the disk in radial and axial directions are denoted by $u[\tilde{r}, \tilde{z}, t]$ and $v[\tilde{r}, \tilde{z}, t]$, respectively. The coupled equations for the piezoelectric response are derived using Hamilton's principle, given as [46, 47]

$$\int_{t_1}^{t_2} (\delta T - \delta U + \delta W_{nc}) dt = 0 \quad (1)$$

where the operator $\delta()$ represents the variation of a quantity. The variables T , U , and W_{nc} denote kinetic energy, potential energy, and work done by non-conservative or external forces, respectively. The potential energy of the receiver in the cylindrical coordinate system assuming zero free charges and zero initial potential [47], is

$$U = \int_{dV} \left(\frac{1}{2} \mathbf{S}^t \mathbf{Y} \mathbf{S} - \mathbf{E}^t e \mathbf{S} - \frac{1}{2} \mathbf{E}^t \varepsilon \mathbf{E} \right) dV \quad (2)$$

where Y , e and, ε are the 6×6 elastic modulus at the constant electric field, 3×6 piezoelectric coupling, and 3×3 permittivity matrices for isotropic piezoelectric materials [47], given in appendix D. The superscript $()^t$ denotes the transpose of a quantity. The strain, \mathbf{S} and, electric field, \mathbf{E} , vectors are defined as

$$\mathbf{S} = \begin{pmatrix} S_r \\ S_\varphi \\ S_z \\ 2S_{r\varphi} \\ 2S_{rz} \\ 2S_{\varphi z} \end{pmatrix} = \begin{pmatrix} \frac{\partial}{\partial \tilde{r}} & 0 \\ \frac{1}{\tilde{r}} & 0 \\ 0 & \frac{\partial}{\partial \tilde{z}} \\ 0 & 0 \\ \frac{\partial}{\partial \tilde{z}} & \frac{\partial}{\partial \tilde{r}} \\ 0 & 0 \end{pmatrix} \begin{pmatrix} u \\ v \end{pmatrix} = [\mathbf{B}] \mathbf{W} \text{ and } \mathbf{E} = \begin{pmatrix} E_r \\ E_z \end{pmatrix} = - \begin{pmatrix} \frac{\partial}{\partial \tilde{r}} \\ \frac{\partial}{\partial \tilde{z}} \end{pmatrix} \bar{V} = -[\mathbf{L}] \bar{V} \quad (3)$$

where \bar{V} is electric potential, \mathbf{W} is the displacement vector given as $\mathbf{W} = (u \ v)^t$ and, B and L are differential operator matrices. Taking variation, Eq. 2 becomes

$$\delta U = \int_{dV} \left(\delta \mathbf{S}' Y \mathbf{S} - \delta \mathbf{E}' e \mathbf{S} - \delta \mathbf{S}' e \mathbf{E} - \delta \mathbf{E}' \varepsilon \mathbf{E} \right) dV \quad (4)$$

The variation of the kinetic energy of the disk is

$$\delta T = \int_{dV} \delta \dot{\mathbf{W}}' \rho_p \dot{\mathbf{W}} dV \quad (5)$$

where an overdot represents differentiation with respect to time. The variation of work done by the external force of acoustic pressure, damping, and electrical energy is

$$\delta W_{nc} = - \int_{\Lambda} \mathbf{p}_{\text{ext}} A_f \delta \mathbf{W}' \Big|_{\Lambda} d\zeta - \int_{dV} c_s \delta \mathbf{W}' \dot{\mathbf{W}} dV - \int_{dV} Q \delta \bar{V} dV \quad (6)$$

Here, the pressure exerted by sound, \mathbf{p}_{ext} , is integrated only over the acoustic-structure interaction surface, Λ , with a total surface area A_f . The variable Λ is defined as $\Lambda = \Lambda_1 \cup \Lambda_2 \cup \Lambda_3$ (Fig. 6.1). The variable c_s is the structural damping coefficient and Q is the net electric charge in the disk. Substituting Eqs. 4-6 in Eq. 1 gives the equation of motion as

$$\int_{t_1}^{t_2} \left(\int_{dV} \left(\delta \dot{\mathbf{W}}' \rho_p \dot{\mathbf{W}} - \delta \mathbf{S}' Y \mathbf{S} + \delta \mathbf{E}' e \mathbf{S} + \delta \mathbf{S}' e \mathbf{E} + \delta \mathbf{E}' \varepsilon \mathbf{E} - \delta \mathbf{W}' c_s \dot{\mathbf{W}} - Q \delta \bar{V} \right) dV - \int_{\Lambda} \mathbf{p}_{\text{ext}} A_f \delta \mathbf{W}' \Big|_{\Lambda} d\Lambda \right) dt = 0 \quad (7)$$

To ensure continuity at the boundary interface, the normal velocity of the structural boundary should be identical to the fluid velocity along the surface normal. Secondly, the acoustic force

acting on the structure should be equal and opposite to the force exerted by the structure on the fluid. These two conditions are expressed as [48]

$$\begin{aligned} [B]p.\tilde{\mathbf{N}} &= -\rho\ddot{\mathbf{W}}.\tilde{\mathbf{N}} \\ p.\tilde{\mathbf{N}} &= -\rho_p\ddot{\mathbf{W}}.\tilde{\mathbf{N}} \end{aligned} \quad (8)$$

where $\tilde{\mathbf{N}}$ is the unit normal to the surface of the boundary.

6.2.1.1. Finite element analysis

Previous works have developed closed-form solutions to estimate the electromechanical response of the disk under acoustic excitation [21, 23]. Such a closed-form approach is generally possible when the disk can be assumed to respond in a piston-like motion. In these scenarios, any shear effects and radial motion of the disk can be neglected. However, disks with finite ratios, such as discussed in Ref. [38], and in this work, do not show a piston-like motion. Therefore, the general convention of assuming spatial dependence of displacement on a single cylindrical coordinate is not valid for such cases. The response of finite-size disks depends both on radial and thickness directions and is complicated to capture analytically [38]. Thus, numerical techniques are adopted to predict their responses accurately. The FE technique formulation will be briefly discussed here for piezoelectric structures [38, 49, 50]. Assuming the piezoelectric disk as an axisymmetric system of discrete non-overlapping elements (denoted by superscript e), the displacement and electric fields for an element are expressed as

$$\mathbf{W} = [\phi]\mathbf{N}^e \text{ and } \bar{\mathbf{V}} = [\phi_e]\mathbf{R}^e \quad (9)$$

where $[\phi]$, and $[\phi_e]$ are $2 \times n$ and $1 \times n$ matrices of quadratic Lagrange shape functions respectively. The vectors \mathbf{N}^e and \mathbf{R}^e are nodal displacements and electric potential vectors respectively, such that $N_i^e = (u_i^e \quad v_i^e)^t$ and $R_i^e = (\bar{V}_i^e)$ at the i^{th} node of the element. Substituting Eq. 9 in Eq. 7 gives

$$\int_{t_1}^{t_2} (\delta \mathbf{N}^e)^t (M^e \ddot{\mathbf{N}}^e + K^e \mathbf{N}^e + k^e \mathbf{R}^e + d^e \dot{\mathbf{N}}^e - \mathbf{F}^e) + (\delta \mathbf{R}^e)^t (-(k^e)^t \mathbf{N}^e + \hat{\varepsilon}^e \mathbf{R}^e - \hat{\mathbf{Q}}^e) dt \quad \text{which yields}$$

the equation of motion as

$$M^e \ddot{\mathbf{N}}^e + K^e \mathbf{N}^e + k^e \mathbf{R}^e + d^e \dot{\mathbf{N}}^e - \mathbf{F}^e = 0 \quad (10)$$

Along with electrical circuit equation

$$-(k^e)^t \mathbf{N}^e + \hat{\varepsilon}^e \mathbf{R}^e = \hat{\mathbf{Q}}^e \quad (11)$$

where $M^e = \int_{V_e} [\phi]^t \rho_p [\phi] dV$, $K^e = \int_{V_e} ([B][\phi])^t Y ([B][\phi]) dV$, $k^e = \int_{V_e} ([B][\phi])^t e [L][\phi_e] dV$, $d^e = \int_{V_e} [\phi]^t c_s [\phi] dV$, $\hat{\varepsilon}^e = \int_{V_e} [L(\phi_e)]^t \varepsilon [L(\phi_e)] dV$ and $\hat{\mathbf{Q}}^e = [\phi_e]^t \mathbf{Q}^e$. Here, \mathbf{Q}^e is the net electric

charge vector at each node in the element. The external forcing is given as $\mathbf{F}^e = \int_{\Lambda_e} [\phi]^t A_j^e \mathbf{p}_{\text{ext}}^e d\Lambda$.

The equations of all elements are assembled to obtain global equations with the help of connectivity matrices [50]. Assuming boundary conditions of axisymmetry, the coupled system of the equation of motion and electrical circuit equation is given as

$$\begin{pmatrix} M & 0 \\ 0 & 0 \end{pmatrix} \begin{Bmatrix} \ddot{\mathbf{N}} \\ \ddot{\mathbf{R}} \end{Bmatrix} + \begin{pmatrix} d & 0 \\ 0 & 0 \end{pmatrix} \begin{Bmatrix} \dot{\mathbf{N}} \\ \dot{\mathbf{R}} \end{Bmatrix} + \begin{pmatrix} K & k \\ -(k)' & \hat{\varepsilon} \end{pmatrix} \begin{Bmatrix} \mathbf{N} \\ \mathbf{R} \end{Bmatrix} = \begin{Bmatrix} \mathbf{F} \\ \bar{\mathbf{Q}} \end{Bmatrix} \quad (12)$$

For the receiver shown in Fig. 6.1, the electrical power is measured by connecting a load resistance across the two radial surfaces perpendicular to the axis (Z direction) of the disk, Λ_1 and Λ_2 . These two surfaces are assumed to be equipotential surfaces. Considering these surfaces as electrodes with a potential difference \mathbf{V}_0 across them, a current equivalent to \mathbf{V}_0/R_l passes through the disk. Assuming Λ_2 as ground, the potential vector of all nodes on Λ_1 , \mathbf{V}_0 , contributes to the electric power across the load. The charge accumulated at the free surface, $\bar{\mathbf{Q}}$,

is expressed as $\bar{\mathbf{Q}} = \int_{\Lambda_1} Q d\Lambda = \int_{t_1}^{t_2} \mathbf{V}_0/R_l dt$. The equation of motion coupled with electrical circuit

equation now becomes

$$\begin{pmatrix} M & 0 \\ 0 & 0 \end{pmatrix} \begin{Bmatrix} \ddot{\mathbf{N}} \\ \ddot{\mathbf{R}} \end{Bmatrix} + \begin{pmatrix} d & 0 \\ 0 & 0 \end{pmatrix} \begin{Bmatrix} \dot{\mathbf{N}} \\ \dot{\mathbf{R}} \end{Bmatrix} + \begin{pmatrix} K & k \\ -(k)' & \hat{\varepsilon} \end{pmatrix} \begin{Bmatrix} \mathbf{N} \\ \mathbf{V}_0 \end{Bmatrix} = \begin{Bmatrix} \mathbf{F} \\ \bar{\mathbf{Q}} \end{Bmatrix} \quad (13)$$

6.2.1.2. Acoustic-structure interaction

For a disk immersed in a fluid and excited by an acoustic source, the motion of the disk will be influenced by the acoustic medium loading on the disk. In parallel, the acoustic pressure field near the disk will also be influenced by the vibration of the disk surfaces. In such cases, the equations of motion are derived similarly using Hamilton's principle. However, an additional term accounting for the work done by acoustic pressure on the disk surface is added. In this

work, since the output response of the disk is of interest, the acoustic-structure interaction problem is formulated only for the disk [48].

In Eq. 10, the forcing term \mathbf{F}^e represents external forcing effects on an element of the disk. If fluid elements are also discretized such that $\mathbf{p}_{\text{ext}}^e = [g]\mathbf{p}_t^e$, where $[g]$ is a quadratic Lagrange shape function and \mathbf{p}_t^e is a nodal pressure vector for a fluid element, the forcing is then expressed

as $\mathbf{F}^e = \int_{\Lambda_e} [\phi]^t A_f^e [g] \mathbf{p}_t^e d\Lambda = [H] \mathbf{p}_t^e$. Here, $[H]$ is known as the acoustic-structure coupling

matrix.

For the disk shown in Fig. 6.1, the total external force on a disk element can be further decomposed as the contributions from incident pressure from acoustic source, $[g]\mathbf{p}_i^e$, the reflected pressure when the disk acts like a rigid body (no motion of surface), $[g]\mathbf{p}_r^e$, and the scattered/radiated pressure due to vibration of disk elements, $[g]\mathbf{p}_{\text{rad}}^e$. The external force, \mathbf{F}^e , now becomes [48]

$$\mathbf{F}^e = [H] \left(\mathbf{p}_i^e + \mathbf{p}_r^e + \mathbf{p}_{\text{rad}}^e \right) \quad (14)$$

When the disk acts as a rigid body, the total pressure on the disk is the summation of only two components, reflected and incident pressure. This sum is known as block pressure $\mathbf{p}_{\text{blo}}^e$ and is equal to $\mathbf{p}_{\text{blo}}^e = \mathbf{p}_i^e + \mathbf{p}_r^e$ [48]. Consequently, the total external force on an element is re-written as

$\mathbf{F}^e = [H](\mathbf{p}_{\text{blo}}^e + \mathbf{p}_{\text{rad}}^e)$. Accounting for these pressure effects individually and assembling to get a global equation of motion coupled with the electrical response, Eq. 13 becomes

$$\begin{pmatrix} M & 0 \\ 0 & 0 \end{pmatrix} \begin{Bmatrix} \ddot{\mathbf{N}} \\ \ddot{\mathbf{R}} \end{Bmatrix} + \begin{pmatrix} d & 0 \\ 0 & 0 \end{pmatrix} \begin{Bmatrix} \dot{\mathbf{N}} \\ \dot{\mathbf{R}} \end{Bmatrix} + \begin{pmatrix} K & k \\ -(k)^t & \hat{\varepsilon} \end{pmatrix} \begin{Bmatrix} \mathbf{N} \\ \mathbf{V}_0 \end{Bmatrix} - \begin{pmatrix} H & 0 \\ 0 & 0 \end{pmatrix} \begin{Bmatrix} \mathbf{p}_{\text{rad}} \\ \mathbf{0} \end{Bmatrix} = \begin{Bmatrix} \mathbf{F}_{\text{blo}} \\ \bar{\mathbf{Q}} \end{Bmatrix} \quad (15)$$

where $\mathbf{F}_{\text{blo}} = [H]\mathbf{p}_{\text{blo}}$. To understand the effects of the radiated pressure field on the vibrational response of the disk, the radiation pressure can be further expressed in terms of radiation impedance matrix, z_{wf}^e , and associated velocity of the disk such that

$$\int_{\Lambda_e} [g] \mathbf{p}_{\text{rad}}^e d\Lambda = - \int_{\Lambda_e} [z_{\text{wf}}^e] [\phi] \dot{\mathbf{N}}^e d\Lambda \quad [51].$$

Here, the radiation impedance is composed of two

components; a resistive part, R_{wf}^e , and an imaginary part, X_{wf}^e . The resistive component contributes to the damping effect, whereas the imaginary portion adds to the inertia and shifts the natural frequency, ω_r , of the disk. Moreover, for a harmonic response of the disk, the reactive term of the fluid wave impedance can further be expressed as an added mass, given by

$$[X_{\text{wf}}^e] \dot{\mathbf{N}}^e = \left[\frac{X_{\text{wf}}^e}{\omega_r} \right] \ddot{\mathbf{N}}^e = [M_{\text{wf}}^e] \ddot{\mathbf{N}}^e.$$

When these two radiation impedance components are

assembled and incorporated into the global equation of motion, the first row of Eq. 15 becomes

$$[M + M_{\text{wf}}^e] \ddot{\mathbf{N}} + [d + R_{\text{wf}}^e] \dot{\mathbf{N}} + K\mathbf{N} + k\mathbf{V}_0 = \mathbf{F}_{\text{blo}} \quad (16)$$

Eq. 15 is solved using COMSOL Multiphysics®, with the setup comprising of a piezoelectric disk in a finite water domain, placed at the focal point of the transducer. The water domain is of

radius 70 mm and lined with a perfectly matching layer of 3 mm to simulate an infinite medium. The disk is poled such that the radial surface enclosed by Λ_2 serves as the ground, while the opposite surface gives the net potential. This ungrounded surface faces the incoming acoustic waves. The disk is also attached to a 1-ohm resistance to estimate the output power at short-circuit natural frequencies corresponding to different modes. A mesh of quadratic Lagrangian elements is chosen with the maximum element size limited to six elements per acoustic wavelength. For time-domain simulations, a generalized alpha solver with a manual time-step size corresponding to the highest frequency component in the acoustic field is used.

6.3. Experimental validation and acoustic-structure interaction characterization

Experiments are conducted with an H-104-4A SONIC Concepts HIFU transducer mounted on one side of a $61.5 \times 31.8 \times 32.5 \text{ cm}^3$ water tank, as shown in Fig. 6.2a. The water tank is filled with deionized water to avoid any electrical short-circuiting. A Precision Acoustics 1 mm needle hydrophone measures the acoustic field of the transducer using a TBS2000 Series Tektronix oscilloscope, Fig. 6.2a. The readings from the oscilloscope are recorded using a built-in MATLAB interface. The hydrophone is connected to the oscilloscope via a DC coupler, which conditions the hydrophone signal and also acts as a power supply. The hydrophone is mounted on a positioning system, which scans the acoustic field in axial and radial directions with respect to the transducer, to acquire pressure measurements. The water tank is lined with Aptflex F28 absorber sheets (purchased from Precision Acoustics Ltd.) on the bottom of the tank and the two side walls of the transducer, to prevent boundary wall reflections. The HIFU transducer is

operated at 0.5 MHz with a 100 μ s burst signal and 10 ms of burst period for different input electrical power to the HIFU amplifier.

6.3.1. Acoustic parameter identification and model validation

To model the acoustic field from the HIFU source used in experiments, the knowledge of the effective radius of curvature and the operational aperture of the transducer is needed. The values of these parameters stated by the manufacturer do not allow the transducer to be modeled as a uniform piston source. Transducer housing, surface waves, and inhomogeneity in the piezoelectric elements of the transducer can distort the source vibration [52]. Therefore, effective values of source curvature and aperture are determined first.

The experimental setup as shown in Fig. 6.2, is used to measure pressure from the transducer at a low input power, along the axis, and in the radial focal plane. At low input power, acoustic nonlinearities are negligible. Therefore, direct relationships to estimate the effective source geometry can be used. Measurements are taken and compared with the linear model ($\beta \approx 0$) in Eq. 1 of chapter 2. Values of source aperture and radius of curvature are varied in the model to obtain the best agreement with the experimentally obtained axial and radial pressure fields. It is determined that the effective value of the radius of curvature is $D = 8$ cm, and the source aperture is $2r = 7.4$ cm. Based on these values, the model in Eq. 1 of chapter 2 is validated with experimental observations and FE simulations in COMSOL in the water domain. The FE simulation setup remains the same as described in the COMSOL implementation in section 6.2, but without the piezoelectric disk. Fig. 6.3 shows a good agreement between the KZK-

calculated, FE, and experimental values of acoustic pressure in axial and transverse directions, under linear propagation. The slight discrepancy in the pre-focal region of the axial pressure field between measured and calculated values is due to parabolic approximation in the KZK model [52]. This validation shows that a single-element HIFU transducer can be modeled as a uniformly vibrating source using a linear equation.

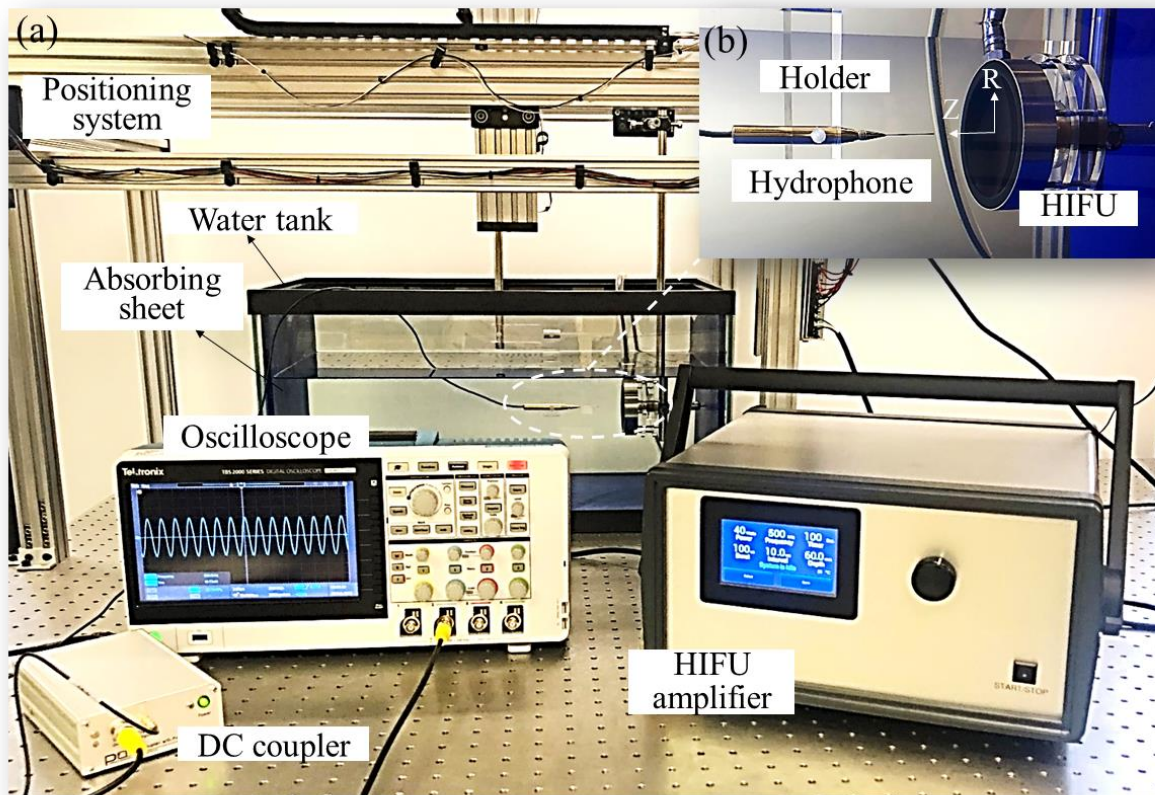


Fig. 6.2. (a) Experimental setup to measure the pressure field of a HIFU transducer in a water tank using a needle hydrophone. (b) A magnified image of the needle hydrophone inside the tank. The tip of the hydrophone traverses in axial and radial directions of the transducer to map the acoustic pressure field.

Having identified the effective characteristic values of the transducer geometry, it is important to find the pressure at the surface of the transducer. This involves estimating the conversion coefficient between the input voltage to the transducer and source pressure amplitude. Since it is difficult to measure the pressure at the source experimentally, an alternative analytical method is used. Using the effective values of transducer geometrical parameters found above, linear focusing gain, G in Eq. 2 of chapter 2 is determined. The source pressure amplitude is then estimated as $p_0 = p_f / G$ where p_f is the pressure at the focal point. For a voltage input, $V_{in} = 4 \text{ V}$, to the HIFU amplifier, the source pressure, p_0 value is calculated as $p_0 = 8 \text{ kPa}$. The conversion coefficient, η_{av} , is then estimated to be $\eta_{av} = p_0 / V_{in}$, with a value of approximately 2 kPa/V. The source pressure is found to linearly increase with input voltage and is estimated using η_{av} for future measurements.

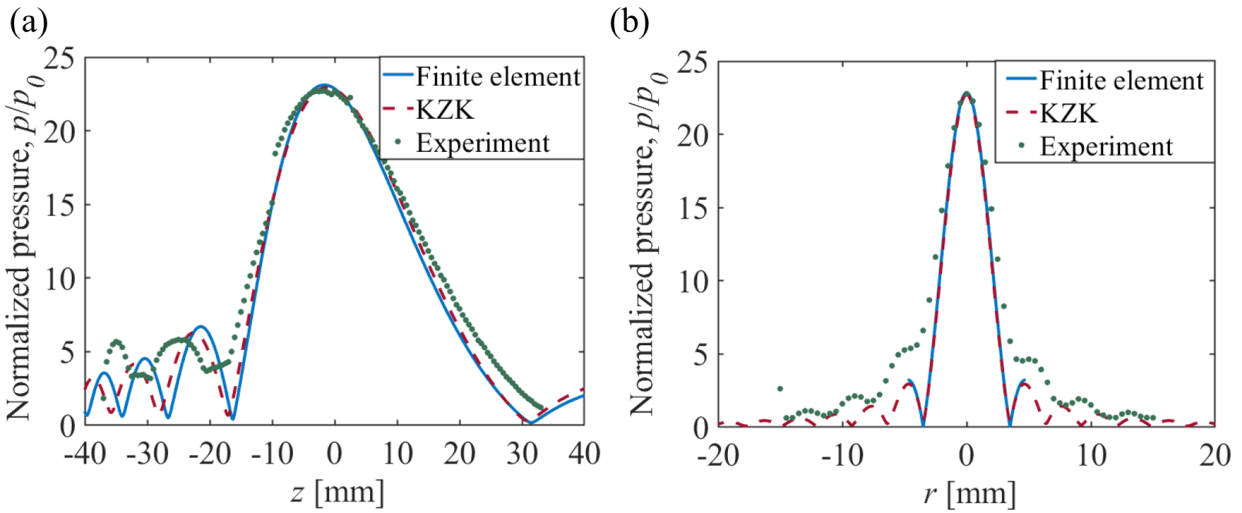


Fig. 6.3. Pressure field of a HIFU source on (a) axial and (b) radial axis ($V_{in} = 4 \text{ V}$ and $p_0 = 8 \text{ kPa}$) in water at 0.5 MHz.

After calibrating the model to account for effective geometrical parameters and boundary conditions in linearized Eq. 1 of chapter 2, the nonlinear acoustic model developed in section 6.2.1 is employed to predict the FU pressure field of the transducer. Figs. 6.4a and 6.4b show the experimental validation of the focal point pressure waveforms predicted by the KZK model with good agreement, at different source pressure, p_0 , in time and frequency domain, respectively. A slight discrepancy can be observed for the experimental values for $p_0 = 0.02$ MPa at higher frequency components in Fig. 6.4b. This is because the amplitude of pressure for higher harmonics, obtained from experiments, is very low for low input power and close to noise which may cause this variation. These observations show that the KZK model can estimate the amplitudes of the higher harmonics arising due to acoustic nonlinearity at high excitation levels, with sufficient accuracy.

6.3.2. Effect of acoustic parameters on acoustic nonlinearity

The usage of FU for different applications can lead to a strong interplay between diffraction, absorption and nonlinearity effects on the wave under various conditions, such as a change in medium or source parameters. Such an interplay ultimately affects the characteristics of the propagating acoustic waves including amplitude, and the number of harmonics in the wave (section 6.2.1). Our previous work [45] conducted an in-depth analysis to study the influence of these effects on the sound pressure field at the focal point. A summary of our earlier work [45] is explained here, that will enhance the understanding of the interaction of the nonlinear acoustic field with piezoelectric structures discussed in the later sections, which is the focus of this work.

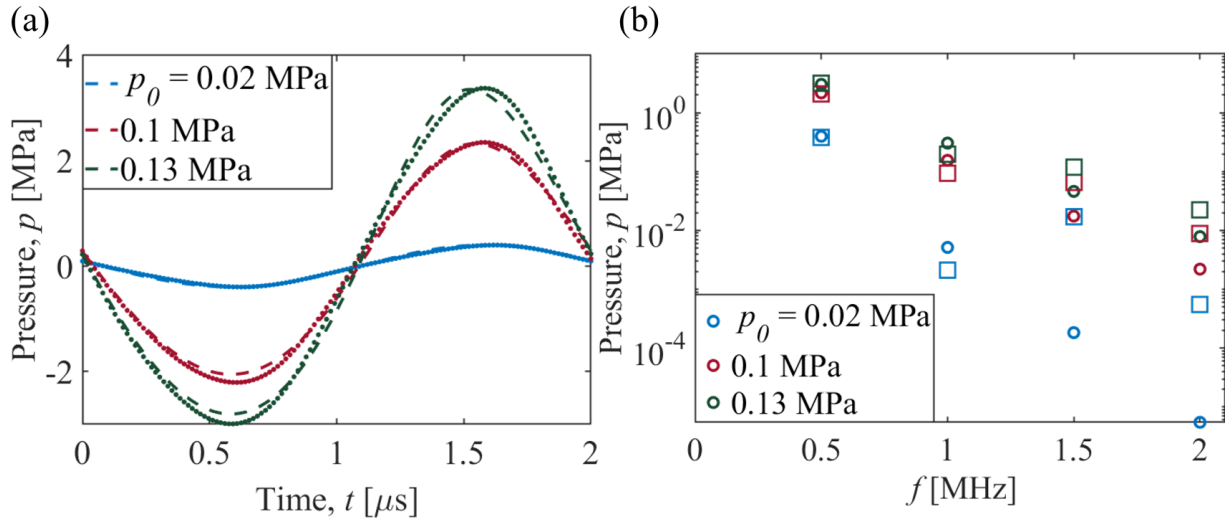


Fig. 6.4. Pressure waveforms at the focal point of the HIFU transducer operating at 0.5 MHz in (a) time and (b) frequency domain for various excitation levels in the water. Dashed and dotted lines in (a) represent KZK model calculations and experimental observations, respectively. Circular and square symbols represent KZK model calculations and experimental observations in (b), respectively.

The parameters that account for focusing gain, absorption, and nonlinearity in the model are G , \bar{A} , and N , respectively, Eq. 2 of chapter 2. Here, \bar{A} is a dimensionless number proportional to the real part of γ_n in Eq. 8 of chapter 2. It is defined as $\bar{A} = \alpha_0 D$ where α_0 represents attenuation at source frequency ω_0 . Since the geometry of the transducer and its operating frequency are fixed for the experimental setup in this study, G remains constant. The nonlinear effects in the medium, accounted by dimensionless parameter \bar{B} in Eq. 2 of chapter 2, is denoted by N in this chapter. Nonlinearity causes the propagation speed of the wave to vary from point to point resulting in the waveform peaks to travel faster as compared to troughs. This leads to distortion of the waveform and generation of higher harmonics. Due to the contribution of higher harmonics, the overall pressure amplitude at the focal point increases. From section 6.2, it is

observed that p_0 and β are two parameters that can change the value of N , Eq. 2 of chapter 2. While p_0 depends on the transducer's input driving voltage (section 6.3.1), β is a medium property and changes with different mediums. Figs. 6.5a and 6.5b show the variation of focal pressure waveforms obtained from the KZK model with changes in p_0 and β , respectively. An increase in the magnitude of both the parameters leads to a nonlinear increase in focal pressure amplitude; however, the mechanism in which they affect this pressure is different. While with an increase in p_0 , the strength of each of the higher harmonics increases, Fig. 6.5a, with amplification in β , the energy from the fundamental harmonic of the acoustic wave is transferred to higher harmonics, Fig. 6.5b [45], which grow under focusing effects.

As opposed to nonlinear effects, absorption effects in the medium cause loss of overall energy in the wave as it propagates. The absorption effects in Eq. 2 of chapter 2 are accounted through a non-dimensional parameter, \bar{A}_n , denoting absorption of n^{th} harmonic of the FU pressure field, defined as $\text{Re}[\mu_n] = \bar{A}_n = \bar{A}|\omega|^{\nu}$. This expression states that attenuation is higher for higher harmonics. Thus, it counters the nonlinear effects since nonlinearity leads to the generation of higher harmonic components. Fig. 6.5c shows the change in the focal pressure field until \bar{A} becomes significantly high (in the case of solids [53, 54]), and pressure wave reduces to a low amplitude linear wave.

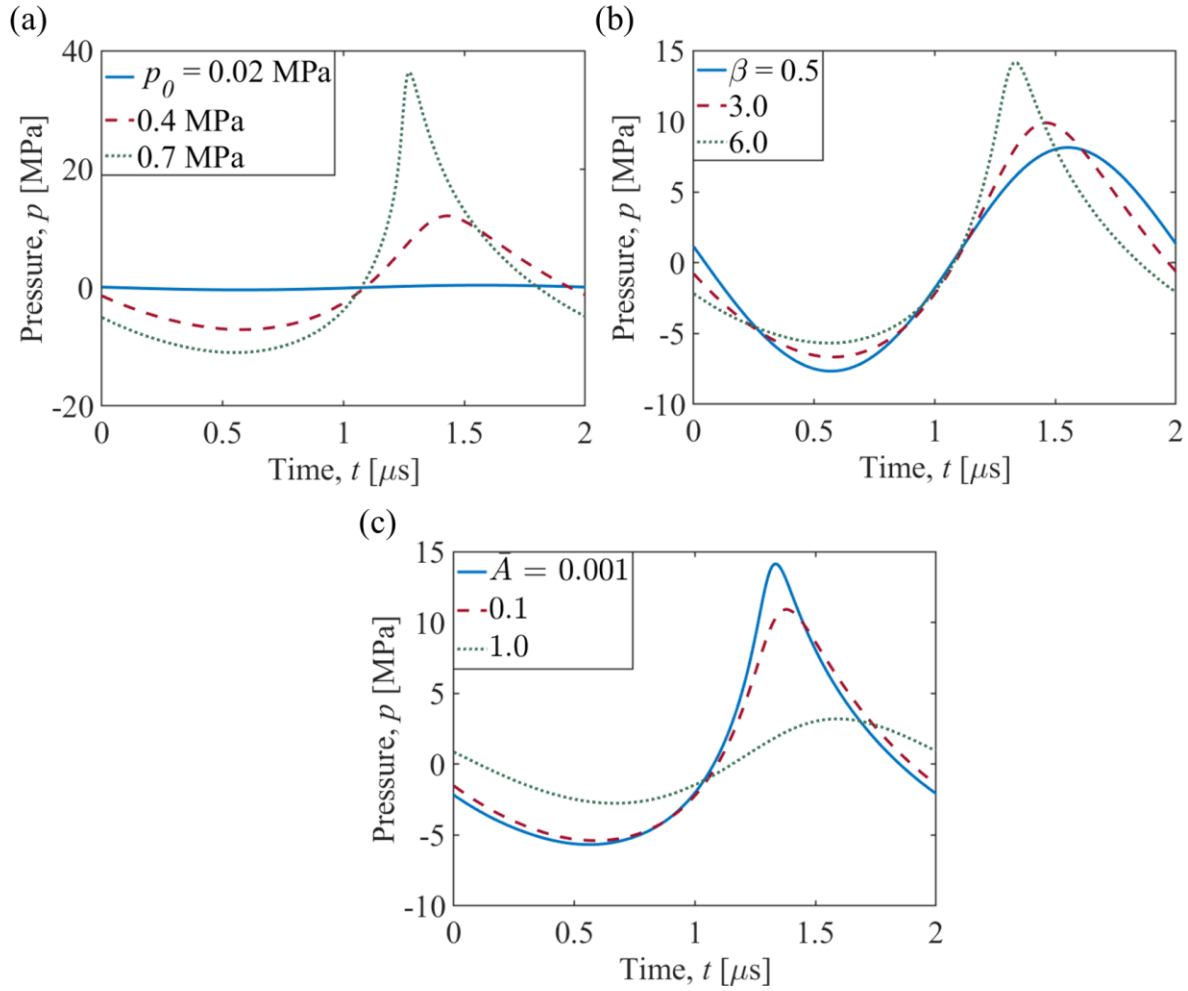


Fig. 6.5. Pressure waveform at the focal point in water, obtained from KZK model, for (a) various source pressure, p_0 , at $\beta = 3.5$ and $\bar{A} = 5 \times 10^{-4}$, (b) various coefficient of nonlinearity, β , at $p_0 = 0.34$ MPa and $\bar{A} = 5 \times 10^{-4}$, and (c) various attenuation parameters, \bar{A} , at $p_0 = 0.34$ MPa and $\beta = 6$.

6.3.3. Experimental validation for a HIFU-UPT system

A UPT system consists of a transmitter generating acoustic waves incident on a receiver, both of which are immersed in the same or different mediums. In this work, the transmitter is the HIFU transducer and the receiver is a piezoelectric ceramic disk, APC760. The disk is made up of

PZT-5A material manufactured by APC International, Ltd. To design a UPT system, impedance measurements of the disk are collected first, in order to identify the disk's electroelastic parameters. The electrical impedance measurement of a freely hanging APC760 disk, suspended in the air with wires, is performed using an HP4192A impedance analyzer in the frequency range of 5 Hz - 3 MHz. The FE formulation for electrical impedance in air is then curve-fitted to the experimentally obtained impedance, by tuning the material properties of the disk given by the manufacturer. The impedance measurements in air are used as a reference to find the disk properties because the fluid loading effects in air are negligible. The FE formulation for the electrical impedance of the disk in air can be derived from Eq. 15, where \mathbf{p}_{rad} is negligible. Since the disk is acting as an actuator in impedance measurements, $\mathbf{F}_{blo} = 0$ and $\mathbf{V}_0 = V^{in} e^{i\omega t}$,

where V^{in} is the driving voltage amplitude. The total charge, in this case, is $\bar{\mathbf{Q}} = \int_{t_1}^{t_2} I^{in} e^{i\omega t + \theta} dt$,

where I^{in} is the current passing through the disk. Thus, the FE formulation for an actuating piezoelectric disk in the air is

$$\begin{pmatrix} M & 0 \\ 0 & 0 \end{pmatrix} \begin{Bmatrix} \ddot{\mathbf{N}} \\ \ddot{\mathbf{R}} \end{Bmatrix} + \begin{pmatrix} d & 0 \\ 0 & 0 \end{pmatrix} \begin{Bmatrix} \dot{\mathbf{N}} \\ \dot{\mathbf{R}} \end{Bmatrix} + \begin{pmatrix} K & k \\ -(k)^t & \hat{\varepsilon} \end{pmatrix} \begin{Bmatrix} \mathbf{N} \\ \mathbf{V}_0 \end{Bmatrix} = \begin{Bmatrix} \mathbf{0} \\ \bar{\mathbf{Q}} \end{Bmatrix} \quad (17)$$

Eq. 17 is implemented in COMSOL, with a disk surrounded by air in a 2-D axisymmetric model. The maximum mesh size is limited to six elements per wavelength. Eq. 17 is then used to identify electroelastic parameters using curve-fitting of the FE calculated impedance curve to the experimentally obtained impedance curve. The curve-fitting is performed for the short circuit frequency around 0.5 MHz since it is the resonant frequency of the HIFU transducer. Figs. 6.6a

and D3a show the FE predicted impedance curves obtained after incorporating the identified parameters, and the experimentally measured one in air. A slight discrepancy is observed at the open circuit frequency in Fig. 6.6a, which can be due to the estimation of material properties based only on one frequency or non-unique combination of material parameters used for curve-fitting. The parameter combination reported here is one of the many combinations that can best fit the impedance response around 0.5 MHz. A detailed optimization can be performed to find the most accurate parameter combination. Further, a sensitivity analysis can facilitate in understanding how sensitive the complete system is to deviations in each parameter. The identified parameters of the disk are reported in Table 1, where ϵ_r is the permittivity of vacuum and ζ is the mass proportional Rayleigh damping. The mass proportional damping is related to Eq. 17 as $d = \zeta M$.

Using the properties mentioned in Table 1, the electrical impedance for APC760 disk is calculated in water. In order to estimate impedance in water, the FE formulation in Eq. 17 is modified to include the radiated pressure, p_{rad} . The experimental setup to obtain the electrical impedance of the disk in water remains the same as the setup for air, however, the disk is now fully submerged in the water domain. Figs. 6.6b and D3b show a reasonable agreement between the impedance predicted from the FE with that of the experimental values. A vertical shift between the two curves is observed in Fig. 6.6b, which can be due to a small change, i.e. $\pm 20\%$, of the capacitance of the APC760 disk after immersing in water. On comparing the impedance curves between air and water in Fig. 6.6, it is observed that the impedance amplitude decreases and the short circuit resonant frequency shifts to the left when the disk is underwater. These

behaviors can be attributed to the added damping and added mass effects due to fluid loading, respectively, as given in Eq. 16 [47]. It is also seen that the impedance calculated from the FE does not match the experimental values at other modes (Fig. D3), for both air and water. A primary reason is that the matching of the impedance curves obtained from two methods is performed only for one mode (around 0.5 MHz). Therefore, the material properties such as damping and electromechanical coupling, which are different for each mode, are not accounted for by the FE formulation and lead to the discrepancy with experimental values.

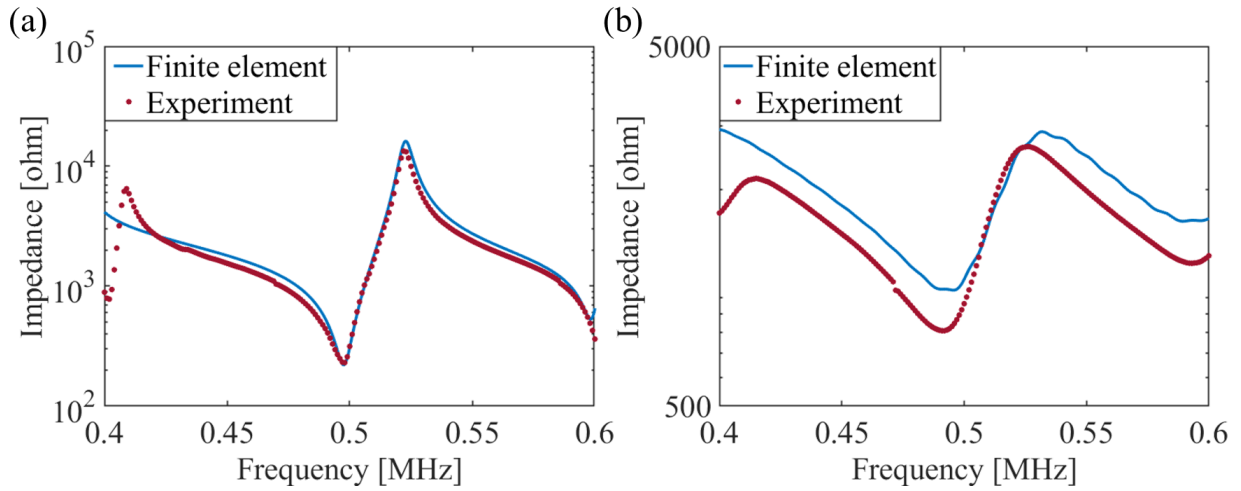


Fig. 6.6. Electrical impedance curves obtained from FE simulations (solid line) and experiments (dotted line) in (a) air and (b) water, for the APC760 disk.

With the developed understanding of the fluid loading effects on the disk in air and underwater, and identifying the material properties of the disk, the UPT system is designed. Fig. 6.7a shows the experimental setup, which is similar to the setup described in Fig. 6.2. However, in Fig. 6.7a, the hydrophone is replaced by the APC760 disk. The disk is soldered using wires and mounted on the positioning system in the free-free boundary conditions. It is required that the focal point

falls on the disk's leading surfaces since the acoustic field is concentrated at the focal point. To achieve this, two laser pointers are used as placeholders for the focal point of the HIFU, which is first located using the hydrophone. Once the hydrophone is removed, the lasers are used to pinpoint the focal point and to place the disk in the desired location; the green laser light can be seen in Fig. 6.6a. The HIFU transducer sends pressure pulses with 10 ms of burst period having 100 μ s of burst (50 cycles) at 0.5 MHz, to avoid any reflections and standing waves between HIFU and the disk. The voltage output of the acoustically excited disk is recorded using the MATLAB interface of the oscilloscope.

Table 6.1: Electroelastic properties of APC760 piezoelectric disk used in this study

Property	Value
ρ_p	7700 kg/m ³
r_p	4.75×10^{-3} m
L	3.9×10^{-3} m
$Y_{11} = Y_{22}$	148 GPa
$Y_{12} = Y_{21}$	105 GPa
$Y_{13} = Y_{31}$	106.82 GPa
Y_{33}	138.99 GPa
$e_{31} = e_{32}$	-1.5 [C/m ²]
e_{33}	22.5 [C/m ²]
$e_{24} = e_{15}$	11.64 [C/m ²]
$\epsilon_{11}/\epsilon_r = \epsilon_{22}/\epsilon_r$	1130
ϵ_{33}/ϵ_r	800
ζ	34000 [1/s]

These experimental observations are used to validate the acoustic-structure interaction formulation developed in section 6.2, for APC760 disk. The FE model has already been validated for acoustic wave propagation in water with experiments and the KZK model, section 6.3.1, as well as for the response of disk for electrical actuation, Fig. 6.6. Consequently, the acoustic-structure FE model is implemented in COMSOL, according to the specifications described in section 6.2. Fig. 6.7b shows typical time histories of the voltage output across an electrical 1-ohm resistive load connected to the receiver disk, obtained from experimental measurements and the FE model. The acoustic excitation is maintained at a low-pressure level, $p_0 = 8 \text{ kPa}$, such that acoustic or geometrical nonlinearities are not triggered. These results show that the proposed FE model is successfully able to capture the acoustic-piezoelectric interaction in the UPT system.

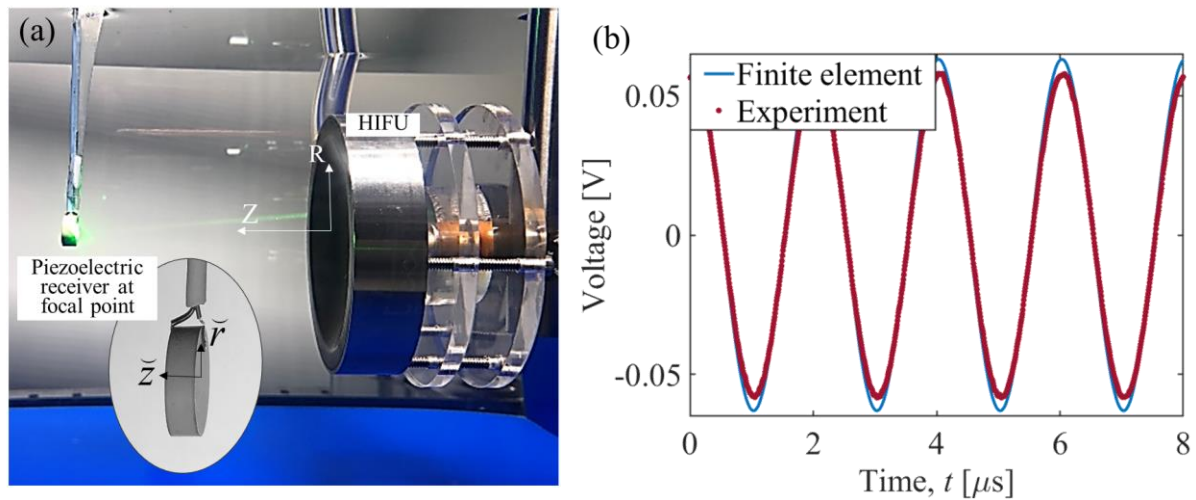


Fig. 6.7. (a) Experimental set up of the UPT system using HIFU source to excite a piezoelectric receiver at focal point ($\approx 52 \text{ mm}$). The magnified image of the disk exposed to HIFU. The laser pointers fall on the top surface of the disk to mark the focal point of FU. (b) The voltage response of the receiver to signals of 10 ms of burst period having 100 μs of burst (50 cycles) at 0.5 MHz.

There are multiple reasons for adopting the FE approach in this work instead of using the reduced-order one-dimensional models [21, 23, 46], to study the structural response of the disk. A primary reason is the finite aspect ratio of the disk. The reduced-order models are based on the assumption of a piston-like motion of the disk, which enables the complete bulk motion of the disk to be expressed in terms of a single function of spatial coordinates. As discussed in previous sections, disks with aspect ratios that are not very large or small (> 20 or < 0.1) [38], do not show the piston-like motion. The mode shapes of such disks are the functions of both radial and axial directions. Another reason for adopting an FE approach is that the structural resonant overtones are not harmonics for such disks. As seen from the eigenvalue analysis of disks having piston-type motion, the maximum voltage output occurs at the fundamental and its harmonic structural resonant frequencies [55]. However, due to the absence of pure-thickness modes in disks with finite aspect ratio, such an assumption does not hold true. This can also be seen from the impedance curves in Fig. 6.8a and Fig. D3 and, power output response in Fig. D1. Two important observations can be made from these figures: (1) The power output is maximum from the receiver at those frequencies which coincide with the disk's short-circuit resonant frequencies in impedance measurements, which is expected; (2) The frequencies at which maximum power is generated are not the harmonics of the fundamental frequency.

In addition, one another reason for adopting an FE approach is shown in Figs. 6.8b1-6.8b4. Figs. 6.8b1-6.8b4 show the normalized displacement profiles of the disk at its first four resonant frequencies, which have considerable power output upon acoustic excitation in water (Fig. D1). A key observation to note in these figures is that the displacement profiles of the top and bottom

surfaces of the disk at each frequency are not the same and differ in pattern from each other. This difference in patterns further complicates the attempts of developing reduced-order models or assuming a single universal displacement profile to describe the complete structural response. A possible reason for the difference between the displacement profiles of top and bottom surface displacements can be the unsymmetrical and nonuniform pressure and velocity profiles on the two leading surfaces. It is seen that the acoustic pressure field at both of these surface boundaries differs by a significant amount (Fig. D2). Since these pressure fields contribute to the radiation impedance, which in turn affects the motion of the disk, Eq. 16, it is possible that they affect the overall displacement pattern differently, for the top and bottom surfaces. Due to these various reasons, developing a comprehensive reduced-order model that accounts for all these effects becomes cumbersome. Thus, an FE based approach is needed for investigating the acoustic-electroelastic UPT system.

6.3.4. Electroelastic response of the piezoelectric receiver in the nonlinear acoustic field

Having validated the FE formulation and understanding the structural response of the receiver disk for low acoustic excitation in a linear framework, the acoustic-structure interaction formulation, Eq. 15, is used to understand the effects of the nonlinear acoustic field on the piezoelectric disk responses. The aim of this investigation is to understand the effects of multiple frequency components in the nonlinear acoustic wave on the receiver's electrical response. Such an investigation is particularly useful when these multiple frequency components become significant due to the inherent nature of the medium such as a high value of β or due to high input power to the transducer, Fig. 6.5. A nonlinear acoustic wave can also be intentionally

generated by sending a multi-frequency input signal to a transmitter. To model the nonlinear acoustic field, the experimentally-validated KZK model, in section 6.2, is used based on the medium (e.g., water) and source parameters (e.g. HIFU), for the setup shown in Fig. 6.2. An advantage of using the KZK model as compared to solving the acoustic wave equation in the FE based time-domain simulation is the computational efficiency of the former method. The KZK model solves the acoustic wave equation using finite difference techniques, with accurate predictions, Fig. 6.4. The model predicted nonlinear pressure field at the focal point is then implemented as an external incident pressure input to the FE formulation, $p_i = \sum p_i^e$, Eq. 14, in the form of its fourier components. This hybrid KZK-FE based model is then solved in COMSOL to estimate the electroelastic response of the disk in the time domain. Such an approach circumvents the heavy memory and computational time costs associated with solving a fully coupled acoustic-piezoelectric interaction in the time domain, using the FE approach.

To assess the effects of the nonlinear acoustic field, four case studies are constructed. It is assumed in all four case studies that the geometrical and material nonlinearities of the piezoelectric disk are not triggered. Besides, a constant damping ratio is assumed in all the case studies since the time-domain simulations do not allow for real-time update of structural damping when the higher frequency components of the disk are excited. However, the damping ratio might be different for different modes and can be considered in the proposed model. The KZK-FE hybrid model is implemented in COMSOL for all case studies, with the simulation setup having an axisymmetric water domain of 70 mm in radius. A perfectly matched boundary

layer of 3 mm is added. The disk is located at the center of the domain, and the KZK predicted focal pressure field is incident on the radial surface enclosed by Λ_1 boundary of the disk.

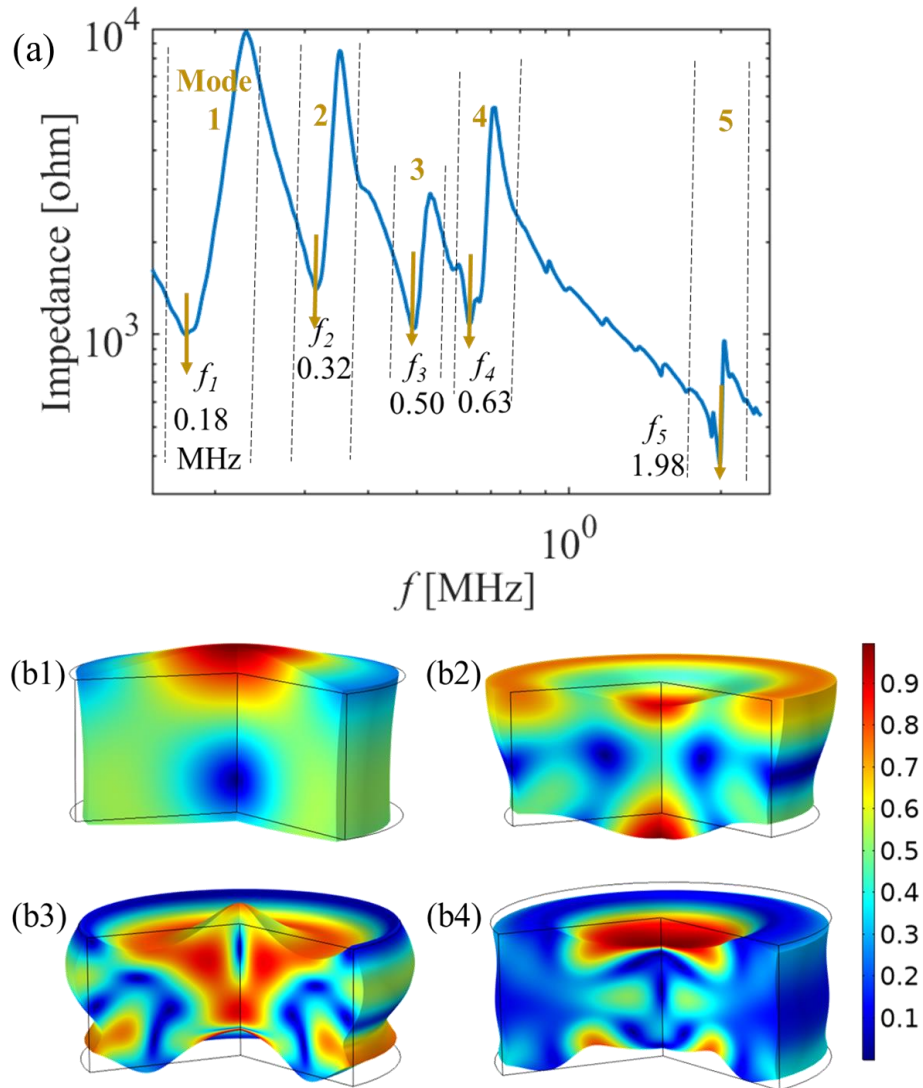


Fig. 6.8. (a) The electrical impedance curve of the APC 760 disk in water calculated from FE formulation include five dominant resonant modes of the APC760 piezoelectric disk. (b) Normalized displacement profiles of the acoustically excited disk obtained from the FE model for the first four short circuit resonant frequencies; (b1) 0.18, (b2) 0.32, (b3) 0.50, and (b4) 0.63 MHz. The normalization is done with respect to the maximum displacement in each case.

The first case study, referred to as M1, is a benchmark study where a linear pressure field is incident on the disk; since in most of the works in the literature, acoustic nonlinearities are not accounted and a pressure wave solution based on linear Helmholtz equation is used [51]. Accordingly, in the linear acoustic model, $\beta = 0$, in Eq. 2 of chapter 2, is used and higher acoustic harmonic components are not considered. Figs. 6.9a and 6.9b show the KZK-FE model-based response of the disk for M1. The values of the non-dimensional parameters that are set as $N = 0$ and $\bar{A} = 0.001$, in Eq. 2 of chapter 2. Due to the linear relation between acoustic and electroelastic model formulations, a mechanical excitation from linear acoustic wave gives a linear electrical response. Fig. 6.9a shows the KZK predicted incoming linear pressure wave, p_i , impinging on the disk and the resulting voltage response from the APC760 disk in the time domain. Fig. 6.9b shows the corresponding frequency domain response.

To understand the effect of higher harmonic components on the electroelastic response, the second case study, referred to as M2, is investigated. The acoustic source/input parameters remain the same as case study 1, however, the value of $\beta = 10$ is used to observe the nonlinear effects at a reasonable scale. Such high values of β is usually seen in fat tissues [56]. As shown in Fig. 6.5b, a high value of β increases the focal pressure amplitude that grows nonlinearly with the generation of higher harmonics in the acoustic field. The value of non-dimensional parameter accounting for the attenuation also remains equal to the value used in M1. Figs. 6.9c and 6.9d show the KZK predicted incident nonlinear pressure wave on the disk and the corresponding voltage response. The KZK predicted wave is first decomposed in its Fourier components and then only the first four components that have a considerable pressure amplitude

are used as an input to the FE formulation. The reason for considering only the first four components of the Fourier expansion is to save the computational cost. Since the structural response of the disk still needs to be solved in the time domain, it limits the maximum mesh size to one-sixth of the highest harmonic wavelength of the excitation force. Therefore, to account for such a fine mesh, the number of frequency components to evaluate this case study is restricted. It is seen that due to the presence of multi-frequency components, the voltage response also becomes nonlinear, obviously, having harmonics at the same frequencies as the incident acoustic field. However, an interesting feature in the response of the disk, Fig 9(d), is that the harmonic components of the voltage waveform are not monotonically decreasing. Because of a linear relation between excitation force and voltage response, this observation is contrary to the monotonically decreasing pattern of the acoustic pressure waveform, Fig. 6.9c, although material nonlinearity is not pronounced. The reason for this non-monotonous variation can be inferred from the impedance curve of the disk (Fig. 6.8a and Fig. D3). The acoustic harmonic components which coincide with the structural resonant short circuit frequencies of the disk are able to elicit a significant voltage response, which in M2 case study are the fundamental (~0.5 MHz) and the fourth harmonic (2 MHz) frequencies. It is seen in Fig. 6.9d that the second harmonic of voltage response is an order-of-magnitude lower, while the third harmonic is two orders lower than the fundamental component. Moreover, although the fourth acoustic harmonic has the lowest pressure amplitude, its corresponding voltage response is comparatively higher when compared to the voltage output from second and third harmonics of acoustic excitation. Due to the additional presence of fourth harmonic in voltage response, the average power output, P_w , 29.5 mW, is higher by 6.1% in this case study as compared to M1, 27.8 mW. However, the

increase in the average power is not significant since only the fourth acoustic harmonic which has the smallest pressure amplitude as compared to other harmonics is contributing effectively to the receiver excitation. The average power is calculated as $P_w = V_{rms}^2 / R_l$, where V_{rms} is the root mean squared (rms) voltage obtained from the time histories of voltage response.

From the observations of M2, it can be inferred that if a nonlinear acoustic field consists of frequency components coinciding with the resonant frequencies of the disk, the voltage response will increase. To verify this inference, the third case study, referred to as M3, is conducted. For M3, the same incident pressure field as in M2 is taken such that the total input energy from the HIFU transmitter remains the same; however, the frequencies of the higher harmonics are adjusted to coincide with the first four short-circuit resonant frequencies of the disk. Figs. 6.9e and 6.9f show this modified nonlinear pressure field and its corresponding voltage response. The average power, 51.5 mW, is significantly higher, by 75%, compared to the case studies M1 and M2. The relative magnitudes of the first to fourth frequency components of the voltage response in Fig. 6.9f, can also be easily understood by observing the impedance curve, Fig. 6.8a, and the magnitude of the acoustic frequency components in Fig. 6.9f. With the lowest impedance and the highest acoustic excitation amplitude, the amplitude of the first frequency component of the voltage output is highest in magnitude. Similar reasoning can explain the almost equal amplitude of the second and third frequencies in the voltage output. It is also seen that unlike the case study M2, the second, third and fourth frequency components of the voltage response are only an order lower as compared to the first component in M3, thus contributing to an increased voltage response than M2.

In previous case studies, the hybrid KZK-FE based model is used to predict the incident pressure field, which eliminates the computational cost of solving the nonlinear acoustic equation in the FE method. However, the structural response in the FE formulation is still solved in the time domain. This incurs a heavy computational cost in terms of memory and time. As a solution, it is proposed to solve the complete FE model in the frequency domain iteratively at each individual frequency of the nonlinear acoustic pressure field, such that the total voltage response, V_{tot} is

$$V_{tot} = \sum_{n=1}^4 V_n e^{i\omega_n t} \quad (18)$$

where V_n is the amplitude of the voltage response at the n^{th} component of acoustic excitation frequency, ω_n . Using Eq. 18, the KZK-FE model in the frequency domain reduces the simulation time from hours/days to minutes. This reduction is because the time domain simulations need to be solved at each time step, which is inversely proportional to the number of acoustic harmonics in the system, until a steady-state response is reached. Whereas in a complete frequency domain-based formulation, the simulations are solved only for pre-defined frequencies. However, this linear superposition, Eq. 18 is only possible when the natural frequencies of the modes are far apart, such that there is no mutual interference between the modes [48]. Also, the presence of any structural or geometrical nonlinearities can interfere with the neighboring frequency components of the acoustic wave, apart from the intended mode, and make the Eq. 18 invalid. To validate the complete frequency domain formulation, the pressure field of M3 is used. The frequency-domain FE model is solved for each of the four acoustic wave frequency components separately, and the individual voltage responses are shown in Fig. 6.10.

Since the frequency components of excitation waves are far apart, they excite only the intended resonant mode. The average power output in M4 is seen to be approximately equal to the power output of case study M3, 51.5 mW.

To summarize the four case studies, it is seen that as compared to a linear acoustic excitation, for the same given input power, a nonlinear excitation produces a higher power output in a UPT system. However, this increase in average power output is more significant when the frequencies of the higher overtones of the nonlinear acoustic wave coincide with the structural resonant frequencies of the disk. Consequently, not much increase in average power (6.2%) is observed between case studies M1 and M2. However, the average power increases significantly (75%) between case studies M2 and M3. It is to be noted that these values of the percentage increase in average output power between individual case studies may change when the constant damping ratio assumption is ignored, and separate damping ratios corresponding to each mode is employed. From these case studies, it can be concluded that accounting for acoustic nonlinearities that are either inherent in the system or generated intentionally, can lead to increased voltage response, as compared to assuming linear acoustic excitation. Moreover, case study M4 shows that the time domain nonlinear acoustic-structure interaction problem can be solved in a complete frequency domain and can reduce the computation time significantly.

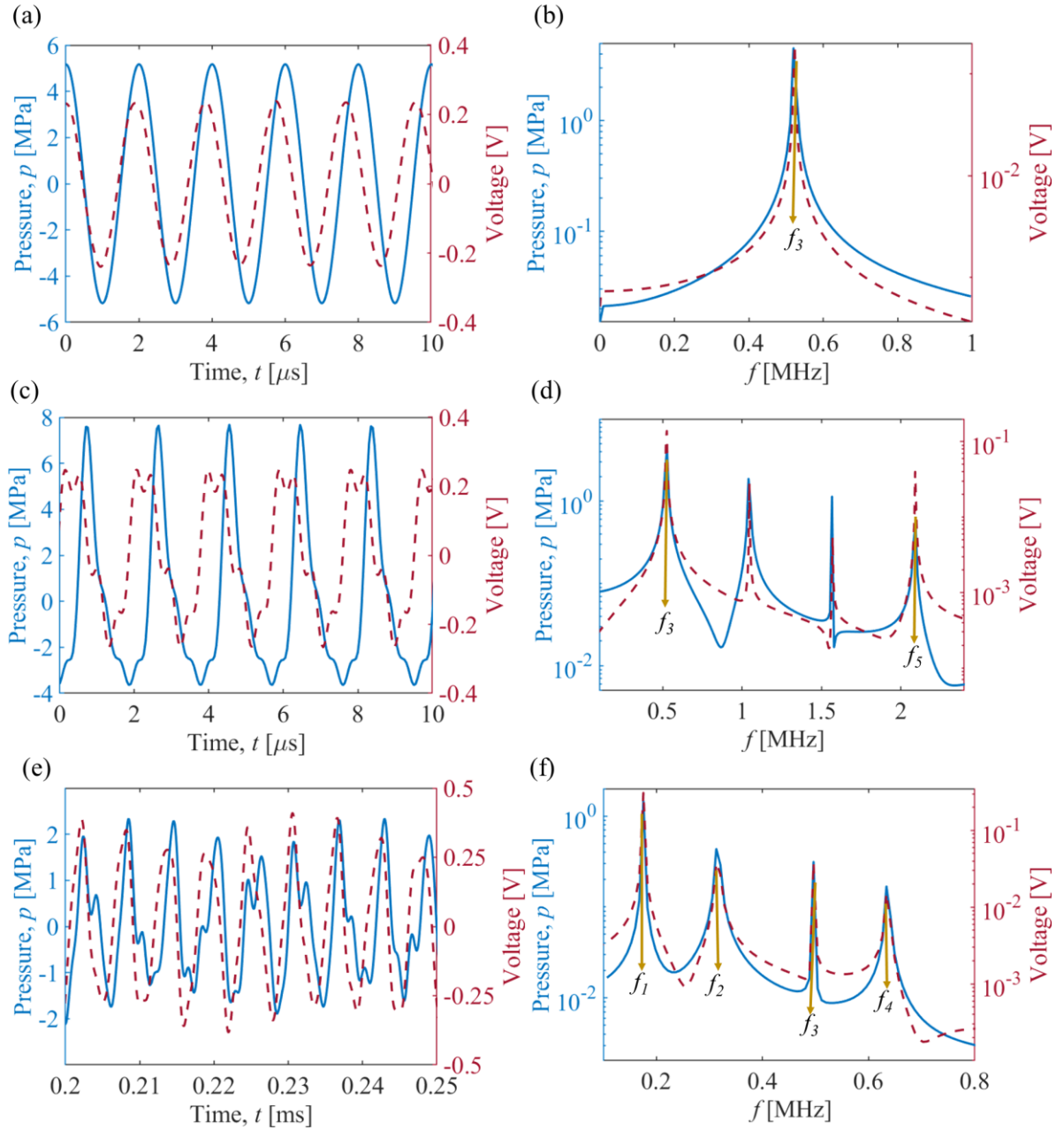


Fig. 6.9. The impinging pressure wave on the disk (solid blue line) and resulting voltage output (red dashed line) of the piezoelectric disk upon acoustic excitation in (a,c, and e) time domain and (b,d, and f) frequency domain, at $p_0 = 0.34$ MPa and $f = 0.5$ MHz ($f = \omega_0/2\pi$). Case studies M1, M2 and M3 are shown by (a)-(b), (c)-(d), and (e)-(f) respectively. The arrows in the frequency domain plots point to the corresponding structural resonant frequencies in Fig. 6.8a.

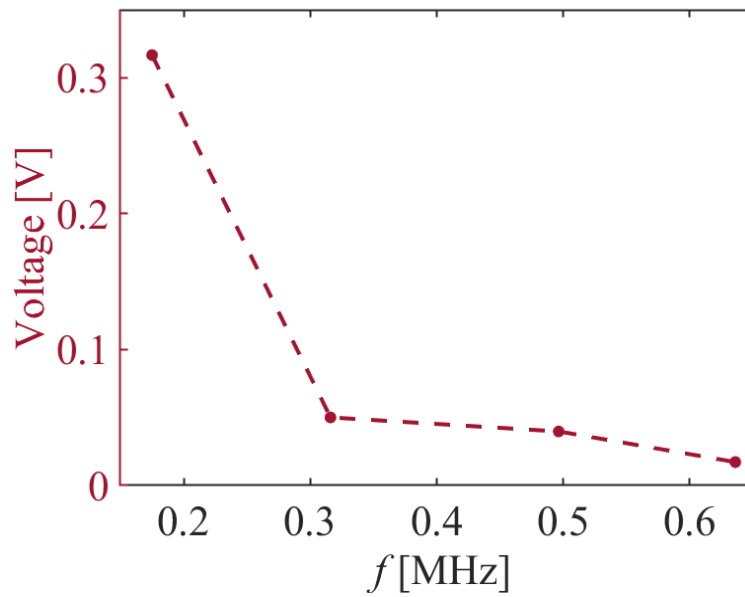


Fig. 6.10. Amplitudes of voltage output solved in the frequency domain for case study M4. The excitation frequencies and amplitudes of the incident pressure field are the same as the frequency components of the pressure field in case study M3.

Based on the conclusions drawn from the experimental and numerical investigations of the HIFU-UPT system, design recommendations for the three interwoven elements of the system are outlined. The first category consists of recommendations for the transmitter parameters. As seen in Eq. 2 of chapter 2 and section 6.3.1, a change in effective geometrical parameters of the transmitter (aperture radius and radius-of-curvature) can change the dimensions of the focal zone as well as the gain in the amplitude of the focal pressure. Knowledge of the focal zone dimensions is crucial for the selection of the receiver size to obtain maximum power output. Moreover, an increase in input voltage to the transmitter increases the amplitude of the focal pressure nonlinearly (Fig. 6.5a), which may result in increased power output based on the earlier discussion in section 6.3.4. The second category of design criteria is the acoustic parameters of

the wave propagating medium. A change in medium parameters, β and \bar{A} , affect the amplitude of the nonlinear pressure field at the focal point and consequently affect the output power response of the receiver. For example, to acoustically excite receivers placed inside the human body, the acoustic waves pass through multiple mediums with different values of acoustic parameters such as through fat ($\beta \approx 10$) and bones ($\bar{A} = 1.4$) [56]. As shown in Figs. 6.5b and 6.5c, high values of these parameters affect the amplitude of the acoustic field at the receiver. Thus, modeling of acoustic nonlinearity due to wave kinematics or medium is essential to design a HIFU-UPT system. The final category for designing criteria is the receiver parameters. Since in a FU field, the higher acoustic frequency components are harmonics, one possible scenario, in which they can actuate a receiver to yield significant power output, is when the structural resonance modes are harmonics of the fundamental mode. This is true for disks with a diameter-to-thickness ratio of less than 0.1 and greater than 20 [21, 36]. For such disks, the frequencies of the acoustic harmonics can coincide with the structural resonant modes of the disk to give a significant power output, as discussed in section 6.3.4. Besides, the receiver's power output can further be increased by adding matching layers and rectifier circuits, as proposed in [6].

Conclusions

We propose a novel concept of using HIFU technology in UPT, for focusing the transmitted energy in space. This configuration strongly excites the receiver with dramatically reduced levels of energy input to the source in comparison to the case of unfocused power transmission, i.e., spherical and cylindrical sources. In a HIFU-UPT system, one of the dominant origins of nonlinearity is acoustic nonlinearity due to wave kinematics in HIFU fields. As the acoustic

wave propagates towards the receiver, the wave distorts and becomes nonlinear with the generation of higher harmonics. In this work, the nonlinear acoustic field is calculated using the KZK equation for a focused source by considering the effects of diffraction, absorption, and nonlinearity in the medium. The pressure field obtained from the KZK model is used as an input to an FE-based acoustic-structure interaction formulation employed in COMSOL multiphysics.

The current studies for modeling UPT systems remain limited in capability due to three main assumptions. The assumptions are: (1) The piston-like deformation is assumed for the thickness mode. This assumption converts the two-dimensional axisymmetrical displacement of the disk to a one-dimensional one and significantly simplifies the model. However, it fails for a finite-size (diameter-to-thickness ratio is greater than 0.1 and less than 20) transmitter or receiver, because the response of finite-size disks depends both on radial and thickness directions. (2) A linear acoustic field is assumed, which considers that all the energy is concentrated in the fundamental frequency component; thus, ignoring the effects of medium nonlinearity, diffraction, and absorption. (3) The acoustic-structure interaction effects on the receiver disk which include reflected, scattered and blocked acoustic pressure distributions arising from the acoustic boundary conditions, are neglected. All these assumptions may lead to an inaccurate estimation of power output from the receiver. This study aims to present a comprehensive model without taking these assumptions. The experimentally-validated FE multiphysics modeling approach aims at filling a knowledge gap by considering the coupling of the acoustic nonlinear effects on the electroelastic response that lead to structural resonances of a finite-size piezoelectric disk receiver placed in a nonlinear dispersive medium. It is assumed that no geometric or material

nonlinearities are triggered in the piezoelectric disk receiver. However, the modeling and identification of electroelastic nonlinearities in UPT systems [57] can be combined with the proposed framework in this chapter. The results show that the existence of the HIFU high-level excitation can cause disproportionately large responses in the piezoelectric receiver if the frequency components in the nonlinear acoustic field coincide with the structural resonant frequencies of the receiver. These acoustic frequency components are significantly influenced by the wave kinematics that increases the power output from a receiver for an efficient UPT system.

Moreover, it is realized that by implementing the FE formulation in the frequency domain instead of the time domain for estimating the structural response of the receiver, the computational cost can be significantly reduced. This frequency-domain formulation is based on the linear superposition of voltage responses obtained from individual frequency components of the nonlinear acoustic incident field on the disk. The superposition is possible under the assumption that excitation frequencies are well separated to avoid mutual modal interference. The investigations of this work aim to provide a guide for all those systems where piezoelectric disks of finite aspect ratios are operating in a nonlinear acoustic sound field.

Appendix D

Y , e and, ε are the 6×6 elastic modulus at the constant electric field, 3×6 piezoelectric coupling, and 3×3 permittivity matrices for isotropic piezoelectric materials, given as

$$Y = \begin{pmatrix} Y_{11} & Y_{12} & Y_{13} & 0 & 0 & 0 \\ Y_{21} & Y_{22} & Y_{23} & 0 & 0 & 0 \\ Y_{31} & Y_{32} & Y_{33} & 0 & 0 & 0 \\ 0 & 0 & 0 & Y_{44} & 0 & 0 \\ 0 & 0 & 0 & 0 & Y_{55} & 0 \\ 0 & 0 & 0 & 0 & 0 & Y_{66} \end{pmatrix}, e = \begin{pmatrix} 0 & 0 & 0 & 0 & e_{15} & 0 \\ 0 & 0 & 0 & e_{24} & 0 & 0 \\ e_{31} & e_{32} & e_{33} & 0 & 0 & 0 \end{pmatrix} \text{ and}$$

$$\varepsilon = \begin{pmatrix} \varepsilon_{11} & 0 & 0 \\ 0 & \varepsilon_{22} & 0 \\ 0 & 0 & \varepsilon_{33} \end{pmatrix}$$

where $Y_{11} = Y_{22}$, $Y_{12} = Y_{21}$, $Y_{23} = Y_{32} = Y_{13} = Y_{31}$, $Y_{44} = Y_{55}$ and $Y_{66} = (Y_{11} - Y_{12})/2$. In the electrocoupling matrix, $e_{31} = e_{32}$ and $e_{24} = e_{15}$. For permittivity matrix, $\varepsilon_{11} = \varepsilon_{22}$ holds true.

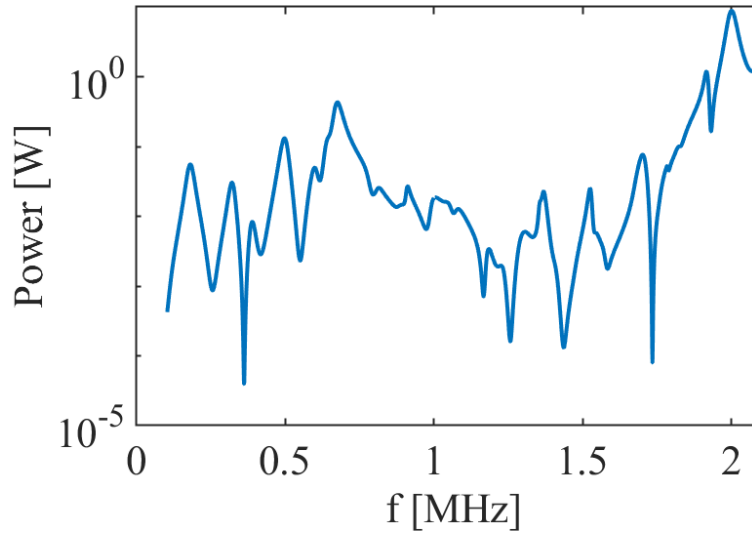


Fig. D1. Normalized power output of the APC 760 disk on acoustic excitation. The incident pressure amplitude is equal for all frequencies and normalization is done with respect to maximum power.

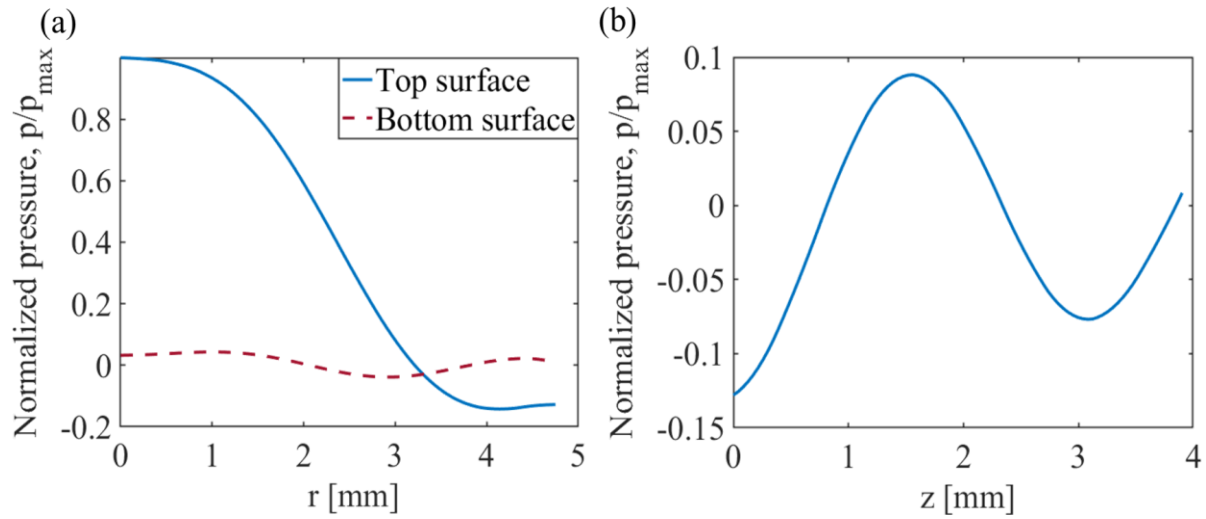


Fig. D2. Normalized pressure profile at the (a) top and bottom radial surfaces and (b) circumferential surface of the disk. The normalization is done with respect to the maximum pressure from the three profiles.

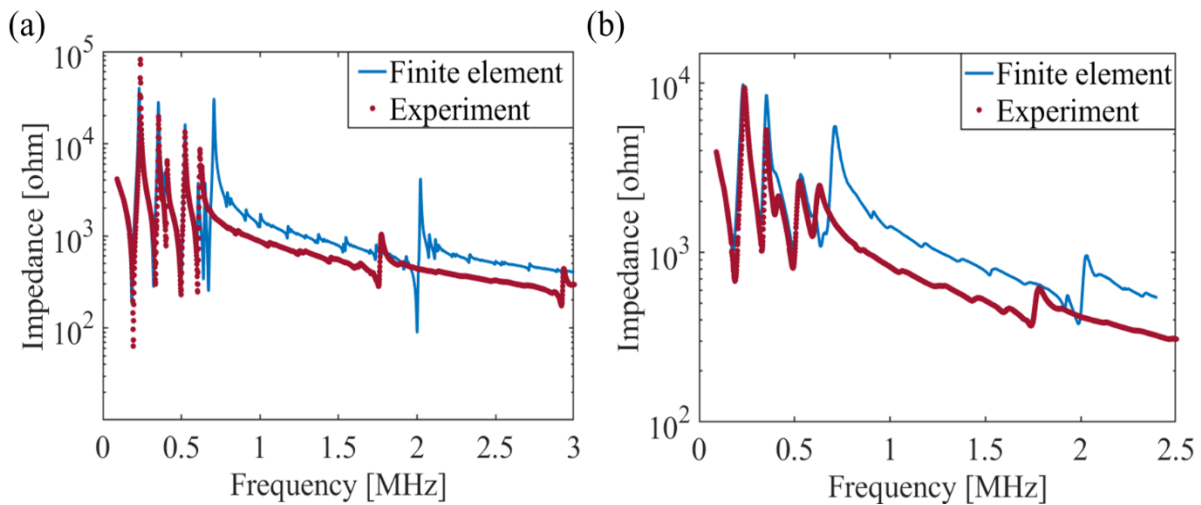


Fig. D3. Electrical impedance curves obtained from finite element simulations (solid line) and experiments (dotted line) in (a) air and (b) water, for the APC760 disk.

References

1. M. R. Awal, M. Jusoh, T. Sabapathy, M. R. Kamarudin and R. A. Rahim, *International Journal of Antennas and Propagation* **2016**, 14 (2016).
2. B. Hamid, B. C. David and R. Shad, *Smart Mater. Struct.* **25** (12), 123001 (2016).
3. M. G. L. Roes, J. L. Duarte, M. A. M. Hendrix and E. A. Lomonova, *IEEE Transactions on Industrial Electronics* **60** (1), 242-248 (2013).
4. T. Zaid, S. Saat, Y. Yusop and N. Jamal, presented at the 2014 International Conference on Computer, Communications, and Control Technology (I4CT), 2014.
5. F. Mazzilli, M. Peisino, R. Mitouassiou, B. Cotte, P. Thoppay, C. Lafon, P. Favre, E. Meurville and C. Dehollain, *Conference proceedings : ... Annual International Conference of the IEEE Engineering in Medicine and Biology Society. IEEE Engineering in Medicine and Biology Society. Annual Con* **2010**, 3751-3754 (2010).
6. S. Ozeri and D. Shmilovitz, *Ultrasonics* **50** (6), 556-566 (2010).
7. S. Ozeri, D. Shmilovitz, S. Singer and C. C. Wang, *Ultrasonics* **50** (7), 666-674 (2010).
8. G. V. B. Cochran, M. P. Kadaba and V. R. Palmieri, *Journal of Orthopaedic Research* **6** (1), 145-147 (1988).
9. K. Hideyuki, K. Tamotsu, S. Hideo, S. Osami and K. Kazuhito, *Jpn. J. Appl. Phys.* **40** (5S), 3865 (2001).
10. A. Sanni, A. Vilches and C. Toumazou, *IEEE Transactions on Biomedical Circuits and Systems* **6** (4), 297-308 (2012).
11. X. Bao, W. Biederman, S. Sherrit, M. Badescu, Y. Bar-Cohen, C. Jones, J. Aldrich and Z. Chang, presented at the SPIE Smart Structures and Materials + Nondestructive Evaluation and Health Monitoring, 2008.
12. D. J. Graham, J. A. Neasham and B. S. Sharif, *IEEE Transactions on Industrial Electronics* **58** (10), 4972-4980 (2011).
13. Y. Hu, X. Zhang, J. Yang and Q. Jiang, *IEEE Transactions on Ultrasonics, Ferroelectrics, and Frequency Control* **50** (7), 773-781 (2003).
14. P. Valdastrì, E. Susilo, T. Forster, C. Strohhofer, A. Menciassi and P. Dario, *IEEE Transactions on Biomedical Engineering* **58** (6), 1846-1854 (2011).

15. Y. Vaiarello, W. Tatinian, Y. Leduc, N. Veau and G. Jacquemod, *IEEE Journal on Emerging and Selected Topics in Circuits and Systems* **1** (4), 622-630 (2011).
16. T. Maleki, N. Cao, S. H. Song, C. Kao, S. Ko and B. Ziaie, *IEEE Transactions on Biomedical Engineering* **58** (11), 3104-3111 (2011).
17. Q. Shi, T. Wang and C. Lee, *Scientific Reports* **6**, 24946 (2016).
18. D. Seo, J. M. Carmena, J. M. Rabaey, M. M. Maharbiz and E. Alon, *Journal of neuroscience methods* **244**, 114-122 (2015).
19. C. Mo, S. Hudson and L. J. Radziemski, presented at the SPIE Smart Structures and Materials+ Nondestructive Evaluation and Health Monitoring, 2013.
20. S. Ozeri, D. Shmilovitz, S. Singer and C.-C. Wang, *Ultrasonics* **50** (7), 666-674 (2010).
21. S. Shahab, M. Gray and A. Erturk, *Journal of Applied Physics* **117** (10), 104903 (2015).
22. M. G. L. Roes, M. A. M. Hendrix and J. L. Duarte, presented at the 2012 IEEE Energy Conversion Congress and Exposition (ECCE), 2012.
23. S. Shahab and A. Erturk, *Smart Materials and Structures* **23** (12), 125032 (2014).
24. M. Bakhtiari-Nejad, A. Elnahas, M. R. Hajj and S. Shahab, *Journal of Applied Physics* **124** (24), 244901 (2018).
25. M. Bakhtiari-Nejad, A. Elnahas, M. R. Hajj and S. Shahab, *Passive metamaterial-based acoustic holograms in ultrasound energy transfer systems*. (SPIE, 2018).
26. J. Kost, K. Leong and R. Langer, *Proceedings of the National Academy of Sciences* **86** (20), 7663-7666 (1989).
27. B. G. De Geest, A. G. Skirtach, A. A. Mamedov, A. A. Antipov, N. A. Kotov, S. C. De Smedt and G. B. Sukhorukov, *Small* **3** (5), 804-808 (2007).
28. D. G. Shchukin, D. A. Gorin and H. Möhwald, *Langmuir* **22** (17), 7400-7404 (2006).
29. G. Ter Haar, *Prog. Biophys. Mol. Biol.* **93** (1), 111-129 (2007).
30. B. C. Towe and R. Rho, *IEEE Transactions on Biomedical Engineering* **53** (7), 1446-1448 (2006).
31. T. S. Hart and M. F. Hamilton, *The Journal of the Acoustical Society of America* **84** (4), 1488-1496 (1988).

32. A. Bhargava, K. Peng, R. Mirzaeifar and S. Shahab, presented at the SPIE Smart Structures and Materials + Nondestructive Evaluation and Health Monitoring, Denver, USA, 2018.
33. A. Bhargava, K. Peng, J. Stieg, R. Mirzaeifar and S. Shahab, presented at the ASME 2017 Conference on Smart Materials, Adaptive Structures and Intelligent Systems, Utah, USA, 2017.
34. M. G. Roes, J. L. Duarte, M. A. Hendrix and E. A. Lomonova, IEEE Transactions on Industrial Electronics **60** (1), 242-248 (2013).
35. M. F. Hamilton and D. T. Blackstock, *Nonlinear acoustics*. (Academic press, San Diego, 1998).
36. H. O'Neil, The Journal of the Acoustical Society of America **21** (5), 516-526 (1949).
37. J. E. Sonesson, AIP Conference Proceedings **1481** (1), 357-361 (2012).
38. N. Guo, P. Cawley and D. Hitchings, Journal of Sound and Vibration **159** (1), 115-138 (1992).
39. T. R. Kane and R. D. Mindlin, *High frequency extensional vibrations of plates*. (Columbia university, Department of Civil Engineering and Engineering Mechanics, 1955).
40. S. Ikegami, I. Ueda and S. Kobayashi, The Journal of the Acoustical Society of America **55** (2), 339-344 (1974).
41. A. Bhargava and S. Shahab, Smart Materials and Structures **28** (5), 055002 (2019).
42. A. Bhargava, K. Peng and S. Shahab, presented at the SPIE Smart Structures + Nondestructive Evaluation, 2019.
43. Y. S. Lee and M. F. Hamilton, The Journal of the Acoustical Society of America **97** (2), 906-917 (1995).
44. W. F. Ames, *Numerical methods for partial differential equations*. (Academic press, 2014).
45. A. Bhargava, K. Peng, J. Stieg, R. Mirzaeifar and S. Shahab, RSC Advances **7** (72), 45452-45469 (2017).
46. A. Erturk and D. J. Inman, *Piezoelectric energy harvesting*. (John Wiley & Sons, 2011).
47. D. J. Leo, *Engineering Analysis of Smart Material Systems*. (Wiley, 2007).

48. F. Fahy and P. Gardonio, (Elsevier).
49. J. N. Reddy, New York (1993).
50. S. A. Ragab and H. E. Fayed, *Introduction to Finite Element Analysis for Engineers*. (CRC Press, 2017).
51. L. E. Kinsler, A. R. Frey, A. B. Coppens and J. V. Sanders, *Fundamentals of Acoustics*, 4th Edition, by Lawrence E. Kinsler, Austin R. Frey, Alan B. Coppens, James V. Sanders, pp. 560. ISBN 0-471-84789-5. Wiley-VCH, December 1999., 560 (1999).
52. M. S. Canney, M. R. Bailey, L. A. Crum, V. A. Khokhlova and O. A. Sapozhnikov, *The Journal of the Acoustical Society of America* **124** (4), 2406-2420 (2008).
53. W. P. Mason, *The Journal of the Acoustical Society of America* **28** (6), 1197-1206 (1956).
54. R. Kishore, *Physical Review* **173** (3), 856-859 (1968).
55. L. Meirovitch, *Fundamentals of Vibrations*. (Waveland Press, 2010).
56. D. G. F. Hasgall PA, Baumgartner C, Neufeld E, Lloyd B, Gosselin MC, Payne D, Klingenböck A, Kuster N, (2018).
57. V. C. Meesala, M. R. Hajj and S. Shahab, *Nonlinear Dynamics* (2019).

Chapter 7 : Focused ultrasound for enhanced wireless power transmission; experimental investigation

Details of publication

Co-authors: Vamsi C. Meesala and Shima Shahab

Citation: Bhargava, A.*, Meesala, V.C.*, and Shahab, S., 2020, Investigation of nonlinear effects in ultrasonic power transfer systems in focused ultrasound fields, **(to be submitted)**.

(*equal contribution)

Abstract

The demand for wireless power transmission has exponentially increased, particularly in sensitive or remote applications. Among all the techniques to wirelessly transmit power, ultrasonic power transfer (UPT) has emerged as one of the most promising techniques. The mechanism of UPT involves transmission of acoustic waves from an acoustic transmitter, that propagate in a medium to actuate a piezoelectric receiver and generate a vibration-induced electrical response. Despite its many advantages, challenges associated with low power transfer efficiency and scattering losses of planar and spherical acoustic waves hinder the widespread usage of this technology. This work proposes to solve these issues by introducing the use of high intensity focused ultrasound (HIFU) in UPT systems. HIFU focuses the entire source energy in a concentrated region at the receiver location, generating the same level of output response with dramatically lower levels of input energy as compared to unfocused sources. This work

addresses the dynamics of the UPT in acoustically nonlinear spatially resonant conditions in a HIFU field. The investigation shows that at high levels of source excitation, the interplay of standing waves, appearance of higher acoustic harmonics, and piezoelectric material nonlinearities can change the location of maximum power output position (MPOP) of the receiver, away from the focus. Thus, in-depth understanding and accounting for this shift in MPOP becomes necessary for designing efficient HIFU-UPT systems.

Ultrasonic power transfer (UPT) has emerged as a promising technique to wirelessly transfer energy in many applications including biomedical devices [1, 2], data delivery [3, 4], and through-wall transmission [5-7]. A UPT system consists of a piezoelectric transducer that converts electrical energy to vibration-induced acoustic waves, that propagate in a medium to actuate a piezoelectric receiver which generates electrical response [8]. The ability of ultrasound waves to travel longer distances, have lower attenuation, enable flexibility in the receiver/transmitter size due to shorter wavelengths, undergo no electromagnetic losses, and be biologically safe [9] has made UPT favorable over traditional wireless energy-transfer techniques, namely capacitive, inductive, and microwave-based methods. However, low power transfer efficiency and spreading losses from planar and spherical acoustic sources are few of the key challenges that prevent the growth of UPT technology [9]. To address these issues, this study proposes to combine high intensity focused ultrasound (HIFU) with UPT. HIFU provides the benefit of focusing acoustic energy in a tight localized focal spot, at the receiver location [10]. Thus, the use of HIFU increases the efficiency of the system and eliminates the scattering losses suffered by spherical or planar waves.

When operated for durations longer than $3\bar{z}/c_0$, where \bar{z} is the distance between surfaces of the transmitter and receiver, and c_0 is the speed of sound in the medium, standing waves form due to reflections from the two surfaces. These standing waves play a significant role in changing the location for maximum power output from the receiver under resonant conditions, thus affecting the UPT performance. In addition, the standing waves become increasingly nonlinear under high source excitation levels. This nonlinearity is due to the generation of higher harmonics and distortion of the standing wave profile arising from the inherent nonlinearity property of the medium [11]. This understanding of the nonlinear effects is important to prevent the operation of the UPT system under acoustic saturation that leads to a decrease in the efficiency of the system. Acoustic saturation represents the conditions when pressure field at a certain point becomes independent of the input excitation to the source and the pressure at the observation point reaches a maximum threshold value [12-14].

While several works have investigated the nonlinear acoustic resonant phenomena [15-17], this work reports the dynamics of focused acoustic resonant field in HIFU-UPT systems, for the first time. The wave distortion is more complex and pronounced in a focused pressure field due to combined nonlinear and diffraction effects, especially in the focal region. This results in acoustic saturation at lower source intensities as compared to planar standing wave fields [13]. Fig. 7.1 presents a schematic outlining the operation of the HIFU-UPT system under nonlinear resonant conditions. Only the fundamental component of the nonlinear pressure field plays the dominant role in determining the disk response due to coincidence with only one of the structural resonant frequencies of the disk, in this study [18]. Due to acoustic nonlinear effects, the amount of

energy transfer from the fundamental to higher harmonics is maximum at the focal point and decreases away from that point. This phenomenon along with the standing wave effect plays a crucial role in determining the maximum power output position (MPOP) of the disk in a spatially resonant HIFU field.

To investigate the dynamic response of the disk under focused nonlinear acoustic resonant conditions in a UPT system, an experiment is designed as shown in Fig. 7.2. A H-104-4A SONIC Concepts HIFU transducer is kept at one end of a $61.5 \times 31.8 \times 32.5 \text{ cm}^3$ water tank which is lined with absorbing sheets to prevent reflection from tank boundaries. The transducer is connected with a signal generator. The tank is filled with deionized water to prevent electrical short-circuiting. In the first step, a Precision Acoustics 1mm needle hydrophone is suspended using a positioning system, to map the HIFU pressure field and identify the focal point, Fig. 7.2b. The hydrophone is connected to an oscilloscope via a DC coupler, which conditions the hydrophone output signal and also supplies power. The oscilloscope is connected to a computational unit and the data is processed in MATLAB. To record the pressure field, HIFU is operated at 0.5 MHz with a 80 μs burst signal and 5 ms of burst period. In the second step, the hydrophone is replaced with a 3.9 mm thick and 9.5 mm wide cylindrical disk suspended at the focal point, Fig. 7.2c. The HIFU operating conditions are changed to 1.4 ms of burst signal with 1 s of burst period, to record the disk response. The duration is long enough to generate a standing wave between the HIFU transducer and the disk at the focal point. The disk is connected to an optimum load resistance of 1000 Ω . A separate experiment is performed to find

the optimum load resistance by sweeping load resistance from 10Ω - $1 \text{ M}\Omega$ and locating the load for maximum power output.

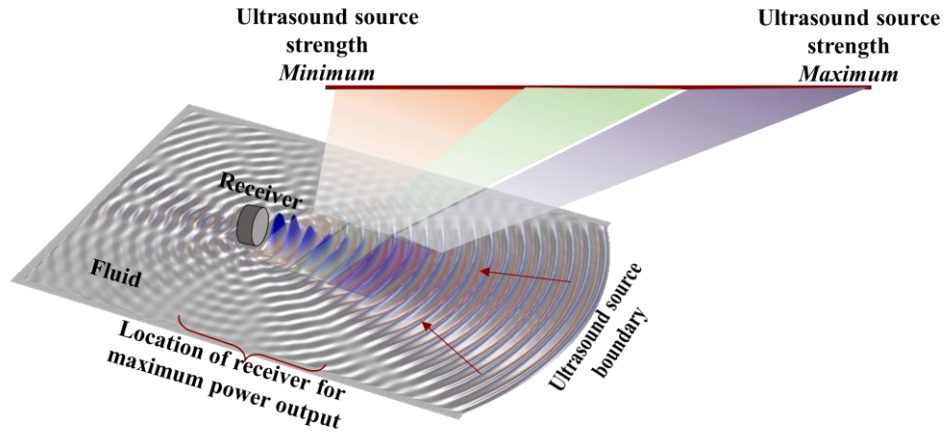


Fig. 7.1. Schematic illustrating the change in location of maximum power output from receiver with increasing level of HIFU source excitation

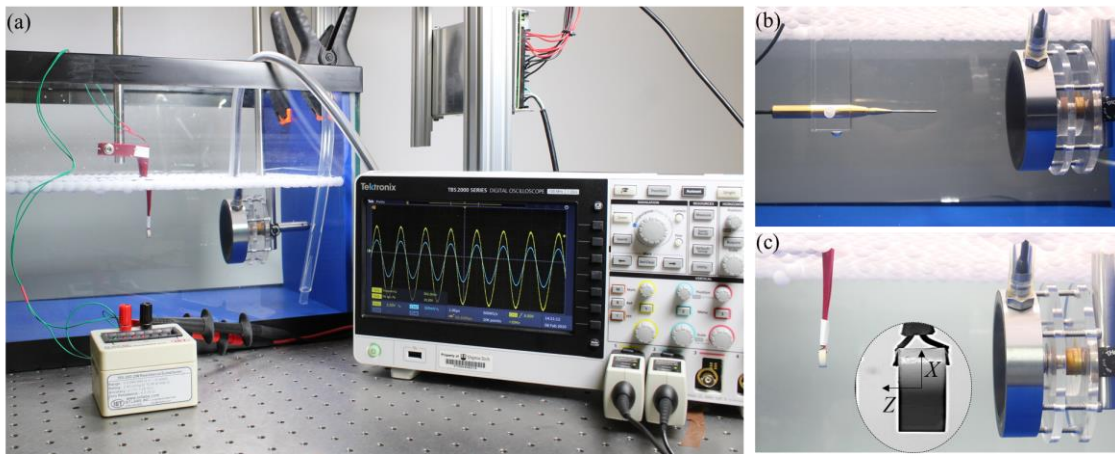


Fig. 7.2. (a) The experimental setup for obtaining the disk response in an acoustic nonlinear resonant HIFU field. Magnified images show (b) the hydrophone where the tip of the needle is the pressure recording entity, and (c) the APC disk suspended at the focal point. The axial axis is denoted as Z and radial axis with X . The focal point is marked as $z = 0$ with negative scale towards the transducer, where z is the distance along the axial axis.

Figures 7.3a and 7.3c show the source input voltage to the HIFU, and Figs. 7.3b and 7.3d show the corresponding output voltage of the disk. The increasing levels of source excitation are labelled as C1-C10. The increase in excitation is achieved by increasing the input from signal generator and recording the input voltage across the transducer, Figs. 7.3a and 7.3c. As the disk traverses along the axial axis, both the HIFU input voltage and disk output voltage fluctuate, exhibiting a typical pattern of a standing wave field with minima (nodes) occurring at $\lambda/2$ distances with $\lambda = c_0/f_0$ (f_0 = source excitation frequency). It is seen that MPOP for low source inputs, C1-C2, is at the focal point, $z = 0$. This behavior is logical as the maximum energy concentration is at the focal point. However, as the source excitation level is increased, the MPOP shifts in negative axial axis towards the transducer, C3-C5. With further increase in input power to the HIFU, the MPOP stops shifting and remains approximately at the same position for C6-C10. The shift in MPOP is contradictory to the logic behind focused excitation, where the focal spot has the highest energy concentration and should result in maximum power output from the disk at all excitation levels [11, 14, 19]. From a designing perspective, this is an important parameter to consider for building efficient UPT systems.

To understand the physical reasoning behind the MPOP shift with increasing source excitation, three axial zones are created defined as zone 1: $z = 0.1$ cm to $z = -0.08$ cm, zone 2: $z = -1.39$ cm to $z = -3$ cm, and zone 3: $z = -4.9$ cm to $z = -7$ cm. The basis for creating these zones is that the MPOP shifts slightly in a random manner, particularly at very high source excitation of C6-C10, although the general trend of shifting is toward the transducer. This slight random shift is possibly due to the triggering of material nonlinearities at high acoustic pressure

levels [20], both in HIFU transducer and receiver disk. These material nonlinearities change the phase of the reflected waves, thus changing the location of the constructive interference of these waves slightly. Thus, three zones are created that contain the locations of MPOP at all excitation levels. Figure 7.4 shows the variation of output voltage with increasing input HIFU excitation for these zones. Based on the interplay of acoustic resonance and nonlinear effects, three regions are identified as linear (L), transition (T) and saturation (S).

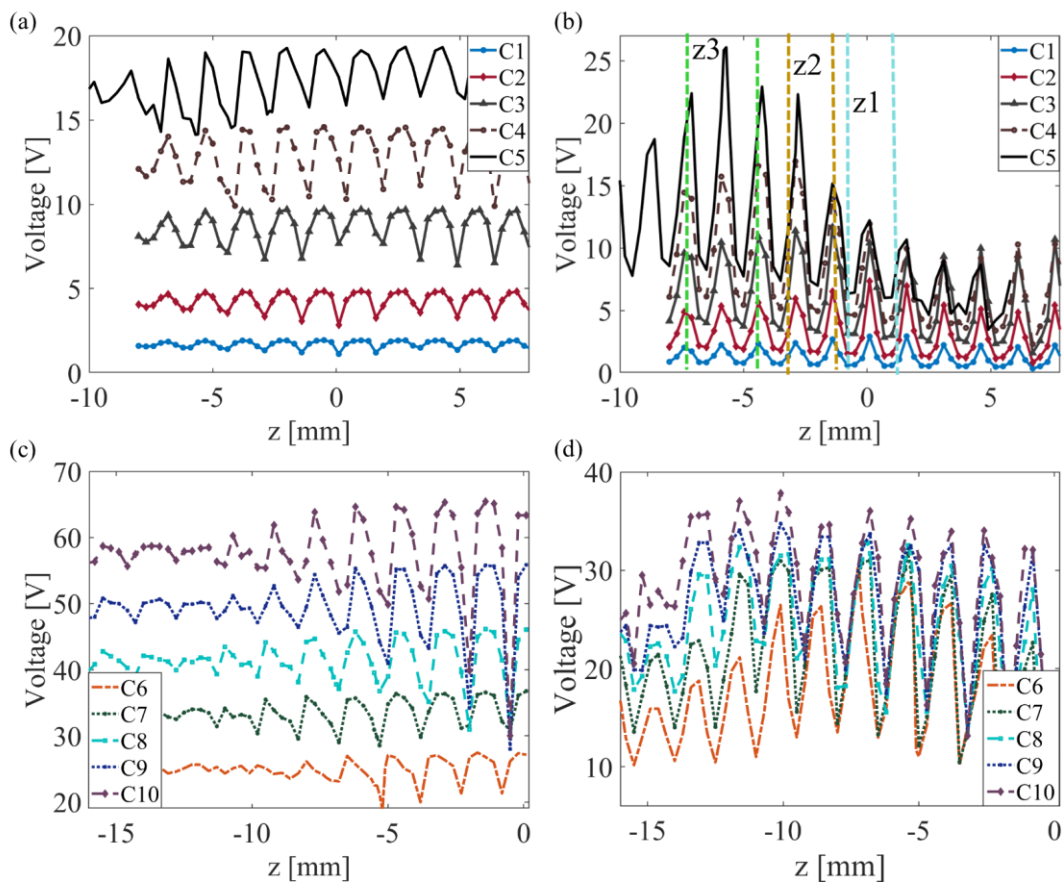


Fig. 7.3. Increasing levels of input voltage to the HIFU transducer, (a) and (c). Corresponding output voltage of the disk (b) and (c). The measurements are obtained at different positions along the axial axis. In (b), z_1 =zone 1, z_2 =zone 2, and z_3 =zone 3. These zones are same for all (a)-(d) and group the positions on z axis.

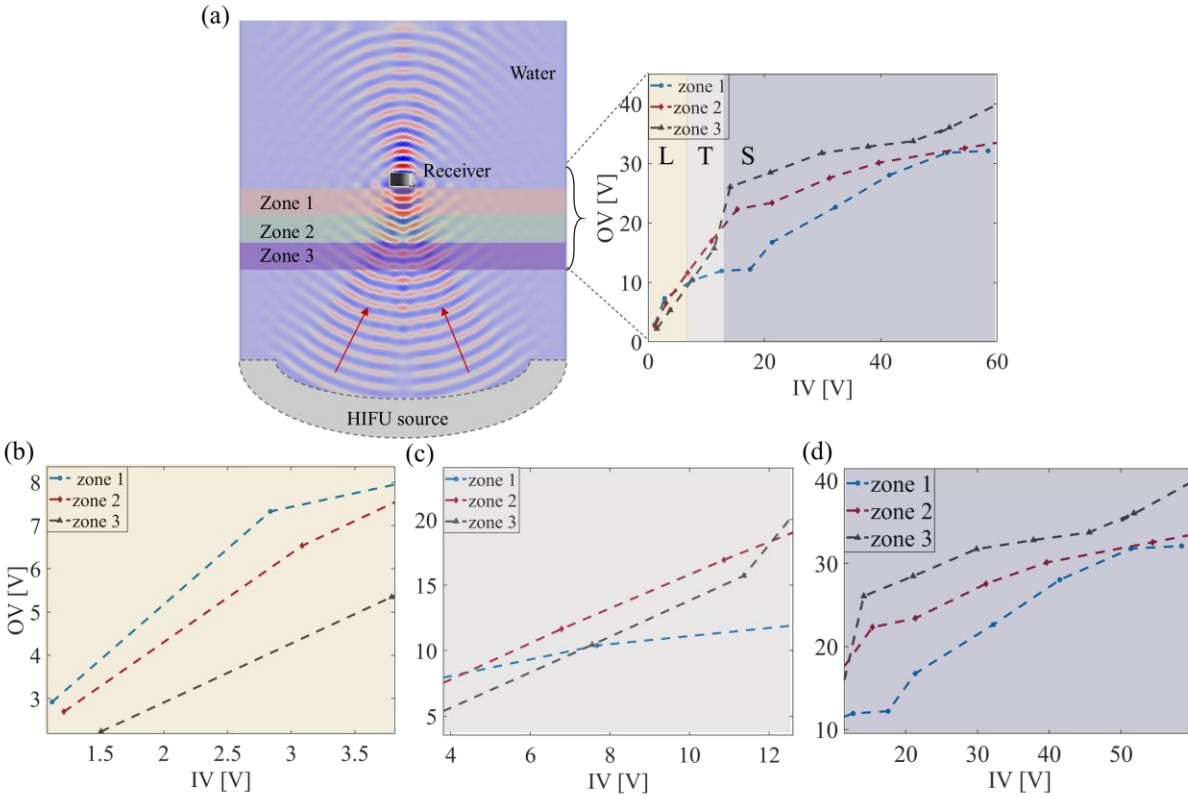


Fig. 7.4. Variation of disk response with different levels of source excitation. The bottom row shows the three regions of (b) linear (L), (c) transition (T), and (d) saturation (S) on a magnified scale.

The first region is the linear (L) region at low source excitation levels, Fig. 7.4b. In this region, the input power is significantly low to trigger any acoustic nonlinear effects. The pressure field at the focus is related to the source pressure through a linear gain, which is dependent on the geometrical parameters of the HIFU transducer [14, 21]. Figure 7.5 shows the axial and transverse (or radial) normalized pressure fields only in water, in the absence of the disk. Normalization is done with respect to the pressure at the source. The transverse (or radial) pressure field shows the pressure on the $z=0$ plane, parallel to the surface of the disk that is closer to the transducer. The axial pressure field in Fig. 7.5a shows that the maximum pressure is

at the focal point, and decreases away from it in either direction on the axial axis. Several studies have reported a similar trend which is characteristic of focused acoustic fields [14, 21, 22]. Consequently, as seen in L region of Fig. 7.4, the MPOP in this region is closest to the focal point i.e. zone 1, with a decrease in disk response in zone 2 and the lowest disk power output is seen in zone 3.

The nonlinear acoustic theoretical model developed by Bhargava *et al.* [10, 23] using Khokhlov Zabolotskaya-Kuznetsov (KZK) equation is validated with the experimental pressure fields, and shows good agreement in Fig. 7.5. This equation predicts the nonlinear pressure field taking into account diffraction, nonlinearity, and absorption effects of the medium. The equation in cylindrical coordinate system is given by Eq. 1 of chapter 2 and Ref. [24]. The first term in this equation represents the diffraction effects, the second term represents absorption with δ as the diffusivity parameter, and nonlinearity effects are denoted by the third term with β as the nonlinearity parameter. Absorption results in decrease in the amplitude of the pressure field due to thermo-viscous attenuation in the medium. Whereas, nonlinearity of the medium causes a nonlinear increase of the pressure amplitude, especially at focus, due to the generation of higher harmonics as the wave propagates [11]. The KZK equation is solved using operator-splitting method in a hybrid time-frequency domain using finite difference techniques [10]. This experimentally-validated equation is used in later sections to understand the acoustic nonlinear effects.

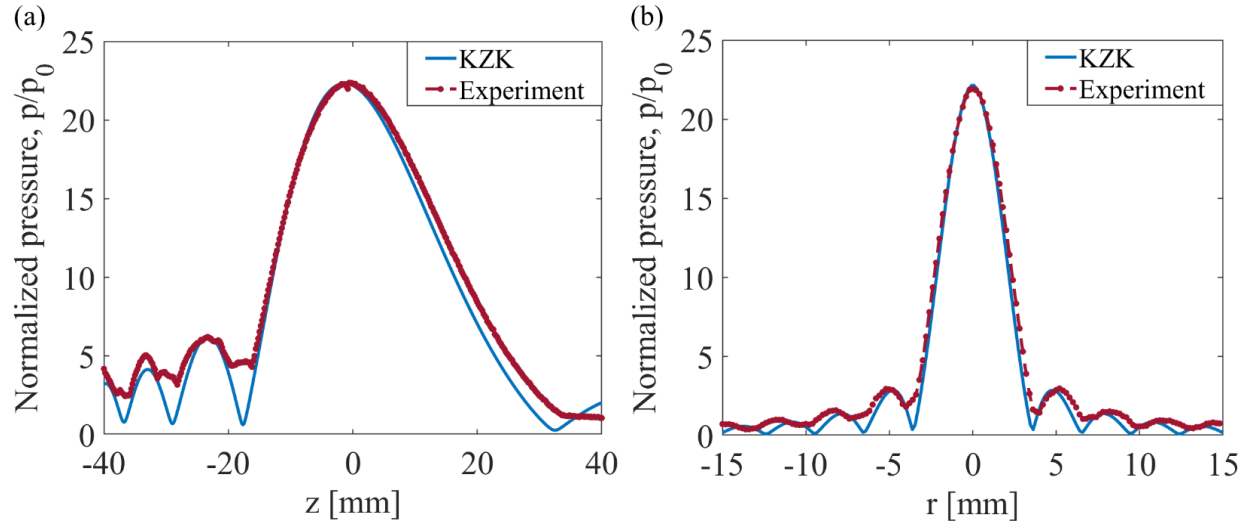


Fig. 7.5. (a) Axial and (b) transverse pressure fields of a HIFU source in water domain under linear conditions. The variable r denotes the radial distance along the along the radial axis, X , of the disk, with $r=0$ denoting the center of the disk. The variables p and p_0 denote pressure at any observation point and at source, respectively.

As the source excitation level increases, the response of the disk enters the transition zone (T) where acoustic nonlinearities become significant. In this region, the energy is transferred from fundamental to higher harmonics [11, 21]. Bhargava *et al.* [18] demonstrated that for a disk of finite aspect ratio, the amplitude of the disk output power depends on the number of acoustic harmonics coinciding with the structural resonant frequencies of the disk. With all acoustic harmonics coinciding with all resonant mode frequencies, the power output is maximum. The power output decreases as the number of coincident frequencies decreases since the entire energy of the acoustic field is not utilized by the disk (Fig. 4 of Ref [18]). For the current study, the HIFU operates at 0.5 MHz with its harmonics occurring at integer multiple of the source frequency. Fig. 7.5 shows the impedance of the disk in air and water. It can be seen that only the

resonant mode near 0.5 MHz coincide with the fundamental component of the HIFU field, while other modes do not coincide with the acoustic harmonics. Therefore, only fundamental pressure field contributes predominantly to the output response of the disk in water. Consequently, for further analysis in this study, only the fundamental acoustic pressure is considered.

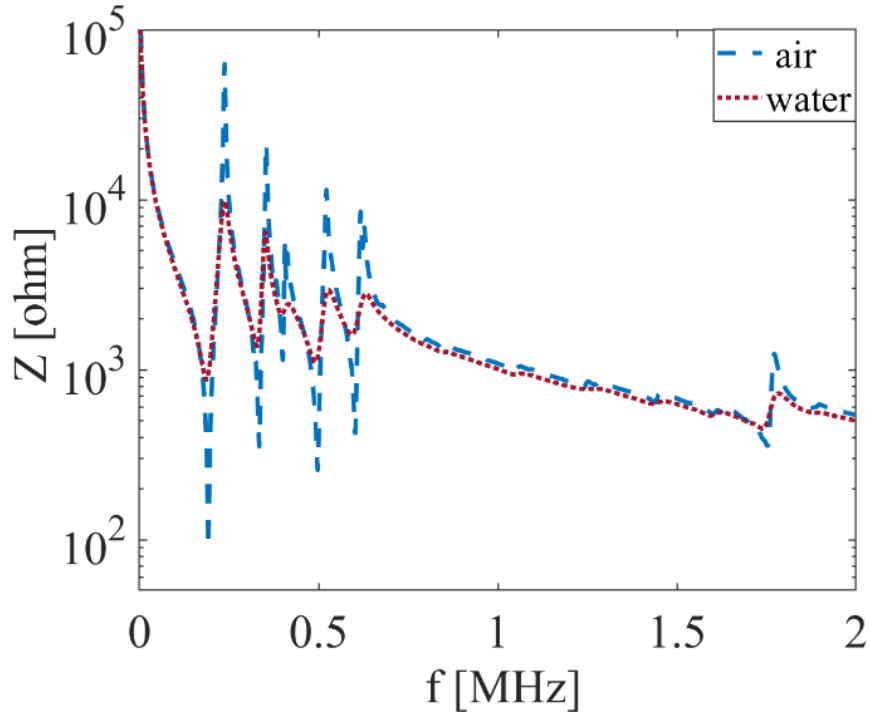


Fig. 7.6. Impedance, Z , of the APC 760 disk in air and water.

As a result of energy transfer to higher harmonics, the amplitude of the fundamental component of the pressure field does not increase proportionally to the increase in input source level; the ratio of increase of the fundamental component is less than the ratio of increase in input source level [25]. Due to cumulation of nonlinear effects with distance and focusing of the pressure field, the energy transfer occurs maximum at the focal point. This transfer lowers for distances

away from the focus leading to a higher ratio of increase in the fundamental pressure amplitude with increase in input excitation, as compared to the ratio of increase in fundamental focal pressure [11, 21]. Thus, the pressure amplitude in zones 2 and 3 become comparable to the pressure in zone 1 at the intermediate excitation levels. Moreover, due to focusing effect, the beam area is the narrowest for zone 1 and the broadest for zone 3. As a combination of the trend of rise in pressure field and beam area in these zones, the effective forcing on the disk (integral of the transverse pressure over the surface of the disk) decreases and so does the power output from the disk with increase in input power to the HIFU, for positions closest to focal point. Figure 7.7 shows the fundamental component of the nonlinear pressure fields along radial axis at different axial distances from the transducer and at various source input voltages, calculated using Eq. 1 of chapter 2. It is seen that the transverse beam area of pressure field increases for positions further from zone 1. It is also observed that with increasing source excitation, the fundamental pressure rise occurs more slowly at the focus as compared to other points closer to the transducer. Similar observations were made by Muir *et al.* [13] for planar acoustic fields along the axial axis of a transducer. This phenomenon explains the trend of disk output voltage in the T region of Fig. 7.4a and 7.4c. With increasing input source power, the fundamental pressure-induced electrical response increases the least in zone 1, followed by zone 2 and the most in zone 3. Thus, with increasing input excitation the electrical response in zone 2 takes over zone 1 and finally, zone 3 observes the highest electrical response due to the least energy transfer from the fundamental pressure field and widest beam area.

In the last S region of Fig. 7.4, the response of the disk is determined by acoustic saturation. Unlike the acoustic saturation in travelling acoustic waves, the saturation threshold level is lower for standing wave fields. This is due to constructive interferences that lead to higher pressure levels as compared to travelling waves [26]. Under acoustic saturation conditions, no further increase is observed at the observation point with increase in source excitation due to nonlinear losses associated with acoustic shocks. Duck *et al.* [27] conducted radiation force measurements and showed that the losses in the pressure field at high excitation levels increase with distance from the transducer and are maximum at the focal point. Thus, the saturation pressure level is lowest at the focal point as compared to the points closer to the transducer. Similar observations were observed by Refs. [13, 25] for planar wave fields due to increasing nonlinear effects with distance. In addition, material nonlinearities, further decrease the response of the disk at higher excitation for a fixed excitation frequency [20].

The interplay of material nonlinearities, acoustic saturation and resonance explains the output response of the disk in the S region of Fig. 7.4. At high source excitation levels, all three zones reach acoustic saturation due to the saturation of the fundamental pressure field. However, due to maximum nonlinear effects at the focus, the nonlinear losses in zone 1 are highest and saturation level of the pressure field is lowest. This is followed by the saturation threshold of zone 2. Lastly, zone 3 has the highest saturation level due to relatively lower nonlinear effects, as compared to other zones.

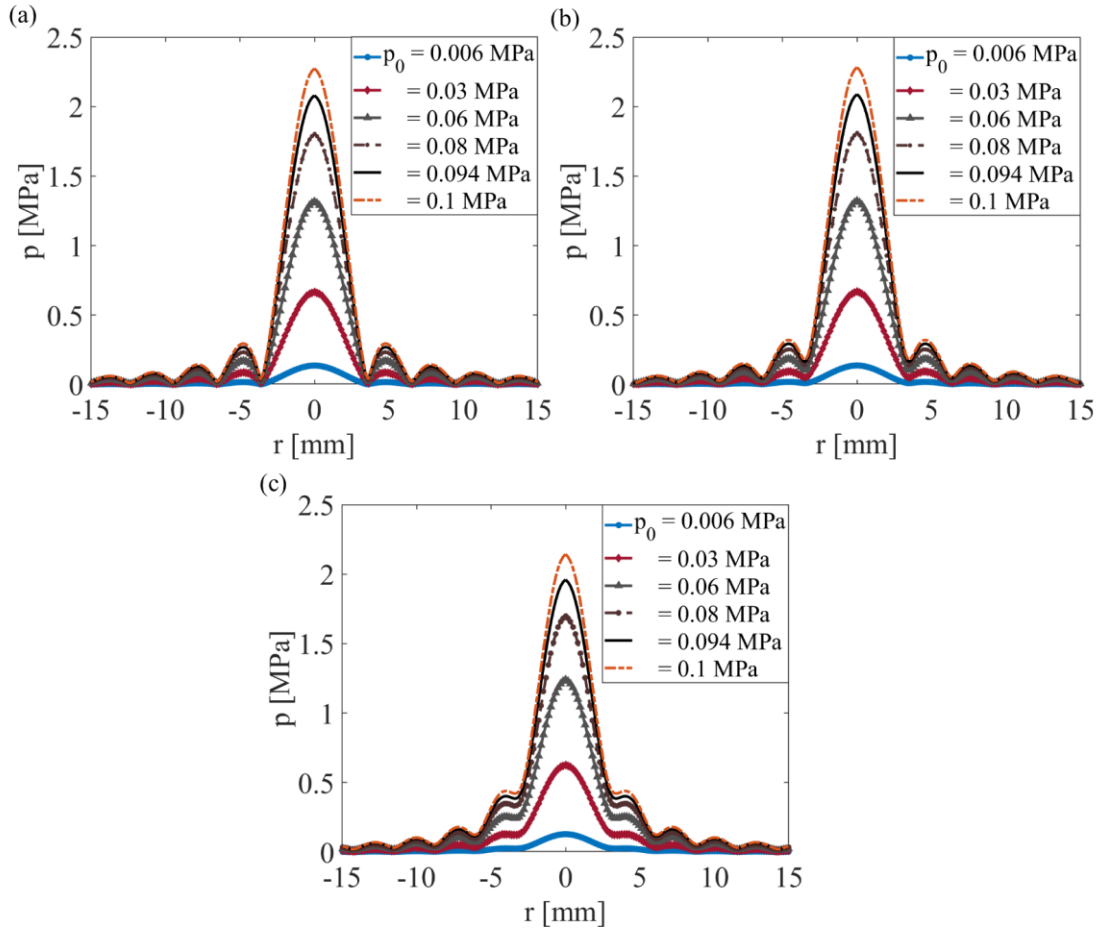


Fig. 7.7. Pressure fields along radial axis at varying source pressure at (a) $z = 0$, (b) $z = -2$ mm, and (c) $z = -5$ mm.

In conclusion, in this work, we investigate the dynamics of the electrical response of a piezoelectric cylindrical receiver of finite aspect ratio in a HIFU-UPT system. The interplay of acoustic and material nonlinearities along with standing wave formation plays a critical role in determining the MPOP of the disk, which is necessary to account for designing efficient UPT systems. The MPOP shifts towards the transducer as the input source excitation increases, upto a certain excitation threshold. This behavior is contrary to the general trend where it is expected

that the focal point will be the MPOP for all levels of source excitation. The transfer of energy from the fundamental to higher harmonics, which is maximum at the focal point, plays a key role in shifting the MPOP. Acoustic saturation at lower threshold levels as compared to travelling waves, is seen for a UPT system in spatial resonant HIFU fields.

References

1. G. V. B. Cochran, M. P. Kadaba and V. R. Palmieri, *Journal of Orthopaedic Research* **6** (1), 145-147 (1988).
2. Q. Shi, T. Wang and C. Lee, *Scientific Reports* **6**, 24946 (2016).
3. H. Kawanabe, T. Katane, H. Saotome, O. Saito and K. Kobayashi, *Japanese journal of applied physics* **40** (5S), 3865 (2001).
4. A. Sanni, A. Vilches and C. Toumazou, *IEEE transactions on biomedical circuits and systems* **6** (4), 297-308 (2012).
5. X. Bao, W. Biederman, S. Sherrit, M. Badescu, Y. Bar-Cohen, C. Jones, J. Aldrich and Z. Chang, presented at the *Industrial and Commercial Applications of Smart Structures Technologies 2008*, 2008.
6. D. J. Graham, J. A. Neasham and B. S. Sharif, *IEEE Transactions on industrial electronics* **58** (10), 4972-4980 (2011).
7. Y. Hu, X. Zhang, J. Yang and Q. Jiang, *IEEE transactions on ultrasonics, ferroelectrics, and frequency control* **50** (7), 773-781 (2003).
8. S. Shahab and A. Erturk, *Smart Materials and Structures* **23** (12), 125032 (2014).
9. M. R. Awal, M. Jusoh, T. Sabapathy, M. R. Kamarudin and R. A. Rahim, *International Journal of Antennas and Propagation* **2016** (2016).
10. A. Bhargava, K. Peng, J. Stieg, R. Mirzaeifar and S. Shahab, *RSC Advances* **7** (72), 45452-45469 (2017).
11. M. F. Hamilton and D. T. Blackstock, *Nonlinear Acoustics*. (Academic Press, 1998).
12. F. A. Duck, *Ultrasound in Medicine & Biology* **28** (1), 1-18 (2002).

13. T. G. Muir and E. L. Carstensen, *Ultrasound in Medicine & Biology* **6** (4), 345-357 (1980).
14. M. S. Canney, M. R. Bailey, L. A. Crum, V. A. Khokhlova and O. A. Sapozhnikov, *The Journal of the Acoustical Society of America* **124** (4), 2406-2420 (2008).
15. O. V. Rudenko, C. M. Hedberg and B. O. Enflo, *Acoustical Physics* **47** (4), 452-460 (2001).
16. C. Vanhille and C. Campos-Pozuelo, *Ultrasonics* **43** (8), 652-660 (2005).
17. A. B. Coppens and J. V. Sanders, *The Journal of the Acoustical Society of America* **43** (3), 516-529 (1968).
18. A. Bhargava and S. Shahab, **(submitted)** (2019).
19. A. Bhargava, K. Peng, J. Stieg, R. Mirzaeifar and S. Shahab, presented at the ASME 2017 Conference on Smart Materials, Adaptive Structures and Intelligent Systems, Utah, USA, 2017.
20. V. C. Meesala, M. R. Hajj and S. Shahab, *Nonlinear Dynamics* (2019).
21. T. S. Hart and M. F. Hamilton, *The Journal of the Acoustical Society of America* **84** (4), 1488-1496 (1988).
22. A. Rozanova-Pierrat, *Mathematical analysis of Khokhlov-Zabolotskaya-Kuznetsov (KZK) equation*. (2006).
23. A. Bhargava and S. Shahab, *Smart Materials and Structures* **28** (5), 055002 (2019).
24. T. H. M. Hamilton, *J. Acoust. Soc. Am* **84**, 1488-1496 (1988).
25. E. L. Carstensen, W. K. Law, N. D. McKay and T. G. Muir, *Ultrasound in Medicine & Biology* **6** (4), 359-368 (1980).
26. L. E. Kinsler, A. R. Frey, A. B. Coppens and J. V. Sanders, *Fundamentals of Acoustics*, 4th Edition, by Lawrence E. Kinsler, Austin R. Frey, Alan B. Coppens, James V. Sanders, pp. 560. ISBN 0-471-84789-5. Wiley-VCH, December 1999., 560 (1999).
27. F. A. Duck and M. A. Perkins, *IEEE transactions on ultrasonics, ferroelectrics, and frequency control* **35** (2), 232-241 (1988).

Chapter 8 : Summary of contributions and prospective future research

8.1. Summary of contributions

This dissertation presents the fundamentals of high intensity focused ultrasound (HIFU) actuation of two types of smart materials; shape memory polymers (SMPs) and piezoelectric disks.

In chapter 2, a novel concept for solving some of the challenges in the field of controlled drug delivery is introduced through the use of SMP-based drug delivery capsules functioning under HIFU. It is proposed that drug delivery can be controlled both spatially and temporally by entrapping the drugs inside the SMP capsules, and only releasing them upon focused ultrasound (FU) actuation at the targeted location. The drug release rate is controlled by controlling the shape recovery behavior responsible for opening and closing the container. A multiphysics framework is developed for the first time in literature, to quantify the SMP actuation under FU exposure. The framework is divided into three interconnected stages, with the first stage predicting the acoustic pressure field in the fluid and SMP mediums. The second stage estimates the thermal field inside the SMP generated due to absorption of ultrasound in the polymer and the consequent oscillation of polymer molecules. The third stage uses a constitutive model to estimate the shape recovery of the polymer that is dependent upon the thermal stresses accumulated inside the polymer. Proof-of-concept experiments are conducted for a SMP filament to validate the theoretical model. A good agreement is observed between experimental

observations and model predictions. Using the model, it is found that increasing the nonlinearity of acoustic waves by increasing the acoustic source intensity or frequency or by choosing a medium with high coefficient of nonlinearity, leads to increased thermal energy deposition and thus, higher shape recovery. Several composition and geometrical parameters are also examined to understand how these factors influence shape recovery. Based on the optimum parameter combination, a flower shaped drug delivery capsule design is proposed.

In chapter 3, the previously built mathematical model in chapter 2 is extended to account for acoustic wave propagation in multi-medium environments, such as human body. The SMP capsule is assumed to be kept inside the artery of a human heart. The multiphysics model is used to investigate the effects of different layers of tissues, muscles, and blood on acoustic waves propagating towards the capsule, which ultimately affects the thermal field generation and subsequent shape recovery behavior of SMP capsule. Numerical simulations from experimentally-validated model show that FU induced thermal field is completely concentrated inside the polymer capsule, keeping the surrounding tissues safe from thermal ablation. This model is also used to propose several geometrically optimized designs for drug delivery capsules, based on the analysis of the effect of geometrical parameters on shape recovery performed in chapter 2. It is demonstrated that by varying the FU operating parameters such as intensity and frequency externally, the motion of the in-vivo capsule can be controlled in a pre-determined manner, thus, achieving the desired drug release rate. 3d printing in collaboration with Medshape company is investigated to realize these capsule designs. Several experimental investigations are conducted to examine how the 3d printed pattern affects the shape memory

effect. Out of all the obtained samples, it is seen that criss-cross geometry and the smallest width shows maximum shape recovery. While the behavior observed with decreasing the width agrees with the model predictions in chapter 2, observation of better shape recovery from criss-cross geometry can be due to better thermal conductivity, heat capacity, or elastic modulus. These material properties depend on 3d printing pattern. These results provide a basic framework for 3d printing optimum designs for drug delivery capsules for in-vivo operation.

The work in chapter 4 stems from a two-fold need. First, developing a dynamic model to provide an in-depth understanding of the thermomechanical behavior of FU actuated shape memory polymers. Second, deriving a simplified analytical expression for the FU induced shape recovery behavior, such that the computationally heavy modeling in chapter 2 is eliminated, and the user can predict the SMP recovery directly with the knowledge of material parameters and operation conditions. Using Hamilton's principle and a constitutive model developed by Liu *et al.* [1], equations of motion are derived for all four stages of shape recovery process for an Euler-Bernoulli SMP cantilever beam considering acoustic, geometric, and thermomechanical nonlinearities. These equations provide an in-depth analysis of the FU induced shape memory behavior from a kinematic perspective, for the first time in literature. A simplified expression using the method of multiple scales is developed for a geometrically weak nonlinear beam, which relates FU operation and material parameters directly to the amount of shape recovery in the SMP cantilever beam. The simplified expression is successfully validated with numerical simulations. The semi-empirical numerical model for equations of motion shows good agreement

with experimental observations for geometrically strong nonlinear beams, thus establishing a groundwork for designing more complex SMP-based systems.

The work in chapter 5 addresses the requirement of understanding remotely actuated shape memory behavior for devices operating underwater. With the increase of SMP use in many applications such as biomedical, robotics, and MEMS systems which work in underwater environments, there is a lack of sufficient studies on the influence of fluid medium on shape recovery behavior. Experimental investigations are conducted which show that the shape recovery is significantly less for SMPs immersed in water, as compared to air. Two possible reasons are discussed in this work. First, fluid loading effects which provide additional damping to the shape recovery amplitude. To examine this effect, the previously built numerical model in chapter 4 is modified to include fluid loading effects and verified with finite element simulations. The model predicts that due to slow rate of shape recovery, velocity dependent fluid damping effects play a negligible role in affecting the SMP cantilever beam shape recovery. Second, thermal cooling effects in water are investigated using finite element method. It is postulated that even though the temperature rise in the SMP immersed in water is higher as compared to air, the rate of temperature rise significantly affects the shape recovery. With high rate of temperature increase in SMP underwater, a longer time is needed to achieve the same amount of shape recovery as in air. Since the FU actuation time is fixed, the SMP recovery in water is lower than air. These results pave the way for efficient operation of SMP based devices in underwater scenarios.

In chapter 6, HIFU actuation of piezoelectric receivers is introduced as a way of solving some of the challenges faced by current ultrasound power transfer (UPT) systems. By focusing the energy exactly at the location of receiver, higher efficiency is achieved due to low scattering losses as compared to unfocused acoustic sources. Moreover, this work develops a comprehensive multiphysics theoretical model to account for the focused acoustic-structure interaction effects and consequent piezoelectric response. This model aims to fulfill the existing need of systematic analysis of UPT systems and provides performance enhancement methods. The model shows good agreement with experimental observations where a piezoelectric disk is placed at the focal point of the HIFU transducer and actuated for a short duration of time. Besides addressing some of the existing challenges, the proposed work also provides an advancement over existing models in three following aspects. First, the existing models assume only piston-like motion of the piezoelectric disk i.e. thickness direction displacement, which significantly simplifies the formulation of electroelastic response of the receiver. However, this work highlights that for a disk with finite aspect ratio, such an assumption does not hold true due to the dependency of displacement profiles of the disk on both radial and thickness directions. Second, the existing models do not account for acoustic-structure interaction effects where the total pressure field falling on the disk is a sum of incident, reflected, and scattered pressure from the disk. Third, with increasing levels of acoustic excitation, acoustic nonlinearities become significant. However, the current models do not address the response of receivers in acoustically nonlinear fields, which may lead to inaccurate results for UPT systems under high acoustic power excitation. The developed model is implemented in a finite element formulation and does not account for geometric or material nonlinearities in the disk. The model predictions show that a

disproportionately high electrical power output can be achieved when the harmonics in the acoustic field coincide with the structural resonant frequencies of the piezoelectric disk. In addition, the model was implemented in a frequency domain formulation to reduce the computation time. The formulation was incorporated such that the total response under a nonlinear acoustic field obtained from time domain simulations is equal to the sum of the power output response of the disk at all significant harmonics, obtained from individual frequency domain simulations. With this formulation, the computation time of time domain simulations was reduced from days to minutes in frequency domain.

Chapter 7 reports a short study where experimental investigations are conducted to understand the response of a finite-size piezoelectric receiver in a FU field. The actuation duration is long enough such that the standing waves are formed due to reflection from the transducer and receiver surfaces. This study aims to inform the maximum power output operating conditions for HIFU-UPT system. Due to the focusing nature of ultrasound, it can be assumed that the maximum energy transfer will happen at the focal spot of the HIFU transducer. However, the experiments showed that the maximum power output position shifts towards the transducer at higher acoustic excitation. This shift is due to an interplay of acoustic nonlinearity, standing waves, material nonlinearities, and acoustic saturation effects with increase in sound excitation level.

Due to the coincidence of only fundamental acoustic frequency with one of the resonant modes of the disk, only fundamental acoustic field plays a role in the power output response. However, the energy in the fundamental field is transferred to higher harmonics and reaches saturation at

high excitation levels. This transfer and saturation occur at a lower acoustic power input level in standing wave field as compared to saturation thresholds for travelling waves, and is maximum at the focus. Thus, with the increase in acoustic excitation, the location of the highest fundamental pressure amplitude shifts and thus, result in higher power output from the disk at locations away from the focal point.

8.2. Intellectual merits

The experimental, numerical, and theoretical investigations of FU actuation of SMPs facilitate the application of this concept in diverse industries. The proposed work of FU actuation of SMPs introduces, for the first time, fully coupled mathematical acoustic-thermoelastic model and aims at filling a knowledge gap for the development of FU actuated SMP systems, which were till now only experimentally tested. The work illustrates the advantages of utilizing fundamentals of nonlinear acoustic field in order to optimize the shape memory effect. The idea is also used to demonstrate a novel mechanism for achieving targeted drug delivery where SMP based drug delivery capsules can be actuated by FU inside the body. By manipulating the FU induced shape memory response, controlled drug release can be attained from these capsules. The proposed mathematical framework gives the flexibility of making geometrically optimized SMP systems and reducing experimental cost. The proposed work also opens the door for understanding how 3d printed patterns can affect the shape memory behavior of polymers.

The above acoustic-thermoelastic model is further extended to give a kinematic perspective to the above system and introduce for the first time, the dynamics of FU actuated SMP systems. It aims to develop equations of motion for the entire shape recovery process using reduced order

mathematical modeling techniques. An analytical solution to predict the amount of shape recovery response as a direct function of FU parameters for a 1-D system is derived. This solution helps to analyze the effect of individual FU parameters directly on the SMP response and eliminates the need of undertaking rigorous modeling efforts to understand the complex physics of the FU actuated SMP mechanism. With such a tool, one gets the flexibility to manipulate several FU parameters and estimate their impact as well as achieve desired SMP response directly. This work is also extended to give an insight on how shape recovery behavior behaves in dense fluid mediums as compared to air, playing a crucial role in designing SMP-based underwater systems.

Another proposed work aims at studying the rarely explored area of focusing acoustic energy on the piezoelectric receivers for increasing the efficiency of existing wireless UPT systems. For the first time in literature, the proposed work looks into the fundamentals of the effects of acoustic nonlinearities, receiver geometry, acoustic resonance, material nonlinearities, and acoustic saturation on FU induced electroelastic response, thus enabling better accuracy and efficient designing of UPT systems, as compared to current works. The research involves developing experimentally-validated mathematical framework to couple the nonlinear acoustic field which takes into account diffraction, absorption, and nonlinearity of the medium, with non-conservative electroelastic response of the receiver at high excitation levels. The proposed framework proposes a technique to reduce the computational cost and complexity while maintaining good accuracy. The mathematical model and experiments provide a way to study individual

characteristics of the acoustic-electroelastic physics and optimize them for designing FU actuated electroelastic receivers for various applications.

8.3. Broader impacts

The proposed works of FU actuated smart material systems open a new category of actuating technique which is biologically safe, spatially and temporally controllable, and remote as compared to other mechanisms such as mechanical, photo or chemical excitation. Thermo-responsive polymers and piezoelectric materials form a large portion of the family of smart materials [2]. Therefore, developing experimentally validated frameworks to quantify their response upon FU actuation paves a way for acoustic-thermoelastic and acoustic-electroelastic analysis of a large category of smart systems. Developing theoretical frameworks give an opportunity to study the individual characteristics of the entire system and increases the overall understanding of the fundamental physics of the otherwise complex multiphysics phenomena. These frameworks allow the optimization of the desired functional response without undertaking expensive experimental investigations. These reports form an essential base for designing and fabricating complex designs. The range of applications that can be explored are numerous such as SMP based drug delivery devices, SMP based space components, SMP based electronic switches, piezoelectric biomedical implants, piezoelectric noise sensors, among others. The research findings are disseminated through conference presentations and scholarly publications.

8.4. Awards, recognitions and media coverage:

Awards

1. Amir Chand and Dewki Bai Batra fellowship 2019
2. Graduate Student Symposium Research Award- Bronze Medal at Virginia Tech, 2019
3. Best Student Paper Award at SPIE/NDE 2019 - Honorable Mention
4. Liviu Librescu Fellowship, 2018
5. Best Student Paper Award at SMASIS 2017- First Place

Journals

1. **Bhargava, A.**, Peng, K., Stieg, J., Mirzaeifar, R., and Shahab, S., 2017, *Focused Ultrasound Actuation of Shape Memory Polymers; Acoustic-Thermoelastic Modeling and Testing*, RSC Advances, 7, 45452 [3].
2. **Bhargava, A.** and Shahab, S., 2019, *Coupling of nonlinear shape memory polymer cantilever dynamics with focused ultrasound field*, Smart Materials and Structures, 28, 055002 [4]
3. **Bhargava, A.** and Shahab, S., 2019, *Contactless acoustic power transfer using high-intensity focused ultrasound* (in review)
4. **Bhargava, A.**,* Meesala, V.* and Shahab, S., *Experimental investigations of nonlinear dynamics of piezoelectric receivers in nonlinear acoustic field*, (in progress). (*equal contribution)

Presentations/proceedings have been contributed to the national and international scientific conferences:

1. International Mechanical Engineering Congress & Exposition, Salt Lake City, Utah, November 2019.
2. SPIE Smart Structures + Nondestructive Evaluation, Active and Passive Smart structures and Integrated Systems 2019 [5]
3. Biomedical Engineering Society Annual Meeting 2018 (poster presentation)
4. SPIE Smart Structures + Nondestructive Evaluation, Active and Passive Smart structures and Integrated Systems 2018 [6]
5. ASME 2017 Conference on Smart Materials, Adaptive Structures and Intelligent Systems [7]

Media coverage:

Study takes a unique approach to new generation of smart drug delivery carriers, Fall 2017

<https://vtnews.vt.edu/articles/2017/10/eng-smartdrugdelivery.html>

8.5. Future prospects

The potential areas, among many others, for extending this research are:

1. Experimental studies of shape recovery behavior inside tissues using ex-vivo setups to understand how tissue layers influence the acoustic waves reaching the SMP and how the surrounding medium affects the SMP recovery. Possible effects that tissue layers can cause is high reflection and scattering of sound waves, possible cavitation, hinder SMP

recovery due to surrounding fibers. In such conditions, a study to investigate the optimum parameters for achieving desired drug delivery should be done.

2. Extend the developed model in chapter 2 to predict the drug release rate in fluid-immersed SMP capsules upon shape recovery and experimental validation. The first step will involve detailed investigation to find the optimum 3d printed patterns selected according to the criterion of obtaining best material properties that support desired shape memory effect. This will be followed by ex-vivo studies for testing various capsule designs and validating the model predictions of drug release rate from the capsules.
3. Extend the theoretical model developed in chapter 4 to include the effects of heating rate, holding time, relaxation effects, and loading duration as it has been shown to affect the shape recovery behavior [8]. The simplified expression obtained from perturbation methods can also be further modified to directly relate all these parameters with the amount of shape recovery.
4. For UPT systems, the work in chapter 7 can benefit from extensive modeling efforts including electroelastic, geometric, and acoustic nonlinearities in a standing FU field to eliminate the cost and time of experiments. The model can serve as a comprehensive groundwork for performance enhancement methods and efficient designing of HIFU-UPT systems.

References

1. Y. Liu, K. Gall, M. L. Dunn, A. R. Greenberg and J. Diani, *International Journal of Plasticity* **22** (2), 279-313 (2006).
2. M. Schwartz, *Encyclopedia of Smart Materials*, 2 Volume Set, by Mel Schwartz, pp. 1176. ISBN 0-471-17780-6. Wiley-VCH, March 2002., 1176 (2002).
3. A. Bhargava, K. Peng, J. Stieg, R. Mirzaeifar and S. Shahab, *RSC Advances* **7** (72), 45452-45469 (2017).
4. A. Bhargava and S. Shahab, *Smart Materials and Structures* **28** (5), 055002 (2019).
5. A. Bhargava, K. Peng and S. Shahab, presented at the SPIE Smart Structures + Nondestructive Evaluation, 2019.
6. A. Bhargava, K. Peng, R. Mirzaeifar and S. Shahab, presented at the SPIE Smart Structures and Materials + Nondestructive Evaluation and Health Monitoring, Denver, USA, 2018.
7. A. Bhargava, K. Peng, J. Stieg, R. Mirzaeifar and S. Shahab, presented at the ASME 2017 Conference on Smart Materials, Adaptive Structures and Intelligent Systems, Utah, USA, 2017.
8. K. Yu and H. J. Qi, *Soft Matter* **10** (47), 9423-9432 (2014).